Laser Ablation – Film Capture – Electrospray Ionization – Mass Spectrometry

LA-FC-ESI-MS

A thesis presented in partial fulfilment of the requirements for the degree of

Master of Science

In

Chemistry

at Massey University, Albany, New Zealand

Zhirui Mao

Abstract

Laser ablation mass spectrometry (LA-MS) is an analytical method widely used in various fields. This study investigates a modified version of LA-MS that involves using a moving liquid film to capture and transfer the laser ablated material into a mass spectrometer. The use of a moving film to capture the ablated material and convey it to the electrospray ionization (ESI) source of a mass spectrometer allows for real time analysis, and the use of a focused laser spot across a translating sample allows for spatial resolution to be achieved. The addition of ionization enhancers, such as formic acid, or metal chelating agents to the liquid film allows additional flexibility when coupled with soft ionization afforded by an ESI source. This method allows for samples to be ablated in an open system under ambient atmospheric conditions. To demonstrate the versatility of this novel technique: solid graphite; caffeine powder and droplets; wood; and school shark vertebrae were all studied using this new method.

Acknowledgements

I would like to express my acknowledgement and appreciation to all those who have inspired me and supported this study. It was only possible to finish this research with guidance, help and support from them.

Thank you to my supervisor Dr John Harrison for always helping and guiding me. I am extremely grateful to have a responsible and supportive supervisor like you. I am grateful for all the feedback, advice, and encouragement during my difficult time.

To my lab co-worker, Alex, thank you for your support and advice. I appreciate all the help and support. Thank you for all the vertebral samples you have prepared and provided. Also, thank you for the image results from the CT scan and microscope.

To my beloved family, thank you for all the support, understanding and love. Thank you for letting me study abroad, so I've experienced such a different academic journey. I am so glad that I chose to complete my master's degree at Massey University.

Thank you all!

Contents

List of Figures

List of Tables

Chapter 1. Introduction of Laser Ablation

Laser ablation in analytical chemistry became popular in recent years based on numerous reviews and many published papers. Physicist Theodore H. Maiman developed the first ruby laser in 1960 after Einstein presented the idea of laser theory. After that, several researchers conducted studies to describe the essential factors of ablation. In 1962, Breech and Cross collected light emitted from ablated metals, which led to laser microprobe emission spectroscopy for elemental analysis of solid materials. Linlor, in 1963, used time-of-flight measurements to determine the energy possessed by ions ejected during ablation (Ravi-Kumar et al., 2019). Laser technology has practical applications in various sectors, including military, health, industrial, and scientific fields. Laser printers were among the first recognized applications, invented by US engineer Gary Starkweather in 1971. Lasers are widely used in manufacturing for drilling, cutting, holography, metal deposition, and additive manufacturing.

Laser ablation is a straightforward process where a short-pulsed high-power laser beam is focused on a sample surface, converting a portion of the solid sample into vapor. The vapor is then analyzed by measuring atomic/ionic emission in the induced plasma (LIBS) or transporting it to another measurement system, such as the inductively coupled plasma (ICP). Compared to conventional dissolution techniques, laser ablation offers several advantages. It eliminates the need for sample preparation procedures and allows for analyzing any solid sample without size requirements. Laser ablation requires smaller sample quantities (micrograms to picograms) compared to solution nebulization (milligrams), and it enables spatial characterization of heterogeneity in solid samples with micron-level resolution.

During LA, accuracy is mainly affected by two properties: laser wavelength and pulse duration. Fractionation from nanosecond pulse lasers is more sensitive to wavelength than fractionation from picosecond lasers. Shorter wavelengths generate more powerful pulses and reduce fractionation. Wavelength also affects the thermal mechanisms of LA, which may cause considerable fractionation (Russo, 2002). With matched calibration standards, the accuracy of the processes can be enhanced (Russo

et al., 2013)

Plasma can absorb or reflect laser energy, which is called plasma shielding. In general, absorption increases as wavelength increases. Short wavelengths and high photon energy travel through the plasma more efficiently, which leads to a higher ablation rate and less fractionation. Plasma shielding can be minimized using helium as an ambient gas because of its light mass and high ionization potential (Russo, 2002).

With LA, only a tiny amount of the sample is required, and even a femtogram target portion could be sufficient depending on the measuring approach. LA measurements require nearly no sample preparation or sample size restrictions. Analyte spatial properties of the solid target can also be obtained (Russo, 2002). In addition, LA is a real-time analytical method that can be carried out under atmospheric pressure. However, LA also has disadvantages, such as difficulty in obtaining suitable standards, fractionation, and sample destruction (Russo et al., 2013).

The physics behind LA involves the absorption of laser energy, rapid heating, vaporization and partial ionisation of a small amount of the mass of the sample. The process and the efficiency of LA are mechanism-dependent (Russo et al., 2013). A small amount of the sample is converted to plasma under the high-powered laser beam. Then the plasma is captured and analyzed using another measuring instrument, such as inductively coupled plasma (Russo, 2002), or the optical emission from the plasma is analysed directly.

One of the main methods for MS imaging is secondary ion mass spectrometry (SIMS). Ambient ionization methods, including desorption electrospray ionization mass spectrometry (DESI-MS), surface-sampling probe electrospray ionization, and laser ablation electrospray ionization (LAESI), have also gained attention (Manicke et al., 2010). DESI imaging and LAESI imaging are promising techniques for mapping the spatial distribution of organic molecules on sample surfaces. DESI uses charged droplets to ionize and desorb analytes directly from the sample surface, while LAESI employs an infrared laser beam to desorb the sample material into the gas phase. Both techniques allow minimal sample preparation before analysis and have been

successfully applied in various fields (Pereira et al., 2022).

One benefit of ambient analysis is that it requires little to no sample preparation, reducing analysis time and simplifying the process. However, untreated samples, particularly in tissue imaging applications, can be chemically complex, requiring high selectivity for successful implementation. DESI-MS has achieved increased selectivity through tandem mass spectrometry, in situ chemical reactions, and high-resolution mass spectrometry (Manicke et al., 2010).

Electrospray ionization (ESI) was developed in the late 1960s by Dole and his team, who successfully introduced a charged polystyrene polymer into the gas phase. John Fenn was awarded a share of the 2002 Nobel Prize in chemistry for his contribution to the development of ESI, which builds on pioneering work by Malcolm Dole's lab (Maher & Emmott, 2022). ESI-MS is a simple technique that involves dissolving a sample in a buffer or solvent, which is sprayed to form charged droplets vaporized with a neutral gas, resulting in ions that desorb into the gas phase. ESI-MS is commonly used for qualitative and quantitative studies of nonvolatile and complex biological structures. The technique has been optimized, and nanospray technology has been developed to improve glycoconjugate analysis. ESI continues to attract researchers investigating new applications and technical improvements (El-Aneed et al., 2009).

Combining mid-IR laser ablation with electrospray ionization, LAESI is a technique that is used for sample analysis. It falls under a category of techniques that includes IR matrix-assisted laser desorption electrospray ionization (MALDESI) and electrospray laser desorption ionization (ELDI); however, for the sake of discussion, they are all referred to as LAESI (Shrestha, 2021). In LAESI, neutrals are generated through mid-IR laser ablation using a 2.94 μm wavelength laser pulse. The water molecules strongly absorb this wavelength due to OH vibrations, making the native water content in the tissue act as a matrix for coupling the laser energy. The neutrals are generated as the ablation plume expands, and they are then intercepted by electrospray and ionized. LAESI has been used to analyze metabolites in various plant organs, human bodily fluids, and animal tissues, as well as in single-cell analysis of plant tissue.

The laser ablation atmospheric pressure photoionization (LAAPPI) is a related ambient ion source that provides complementary molecular detection to LAESI, particularly for larger nonpolar compounds. LAAPPI and LAESI can achieve sub-100 μm spatial resolution imaging mass spectrometry of the rodent brain with novel strategies for IR beam focusing.

MALDI is a commonly used ionization source for protein sequencing and proteomic research, often used to ionize molecules for analysis by MS, providing high sensitivity, high throughput, and simplicity of operation (Fenselau, 1997). In MALDI, a sample is dissolved in a solvent, mixed with a matrix, then spotted on a MALDI plate and air-dried. A laser beam is then used to desorb ions from the solid phase and ionize the analytes in the sample. The choice of matrix can affect ionization mode, with basic matrices preferred for negative mode and acidic matrices preferred for positive mode. Laser ablation has gained significant interest in analytical optical and mass spectrometry, particularly in laser ablation optical and mass spectrometry with inductively coupled plasma (LA-ICP-AES/MS). This approach enables the nearly non-destructive determination of various elements with very low detection limits, finding applications in various academic and industrial fields, such as environmental analysis, geology, archaeology, forensics, and semiconductor manufacturing.

In 1985, Alan Gray introduced laser ablation - inductively coupled plasma - mass spectrometry (LA-ICP-MS). Laser ablation is commonly coupled with the ICP-MS method because of the high sensitivity of ICP-MS (Russo, 2002). LA-ICP-MS has become a widespread technique across various research fields for analyzing the elemental compositions of samples and generating nanoparticles from the target subjects (Sylvester & Jackson, 2016). An LA system usually contains a laser, an ablation stage, and a detection system. Several lasers have been employed in LA-ICP-MS systems, such as Nd^{3+}:YAG, ruby, and excimer lasers, but Nd^{3+}:YAG lasers are the most economical since they do not require gas-filled chambers or considerable maintenance. The fundamental wavelength of the Nd^{3+}:YAG laser is 1064 nm, and this frequency can be doubled, tripled, etc. (Russo, 2002), whereas the wavelength of the

excimer laser is related to the operating gas (Durrant & Ward, 2005). $Nd3^{+}$: YAG lasers have a Gaussian beam profile and can be focused on a small beam area. The shape of the ablation crater tends to be cone-like with the Gaussian beam profile, but specific imaging optics can be used to make the crater flat-bottomed (Russo, 2002).

A difficulty in interpreting LA results is the fractionation that can occur during the process. Fractionation that is specifically related to laser irradiance can be compensated for using calibration, such as standard matrix matching, to improve measurement accuracy. Element fractionation can occur during LA, transportation between ablation and ICP, or the ICP process. Fractionation is related to melting, boiling, and other elemental properties. Chan et al. have stated that elements with lower melting points are more likely to exist in a vapor phase (Russo, 2002).

In the ICP, particles are vaporized and ionised. Depending on their mass-to-charge ratios, the ions are separated by a mass spectrometer and analyzed by a detector. Calibration standards can be used to convert ion intensities into element concentrations. After correcting for measurement bias related to sample mass, ion intensities can also be converted into isotopic ratios or ages (Sylvester & Jackson, 2016). Gas is applied to transport the plasma to the ICP. Multiple articles mention that sensitivity and transport efficiency could be improved by employing helium gas or a mixture of helium and argon in the LA system. A high flow rate reduces sample deposition and increases transport efficiency (Russo, 2002).

Quadrupole mass spectrometers and single collector sector-field mass spectrometers (SF-MS) are widely applied in ICP-MS systems, but other systems such as the multi collector sector-field mass spectrometry (MC-SF-MS), and time-of-flight mass spectrometry (TOF-MS) are also used with ICP-MS (Sylvester & Jackson, 2016). Although high-quality isotope ratio data can be obtained from the MC-SF-MS system, the cost of the instrument is prohibitive. In 2016, Gundlach et al. proved that TOF-MS can generate multi-element imaging with high speed. In another research study, two types of MS were used in one system, which is known as laser ablation split stream (Sylvester & Jackson, 2016). LASS can scan between selected masses, but large

particles induce space changes in the MS. “AES has high simultaneous multi-element but has much sensitivity and spectral interferences” (Russo, 2002).

Matrix matching is used to calibrate LA-ICP-MS systems. Ablation rates vary according to the sample matrices. There are three ways to gain matrix-matched standards: mixing compounds with a powdered matrix and pressing with or without a binder, mixing standard solutions and a powdered matrix, and adding a single element solution to a matrix (Russo, 2002).

The applications for LA-ICP-MS are expansive. In environmental science, tree bark, seashells, and airborne particulates are analyzed using LA-ICP-MS. For geological applications, the method has been used to measure U/Pb ratios to determine the earth’s age. Steven has pointed out that in marine chemistry, the teeth, bones, and other organs of marine animals have been analyzed using LA-ICP-MS, which has assisted with determining environmental changes. Using such research as inspiration, more research can be done on human tissues to study health, disease, and other problems (Durrant & Ward, 2005).

LA-ICP-MS, with the aid of matrix-matched standards, has been used to acquire precise quantitative data. Unlike simple homogenous samples, biological tissues are intricate, so the acquisition of matrix standards is challenging. Bonta solved this problem by coating samples with homogenous gold film. Gold works as a reliable internal standard and improves the quality of the experiment results (Bonta et al., 2014).

Chapter 2 Experimental

2.1. Laser Ablation – Film Capture – Electrospray Ionization – Mass Spectrometry (LA-FC-ESI-MS)

Our Laser Ablation – Film Capture – Electrospray Ionization – Mass Spectrometry (LA-FC-ESI-MS) method is unique because we will introduce a thin film of liquid on a glass slide to capture the material ejected from the surface of the laser ablated sample. Traditionally, a small amount of the sample surface is vaporized and converted to plasma because of the laser beam's high pulse energy. Then the plasma is captured by ICP-MS, where the ions in the plasma are further excited and subsequently introduced to the mass spectrometer for elemental composition analysis. However, we will use a combination of FC and MS instead of ICP-MS; ideally, the liquid film will capture the hot plasma. Later, the liquid film will be collected and pumped to MS through capillary tubes. To ensure a high ionization efficiency ESI and APCI in the dual ion source of the MS were utilised. Electrospray Ionization (ESI) is usually used for ionization of analytes in LC/MS systems because it works well for a wide range of analytes. Nevertheless, there are some situations in which specific analytes are not well ionized with ESI. In these cases, Atmospheric Pressure Chemical Ionization (APCI) can be used to increase sensitivity. Although both positive ESI and APCI produce a charged analyte, the ionization process is very different. ESI involves protonation of the analyte in the liquid phase, while APCI involves a protonated solvent molecule donating a proton to the analyte in the gas phase. APCI is usually more effective for ionizing non-polar, low molecular weight molecules, while ESI is better suited for polar, non-volatile molecules. However, depending on the characteristics of the analyte, a single ionization source may not provide sufficient information. That is where having access to both ESI and APCI ionization methods comes in handy, which can enhance the ability to ionize a variety of analytes (Beck & Schmidt, 2003). The experimental setup and principles are described in the method section.

By treating the glass slide to provide a hydrophilic surface it was possible to generate thin liquid films with acceptable optical properties, necessary for passing the

laser beam through onto the ablation target as shown schematically in Figure 2.1.1. It is crucial that both the film and slide are clear to ensure that most of the laser energy can pass through the slide and ablate the sample, without distortion of the laser beam. We selected standard microscope glass slides for their optically clear property and chose either pure MilliQ water, 0.1% formic acid, or 10^{-4} M EDTA, in MilliQ water as the liquid films for our experiments. We took into consideration the hydrophilicity of the glass slide, as all three solutions are water-based and need to adhere to the slide. Since the surface of the glass slide is typically hydrophobic, we utilized either a chemical approach (piranha solution) or physical treatment (plasma) to modify its hydrophilicity. Without surface modification the surface layer was prone to meniscus break and effectively unusable.

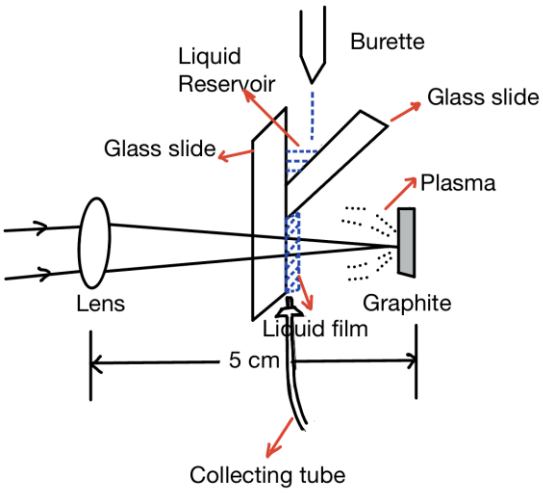

Figure 2.1. 1 A diagram of the FC system setup: Burette: Filled with the solution. Liquid Reservoir: Used to create pressure on the connection part between two glass slides. The pressure aids in the formation of a homogeneous liquid film. Liquid film: Designed to capture plasma. Lens: Used to focus the laser beam on the sample. The focal length is 5 cm.

2.2 Surface Cleaning

2.2.1 Piranha solution

Glass surfaces can be cleaned in several ways using wet chemicals, and some economic methods are available. For instance, one could use piranha solution, which is widely used in the industry to clean silicate-based surfaces and remove organic residues, carbonates, and metal oxides. Another affordable option is to place glass samples in oversaturated water vapors in an autoclave. Additionally, a base piranha treatment and a UV laser irradiation method have been introduced by Canning, which can reduce the contact angle and improve the hydrophilicity of the surface (Canning et al., 2012). Ultrasonication can also be used to treat glass with the help of a non-ionic detergent. Moreover, baking is suitable for treating the silicate surface, as mentioned by Kim: Quartz windows are cleaned with hot chromic acid, immersed in the solution for more than 3 hr, washed with excessive water, and baked overnight at 400 °C (Kim et al., 2001). A similar approach was used by Cremer, where a glass coverslip was baked in a kiln at 425 °C for around 4 hr (Cremer & Boxer, 1999). However, if samples are not delicate, a flame treatment can be considered.

The highly corrosive piranha solution that is widely used in the industry to clean silicate-based surfaces is often a mixture solution with a 3:1 ratio of sulfuric acid to hydrogen peroxide. The hydrogen peroxide concentration should be lower than 30%; the higher the concentration of peroxide, the higher the risk of explosion. Only the required amount of solution should be created, and it should not be stored. The acid should be added first, followed by the peroxide, which reduces the explosion risk. The hydrogen peroxide must be added slowly to allow the mixture to stabilize. Piranha solution acts as a strong oxidizer, as it increases the silanol groups and Si-O- on the glass to make the surface more hydrophilic. In one journal article, glass slides were treated with piranha solution for different times (5, 20, 40, and 60 min), rinsed with MilliQ water, and dried using nitrogen gas (Seu et al., 2007). In another journal article, glass slides were placed in the piranha solution for around 60 min to make their surfaces

more hydrophilic (Hull et al., 2005). The clean glass surfaces could be easily recoated with adsorbates, so the glass should be stored in a closed container filled with MilliQ water to maintain hydrophilicity.

Piranha solution was used to make glass slides hydrophilic, which was a necessary step in our laser ablation (LA) experiment since we will try to create a homogenous water or liquid film on the glass slide to capture the hot plasma. Different immersion times and position angles were tested to find a suitable way to efficiently treat the glass slides.

2.2.2 Plasma Cleaning

Plasma cleaning is a highly effective method of treating the surface of a solid object. It was introduced by Strong in 1935 and has become a major application of plasma materials treatment. However, the structures of the surface layers of glass, metal, and other subjects are quite complicated, so it is difficult to remove natural and technological contaminants from these surfaces (Belkind & Gershman, 2008). Natural contaminants are compounds that contain hydrogen or oxygen and carbon due to the sample's exposure to the atmosphere, whereas technological contaminents are compounds such as residual grease. The hydrophilicity and wettability of surfaces can be enhanced through plasma cleaning, and the surface structures can even be changed.

Compared to wet chemical treatments, such as piranha solution cleaning, plasma treatment is faster, more cost-effective, and more environmentally friendly. For example, chlorofluorocarbons (CFCs) and chlorinated hydrocarbons (CHCs) were used in chemical cleaning, but CFCs were banned in 1987 due to their environmental impact (Petasch et al., 1997). In any case, wet chemical cleaning cannot achieve atomic-level cleaning. Gas molecules convert to charged particles under high temperatures obtained through radiofrequency (RF) heating, and the result is a plasma forms. This process can lead to three phenomena: heating, sputtering, and etching, which occur when electrons and ions interact with the surface. DC, RF, and microwave glow are common plasma sources, and RF discharge sources are widely applied (Petasch et al., 1997). Different gases are employed into the system depending on the cleaning purpose and the type of

materials. For instance, oxygen gas is an appropriate choice for hydrocarbon removal.

2.2.3 Glass slide treatment

In this research, two methods for cleaning glass slides were tested. The first method involved using a chemical cleaning solution. To prepare this solution, 80 ml of piranha solution was created using 60 ml of H_2SO_4 (S.G. 1.83, ≥95%, A.R.G, Fisher chemical) and 30 ml of H_2O_2 (30% 100vol, analytical reagent grade, Fisher chemical). First, 30 ml of H_2SO_4 was poured into a clean beaker on a stir plate, followed by the slow addition of 10 ml of H_2O_2 using a glass pipette. The solution was stirred for approximately 5 minutes before being transferred to a larger container. An additional 50 ml of the piranha solution was prepared using the same procedure, but only 30 ml was made each time due to the high acidity and oxidation of the piranha etch.

Six glass microscope slides were then placed in a container filled with piranha solution for an hour. Following this, the slides were carefully taken out of the solution using tweezers and placed in a clean beaker with MilliQ water. The slides were then rinsed with MilliQ water three times to ensure they were completely clean. Finally, the treated slides were stored in a plastic container filled with MilliQ water.

The hydrophilicity of the glass slides was tested because we intended to form a homogeneous water film on the surface of the slide. The slide was placed under a 25 mL burette filled with MilliQ water to allow the water to run along the slide, and the extensiveness of the water film was checked. Two parameters, the angle and flow rate of the water, were determined. To determine the parameters, the incident angle of the glass slide with respect to the burette was changed, with the flow rate remaining the same. In addition, the flow rate was changed but the same incident angle was retained. Following this, the average thickness of the water film, the average speed of the water film formation, and other important parameters were calculated.

To roughly analyze the thickness of the water film on the glass slide, the weight, length, and width of the glass slide were measured. The glass slide was placed under a 25 mL burette, and the initial volume and the final volume of the MilliQ water in the burette were recorded. As soon as a water film formed on the glass slide, it was moved

to a pre-weighed clean beaker, and weighed using an analytical balance (METTLER TOLEDO, d=0.0001g, max=220g). In addition, the time at which the burette was turned on was also recorded. In the final water film system, two glass slides were used to form a reservoir at the top of the slide as shown in Figure 2.1.1 because the formation of the water film was neither stable nor did it completely cover the width of the slide when only one glass slide was used.

In the second method, glass slides were cleaned using a plasma etcher system consisting of a Harrick Plasma PDC-32G-2 plasma cleaner, an Edwards 1101 vacuum gauge controller, and an Edwards RV5 vacuum pump. Two glass slides were placed in the plasma chamber for 5 and 10 min, respectively, under low RF at around 1.2 mbar. The pressure was controlled by using a needle valve to leak laboratory air into the RF chamber at an appropriate rate to compensate for the pump out rate. Then, the glass slides were stored in a plastic container filled with MILLI-Q water. The slide with the longer treatment time became more hydrophilic but the water film on the slide was incomplete. Another two slides were placed in the cleaner with high RF at 1.4 mbar. The pressure dropped to 1.1 mbar within 10 min, and the water film was flawless. The slides were pretreated with piranha solution, but the slides that lost hydrophilicity were also put into the plasma chamber, and the slides became hydrophilic again. After comparing the conditions under which a water film formed, we selected placing two glass slides in the plasma cleaner under high RF for around 15 min as the final glass slide treatment.

Figure 2.2.3. 1 Plasma cleaner showing the needle valve, plasma cleaner and pressure gauge.

Figure 2.2.3. 2 The chamber of the plasma cleaner with slides in situ.

Figure 2.2.3. 3 The cleaner is on and under the high RF mode the glow from the plasma is clearly visible.

2.2.4 Result and Discussion

Once the glass slides were treated with piranha after one hour, they were stored in plastic containers filled with MILLI-Q water. However, we noticed that the glass slides lost their hydrophilicity over time, which meant a longer treatment time was required. After considering different options, we decided to leave the slides immersed in the piranha solution overnight. The hydrophilicity of the slides that were treated overnight was more stable and lasted longer.

The piranha etch method can be used to clean glass slides and enhance the affinity of the glass slide's surface for water. However, slides should be treated with the solution overnight, and the solution is extremely hazardous and needs to be handled with the utmost caution. With those issues in mind, another treatment method, plasma cleaning, was developed. Under high RF mode, only 15 minutes are required to boost the wetting

ability of the glass slides. Plasma cleaning seems to be a better option than the piranha chemical technique because it is safer, faster, and less expensive. With this simplified method, we no longer need to prepare the hazardous chemical solution and consider the immersion angles and other parameters.

In conventional laser ablation inductively coupled plasma MS method, hot plasma from the ICP is typically directed into the MS directly through an inlet. However, in our experiment, a water film was used to capture plasma during the ablation process. To obtain all the plasma with spatial characteristics, the water film needed to be homogeneous and stable. Therefore, the angle (between slide and burette), flow rate, time, and other factors were optimized during the design of the water film system.

It was found that when only one glass slide was employed, it was difficult to gain a consistent water layer that would last for over half an hour, regardless of the incident angle or flow rate. Therefore, two glass slides were introduced to the system, and a metal clip with Teflon seal was used to hold them in the correct position. After a few trials, we found that the surface of the glass slide was evenly and consistently coated with MilliQ water, and the water film would persist for more than 30 min.

2.3 LA-FC-ESI-MS system setup

The laser ablation source was the 532 nm output of a Quantel Q-Smart 850 with second harmonic module installed. All of the samples were ablated at room temperature under ambient atmospheric pressure.

Figure 2.3. 1 Laser instrument: Q-Smart 850

The average energy, maximum energy, and minimum energy of different Q-switch delays were recorded. For 15 and 10 μs Q-switch delay, energy values were measured twice, which showed that the average energies of the pulse were not constant (Table 2.3.1). Therefore, it is important to measure the average energy data before each ablation trial.

Table 2.3. 1 Average, max and min energy per pulse of various Q-switch delays of the laser.

Q-switch Delays (μs)	Average E (mJ)	Max E(mJ)	Min E (mJ)
150	9.27	11.8	7.50
135	20.8	23.4	18.6
120	34.3	38.1	31.2
105	58.7	63.0	54.7
90	82.8	87.4	77.3
75	114	121	108
60	159	168	153

45	222	232	213
30	278	291	265
15(1st)	317	328	304
15(2nd)	262	272	248
10 (1st)	292	304	278
10 (2nd)	246	259	232
7	231	242	220

The laser beam was directed onto the sample using three beam steering prisms (Newport), a short 50 mm focal length lens, a metal leaf iris, the slide/liquid film generation system, and a sample stage connected to a NE1000 syringe pump (New Era). The syringe pump served no other purpose than acting as a sample translation stage. The iris was placed in front of the lens to control the laser beam power passing through onto the target.

An examination of the back-reflection points from each prism face or from the lens was conducted to ensure the safety of the laser instrument and prevent any damage caused by the laser beam reflecting directly back to the source. Several metal shields were also used to prevent reflections of the laser beam from damaging the surroundings.

Figure 2.3. 2 Laser ablation system set up.

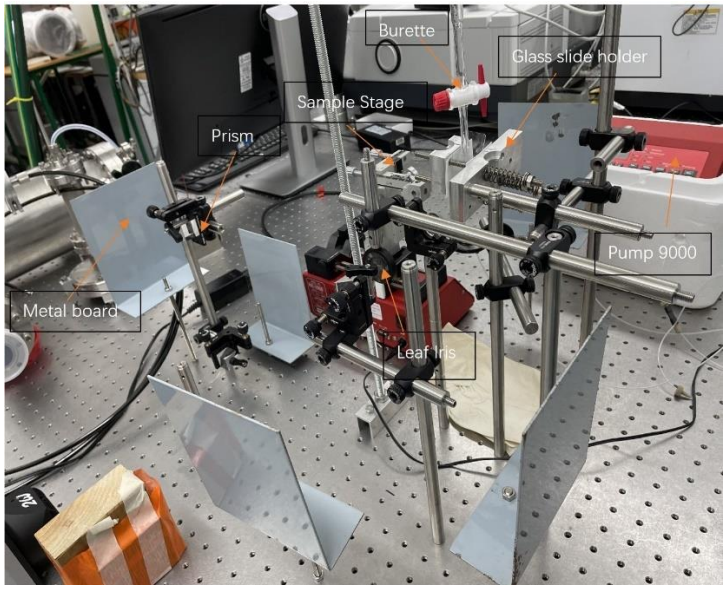

Figure 2.3. 3 The sample stage is set on the syringe pump NE1000.

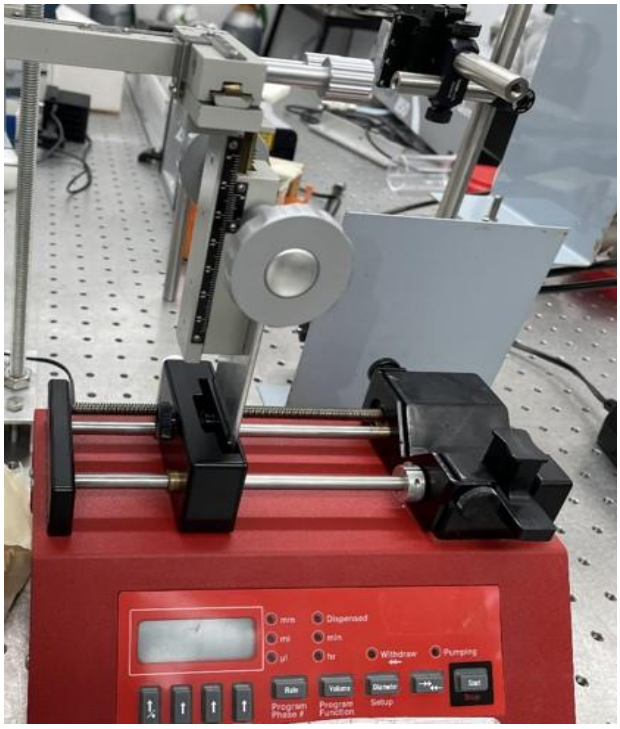

Figure 2.3. 4 The position of the lens and the FC glass slide setup.

Figure 2.3. 5 Glass slide A and B on the glass slide holder.

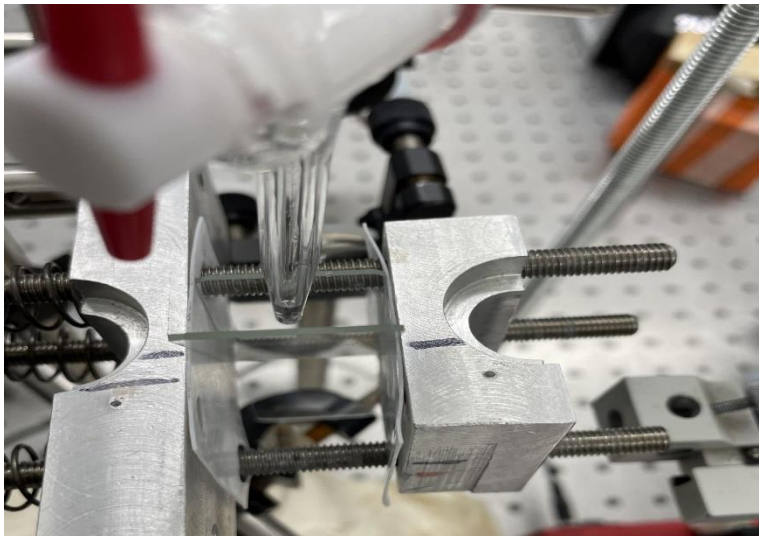

A separating funnel was placed above a 25 mL burette (0.05ml, MARIENFELD) for use as a convenient reservoir in refilling the burette. The burette was used as a convenient way of monitoring the liquid flow rate onto the slide. Glass slides that were cleaned with the plasma cleaner were placed under the burette that was filled with Milli-Q water. One glass Slide A was placed vertically in the metal glass holder, and another slide was cut in half and placed on an angle. When the solution ran through the burette, solution droplets accumulated where the two glass slides were in contact. The liquid reservoir caused pressure on the attachment, which aided the formation of an even liquid film on the surface of glass Slide B. After a few tests, a (moving) liquid film appeared and was still there after 30 min. The flow rate of the Milli-Q water was around 0.202 mL/sec. The glass slide should be placed in the range of the plasma to catch it in the liquid film, but care should be taken as the slide might be damaged by being close to the laser focus.

To collect the solution containing plasma following laser ablation of the sample, Tube A was attached to the bottom edge of the vertically straight glass slide. Only a portion of the solution was captured by the tube, while the rest of the solution dripped into a waste beaker. The other side of Tube A was connected to a New Era 9000 peristaltic pump. The sample solution was pumped to the MS ESI/APCI source through output capillary Tube B. The flow rate was set between 0.1 to 0.2 mL/sec.

2.4 Mass Spectrometer Setup Parameters

The ion source for the single quadrupole MS (Shimadzu LCMS 2020) was the DUIS (DUIS = dual ionization source: ESI + APCI). The other relevant MS parameters used were: desolvation line and heat block temperatures were 250 and 400 °C, respectively. The voltage of the detector was 1.45 kV, the interface voltage was 4.5 kV, and the voltage placed on the APCI needle was 4.5 kV. Nebulizing gas flowed at 1.5 L/min, while the drying gas flowed 10 times faster at 15.0 L/min. The pressures of the ion gauge and Pirani gauge vacuums were 7.5×10^{-4} and 1.1×10^{2} Pa, respectively.

Chapter 3. Applications

3.1 Graphite

3.1.1 Introduction

In our LA system, samples would be exposed to the atmosphere when ablated. Graphite is a thermally converted form of diamond with better light absorption properties. Wyszyński coated a diamond in graphite to prevent the sample from undergoing thermal shock when using a 115 ns-pulsed Nd^{3+}:YAG laser at 532 nm with a 10 Hz repetition rate to precisely machine diamond. The underlying diamond transformed to graphite to provide efficient absorption (Wyszyński et al., 2013). Again, the parameters of this laser system are the same as ours, excluding the length of the pulses. LA effectively laser drilled the material's surface; this was beneficial since laser drilling is more efficient than traditional mechanical drilling.

In 1994, Puretzky investigated the mechanism of creating fullerene from graphite rods in different inert gasses by applying a 30 ns-pulsed KrF laser beam at 248 nm with 20 J/cm^2 of energy to ablate the sample at 30-degree incident angles. Fullerene existed in both the soot of the sample surface and the material removed from the sample disk, but the fullerene from the ablated sample was dependent on the buffer gas (Puretzky et al., 1996). Our graphite sample will not be placed in a sealed chamber with buffer gas, so the mass loss of the target may be difficult to record due to the generation of fullerene, which means the ablation depth per a single pulse would be difficult to determine.

Veiko has tried a novel method of analyzing graphite samples using LA. Veiko introduced the method of studying laser-induced microplasma (LIMP), which is the plasma generated "at the interface of transparent and absorbing media" during ablation (Veiko et al., 2017). Transparent medium refers to a liquid or solid subject that may or may not be in complete contact with the ablated target. In Veiko's study, the silica transparent medium was in complete contact with the graphite, which provided nearly 100% energy efficiency of the LIMP to prove the method's capabilities. A 200 ns-pulsed laser beam with a repetition rate of 20 kHZ was focused by a lens, and the graphite was

adjacent below to a fused silica plate. Veiko summarized that LA methods that utilize transparent media have highly efficient laser energy and material removal along with great controllability. The experiment results for LIMP demonstrated relatively high precision and were very productive.

Veiko used a solid medium with a high repetition rate laser pulse to modify the surface of a graphite sample to create microplasma, whereas we will use a liquid medium formed on the glass slide to collect the hot plasma produced by the laser.

3.1.2 Method

It is assumed that graphite could oxidize during the ablation process in an open-air system, which is why it was chosen as the sample to test the laser ablation system. Prior to the ablation of the graphite sample, measurements were taken to determine the average energy, maximum energy, and minimum energy of different laser Q-switch delays.

The solid graphite block was ablated using a 10 ns pulsed Nd^{3+}:YAG at 532 nm with 10 Hz repetition rate. During the ablation, the sample was translated from left to right with the laser focus spot fixed. The purity of the sample was unknown. The focal length was 50 mm, and a glass slide with a water film was placed between the sample and focal lens, which was 43.6 mm from the graphite sample. The flow rate of the pump attached to the sample stage was 0.4 mL/min, and the translational velocity of the sample was calculated to be approximately 0.387 mm/sec. The flow rate of the New Era 9000 syringe pump was 2.2 mL/sec, and 20 mL glass vials were used to store the solution containing plasma. The Milli-Q water running through the water film was also collected into a vial used as a blank for the UV spectrometer.

To determine the best Q-switch delay option for the graphite ablation, five different pulse energies were applied to ablate the graphite once. For each run, a clean glass vial was used to collect the solution. Before each ablation, the energy value of the laser beam with the different Q-switch delay was measured by an energy meter (New Port Model 841-PE).

In addition, a second trial was conducted to determine the best compromise

between the distance between the slide and the target and the absorption intensity. Different laser pulse energies were chosen to ablate the graphite at different distances between the graphite and the slide with the water film. During the second trial, the repetition rate of the laser was changed to 5 Hz. Since the laser at this time was not stable, only two different distance were applied (42.7 mm and 38.2 mm) as the laser ceased working after the second distance had been measured.

All the solution samples were analyzed (offline) using 1 cm quartz cuvettes and a Shimadzu UV-2700 spectrometer to obtain UV-Vis absorption spectra. The wavelength range of measurement was between 190.00 to 1000.00 nm, with a medium scan speed and a slit width of 5.0 nm. The accumulation time was 0.5 sec and the wavelength of the light source change was 350.0 nm. The instrument was baselined using Milli-Q.

To further analyze the components in the graphite plasma, a high resolution mass spectrum (ThermoFisher orbitrap) measurement was obtained. Variables such as mass, intensity, laser pulse energy, and the distance between the glass slide and the sample were used to plot 3D scatter graphs using the RS studio program. These initial experiments were done in an offline mode where the sample was collected and then analysed at another location.

Later on, the graphite was ablated again with the laser source at full power, but 0.1% formic acid was used instead of pure Milli-Q water to create a liquid film on the slide. Formic acid is frequently used in ESI-MS analysis as a weak organic acid that is added to the sample solution under positive ion polarity mode (Wu et al., 2004). This helps in the formation of positive ions by facilitating the protonation of polar or neutral analytes (Cech & Enke, 2001). When it comes to the analysis of caffeine, which has two amine and two amide basic functional groups, an acidic solvent like formic acid is an ideal choice. The solution containing plasma was directly analyzed in real time by the MS without being collected into vials.

3.1.3 Result

The graphite sample was ablated five times, and the weight values were examined each time.

Table 3.1.3. 1 Time and mass change of the graphite sample were recorded, and the table showed that graphite was able to be ablated by the laser equipment. (A 7 ns Q-switch was applied, resulting in an average energy per pulse of around 230 mJ. Δn_C represents the moles of carbon lost by the target per laser pulse. Over a period of 60 seconds, the number of laser pulses used was $8x10^9$. Considering the molar mass of C is 12.011 g/mol, the average Δn_C was calculated to be 0.08058 mmol. Consequently, for each pulse, the average amount of carbon lost was 1.0×10^{-11} mmol.) This then gives an upper limit to the amount of material transferred at the lower pulse energies.

Time (sec)	Initial Mass (g)	Final Mass (g)	ΔM (mg)	Δn_C (mmol)
60	11.0339	11.0327	1.2	0.0999
60	11.0327	11.0319	0.8	0.0666
60	11.0319	11.0313	0.6	0.0499
60	11.0313	11.0299	1.4	0.1166
60	11.0299	11.0290	0.9	0.0749

3.1.3.1 UV-Vis Spectrometry Measurement of Plasma Produced by Graphite Ablation

Five different Q-switch delays and an additional blank sample obtained from running with the laser off were tested to ensure optimal results in ablating the solid graphite, and the spectra were obtained through a UV-vis spectrometer, which will help us determine the most efficient laser pulse for future experiments. The dependence of the signal on the laser pulse energy is not expected to be a simple linear relationship. In particular at higher pulse energies extensive atomization is expected to occur and subsequent atmospheric oxidation could result in only a small amount of material being captured by the liquid film.

Table 3.1.3. 2 Average, max and min energy per pulse of five Q-switch delays of the laser.

Average Energy per pulse (mJ)	Max Energy per pulse (mJ)	Min Energy per pulse (mJ)	Q-switch delay
11.1	13.1	9.99	130
53.6	59.7	49.2	105
114	122	108	75
231	245	218	60

272	286	261	45

Figure 3.1.3. 1 Overlay UV spectra of compounds from graphite ablation with different pulse energies. The distance between the water film glass slide and the sample was 43.6 mm. (11.1 mJ pulse energy --- blue color spectrum, 53.6 mJ pulse energy --- green color spectrum, 114 mJ pulse color energy --- purple color spectrum, 231 mJ --- blue color spectrum, 272 mJ pulse energy --- red color spectrum, blank (Milli-Q water run through the system)--- black color spectrum).

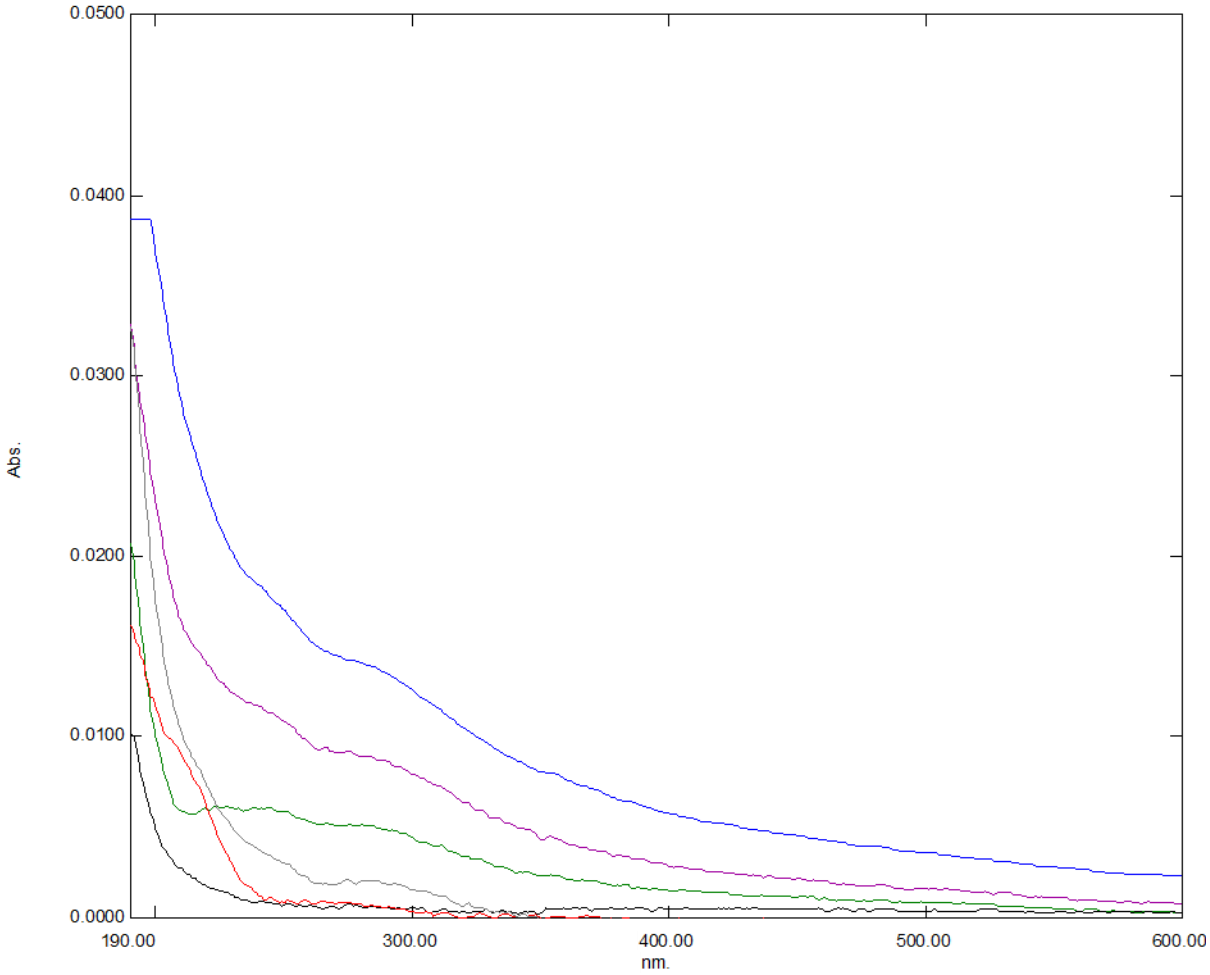

Table 3.1.3. 3 Laser pulse energies, and absorbance of different pluse energies at λ = 280 nm

Laser pulse energy (mJ)	Absorbance
0	0.0006
11.1	0.0020
53.6	0.0050

114	0.0089
231	0.0142
272	0.0007

Figure 3.1.3. 2 The graph shows the relationship between the laser pulse energy and the absorbance. In the pulse energy range of 0 to 231 mJ, the absorbance at 280 nm increased with higher pulse energy. Therefore, the upper limit of laser pulse energy required to ablate the graphite was around 231 mJ. However, once the pulse energy exceeded this upper limit, the absorbance started to decrease as the pulse energy increased.

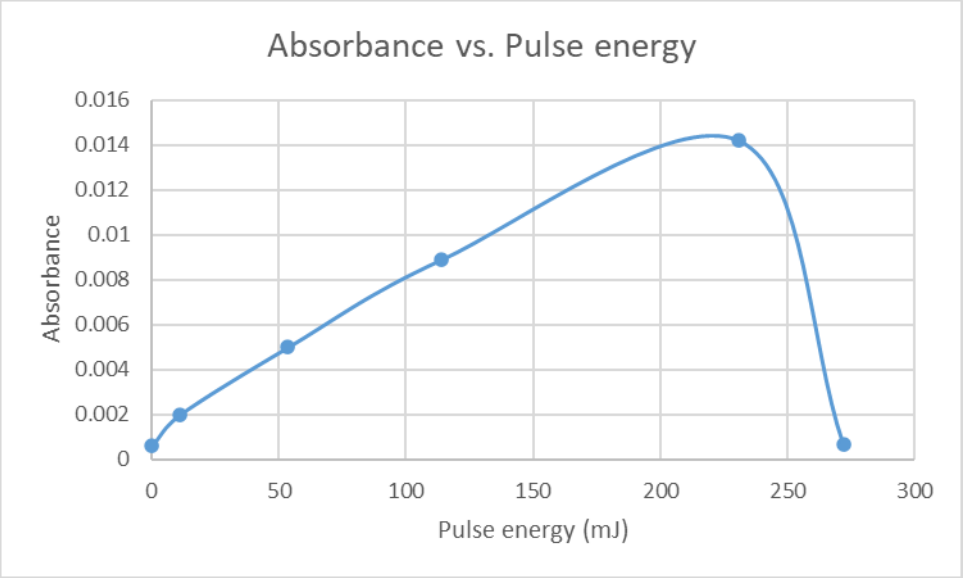

During the ablation process of the graphite, if the applied pulse energy exceeds the upper limit, the plasma's products might be decomposed into CO2 and released into the surroundings.

3.1.3.2 MS measurement of plasma produced by graphite ablation

The mass spectra of plasma from the graphite were presented below. The MS scan range was set from 100 to 1500 m/z (ESI +), but there were hardly any peaks over 800 m/z. This suggests that whatever was being ionized wasn't present in significant quantities. These mass spectra were obtained with a delay of about two weeks between sample collection and analysis because of the need to ship samples to a different location.

Figure 3.1.3.2. 1 MS spectrum of the blank of the LA system (MILLI-Q water) (The spectrum was normalized to the most intense peak.)

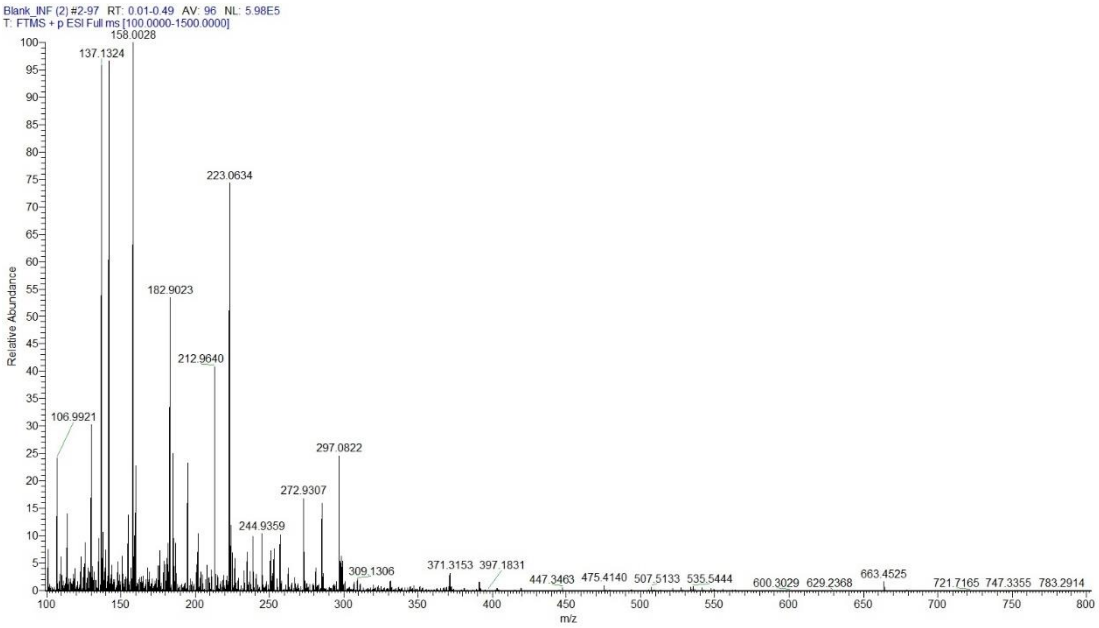

Figure 3.1.3.2. 2 MS spectrum of the plasma produced by graphite ablation. (The Q-switch was 105 μs, the average energy of each pulse was 53.6 mJ, and the distance was 43.6 mm. The spectrum was normalized to the most intense peak.)

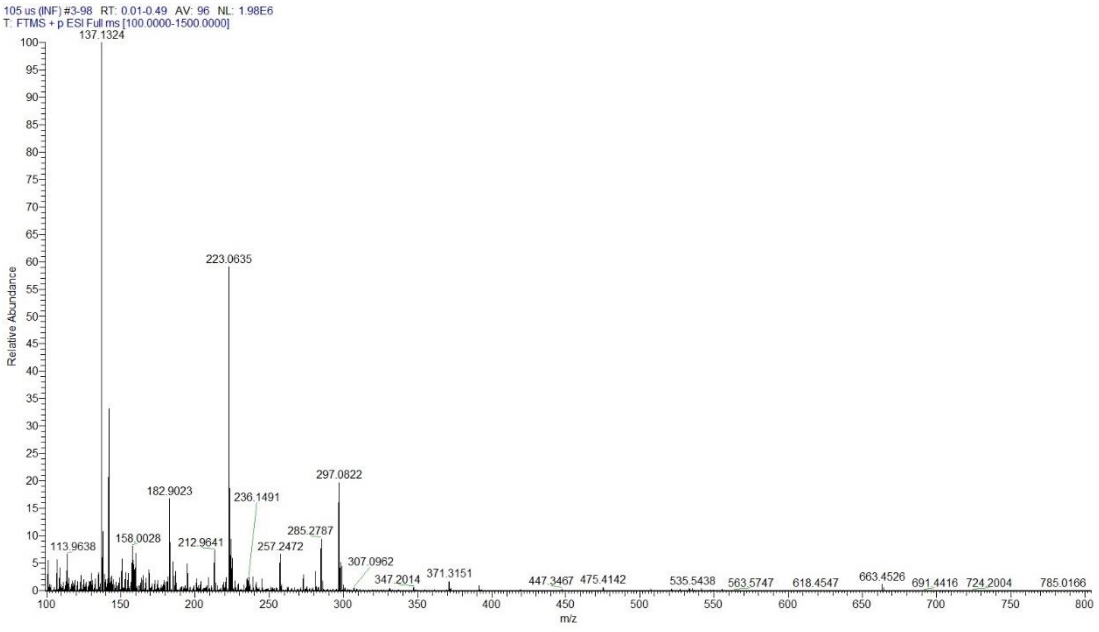

Figure 3.1.3.2. 3 3D scatter graphs. Three variables, mass, intensity, and the pulse energy value of each Q-switch delay, were used to plot another seven graphs. The 3D diagrams were plotted using raw MS data, and no normalization process was applied.

a. The range of mass is100-200 m/z.

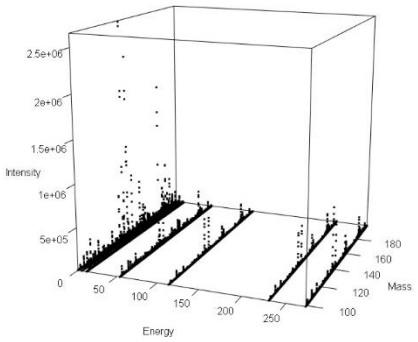

b. The range of mass is 200-300 m/z.

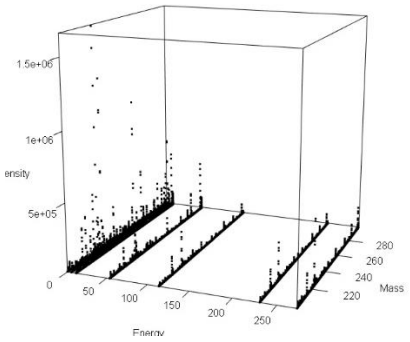

c. The range of mass is 300-400 m/z.

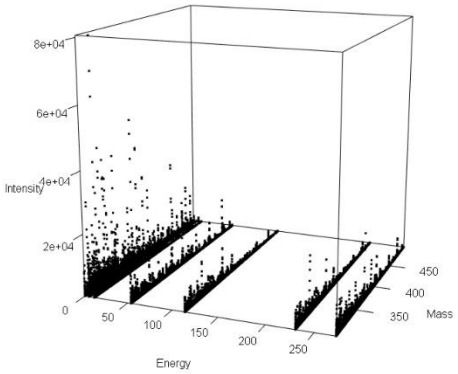

d. The range of mass is 400-500 m/z.

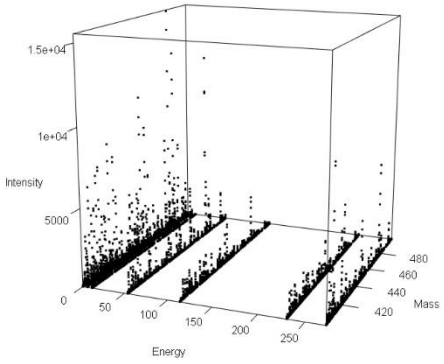

e. The range of mass is 500-600 m/z.

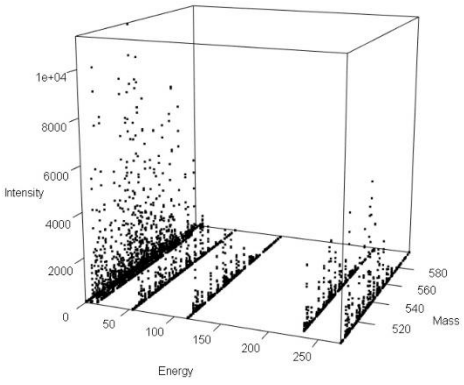

f. The range of mass is 600-700 m/z.

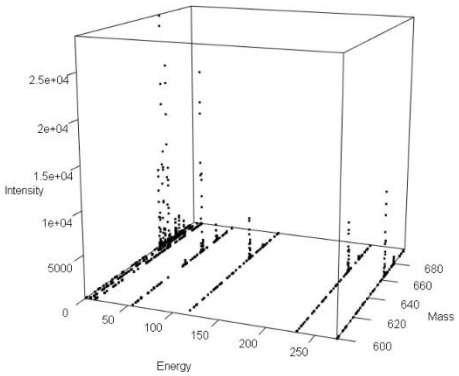

g. The range of mass is 700-800 m/z.

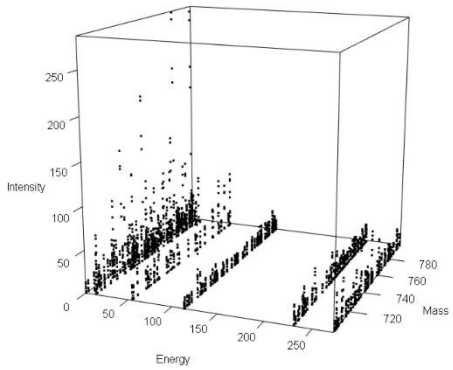

Table 3.1.3.2. 1 Mass peak from MS spectra and the compound prediction of each peak. The compound formulas were calculated using the Freestyle software (Thermofisher). The percentage of C, H, O, and N in each compound was determined based on the compound formula and molar mass. This chart was utilized to assess the degree to which the ablated graphite reacts with molecules in the atmosphere and transfers to the film. Additionally, it helped to understand how this process varies with pulse energy.

Q switch = 45 μs, E = 272mJ, d = 43.6 mm					
mass	compound	C%	H%	O%	N%
407.2219	$C_{26}H_{31}O_4$	76.6	7.7	15.7	0
475.4139	$C_{29}H_{53}O_2N_3$	73.2	11.2	6.7	8.8
663.4555	UNKNOWN				
766.6315	UNKNOWN				
Q switch = 60 μs, E = 231 mJ, d = 43.6 mm					
298.0826	$CH_{14}O_{10}N_8$	4.0	4.7	53.7	37.6
371.3149	$C_{22}H_{43}O_4$	71.1	11.7	17.2	0
447.3453	$C_{26}H_{45}O_3N_3$	69.7	10.1	10.7	9.4
547.26	$C_{19}H_{41}O_{13}N_5$	41.7	7.5	38	12.8
1194.806	UNKNOWN				
1247.694	UNKNOWN				
1302.637	UNKNOWN				
1430.482	UNKNOWN				
Q switch = 75 μs, E = 114 mJ, d = 43.6 mm					
184.9691	UNKNOWN				
405.2445	$C_{14}H_{31}O_5N_9$	41.5	7.7	19.7	31.1
493.2404	$C_{22}H_{33}O_7N_6$	53.5	6.7	22.7	17
539.279	UNKNOWN				
583.4374	$C_{24}H_{57}O_7N_9$	49.4	9.8	19.2	21.6
882.3004	UNKNOWN				
997.5286	UNKNOWN				

Q switch = 105 μs, E = 53.6 mJ, d = 43.6 mm					
257.2473	$C_{16}H_{33}O_2$	74.6	12.9	12.4	0
679.4284	$C_{24}H_{59}O_{12}N_{10}$	42.4	8.74	28.2	20.6
Q switch = 135 μs, E = 11.1 mJ, d = 43.6 mm					
262.2374	$C_{14}H_{32}O_3N$	64.1	12.3	18.3	5.3
290.2686	$C_{16}H_{36}O_3N$	66.2	12.5	16.5	4.8
291.2721	$C_{10}H_{31}N_{10}$	41.2	10.7	0	48.1
333.1665	$C_{15}H_{21}O_3N_6$	54	6.4	14.4	25.2
445.1196	UNKNOWN				
519.1378	UNKNOWN				
566.4417	UNKNOWN				
616.4393	C29H58O7N7	56.5	9.5	18.2	15.8
712.6354	UNKNOWN				
780.6323	UNKNOWN				
861.3693	UNKNOWN				
Q switch =150 μs, E = 4.88 mJ, d = 43.6 mm					
182.9022	UNKNOWN				
736.6475	UNKNOWN				
779.1562	UNKNOWN				
Q switch = 45 μs, E= 169 mJ, d = 38.2 mm					
mass	compound	C%	H%	O%	N%
212.9638	UNKNOWN				
405.2462	$C_{16}H_{33}O_6N_6$	47.4	8.2	23.7	20.7
507.3157	$C_{24}H_{41}O_5N_7$	56.8	8.14	15.8	19.3
754.8738	UNKNOWN				
847.8952	UNKNOWN				
928.5919	UNKNOWN				
965.1984	UNKNOWN				
1067.306	UNKNOWN				
1237.182	UNKNOWN				
1369.664	UNKNOWN				
Q switch = 45 μs, E = 182 mJ, d = 42.7 mm					
920.962	UNKNOWN				
1136.347	UNKNOWN				
1208.488	UNKNOWN				
1362.428	UNKNOWN				
Q switch = 60 μs, E = 158 mJ, d = 38.2 mm					
557.1122	UNKNOWN				
897.9808	UNKNOWN				
1031.863	UNKNOWN				
Q switch = 60 μs, E = 138 mJ, d = 42.7 mm					
1163.17	UNKNOWN				

Q switch = 150 µs, E = 6.25 mJ, d = 38.2 mm					
647.4571	$C_{28}H_{59}O_7N_{10}$	51.9	9.2	17.3	21.6
679.4302	$C_{24}H_{59}O_{12}N_{10}$	42.4	8.8	28.2	20.6
978.097	UNKNOWN				
Q switch = 150 µs, E = 6.19 mJ, d = 42.7 mm					
479.4808	$C_{28}H_{59}N_6$	70.1	12.4	0	17.5
516.1699	$C_{20}H_{28}O_{12}N_4$	46.5	5.5	37.2	10.8
614.8098	UNKNOWN				
701.9299	UNKNOWN				
721.5247	UNKNOWN				
1222.397	UNKNOWN				
1334.941	UNKNOWN				

Figure 3.1.3.2. 4 The graph shows the relationship between the element percentage for those molecules which had assignable masses and the energy of the laser pulse.

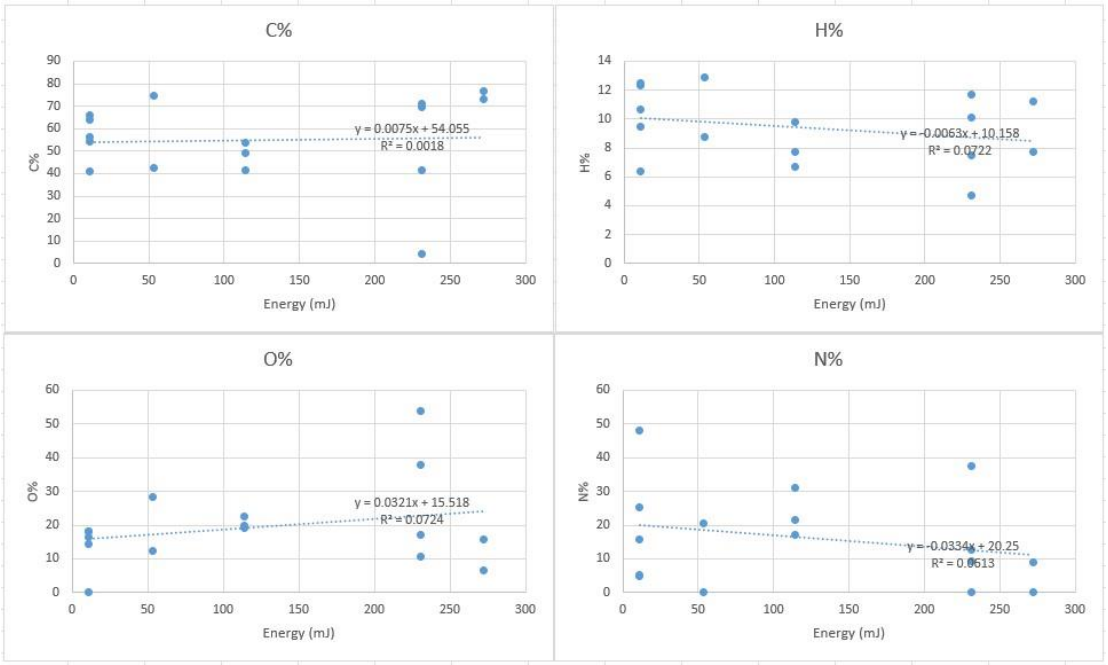

Figure 3.1.3.2. 5 The graph states the relationship between mass of compounds and the energy of the laser pulse

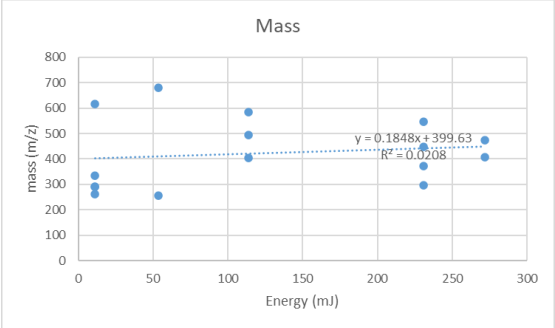

3.1.3.3 Graphite part 2

A Second series of graphite laser ablation were performed but for this series this was done using a low resolution mass spectrometer in real time. Both total ion count (TIC) and the mass spectrum of the products captured by the film are shown in the following figure. Solid Graphite was ablated by the laser pulse, and the plasma was captured by the liquid (0.1% formic acid) film. The liquid film was collected and transferred through the tube and pump to the MS directly. Based on the tube length and the flow rate of the pump, the delay time of the MS detection of liquid film was around 3.4 mins.

Figure 3.1.3.3. 1 shows MS spectra of the compounds produced by the ablation of graphite block. Top: Time dependence of the TIC (+), the spectrum of the raw data. Bottom: The signal was integrated from t = 5.828 min to t = 9.217 min, and the background was subtracted by integrating from t = 0.000 to t = 3.400

The Q-switch delay was 90 µs, the average energy was 72.5 mJ, and the range of the energy was between 80.2 mJ to 65.9 mJ. The ablation process started at t = 2.428 min and ended at t = 5.827 min. Since the delay time was approximately 3.4 min, the actual MS measurement time was from 5.828 min to 9.227 min.

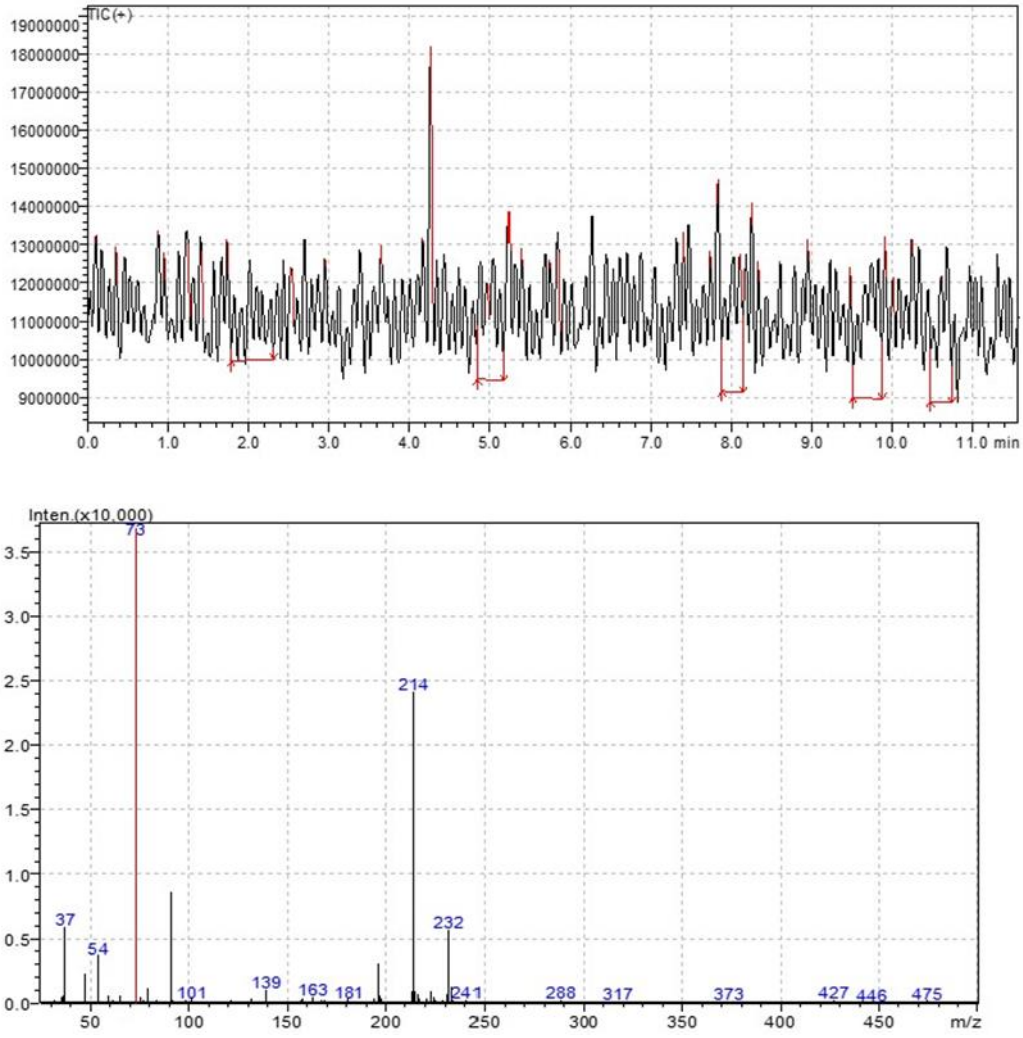

3.1.4 Discussion

Before attempting more challenging and complex sample matrices, solid graphite

was chosen as a test sample to optimize the LA system. The water film solution containing plasma was collected with vials and then analyzed by the MS either using high resolution MS off site or in an online configuration using low resolution MS.

Specific molecules are generated in plasma from the laser ablation of graphite in the air under atmospheric pressure. Diaz investigated the plasma produced by the laser ablation of graphite in different ambient gases. Laser-induced plasma can be produced in different phases of substances under various carrier gases once the ablation threshold is reached. It has been proven that the chemical properties and emission parameters of plasma generated under air differ from plasma produced with pure gases, such as Ar, N_2, and He.

In the laser ablation process of graphite under air or N_2 gas, C_2 is formed and can react with N_2 to convert to CN on the boundary layer of the laser-induced plasma (St-Onge et al., 1999). When using air as the carrier gas, emission bands of C I, C II, C_2, and CN are observed. The intensities of C and C_2 species reach their maximum within the first few hundred nanoseconds, but then quickly decrease. The wavelength range of CN peaks is between 376 and 390 nm based on the emission spectra. The increase in the intensity of C_2 and CN may be due to the rise in plasma temperature. Additionally, it should be noted that high temperatures during the process can lead to the destruction of the original sample's molecules. In Germain's study, the sample was placed in a vacuum chamber, which is typical for most laser ablation of graphite experiments. C^+ intensity peaks were observed at 588.9 and 723.6nm, while C^{2+} had peaks at 589.4 nm. The intensities of these species increased as the fluence values increased (Germain et al., 1993).

We discovered that the products captured by the film from graphite plasma varied depending on the laser energy applied. Diaz stated that since the percentage of O_2 in air is around 21%, which is relatively high, the formation of oxygen compounds is favored, leading to a decrease in the intensity and lifetime of CN and C_2 emissions (Diaz & Hahn, 2020). Choi's study found that C_n^+ ions (n = 1, 3, 5, 7, 11, and 15) were produced directly from the graphite surface. The intensities of C_1^+ and C_3^+ increased as the

energy of the laser increased, whereas C_5^+ and C_7^+ reached the maximum intensities first and then decreased as the laser fluence continued to increase. In other words, they believed large ions converted to small cluster ions (Choi et al., 1999). However, we found that more carbon compounds were produced at the lower energy levels, specifically in the range of 0 to 50 mJ (Figure 3.1.3.2. 3).

The possibilities for the molecular compositions of peaks from the MS spectra of the laser ablation of graphite are listed in Table 3.1.3.2.1. The compound formulas were calculated through the Freestyle software (Thermofisher). The ablation was carried out in air under atmospheric pressure, hence, the compounds formed in the plasma should only contain C, H, O, and N atoms. It can be seen from the table that the majority of peaks in the high resolution MS were not able to be assigned. The reasons for this are unclear. The relationship between the molecular composition and energy of the laser pulse was also studied. The R^2 values for all the plots obtained were below 0.1, hence, there was no linear trend between these two variables. Whether the intensities of molecular species increased as fluence values increased was uncertain. The intensity of these peaks was relatively low.

In 1985, it was discovered through the laser evaporation of graphite that spherical fullerene has a pyramidalization angle (Kroto et al., 1985). One of the most common stable fullerenes is Buckminsterfullerene (C_{60}). C_{70} and C_{60} are the two most abundant fullerene products derived from various physical processes (Kern et al., 2016). The C_{60} was first found in the graphite vapor generated by the laser ablation of solid graphite (Junaid et al., 2016). According to the results in Table 2.4, no C_{70} or C_{60} were detected through the MS. The graphite plasma in our LA-MS system was not transferred to the MS directly, and it was collected by the water film. Junaid stated that C_{60} is completely insoluble in water and the solubility in most organic solvents is limited. Ruoff mentioned that fullerene species have high solubility in solvents with a large index of refraction, a dielectric constant around 4, and a large volume of molecules (Ruoff et al., 1993). The refractive index and molecular volume of water are 1.33 and 18 ml/mol, respectively, which are small, although the dielectric constant of water at around 80 is

quite large. In other words, the C_{60} and C_{70} are highly insoluble in water. Therefore, it is reasonable that C_{60} and C_{70} could not be found by our LA-MS processes. Heymann found that the solubility of C_{60} is approximately $1.3x10^{-11}$ and C_{70} is approximately $1.3x10^{-10}$ ng/ml (Heymann, 1996).

Another round of graphite ablation was conducted, and the plasma was examined using the low resolution MS immediately afterwards. The laser was operated at full power, with the highest energy of the laser pulse exceeding 300 mJ. Signals ranging from 300 to 500 m/z were detected, indicating that the graphite was successfully ablated by the laser and that some plasma compounds were captured by the 0.1% formic acid film (Figure 3.1.3.3.1). Both high resolution and low resolution MS detected peak signals from 400 to 500 m/z. With high-resolution MS, raw data can be further analyzed through the software to obtain the possible formulas of the peaks. In contrast, in low resolution MS, the compound composition of detected peak signals remains unknown.

3.2 Caffeine

3.2.1 Introduction

Matrix-assisted laser desorption/ionization (MALDI), which is one of the essential techniques for analyzing large compounds, has been commonly applied in the biological field to study biomolecules with high molecular weights (Zenobi & Knochenmuss, 1998). One of the crucial parameters for MALDI is matrix selection, and selection generally occurs from a modest proportion of an established chemical matrix, such as benzoic acid. The actual choice of the matrix is highly correlated with the analytes. To detect the signal, targets are co-crystallized with a matrix compound, generally a small organic molecule. During the process, most of the energy from the laser pulse is absorbed by the matrix and then transferred to the targets (Harvey, 1999). Two-phase matrix-assisted laser desorption/ionization, graphite-assisted laser desorption/ionization (GALDI), and surface-assisted laser desorption/ionization (SALDI) are closely related approaches (Dreisewerd, 2003). Graphite can work as an alternative matrix for MALDI, which has been mentioned in several studies. In the

sample preparation of common GALDI, graphite suspension can be sprayed on the target, using pencil lead or a graphite plate to create a thin surface on the analyte (Dittrich et al., 2018). GALDI-MS has been used for the direct analysis of complex mixtures to obtain spectra (Dietemann et al., 2000).

Caffeine is a widely consumed stimulant found in coffee, tea, chocolate, soft drinks, and prescription drugs (Dalmázio et al., 2005). Caffeine is abundant in the environment and is easy to be detect through MS, so it was selected as one of the study targets. Caffeine solution was used to test the efficiency of the modified LA-MS method. Initially caffeine solution droplets were deposited on a glass slide and left to dry. These were then used as ablation targets, but under these conditions desorbed caffeine was not detected by the MS. Most of the laser energy was transmitted through the glass slide, or ended up ablating the glass so the caffeine was undetected. Therefore, we considered applying the caffeine onto a matrix to absorb the energy. The heating of the underlying matrix could then desorb molecules from the surface. From the previous study solid graphite provides very few background molecules when unfocussed laser pulses at 532 nm are used. However, the wide UV/Vis absorption spectrum allows the graphite to absorb 532 nm which makes it an ideal matrix.

3.2.2 Method

To make a saturated caffeine solution, 0.0274 g of caffeine powder was dissolved in ethanol. Next, 4 mL of concentrated formic acid (CH_2O_2, for MS, ~98%, Fluka Analytical) was added into 4 L of MILLI-Q water to obtain a 0.1% formic acid solution. The burette was filled with 0.1% formic acid rather than MILLI-Q water. For this series of experiment all samples were analysed using the realtime low resolution MS configuration. To establish whether the MS could detect caffeine, and what the fragmentation pattern of the caffeine was drops of caffeine solution were added to the MS system directly through the solution collecting tube to check whether the caffeine solution could be detected by the MS. This allowed the system time constants (time for the solution to pass through the peristaltic pump into the MS ion source, and subsequent time for the solution to be washed out of the system).

The caffeine solution was then dropped on the cleaned glass slide, and the solvent was allowed to dry to create caffeine deposits on the slide. The slide was then ablated by 532nm laser pulses and analyzed through MS. This proved unsuccessful at giving any detectable caffeine into the thin film. The glass slide was then replaced with a graphite block because graphite is believed to absorb laser energy and transfer it to caffeine. The final caffeine sample was created by rubbing caffeine powder on the surface of the graphite block. During the ablation process, all the samples were placed on the sample stage. The energy of the laser pulse was measured before each ablation. The flow rate of the NE 9000 peristaltic pump supplying the solution into the MS ion source was 0.1 mL/sec, and the polarity of the MS measurement was positive.

Figure 3.2.2. 1 Caffeine droplets glass slide. The ablation tracks indicating damage to the glass slide are clearly visible.

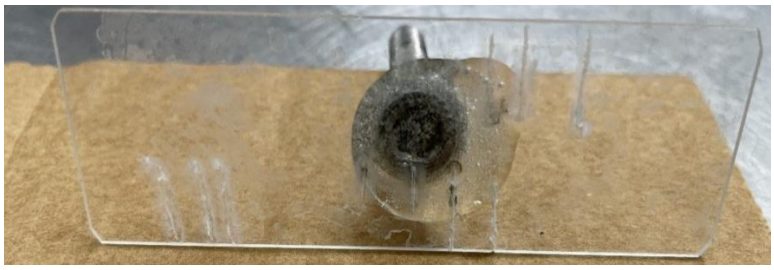

Figure 3.2.2. 2 Caffeine powder on the graphite block. The removal of the powder from the surface of the graphite block by the (unfocussed) laser is clearly visible.

3.2.3 Result

Low resolution mass spectrometry (MS) was used to detect caffeine and study its fragmentation pattern. Initially, caffeine powder was dissolved in ethanol to create the

saturated caffeine solution. Drops of the caffeine solution were directly introduced into the MS system to check its detectability and establish system time constants. However, the results from ablating the caffeine solution on a glass slide were not consistent. To improve the detection, the glass slide was replaced with a graphite block, known to absorb laser energy and transfer it to caffeine. Caffeine powder was rubbed on the surface of the graphite block to create the final caffeine sample. During the ablation process, all samples were placed on the sample stage, and the laser pulse energy was measured before each ablation. Overall, the measurement aimed to optimize the caffeine detection process using MS and explore the fragmentation pattern of caffeine under laser ablation.

Figure 3.2.3. 1 MS spectrum of one drop of caffeine solution, the flow rate of the pump was 0.2 ml/sec. The droplet was added into the system at t = 1.50 min. The delay time of this stage was around 3.4 mins. The data was integrated, and the background was subtracted (bottom figure). Caffeine compound (195 m/z) and caffeine + water compound (214 m/z) were found.

a). Time dependence of the TIC (+), the spectrum of the raw data.

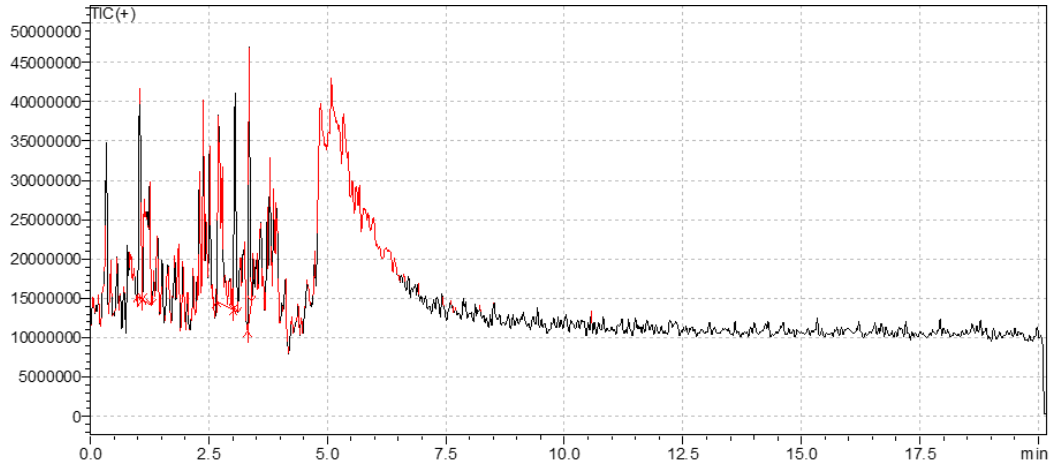

b). The signal was integrated from t = 4.90 min to t = 7.50 min, and the background was subtracted by integrating from t = 0.000 to t = 4.90.

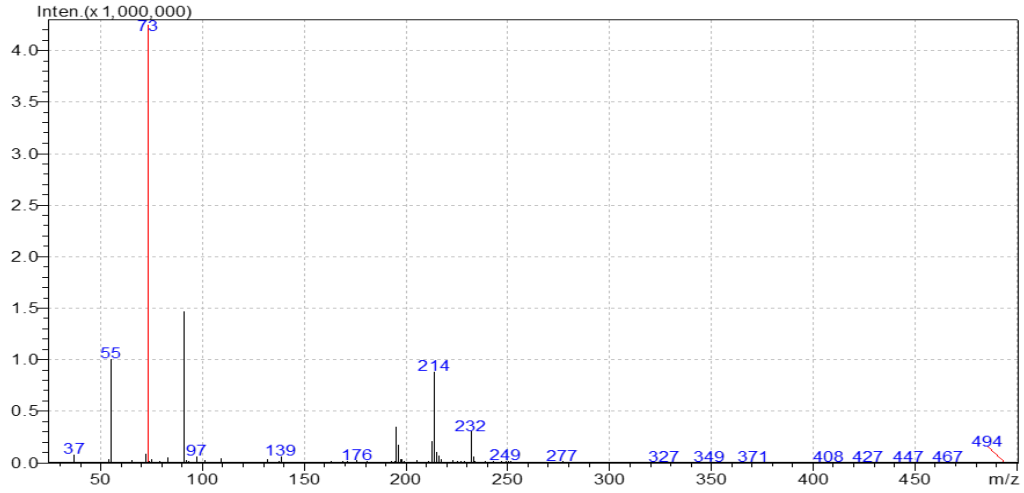

Figure 3.2.3. 2 MS spectra of the compounds produced by the ablation of caffeine droplets on the glass slide. The average energy was 244 mJ, and the range of the energy was between 266 mJ to 226 mJ. The ablation process started at t = 3.37 min and ended at t = 9.87 min. The second ablation process started at t = 15.58 min and ended at t = 22.02 min. The data was integrated (b & c) . Caffeine compound (195 m/z) and caffeine + water compound (214 m/z) were found.

a). Time dependence of the TIC (+), the spectrum of the raw data.

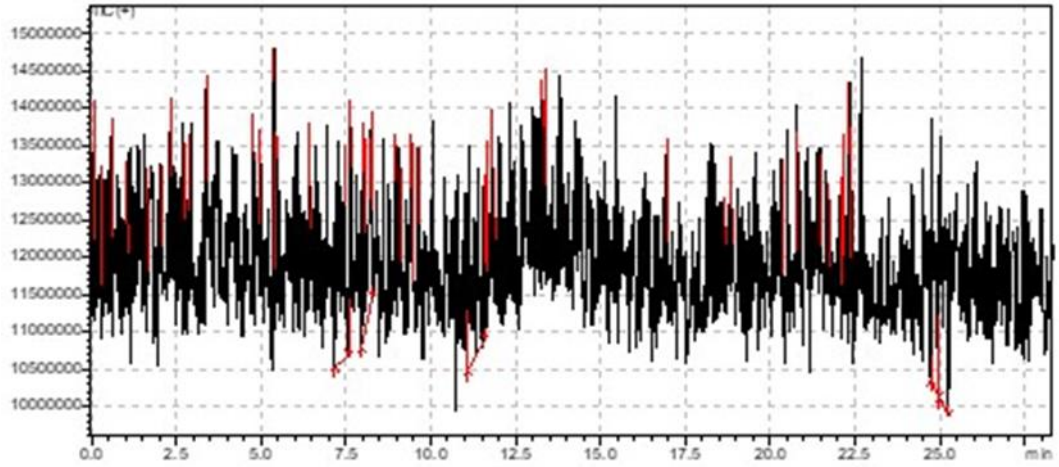

b). First ablation. The signal was integrated from t = 6.77 to 13.27 min, and the background was subtracted by integrating from t = 0.00 to 4.50 min

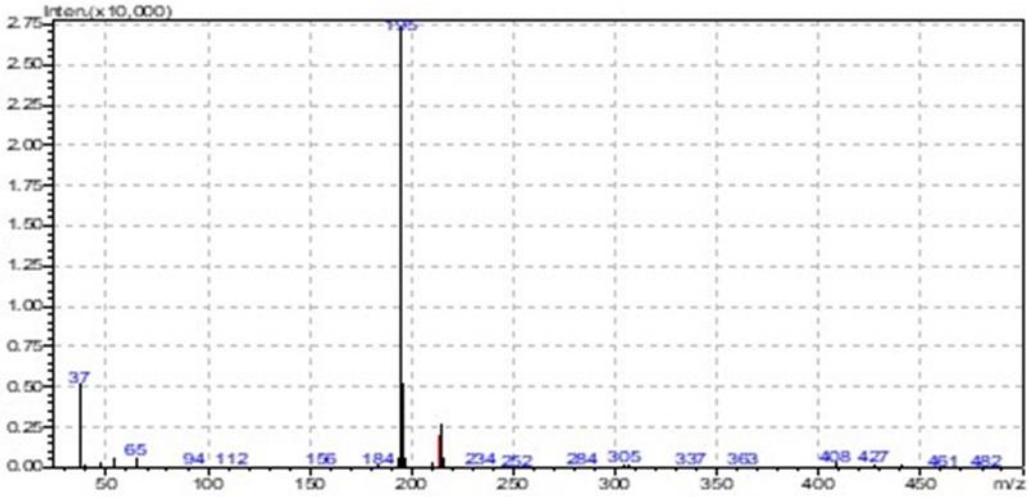

c). Second ablation. The signal was integrated from t = 18.98 to 25.42 min, and the background was subtracted by integrating from t = 0.00 to 4.50 min

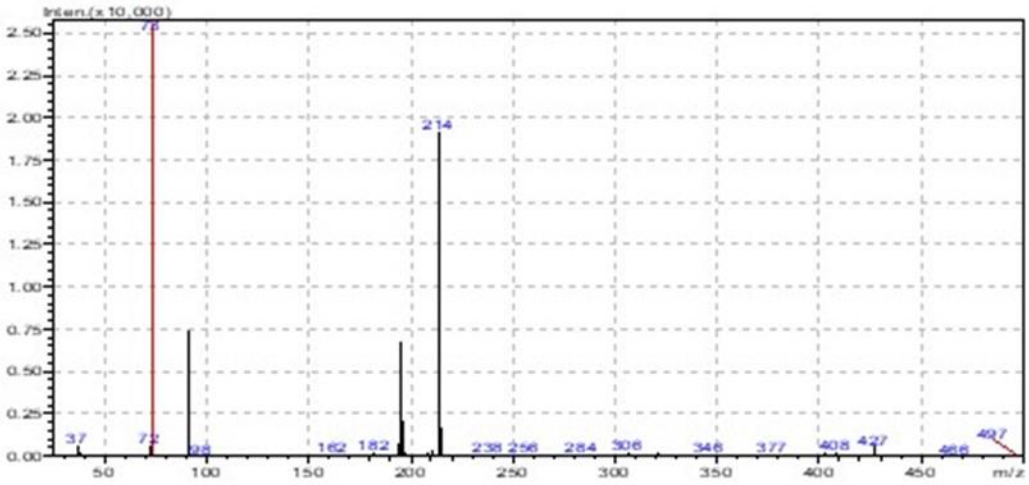

Figure 3.2.3. 3 MS spectra of the compounds that are produced after the ablation of caffeine droplets on the graphite surface. The focus lens was removed, and only the leaf iris was used. The average energy was 214 mJ, and the range of the energy was between 227 mJ to 192 mJ. The ablation process started at t = 3.67 min and ended at t = 9.43 min. The second ablation process started at t = 18.30 min and ended at t = 25.65 min. The data was integrated (b & c) . Caffeine compound (195 m/z) and caffeine + water compound (214 m/z) were found.

a) Time dependence of the TIC (+), the spectrum of the raw data

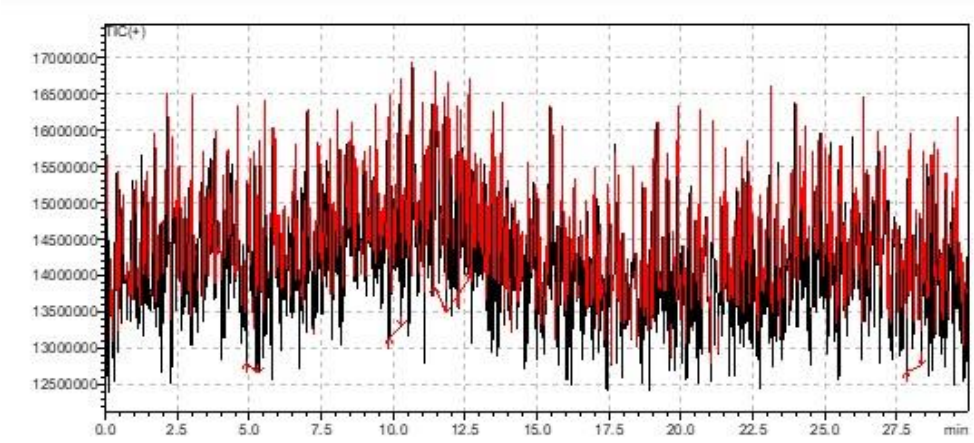

b) First ablation. The signal was integrated from t = 7.07 to 12.83 min, and the background was subtracted by integrating from t = 0.00 to 5.00 min

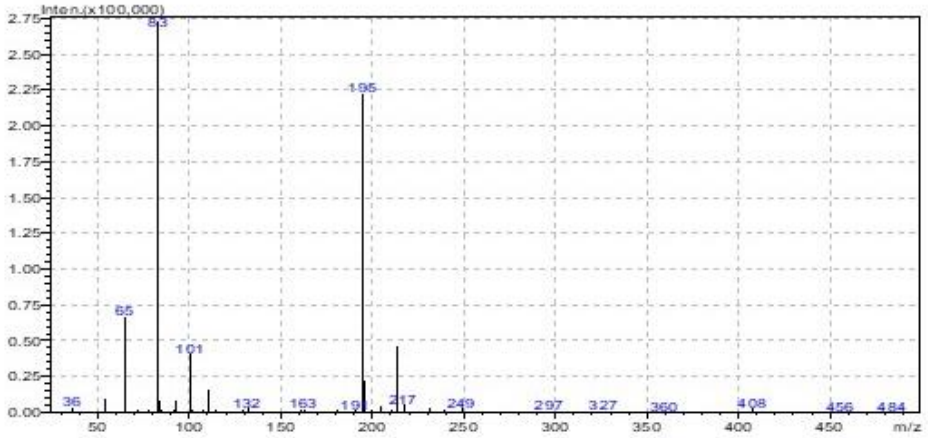

c) Second ablation. The signal was integrated from t = 21.70 to 29.05 min, and the background was subtracted by integrating from t = 0.00 to 5.00 min

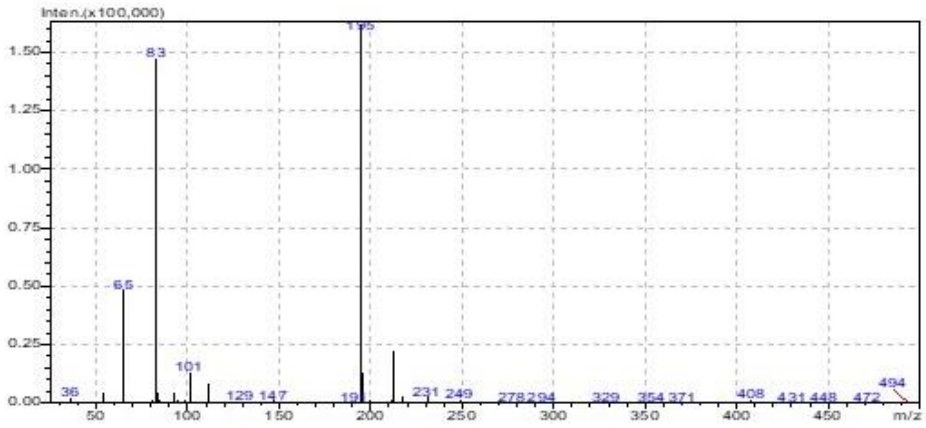

Figure 3.2.3. 4 MS spectra of the compounds produced after the ablation of caffeine powder on the graphite block surface. The laser beam was not focused through the focus lens. The data was integrated (b & c) . Caffeine compound (195 m/z) and caffeine + water compound (214 m/z) were found. The average energy was 210 mJ, and the range of the energy was between 220 mJ to 190 mJ. The ablation process started at t = 2.72 min and ended at t = 5.17 min. The second ablation process started at t = 14.58 min and ended at t = 16.93 min.

a) Time dependence of the TIC (+), the spectrum of the raw data

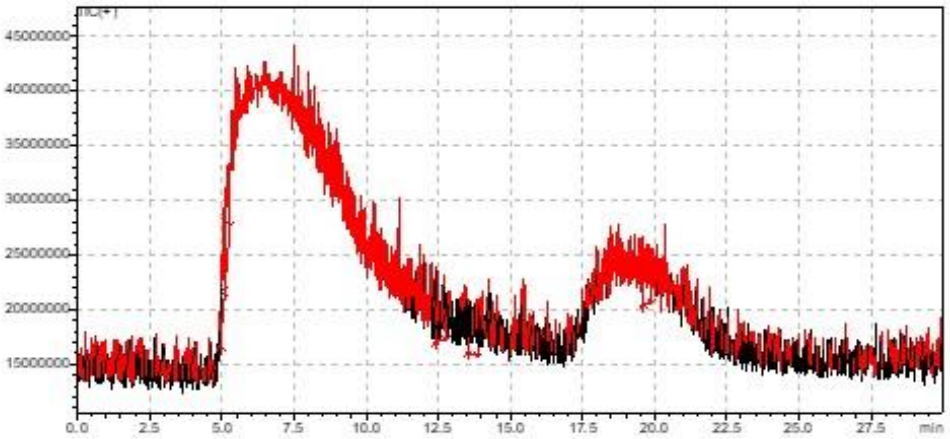

b) First ablation. The signal was integrated from t = 5.00 to 8.57 min, and the background was subtracted by integrating from t = 0.00 to 4.50 min

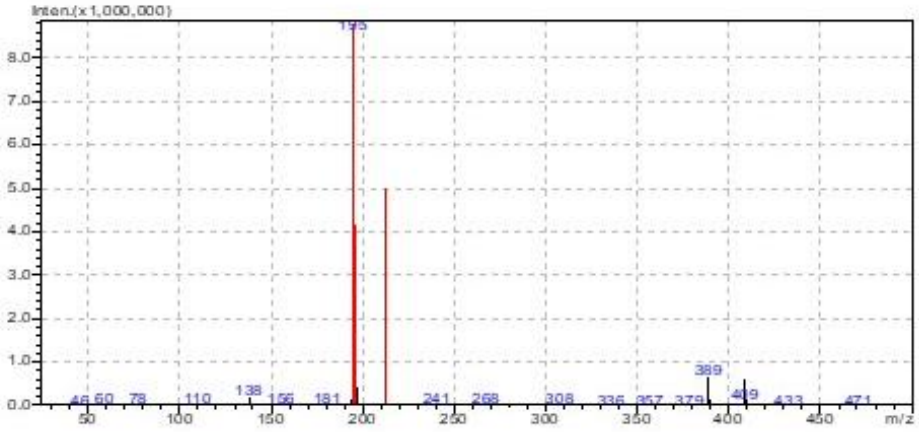

c) Second ablation. The signal was integrated from t = 17.5 to 20.33min, and the background was subtracted by integrating from t = 0.00 to 4.50 min

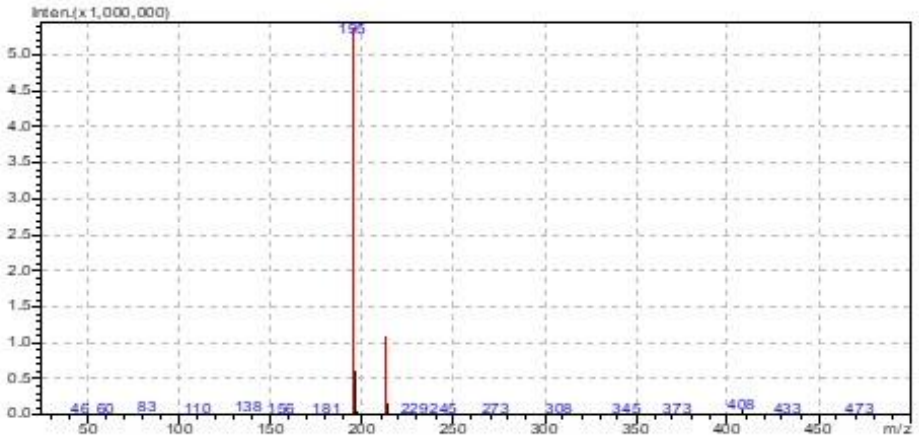

3.2.4 Discussion

We used 0.1% formic acid as the water film solution and the MS measurement was conducted under positive polarity mode. The MS spectra showed an m/z peak at 195, which corresponds to protonated caffeine $[M + H]^+$, and at m/z 213 for protonated caffeine with one water molecule $[M + H + H_2O]^+$. It can be observed in Figure 3.2.3.2 that caffeine molecules were detected by the MS, but no caffeine was found in the other trials. The results were not consistent, and it was suggested that most of the laser energy had passed through the transparent glass slide, or been absorbed by the slide itself leading to ablation of the slide. As a solution to this problem, the glass slide was

replaced with a solid graphite block, but the focus lens was not employed in order to prevent excessive ablation from the graphite, and only the iris was used to restrict the size of the laser beam. In this way, most of the laser energy was absorbed by the graphite and then transferred to the caffeine on the surface of the graphite. The graphite had a relatively high ablation damage threshold hence the plasma had less likelihood of damage and subsequent contamination. Figure 3.2.3.3 shows the signals and spatial features of the deposits on the surface of the graphite. The caffeine was not evenly distributed on the surface, and some areas of the surface had no caffeine.

However, by rubbing caffeine powder onto the graphite surface, it was possible to form a relatively homogenous layer. By using this dry deposition method, the intensity of the caffeine and caffeine water adduct was higher than that obtained from the solution droplet deposition. The focus lens was not applied, so the ablation spot was larger than the spot of LA focused onto the caffeine/glass slide. This resulted in more stable results with a higher intensity of caffeine than other measurements, clearly evidenced by the mass spectra presented above. The peak at m/z 55 refers to one of the fragments of caffeine $C3H5N^{+}$. Spectra of the caffeine powder rubbed on the graphite indicated that less caffeine fragments were generated under this condition. Peaks at m/z 55 and 83 still existed, but their ratio in relation to the caffeine peak at m/z 195 was quite small. Fewer fragments were obtained due to the absence of the focus lens. The ablation fluence on the sample was equal to the pulse energy divided by the ablated spot area of the surface. Without using the focus lens, a much larger spot area appeared. Although most of the energy was absorbed, those amounts of energy were still lower than the energy applied to the caffeine slides. From this series of experiments, it is clear that by using an underlying absorbing target (in this case graphite), non-absorbing molecules could be transferred from the target surface to the moving thin film of 0.1% formic acid solution without significant fragmentation. This clearly demonstrates the viability of the LA-FC technique as an ESI-MS sample introduction methodology. In particular the absence of significant molecular fragmentation observed in the desorption/FC step is compatible with the soft ionization ESI MS source.

3.3 Wood

3.3.1 Introduction

Wood trafficking has become a severe problem, yielding profits of approximately 150 billion US dollars per year. Wood fingerprinting commonly uses the ambient ionization method of direct analysis in real-time (DART-MS) developed by chemists from the US Fish and Wildlife Service (USFWS) (Oldach, 2023). Other methods such as stable isotope analysis, NIRS, and genetic analysis have also been introduced. Several studies apply LA-ICP-MS in tree ring and carbon isotope research. Our goal is to use the LA-FC-ESI-MS method to investigate the non-structural metabolites in lumber samples to determine whether this technique can provide a fingerprint for different tree species. For example, phenylethylchromone is a typical aromatic compound that occurs in the agarwood spectrum.

3.3.2 Method

Three conifer species: Yaka (Dacrydium nidulum), NZ Rimu (Dacrydium cupressinum), and Pine (Pinus radiata), were selected and cut into small pieces and placed on the sample stage. The plasma-containing solution was pumped at a rate of 0.4 mL/sec, with 0.1% formic solution in the burette.

Figure 3.3.2. 1 Wood samples

3.3.3 Result

Three conifer species were ablated by the laser, and the plasma-containing solution was pumped directly to the low-resolution MS to obtain spectra. Each wood sample was ablated three times. Raw MS data were integrated to identify the m/z peaks of the samples. To visualize the spectra pattern, the intensity and mass peaks were used to plot a stick diagram.

Figure 3.3.3. 1 MS spectra of plasma produced through the LA of Pinus radiata wood. The delay time of this stage was around 0.5 mins based on the length of the tube and the pump flow rate.

a). The first measurement. The ablation started at T = 3.33 min and stopped at T = 15.73 min. The average energy of the laser pulse was 214 mJ (225-198 mJ). The actual MS measurement time started at T = 3.83 to 16.23 min.

Top: Time dependence of the TIC (+), the spectrum of the raw data

Bottom: The signal was integrated from t = 3.83 to 16.23 min, and the background was subtracted by integrating from t = 0.00 to 3.00 min

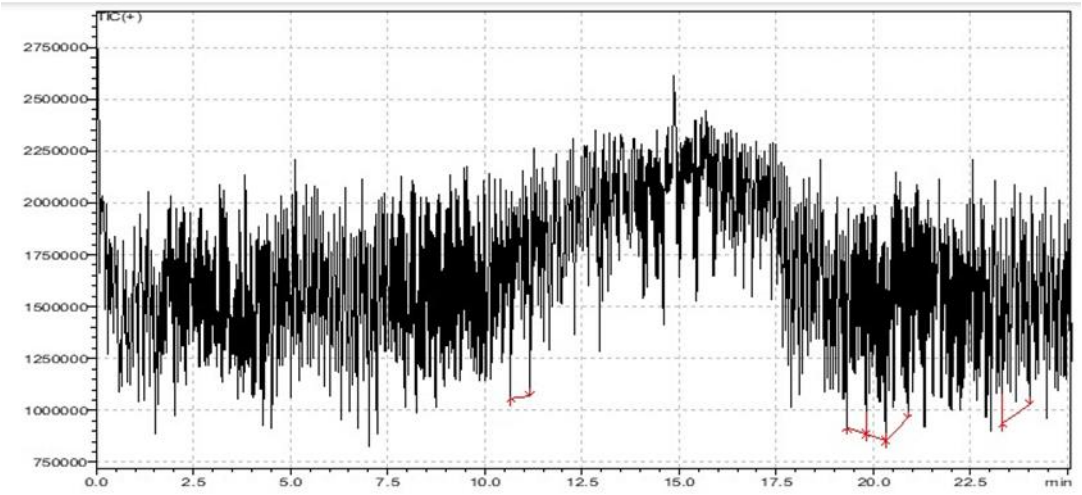

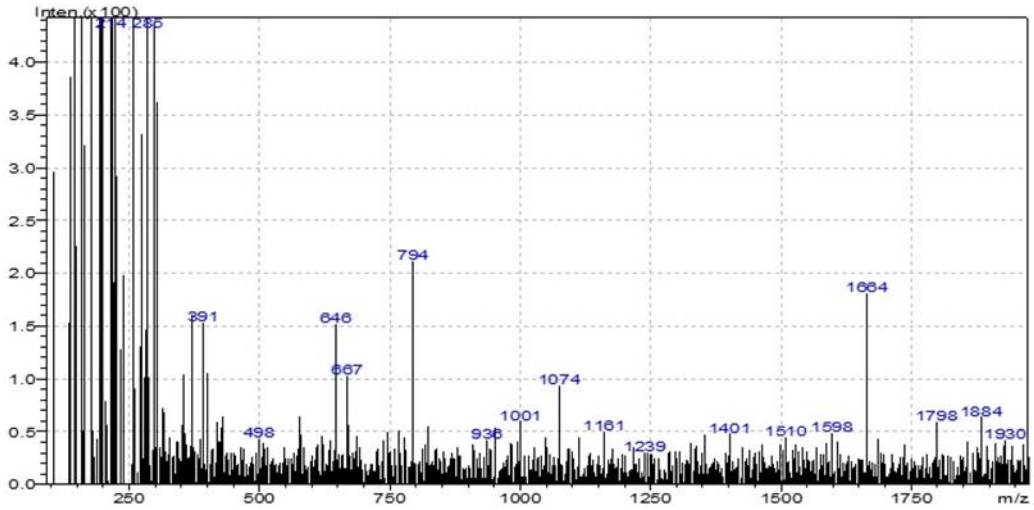

Table 3.3.3. 1 m/z Peaks from the spectrum. The intensity of each peak was recorded. Standard deviation and a 95% confidence interval were calculated. The decision on whether the peak is real or not was based on the 95% confidence interval.

m/z	Intensity	Intensity2 (subtract the background)	ΔIntensity	σ	95%CI	Peak (Y/N)
285.15	1176	560	616	24.82	50	Y
391.10	687	154	533	23.09	46	Y
498.30	243	44	199	14.11	28	Y
646.00	373	152	221	14.87	30	Y
667.45	418	103	315	17.75	35	Y
793.60	412	212	200	14.14	28	Y
936.30	246	42	204	14.28	29	Y
1001.00	243	60	183	13.53	27	Y
1074.40	307	94	213	14.59	29	Y
1161.20	241	50	191	13.82	28	Y
1239.30	229	31	198	14.07	28	Y
1401.15	227	48	179	13.38	27	Y
1509.80	275	45	230	15.17	30	Y
1597.85	202	49	153	12.37	25	Y
1664.25	435	181	254	15.94	32	Y
1798.45	249	60	189	13.75	27	Y
1884.20	295	64	231	15.20	30	Y
1930.05	231	43	188	13.71	27	Y

Figure 3.3.3. 2 Diagrams of MS raw data (The y-axis represents log10-based intensity values).

Orange color: MS raw data of the background [0.033->2.250],(scan:[3->136])

Blue color: MS raw data of the plasma [3.000->15.017],(scan:[181->902])

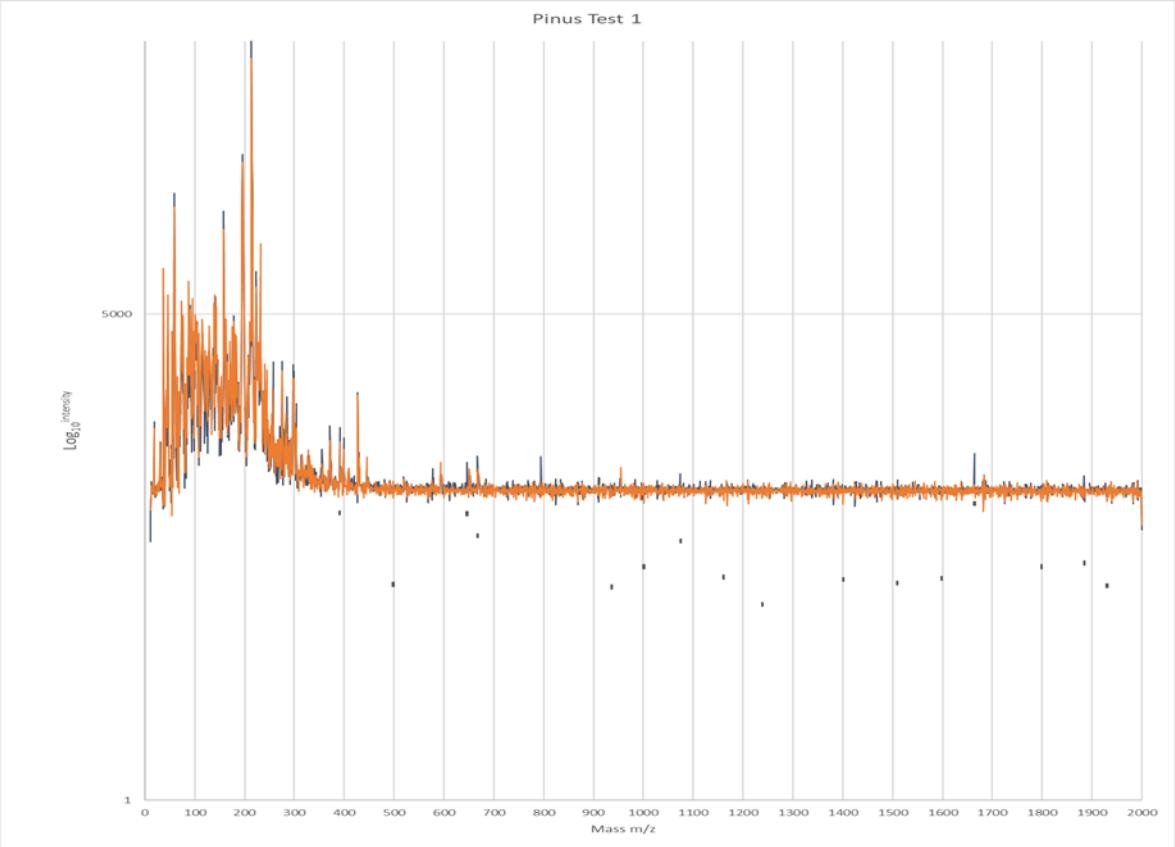

Figure 3.3.3. 3 Stick diagram of selected peaks.

Blue stick: measurement a (Figure 3.3.3.1 a)

Orange stick: measurement b

Black stick: measurement c

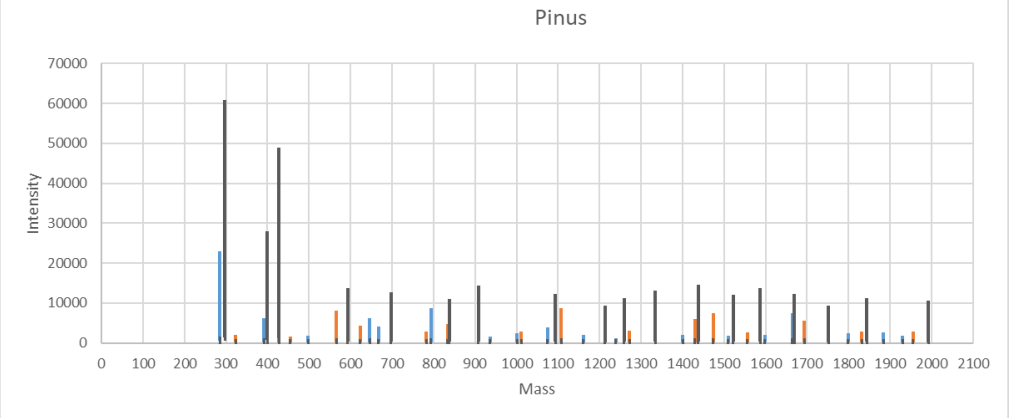

b). The second measurement. The ablation started at T = 3.03 min and stopped at T = 15.30 min. The average energy of the laser pulse was 233 mJ (256-204 mJ). The actual MS measurement time started at T = 3.53 to 15.80 min.

Top: Time dependence of the TIC (+), the spectrum of the raw data

Bottom: The signal was integrated from t = 3.53 to 15.80 min, and the background was subtracted by integrating from t = 0.00 to 3.00 min

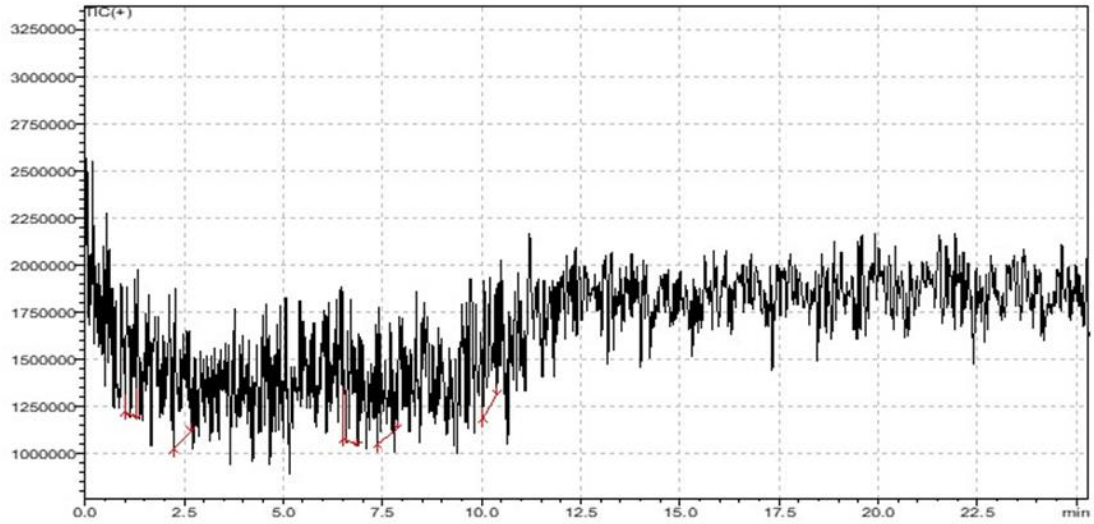

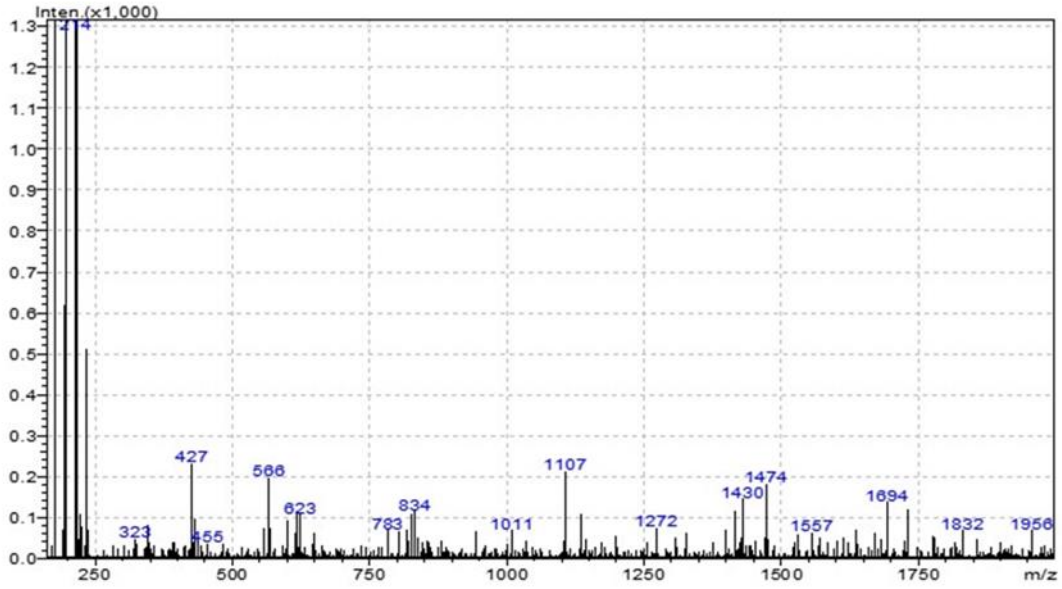

Table 3.3.3. 2 m/z Peaks from the MS spectrum

m/z	Intensity	Intensity2 (subtract the background)	ΔIntensity	σ	95% CI	Peak (Y/N)

323.05	380	49	331	18.19	36	Y
427.2	786	233	553	23.52	47	Y
454.65	245	38	207	14.39	29	Y
566	420	199	221	14.87	30	Y
623.1	353	108	245	15.65	31	Y
782.7	297	69	228	15.10	30	Y
833.8	344	116	228	15.10	30	Y
1011.2	286	69	217	14.73	29	Y
1107.55	450	213	237	15.39	31	Y
1272.45	277	76	201	14.18	28	Y
1429.8	356	146	210	14.49	29	Y
1473.6	417	182	235	15.33	31	Y
1556.6	298	64	234	15.30	31	Y
1694.05	342	139	203	14.25	28	Y
1832.3	307	69	238	15.43	31	Y
1955.7	293	69	224	14.97	30	Y

c). The third measurement. The ablation started at T = 4.75 min and stopped at T = 16.17 min. The average energy of the laser pulse was 215 mJ (221-201 mJ). The actual MS measurement time started at T = 5.25 to 16.67 min.

Top: Time dependence of the TIC (+), the spectrum of the raw data

Bottom: The signal was integrated from t = 5.25 to 16.67 min, and the background was subtracted by integrating from t = 0.00 to 4.50 min

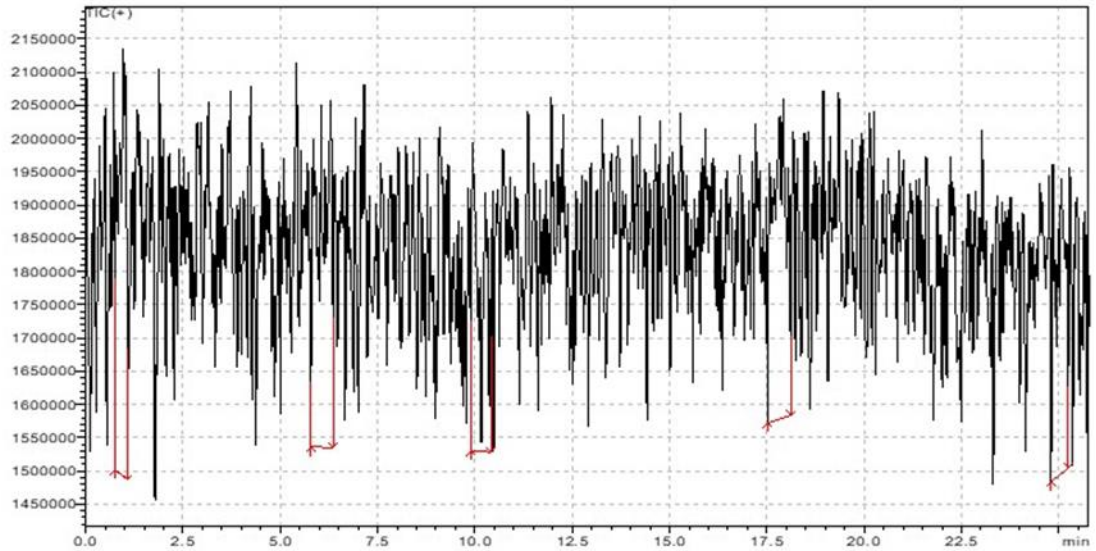

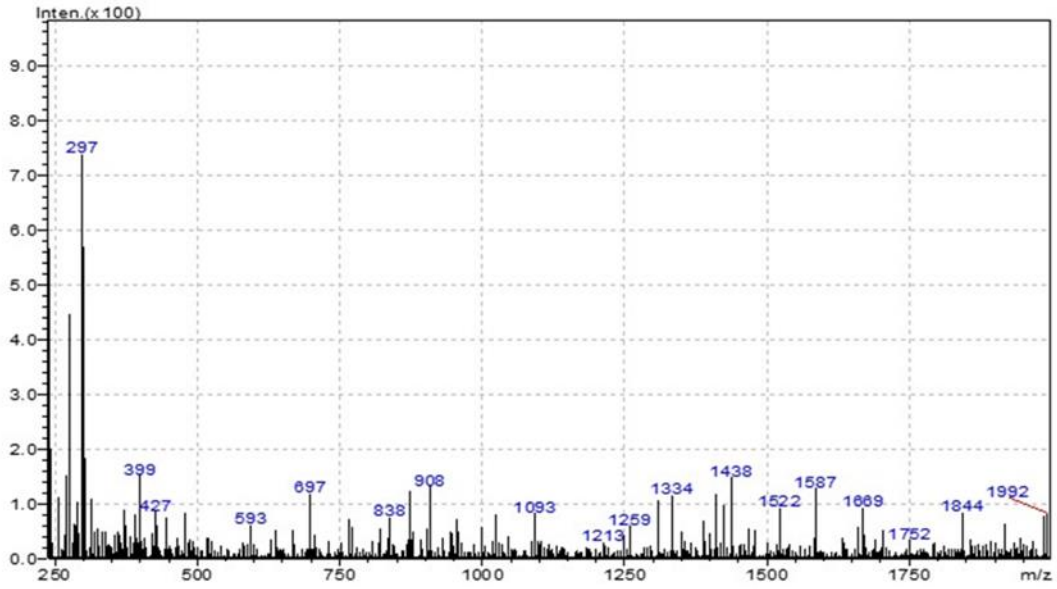

Table 3.3.3. 3 m/z Peaks from the spectrum

m/z	Intensity$_1$	Intensity2 (subtract the background)	ΔIntensity	σ	95% CI	Peak (Y/N)
296.9	1484	738	746	27.31	55	Y
399.2	681	152	529	23.00	46	Y
427.15	1191	86	1105	33.24	66	Y
593.5	337	61	276	16.61	33	Y
697.55	308	118	190	13.78	28	Y
838.25	271	76	195	13.96	28	Y
907.65	350	132	218	14.76	30	Y
1093.55	302	83	219	14.80	30	Y
1213.2	228	31	197	14.04	28	Y
1259.1	275	60	215	14.66	29	Y
1334.25	320	116	204	14.28	29	Y
1437.65	357	149	208	14.42	29	Y
1521.8	296	92	204	14.28	29	Y
1587	337	129	208	14.42	29	Y
1669.4	301	92	209	14.46	29	Y
1751.65	228	34	194	13.93	28	Y
1844.3	276	84	192	13.86	28	Y
1992	260	83	177	13.30	27	Y

Figure 3.3.3. 4 MS spectra of plasma produced through the LA of NZ rimu wood. The delay time of this stage was around 0.5 mins.

a). The first measurement. The ablation started at T = 3.10 min and stopped at T = 15.15 min. The average energy of the laser pulse was 183 mJ (200-152 mJ). The actual MS measurement time started at T = 3.60 to 15.65 min.

Top: Time dependence of the TIC (+), the spectrum of the raw data

Bottom: The signal was integrated from t = 3.60 to 15.65 min, and the background was subtracted by integrating from t = 0.00 to 3.50 min

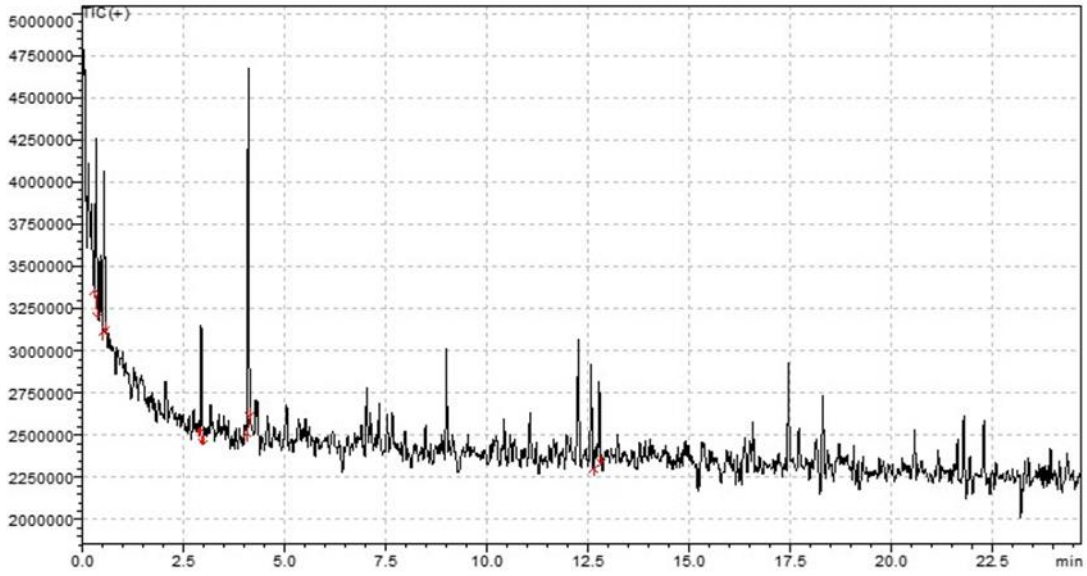

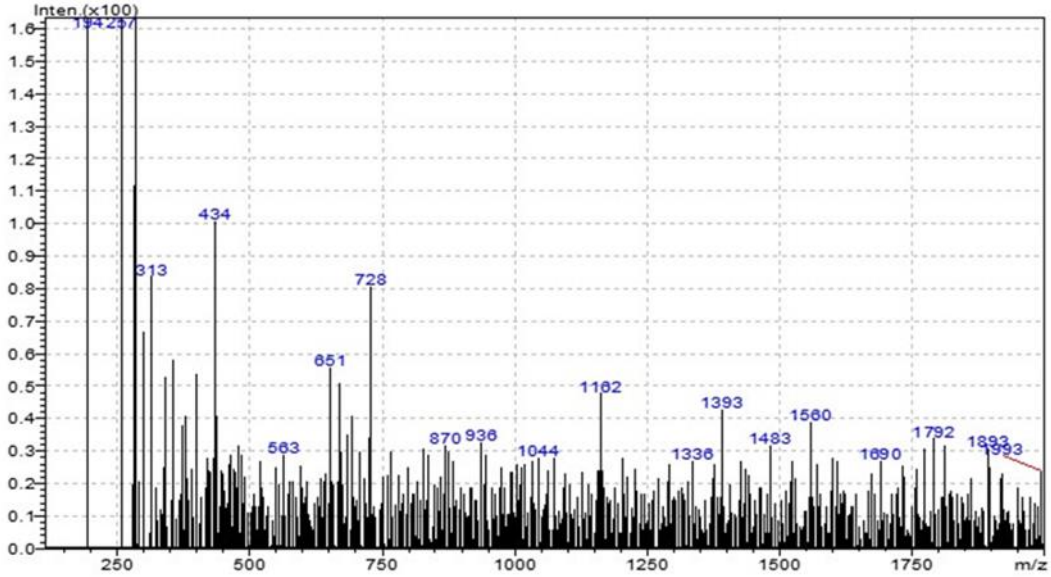

Table 3.3.3. 4 m/z Peaks from the spectrum

m/z	Intensity	Intensity2 (subtract the background)	ΔIntensity	σ	95%CI	Peak (Y/N)
257	2927	569	2358	48.56	97	Y
313	536	84	452	21.26	43	Y
434	338	101	237	15.39	31	Y
562.6	221	29	192	13.86	28	Y
651.15	323	56	267	16.34	33	Y
728.4	285	81	204	14.28	29	Y
870.2	200	32	168	12.96	26	Y
936.4	218	33	185	13.60	27	Y
1044.35	214	28	186	13.64	27	Y
1161.75	239	48	191	13.82	28	Y
1335.6	209	27	182	13.49	27	N
1392.75	238	43	195	13.96	28	Y
1483.25	213	32	181	13.45	27	Y
1559.6	215	39	176	13.27	27	Y
1689.8	213	27	186	13.64	27	N
1792.25	209	34	175	13.23	26	Y
1893.3	207	31	176	13.27	27	Y
1993.45	217	24	193	13.89	28	N

b). The second measurement. The ablation started at T = 2.17 min and stopped at T = 15.15 min. The average energy of the laser pulse was 217 mJ (236-193 mJ). The actual MS measurement time started at T = 2.67 to 15.65 min.

Top: Time dependence of the TIC (+), the spectrum of the raw data

Bottom: The signal was integrated from t = 2.67 to 15.65 min, and the background was subtracted by integrating from t = 0.00 to 2.50 min

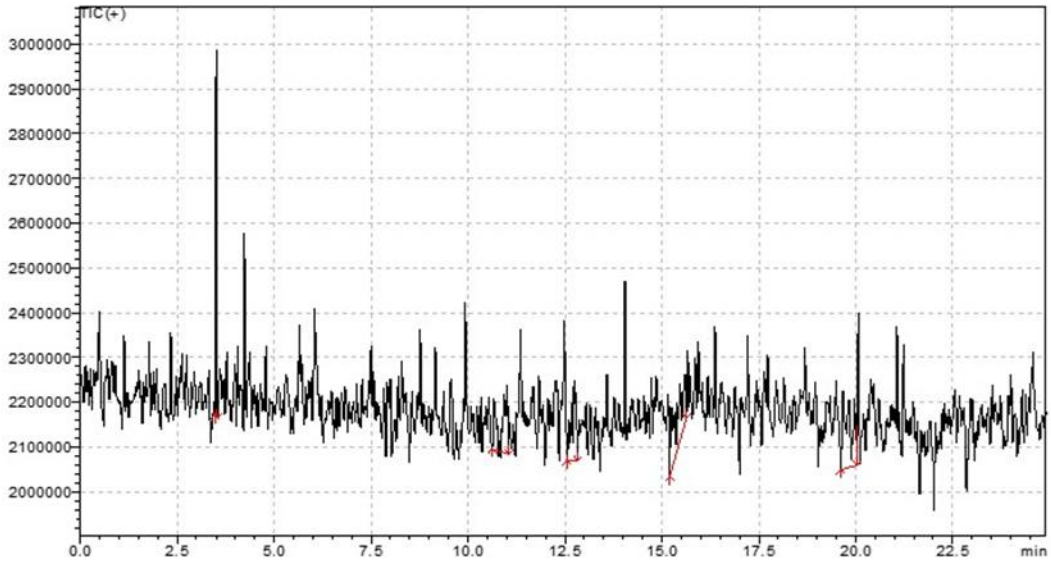

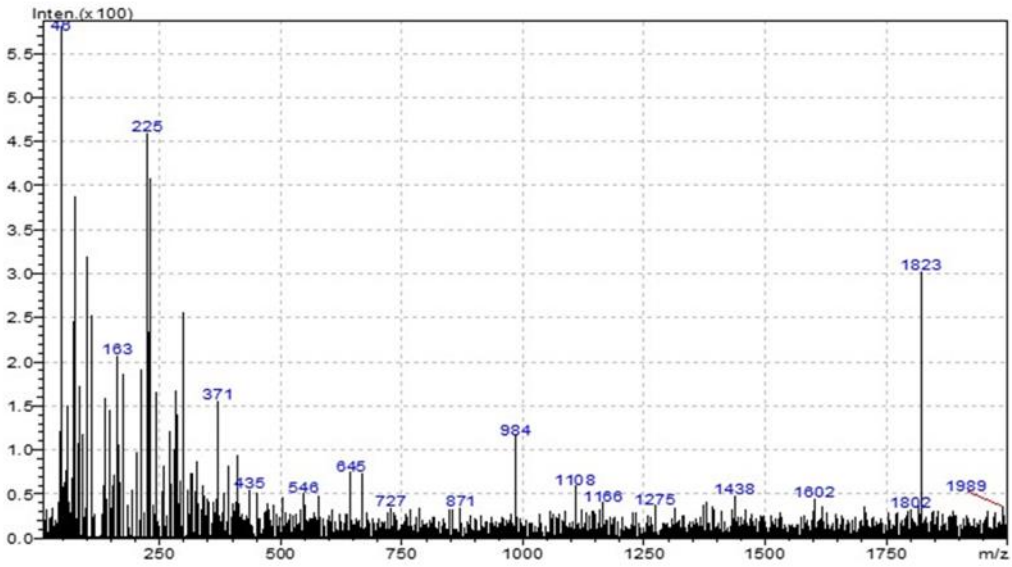

Table 3.3.3. 5 Peaks from the spectrum

m/z	Intensity	Intensity2 (subtract the background)	ΔIntensity	σ	95%CI	Peak (Y/N)
225	6318	460	5858	76.54	153	Y

371.3	979	156	823	28.69	57	Y
435.5	307	55	252	15.87	32	Y
546.5	240	51	189	13.75	27	Y
644.85	296	75	221	14.87	30	Y
727.05	262	36	226	15.03	30	Y
871.35	228	35	193	13.89	28	Y
983.65	357	116	241	15.52	31	Y
1107.6	262	60	202	14.21	28	Y
1166.15	228	41	187	13.67	27	Y
1274.85	226	37	189	13.75	27	Y
1438.4	269	49	220	14.83	30	Y
1602.4	236	45	191	13.82	28	Y
1801.75	219	33	186	13.64	27	Y
1823.25	506	303	203	14.25	28	Y
1989.45	247	36	211	14.53	29	Y

c). The third measurement. The ablation started at T = 2.40 min and stopped at T = 14.87 min. The average energy of the laser pulse was 189 mJ (215-159 mJ). The actual MS measurement time started at T = 2.90 to 15.37 min.

Top: Time dependence of the TIC (+), the spectrum of the raw data

Bottom: The signal was integrated from t = 2.90 to 15.37 min, and the background was subtracted by integrating from t = 0.00 to 2.50 min

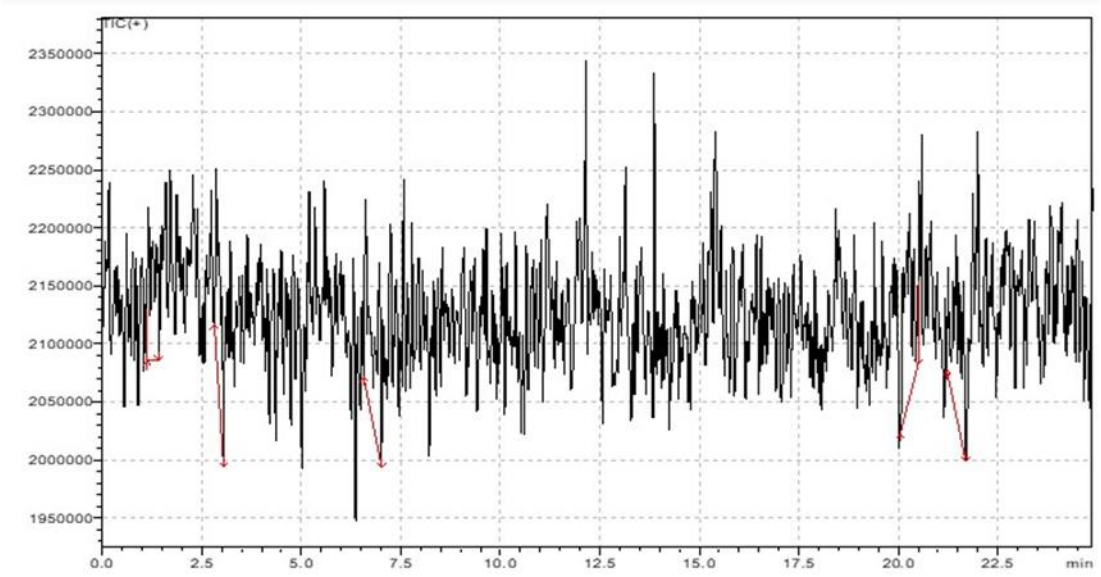

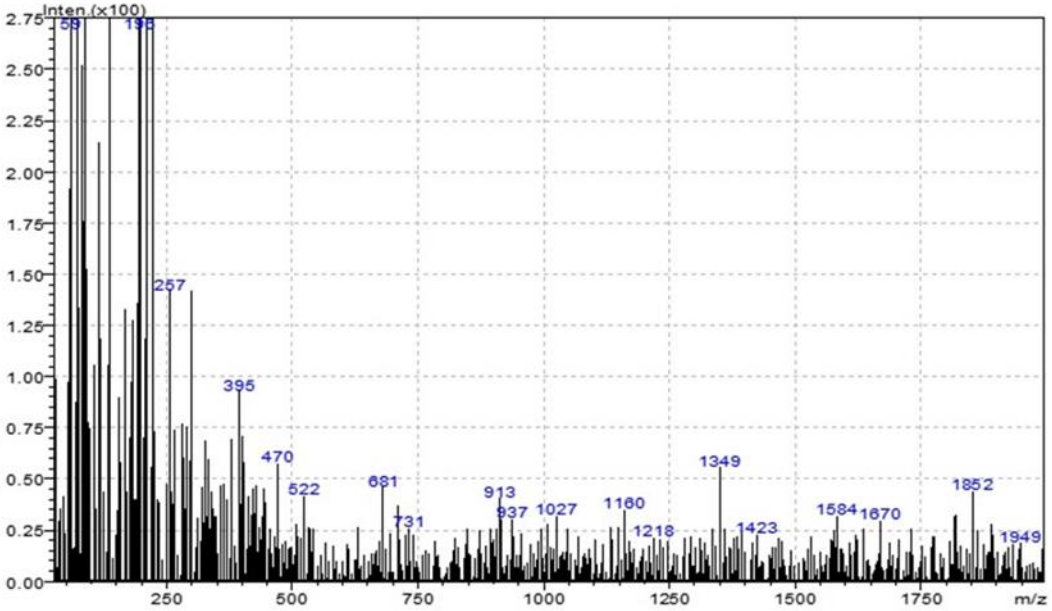

Table 3.3.3. 6 Peaks from the spectrum

m/z	Intensity	Intensity2 (subtract the	ΔIntensity	σ	95%CI	Peak (Y/N)

		background)				
257.1	3025	142	2883	53.69	107	Y
394.7	388	93	295	17.18	34	Y
470.1	277	58	219	14.80	30	Y
522.2	234	42	192	13.86	28	Y
680.8	231	46	185	13.60	27	Y
730.8	224	26	198	14.07	28	N
912.85	223	41	182	13.49	27	Y
936.95	215	31	184	13.56	27	Y
1026.7	247	32	215	14.66	29	Y
1160	222	35	187	13.67	27	Y
1218.5	221	22	199	14.11	28	N
1349.4	275	56	219	14.80	30	Y
1423.3	216	23	193	13.89	28	N
1583.65	202	32	170	13.04	26	Y
1670.35	223	30	193	13.89	28	Y
1852.05	254	44	210	14.49	29	Y
1948.6	219	19	200	14.14	28	N

Figure 3.3.3. 5 Stick diagram of selected peaks

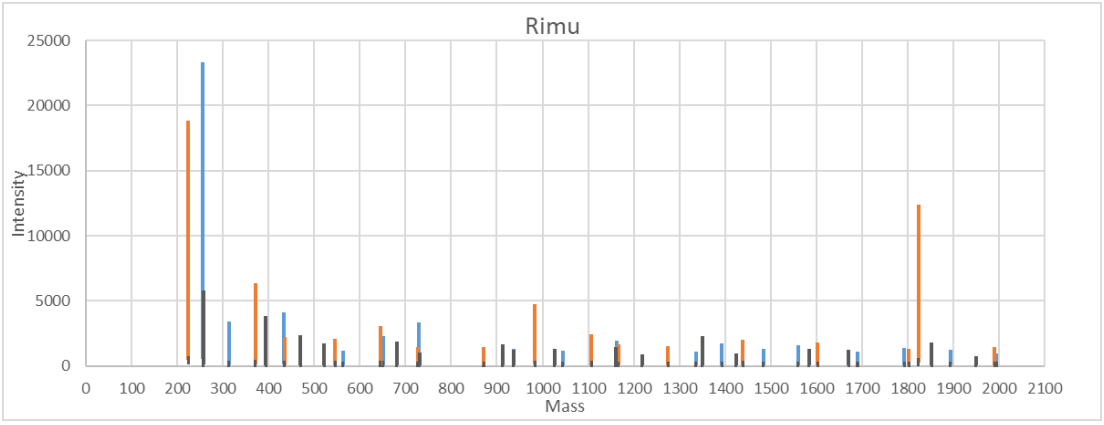

Figure 3.3.3. 6 MS spectra of plasma produced through the LA of Yaka (Fiji Rimu) wood. The delay time of this stage was 0.5 mins.

a). The ablation started at T = 2.64 min and stopped at T = 15.70 min. The average energy of the laser pulse was 189 mJ (204-259 mJ). The actual MS measurement time started at T = 3.14 to 16.20 min.

Top: Time dependence of the TIC (+), the spectrum of the raw data

Bottom: The signal was integrated from t = 3.14 to 16.20 min, and the background was subtracted by integrating from t = 0.00 to 3.00 min

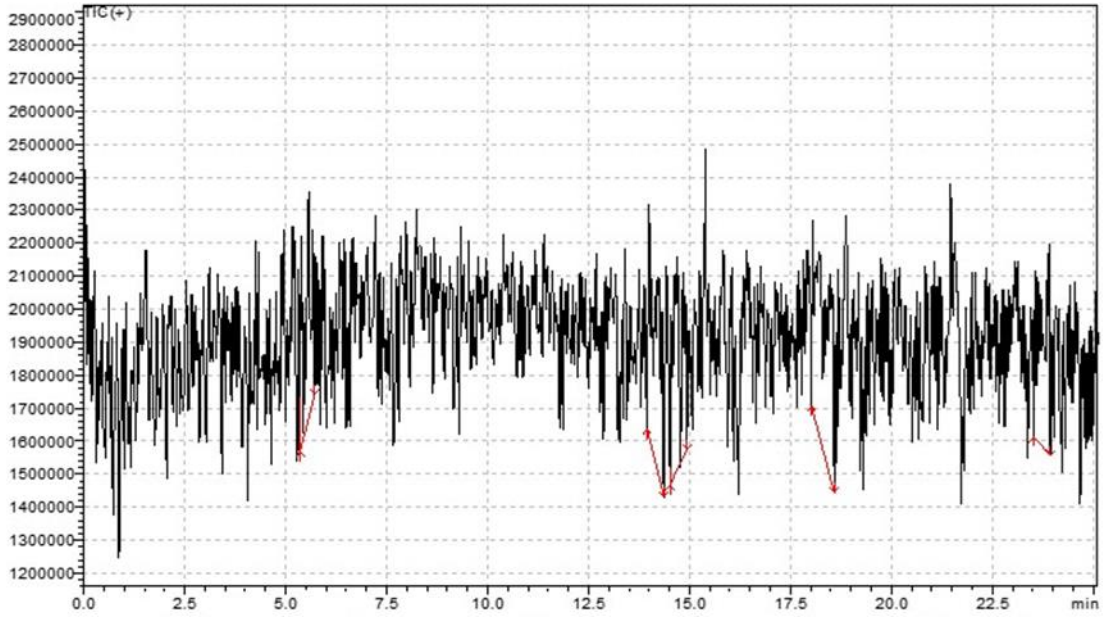

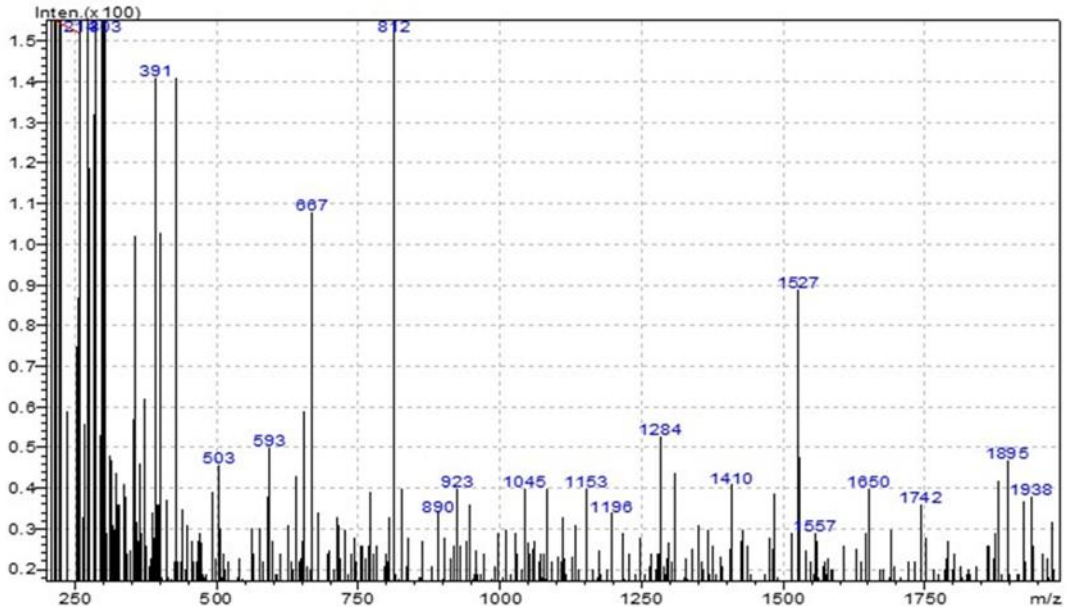

Table 3.3.3. 7 Peaks from the spectrum

m/z	Intensity	Intensity2 (subtract the background)	ΔIntensity	σ	95%CI	Peak (Y/N)
257.15	2628	783	1845	42.95	86	Y
391.15	749	141	608	24.66	49	Y
503.15	251	46	205	14.32	29	Y
593.4	267	40	227	15.07	30	Y
667.3	439	108	331	18.19	36	Y
812.05	402	213	189	13.75	27	Y
889.65	245	34	211	14.53	29	Y
923.1	220	40	180	13.42	27	Y
1045.1	240	40	200	14.14	28	Y
1153.15	222	40	182	13.49	27	Y
1196.3	228	34	194	13.93	28	Y
1284.05	248	53	195	13.96	28	Y
1409.65	255	41	214	14.63	29	Y
1527.25	281	89	192	13.86	28	Y
1557.25	214	29	185	13.60	27	Y
1650.5	243	40	203	14.25	28	Y
1742.25	222	36	186	13.64	27	Y
1895.35	255	47	208	14.42	29	Y
1938.15	257	38	219	14.80	30	Y

b). The second measurement. The ablation started at T = 2.68 min and stopped at T = 15.08 min. The average energy of the laser pulse was 201 mJ (219-181 mJ). The actual MS measurement time started at T = 3.18 and ended at 15.58 min.

Top: Time dependence of the TIC (+), the spectrum of the raw data

Bottom: The signal was integrated from t = 3.18 to 15.58 min, and the background was subtracted by integrating from t = 0.00 to 3.00 min

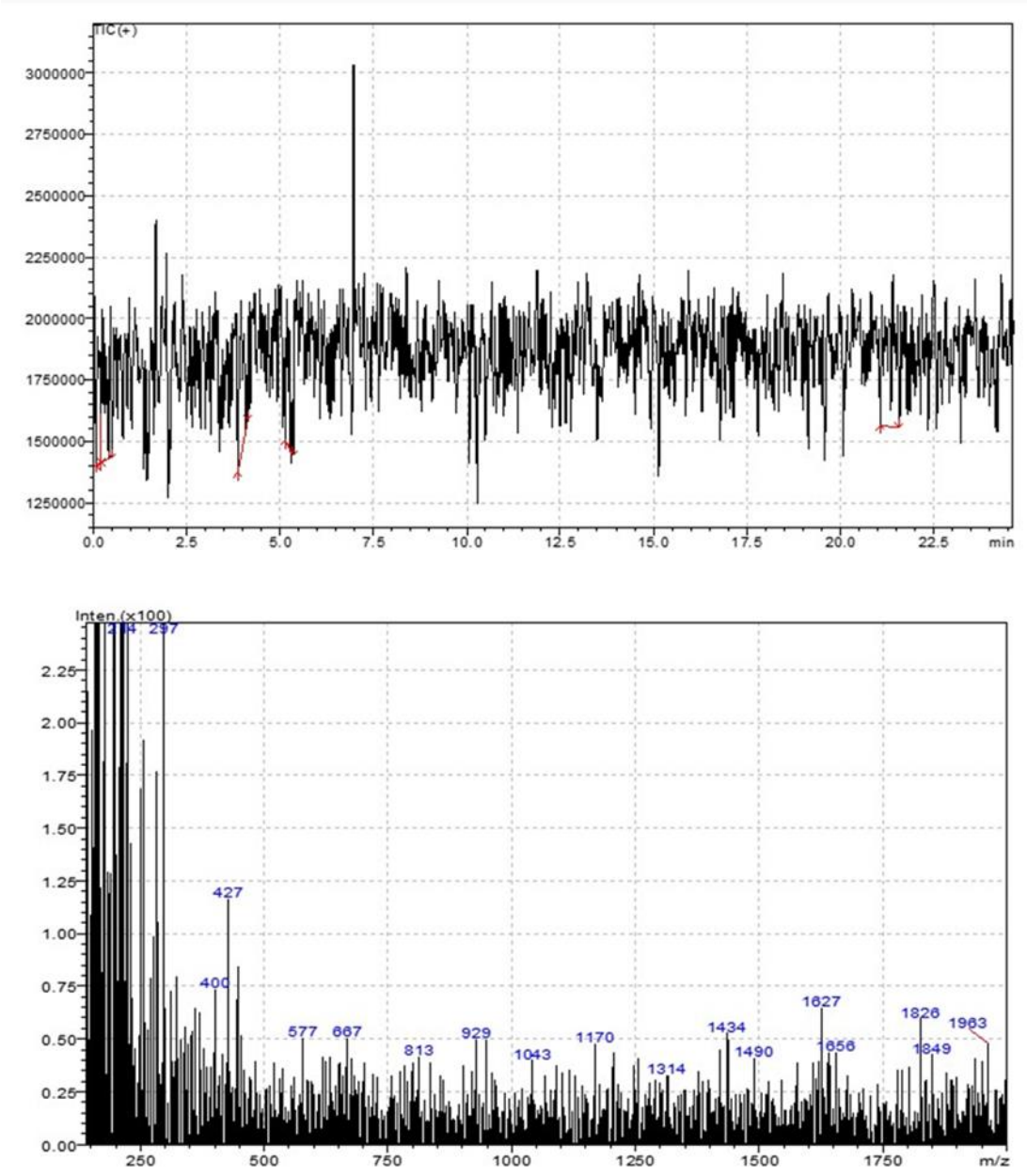

Table 3.3.3. 8 Peaks from the spectrum

m/z	Intensity	Intensity2 (subtract the	ΔIntensity	σ	95%CI	Peak (Y/N)

		background)				
297	2755	254	2501	50.01	100	Y
400.5	340	74	266	16.31	33	Y
427.25	1442	117	1325	36.40	73	Y
576.7	281	51	230	15.17	30	Y
666.8	438	51	387	19.67	39	Y
812.85	269	42	227	15.07	30	Y
929.2	225	50	175	13.23	26	Y
1042.75	224	40	184	13.56	27	Y
1169.8	221	48	173	13.15	26	Y
1313.95	211	33	178	13.34	27	Y
1434.25	258	53	205	14.32	29	Y
1490.2	261	41	220	14.83	30	Y
1626.6	286	65	221	14.87	30	Y
1656.15	235	44	191	13.82	28	Y
1826.2	267	60	207	14.39	29	Y
1848.85	216	43	173	13.15	26	Y
1962.85	219	48	171	13.08	26	Y

c). The third measurement. The ablation started at T = 2.70 min and stopped at T = 15.07 min. The average energy of the laser pulse was 216 mJ (238-183 mJ). The actual MS measurement time started at T = 3.20 and ended at 15.57 min.

Top: Time dependence of the TIC (+), the spectrum of the raw data

Bottom: The signal was integrated from t = 3.20 to 15.57 min, and the background was subtracted by integrating from t = 0.00 to 3.00 min

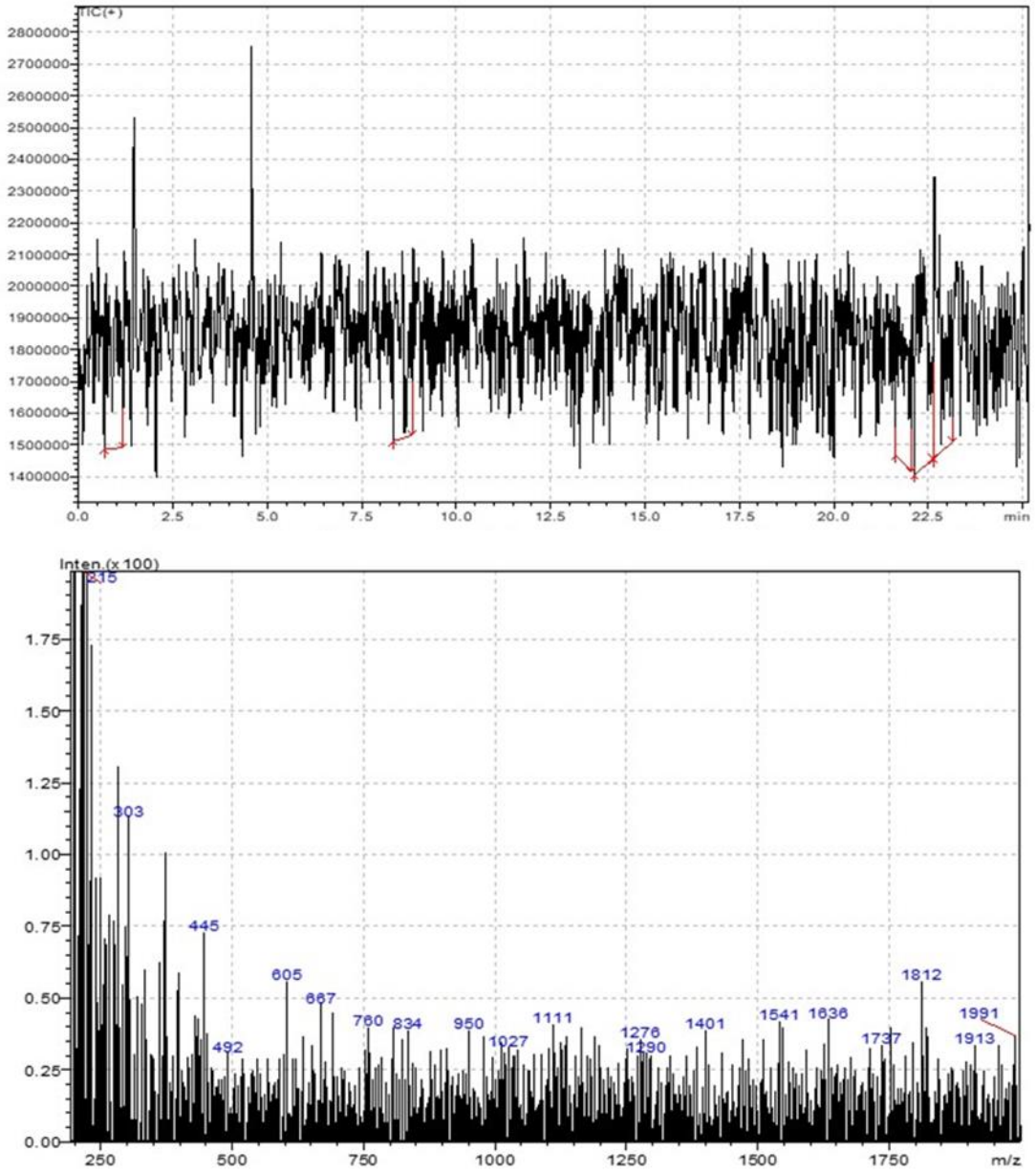

Table 3.3.3. 9 Peaks from the spectrum

m/z	Intensity	Intensity2 (subtract the background)	ΔIntensity	σ	95% CI	Peak (Y/N)

303.3	815	110	705	26.55	53	Y
373.2	396	93	303	17.41	35	Y
445.1	458	77	381	19.52	39	Y
492.5	222	31	191	13.82	28	Y
605.3	253	64	189	13.75	27	Y
667.35	396	31	365	19.10	38	N
759.65	224	42	182	13.49	27	Y
833.75	258	41	217	14.73	29	Y
949.95	237	44	193	13.89	28	Y
1027.25	242	35	207	14.39	29	Y
1111.25	229	42	187	13.67	27	Y
1276.25	208	34	174	13.19	26	Y
1289.65	216	31	185	13.60	27	Y
1401.2	209	41	168	12.96	26	Y
1541.05	244	38	206	14.35	29	Y
1635.75	232	43	189	13.75	27	Y
1736.9	229	35	194	13.93	28	Y
1811.85	249	59	190	13.78	28	Y
1913.35	226	32	194	13.93	28	Y
1990.7	248	36	212	14.56	29	Y

Figure 3.3.3. 7 Stick diagram of selected peaks

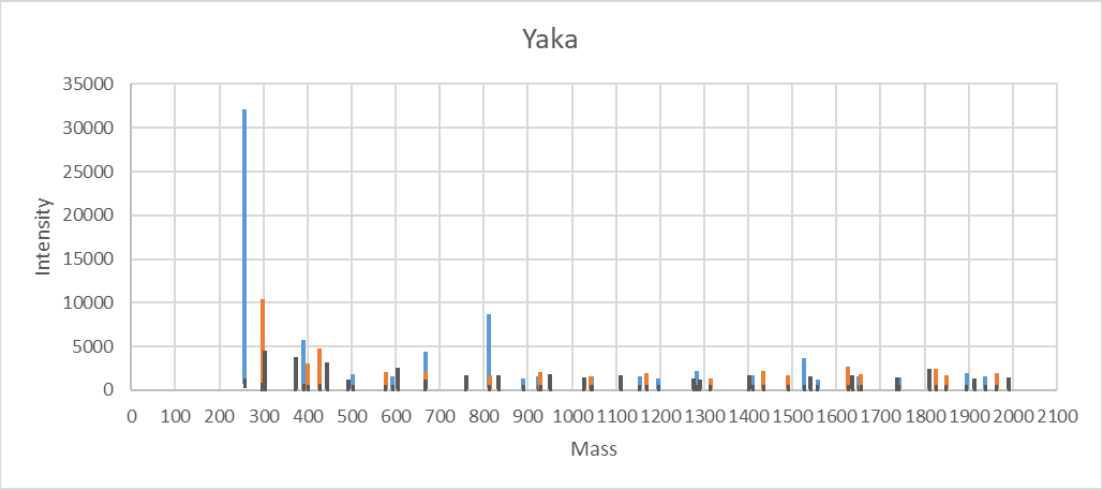

3.3.4 Discussion

The next target studied using the modified LA-MS technique was lumber. Three species – Yaka (also known as Fijian Rimu), New Zealand Rimu, and Pinus radiata wood – were selected for analysis. Some similarities were expected in the mass spectrum signatures of Fijian Rimu and NZ Rimu because they originate from the same family. The peak intensities of the wood samples were small, and the noise level was relatively high. To distinguish between real and noise peaks, the standard deviation and 95% confidence interval approaches were employed (Table 3.3.3.1-3.3.3.9) for those masses which had significant intensity above background levels.

For each species, three measurements were taken to obtain three spectra, which were intended to be added together and averaged. However, the number of data points collected by the MS instrument from the three raw spectra differed, and the addition process therefore proved problematic. The spectra of each wood sample were therefore analyzed individually.

For the Pinus sample, an m/z peak at 472 appeared in both measurements 2 and 3, based on the peak tables. For the Rimu sample, an m/z peak at 257 showed up in tests 1 and 3, and at m/z 434 in tests 1 and 2. For the Yaka sample, all three measurements had a mass peak at 667, and only measurements 1 and 2 had an m/z peak at 812. Although several signals of different measurements were found in each spectrum, the peak results were not reproducible.

To find the pattern of the spectra, it is necessary to examine the peak region rather than the signal peak. The intensity and the mass peak were used to plot a stick diagram for the three wood species. For each kind of wood, the datasets of the three tests were plotted on the same graph. Compared with the Rimu and Yaka diagrams, the Pinus graph showed significantly higher peaks for the m/z range from 500 to 2000. Some trend similarities could be found in the Rimu and Yaka diagrams in the mass range from 1000 to 2000. Among the three diagrams, the variation in the intensity of all the selected peaks was the smallest in the Yaka wood diagram.

Based on the peak patterns of the spectra, the LA-FC-ESI-MS method used in this

research has the potential to distinguish between wood species. However, more measurements are required due to the inconsistent reproducibility. Because of the variation of the spatial distribution of different molecules in natural products it isn't clear whether the source of the reproducibility is the wood sample itself, or the LA-FC-ESI technique. Furthermore, organizations such as USFWS and World Forest ID are collecting the mass spectra of known tree species to establish a data library that can be used to aid in the identification of wood species using DART-MS (Oldach, 2023) and it would be instructive to compare the spectra obtained from the different methods.

3.4 Shark Vertebrae

3.4.1 Background

The survival of sharks as top predators in marine ecosystems is jeopardized by overfishing and habitat loss. Studies that track shark movements and detect patterns of habitat utilization in coastal locations commonly use conventional (numerical), satellite, or sonar tags. However, because these techniques include capturing, tagging, and releasing the shark, they are usually logistically challenging and costly. A new method for tracing age-related migrations of sharks throughout habitats over their lifetimes examines natural chemical signatures—from either pollution or naturally occurring elements in the Earth's crust weathering and leaking into water systems—to overcome constraints associated with traditional age determination methods. For shark species, trace elements can either replace calcium in rigid structures such as vertebrae or become trapped in protein matrices in the skin and gills (Tillett et al., 2011). Elasmobranch vertebral cartilage comprises mineralized hydroxyapatite surrounded by a protein-rich extracellular matrix. The elemental chemistry of elasmobranch vertebrae is ideal for assessing age and growth, and even potentially reconstructing earlier environmental life histories, due to the mineralization of the calcium structure giving rise to vertebral growth bands (Mohan et al., 2017). A study showed that the Sr concentration in vertebrae was associated with temperature and growth rate. Different shark species have distinct band-pair elemental arrangements, which are correlated to elemental changes in vertebrae and band-pair deposition (Mohan et al., 2018).

A shark's age is most frequently determined by analyzing growth bands in vertebral centra using various techniques such as X-ray imaging, chemical staining, and micro-topography (Geraghty et al., 2012). The School shark in NZ is a commercial species with catch limited by the quota management system. In order to properly manage the fishery, it is necessary to have a good understanding of the growth and reproductive rates of the shark. Crucial in this modelling is the ability to perform accurate age determination for individuals. Typically, this is done via counting the growth bands in vertebrae in a similar way to counting tree rings. However, the process for doing this is

complicated by the presence of sub-bands which can cause false age determinations. In this series of experiments, we will attempt to apply LA-FC-ESI-MS to the problem.

3.4.2 Cleaning and Storage of Shark Vertebrae

In 2017, Mohan proved the importance of cleaning shark vertebrae samples and choosing appropriate storage methods, which influences the elemental composition. The fundamental elemental compositions of hydroxyapatite structures may be altered by cleaning and storing techniques (Mohan et al., 2017).

Sharks' (Carcharhinus limbatus) vertebrae were cleaned using bleach (NaOCl) for time intervals of 5 min, 1 hr, and 24 hr. Different storage methods were used: Samples were directly frozen, stored in a 70% ethanol solution, or stored in a 10% formalin solution. Vertebrae were cut into 2 mm thick bowtie-shaped sections using a low-speed Isomet saw with a diamond-coated blade. The sections were then cut in half and mounted on petrographic slides. An NWR193 excimer laser at 193 nm with a 10 Hz repetition rate was used to ablate the sample. Sections were pre-ablated with 2 s dwell interval to avoid sample contamination. There were 14 elements (^{23}Na, ^{24}Mg, ^{25}Mg, ^{43}Ca, ^{55}Mn, ^{88}Sr, ^{7}Li, ^{63}Cu, ^{66}Zn, ^{68}Zn, ^{208}Pb, ^{138}Ba, ^{139}La, and ^{140}Ce) analyzed, and the Ca in the vertebrae with a constant weight percentage worked as an internal standard (Mohan et al., 2017).

According to the data, Mohan concluded that the ^{23}Na:^{43}Ca ratio was greatly influenced by bleach cleaning. As for the effects of the storage methods, the ^{23}Na:^{43}Ca and ^{25}Mg:^{43}Ca ratios of samples stored in formalin declined, whereas the elements to ^{43}Ca ratio of the vertebrae placed in ethanol showed no changes. Vertebrae from different sharks had distinct values for their ^{88}Sr:^{43}Ca, ^{138}Ba:^{43}Ca, and ^{25}Mg:^{43}Ca ratios due to variations in the sharks' habitats (Mohan et al., 2017). In short, when treating vertebrae with a bleaching method, we must be aware of the exposure time, and ^{23}Na might not be a suitable target element for examination. In addition, cleaned samples can be stored in either ethanol or a freezer.

One of the final goals of our LA-FC-ESI-MS experiment is to test the method on shark vertebrae with a view to developing a way of determining the ages of sharks.

Sharks have cartilaginous skeletons instead of bones, so they are characterized as elasmobranch fishes. Most of them live in seawater, and only certain species can be found in both seawater and river water. Shark populations are negatively influenced by human activities, and the global shark population has declined by 71% since 1970, mainly due to overfishing (Sims, n.d.). Our research targets are school sharks, also known as tope and snapper sharks, from the ocean in New Zealand. They are vulnerable to overfishing and are currently identified as an extremely endangered species by the IUCN in its Red List of Threatened Species.

Most elasmobranch species grow quickly in the summer, which forms the wider organic-rich hypomineralized translucent zone, whereas during wintertime, narrow hypermineralized opaque bands are formed due to slower growth, producing a band pair (Mohan et al., 2018; Scharer et al., 2012). Opaque bands can be used to determine the age of a species only if the alternate banding pattern occurs periodically (Scharer et al., 2012). Numerous techniques have been employed to estimate the band pair periodicity in different elasmobranch species (Mohan et al., 2018).

Valid age and growth parameter estimates are critical factors of precise capture records, which is why it is important to analyze shark population demography and determine appropriate exploitation rates. Invalid age estimations can result in incorrect inferences about growth rates and population sizes, which can have serious consequences for shark conservation (Mohan et al., 2018).

In 2011, Tillett studied bull sharks and pigeye sharks (C. ambinensis) from coastal waters of north Australia using LA-ICP-MS to identify the relationship between changes in the microchemistry of vertebrae and habitat shifting behavior (Tillett et al., 2011). In 2018, McMillan et al. used the same method to detect the elemental compositions of vertebrae from school sharks (Galeorhinus galeus) to study whether the target female sharks used regular pupping areas. Sharks born in different pupping areas have distinct elemental signatures, which are called post-natal elemental signatures, in their vertebral structures due to variations in their eating habits, water conditions, and other environmental influences (McMillan et al., 2018). In the same

year, Mohan studied shark vertebrae to analyze the elemental mineralization of three species from the eastern North Pacific Ocean: shortfin mako (Isurus oxyrinchus), common thresher (Alopias vulpinus), and blue sharks (Prionace glauca) (Mohan et al., 2017). A year later, Coiraton et al. published a paper about determining the ages of juvenile hammerhead sharks (Sphyrna lewini) from the Mexican Pacific Ocean. Marginal increment analysis and centrum edge analysis were two major methods utilized to confirm the periodicity of growth increments, and LA-ICP-MS was used to examine the elemental compositions to determine the sharks' ages (Coiraton et al., 2019). The age estimations were believed to be useful for solving the overfishing issue due to shark's slow reproductive life cycles.

In McMillan's study, vertebrae samples were collected from 154 individual school sharks (Galeorhinus galeus) captured in South Australia and Bass Strait. Bleaching was used to remove tissue from vertebrae that would not influence trace element concentration, except for Na. McMillan's specimens were the same as ours, but our sharks will be fished from New Zealand. In addition, many samples are usually examined when using LA-ICP-MS in shark studies, but we will analyze only 16 samples. Our research focuses more on comparing methods to establish the utility of LA-FC-ESI-MS instead of simply determining a shark's age using only one method.

McMillan also determined the sharks' ages in a traditional way so the age results could be compared. Some vertebrae samples were cut into 250 μm thick sections and used in the traditional age counting method, whereby sections were placed under a microscope with transmitted light to count the growth rings. This traditional age determination will be carried out in our research as well.

For the LA-ICP-MS method, vertebrae were cut into 500 μm thick sections using a diamond saw at low speed (Tillett et al., 2011; McMillan et al., 2018). The section was rinsed using MILLI-Q water and mounted on glass slides using Crystalbond 509 or Bostik Blu Tack. Lapping film and ultrapure water were used to polish the vertebrae sections until the growth bands showed sufficient contrast, and then the sections were rinsed (McMillan et al., 2018; Coiraton et al., 2019). The cleaned sections were then

glued onto a glass slide using thermoplastic glue and placed under a microscope to determine the desirable starting count point of the sections. The growth bands were counted by focusing on the outer centrum edge, which allowed them to count the bands on the corpus calcareum using imaging software (Tillett et al., 2011; McMillan et al., 2018). Thin vertebral sections are commonly used in LA studies, but we plan on utilizing half vertebral samples. Glues will be applied to mount the sample on the holder.

In Tillett's study, 213 nm Nd^{3+}:YAG laser was applied for the LA-ICP-MS system with He and Ar worked as carrier gas, whereas a New Wave 213 laser and a 193 excimer UV laser instrument were used in McMillan and Coiraton's research, respectively. Also, McMillan and Coiraton both mention an Agilent 7500cx mass spectrometer were employed. Pre-ablation process was applied to remove any contaminations, sample was ablated at a speed of 108 μm s^{-1} with 2Hz frequency, and a 180-μm size spot was made (Coiraton et al., 2019). To collect data, vertebrae were ablated at the speed of 10 μm/s with10Hz frequency, and a 83 μm sized spot. Our laser uses 532 nm light (second harmonic) compared to the 213 nm (5^{th} harmonic) in Tillett's work. The edge of vertebral sections were ablated "perpendicular to its axis" at 5 μm s^{-1} speed, 80 μm width, at a frequency of 10 Hz, and the process stopped immediately once the distal point of the edge (McMillan et al., 2018) was reached. The position of the sample and the ablation direction used by McMillan are the same set up we will apply.

The system was optimized by ablating the National Institute of Standards and Technology's (NIST) glass standard 612 (Tillett et al., 2011). NIST-612 glass was also used as an internal calibration reference since no matrix suited the vertebrae samples (Coiraton et al., 2019). NIST-612 glass was ablated after and before the ablation of every 5^{th} or 7^{th} sample (Tillett et al., 2011; Coiraton et al., 2019).

Tillette initially measured 13 elements that were not related to diet (^{7}Li, ^{25}Mg, ^{27}Al, ^{31}P, ^{43}Ca, ^{55}Mn, ^{54}Fe, ^{63}Cu, ^{64}Zn, ^{86}Sr, ^{139}La, ^{137}Ba, and ^{238}U). However, only six elements (^{7}Li, ^{25}Mg, ^{55}Mn, ^{64}Zn, ^{86}Sr, and ^{137}Ba) were further investigated because of insufficient detection limits for the other elements. As in a few other studies, ^{43}Ca with a 43% mass composition worked as an internal standard to normalize all elements' data,

with the result presented as an element:^{43}Ca ratio. McMillan studied ^{203}Pb instead of ^{64}Zn along with the other five elements, but only ^{31}P and ^{55}Mn were considered by Coiraton. The ratios of ^{31}P:^{43}Ca and ^{55}Mn:^{43}Ca were obtained and plotted with growth band distance.

Changes in the^{86}Sr:^{137}Ba ratio were highlighted, as the^{86}Sr:^{137}Ba ratio increased as the bull shark pups became juveniles and then adults because they moved from their birthplaces to habitats with greater salinities. The movement patterns of adult bull sharks may also be defined by the difference in the ^{86}Sr:^{137}Ba ratios of bull sharks and pigeye sharks. Therefore, it seems likely that vertebral microchemistry could be considered an efficient system for interpreting the connection between shark movement behaviors and habitat environments (Tillett et al., 2011).

The concentration of ^{55}Mn in the hypomineralized band is higher due to the sharks' higher food consumption and faster growth in summer, so ^{55}Mn composition can reflect age. The ^{55}Mn in the band might also be related to vertebral tissue that has more organic or protein compounds during the summer. In addition, the ^{137}Ba:^{43}Ca ratio is incorporated into environmental upwelling intensity. However, shark type, temperature, metabolic rates, and other factors affect the pattern (Mohan et al., 2017).

In 2020, Coiraton tested a few hypotheses related to vertebral microchemistry in reproductive female scalloped hammerhead sharks (Sphyrna lewini) from the Mexican Pacific using LA-ICP-MS to examine their vertebrae and embryo samples. Vertebrae were attached with holders and cut into 0.4 mm sections using a low-speed saw. Cleaned sections were placed on an HNO_3 acid-washed silicate slide. A 60 s pulsed duration excimer UV LA instrument was used to ablate samples with a repetition rate of 5 Hz, which caused 83 μm spots. The signals of 21 elements (^{7}Li, ^{24}Mg, ^{43}Ca, ^{45}Sc, ^{5}1V, ^{53}Cr, ^{55}Mn, ^{57}Fe, ^{59}Co, ^{63}Cu, ^{72}Ge, ^{85}Rb, ^{88}Sr, ^{89}Y, ^{114}Cd, ^{118}Sn, ^{137}Ba, ^{197}Au, ^{208}Pb, ^{232}Th, and ^{238}U) were recorded (Coiraton & Amezcua, 2020).

According to the element analysis described above, ^{31}P, ^{43}Ca, ^{55}Mn, ^{86}Sr, and ^{137}Ba from vertebrae will be the examination targets in our research. Of particular concern are ^{31}P and ^{55}Mn since other studies have shown that they strongly correlate to a shark's

aging (Coiraton et al., 2019; Mohan et al., 2017), although the shark species from the previous research were not school sharks.

3.4.3 LA-FC-ESI-MS of shark vertebrae

3.4.3.1 Method

This section outlines the process of collecting and preparing vertebrae samples from male and female school sharks in New Zealand, and analyzing them a mass spectrometer. The vertebrae were sectioned into thin slices and attached to stainless-steel rods for analysis. Various solutions were prepared, including a solution of ethylenediaminetetraacetic acid (EDTA) disodium salt and a solution of Ca^{2+} ions. Laser ablation on the corpus calcareum of vertebral halves was performed, and the mass spectrometer was operated in selected ion monitoring mode.

Part 1. Vertebral Sample collection and preparation

All the vertebrae were from female and male school sharks that had been captured in New Zealand. The vertebrae were chosen based on the largest centrum along the whole vertebral column and ranged between 300 mm to 1650 mm in total length. After being manually cleaned and stored in a freezer, the vertebrae were further sectioned and analyzed. The arch of each vertebra was then glued to a 6mm diameter stainless-steel rod using 5-minute Araldite adhesive (Selleys, Epoxy Adhesive) and placed on the sample stage. The sample stage can be moved in the x-axis direction and the moving distance is precise to 0.01 mm.

The vertebra was longitudinally sectioned into a 0.5 mm thin bowtie-shaped slice using a home made saw based on a diamond-coated disc (Komet 987P-480) driven by a DREMEL 4000 with a micrometer driven optical translation stage for positioning the sample, as shown below in Figure 3.4.3.2. 1. The saw was lowered through the sample by making use of a manually operated, home made, vertically oriented translation stage. To cut the thin section accurately, the vertebra was first sectioned in half, with the blade at 0.5 mm to the right of the center. The smaller half was placed in a clean cell, and the

blade was then used to cut the larger half of the vertebra, which was still mounted to the rod, to obtain the 0.5 mm section. The blade did not completely cut through the vertebra in the second cut, hence, the thin section was still slightly attached to the other part of the vertebra. A scalpel was used to cut the last attached piece to stop the thin section from flying away as a result of the diamond blade rotation. A stream of reverse osmosis (RO) water was applied to the blade during cutting to reduce friction and prevent the vertebra from burning. The thin section was placed in a plastic vial filled with ethanol to maintain hydration, while the rest of the vertebra was placed in a plastic multiwell plate. The vertebral parts were left in the fume hood to air dry overnight. The plate was then preserved in the freezer, but vials containing thin sections were stored under room temperature. The sections and parts were not polished with lapping film.

Figure 3.4.3.2. 1 Setup of vertebral sections cutting system.

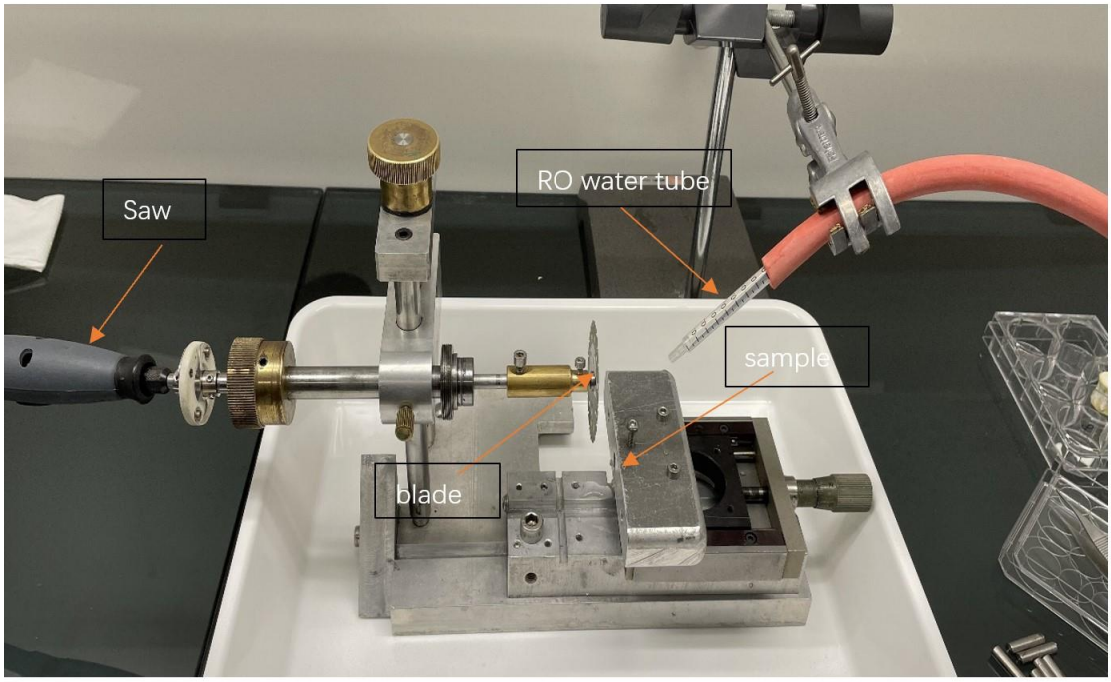

Part 2. Ethylenediaminetetraacetic Acid Disodium

To prepare a 2.01×10^{-2} M solution, 0.7482 g of ethylenediaminetetraacetic acid (EDTA) disodium salt (2Na) (Analytical Reagent Grade) was dissolved in 100 ml

MILLI-Q water. The solution was then diluted to 2.01 x 10^{-4} M and transferred to a clean beaker. To prepare 0.1M NaOH solution, 0.4 g of sodium hydroxide pellets (AR, ECF-Analytical Reagent, MW 40.00 g/mol) were dissolved in 100 mL MILLI-Q water. Drops of 0.1M NaOH solution were added into 10^{-4} M EDTA·2Na solution to change the pH to 5. The pH was measured by using the pH indicator strips. The solution collecting tube was placed in the beaker, the EDTA 2Na solution (pH~5) was pumped into the MS at a rate of 0.4 mL/sec. The positive ion mode of MS was selected.

Part 3. $^{40}Ca^{2+}$ Ions

To prepare a 10^{-4}M Ca^{2+} solution, 0.0070g of solid calcium nitrate tetrahydrate was dissolved in 10^{-4} M EDTA (pH~5). Then, the solution was pumped into the MS at a rate of 0.4 mL/sec.

Part 4. Metal Ions Mixture

After the analysis of Ca^{2+} solution, a drop of wavelength calibration solution (ICP-OES Wavelength Calibration Solution: 50mg/L Al, As, Ba, Cd, Co, Cr, Cu, Mn, Mo, Ni, Pb, Se, Sr, Zn and 500mg/L K in 5% HNO_3, Agilent Technologies) for ICP-OES and MP-AES was added into 10 mL of 10^{-4} M EDTA·2Na. The pH of the mixture was adjusted to 5 with 0.1M NaOH solution. Both positive and negative ion modes were applied during the measurement processes. The flow rate of the solution to the MS was 0.4 mL/sec.

Part 5. Vertebrae LA

The edge of the corpus calcareum of vertebral halves were ablated by the laser (532 nm wavelength, 10Hz repetition rate, 280-175 mJ pulse energy). The sample was placed on the x-axis and y-axis manually movable sample stage, which was attached to a syringe pump (New Era Pump Systems, NE-1000), and the flow rate of the pump was set so that the translational velocity of the stage was ?? . In the vertebral experiment, 10-4 M EDTA (pH~5) was used as the collecting solvent rather than 0.1% formic acid solution because the plasma will contain various metal ions, and EDTA is usually utilized to bind and dissolve metal ions of interest. The glass slide coated in liquid film

was changed, and the tube was rinsed with MILLI-Q water before each ablation.

The acquisition mode of the MS was changed to selected ion monitoring mode (SIM), and m/z 355 and 371 were selected. The flow rate of the pump connected to the MS was set to 0.4 mL/sec. The diameter of the laser ablated spot was 0.53 mm.

Figure 3.4.3.2. 2 The ablation mark on the surface of shark vertebra half.

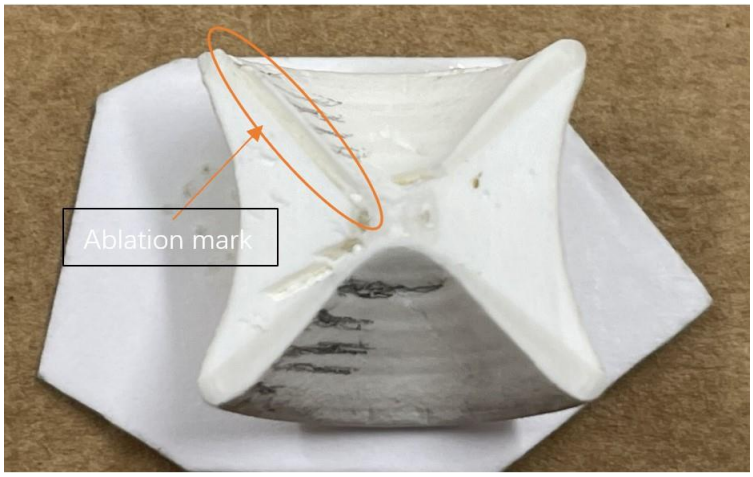

3.4.3.2 Result

EDTA·2Na solution was pumped directly to the low-resolution MS for analysis. Both positive and negative ion modes were applied to determine the best option for EDTA·2Na measurement.

Figure 3.4.3.3. 1 MS spectra of EDTA·2Na solution

a). positive mode

Top: Time dependence of the TIC (+), the spectrum of the raw data

Bottom: The signal was integrated from t = 1.40 to 10.00 min

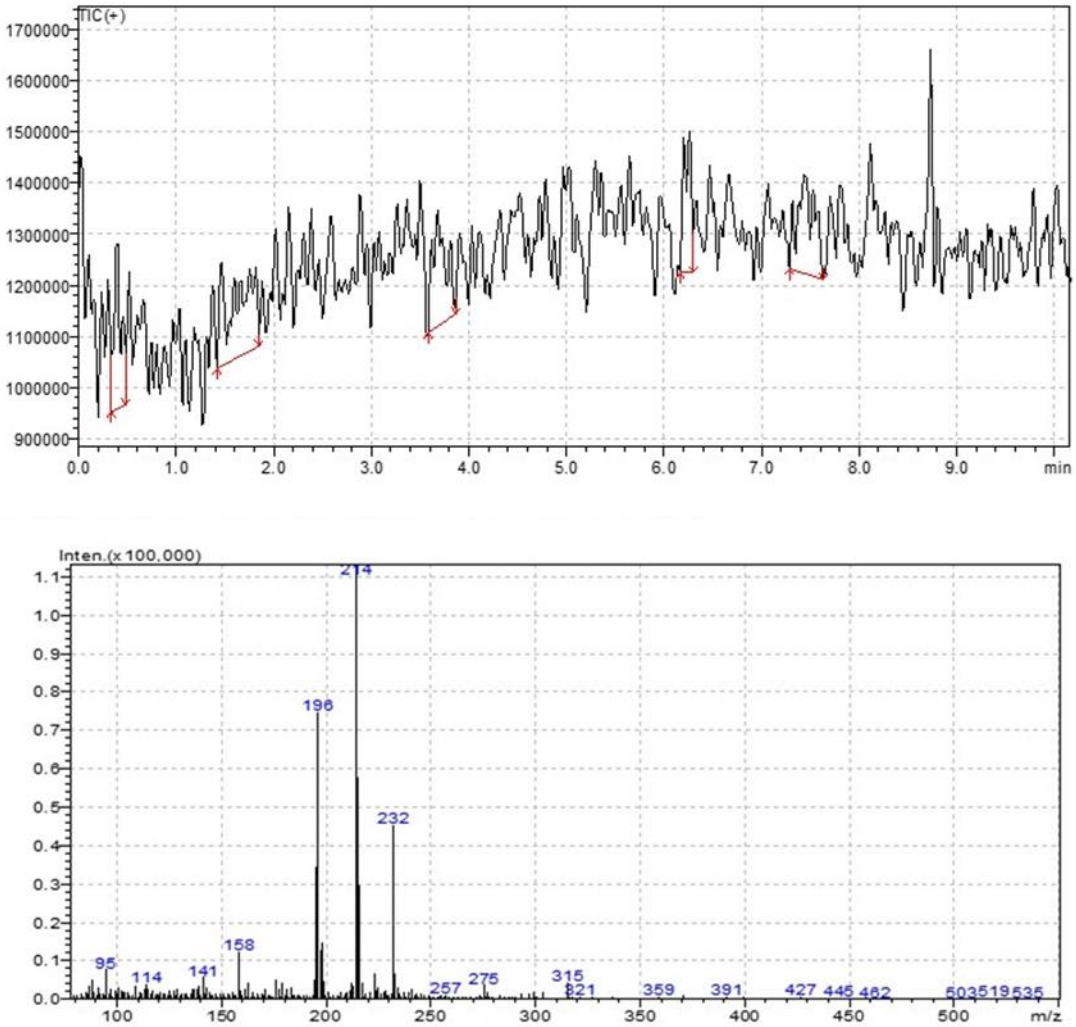

b). negative mode

Top: Time dependence of the TIC (-), the spectrum of the raw data

Bottom: The signal was integrated from t = 0.00 to 10.00 min

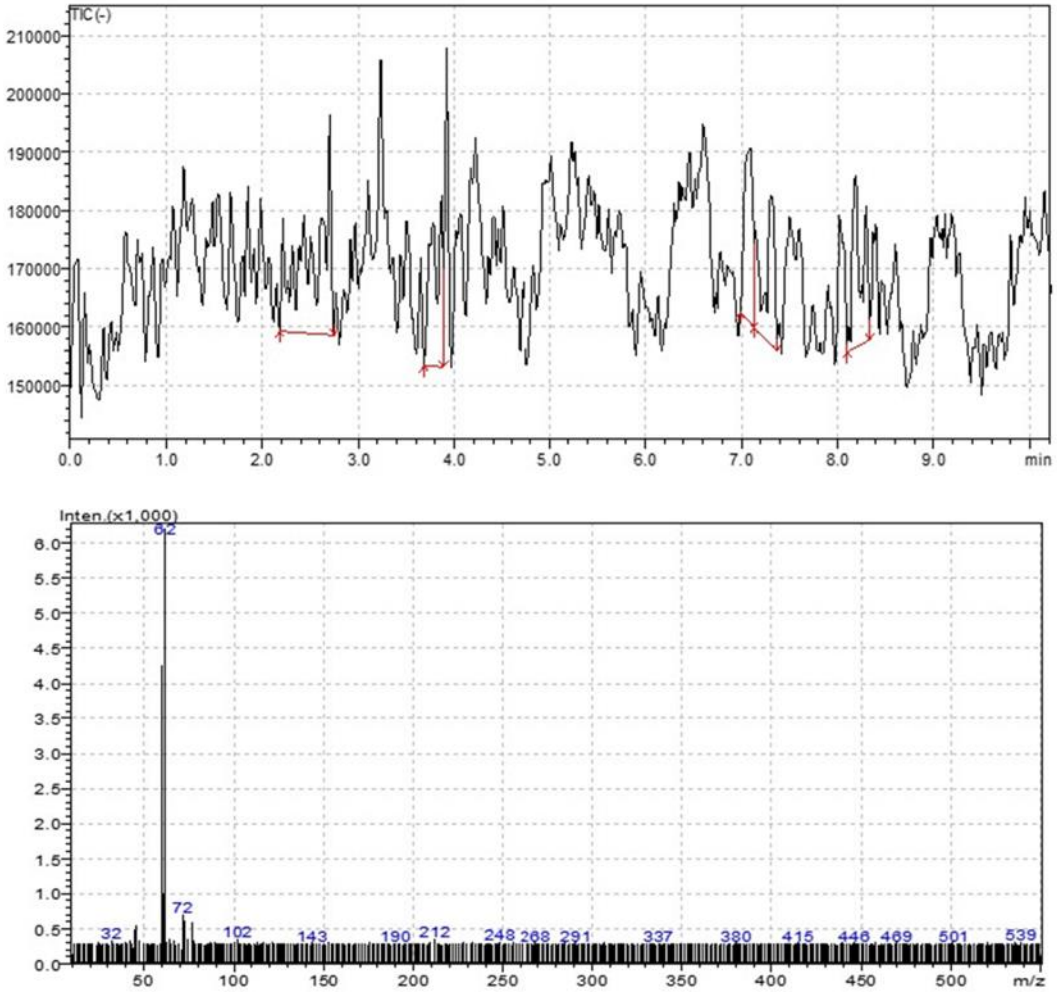

The mixture of $Ca(NO_3)_2 \cdot 4H_2O$ and EDTA·2Na solution was pumped directly to the low-resolution MS for analysis. Only positive ion mode was applied.

Figure 3.4.3.3. 2 Three MS spectra of the mixture of $Ca(NO_3)_2 \cdot 4H_2O$ and EDTA·2Na solution, and all the measurements were carried out under positive ion mode.

a). Top: Time dependence of the TIC (+), the spectrum of the raw data

Bottom: The signal was integrated from t = 3.00 to 10.00 min

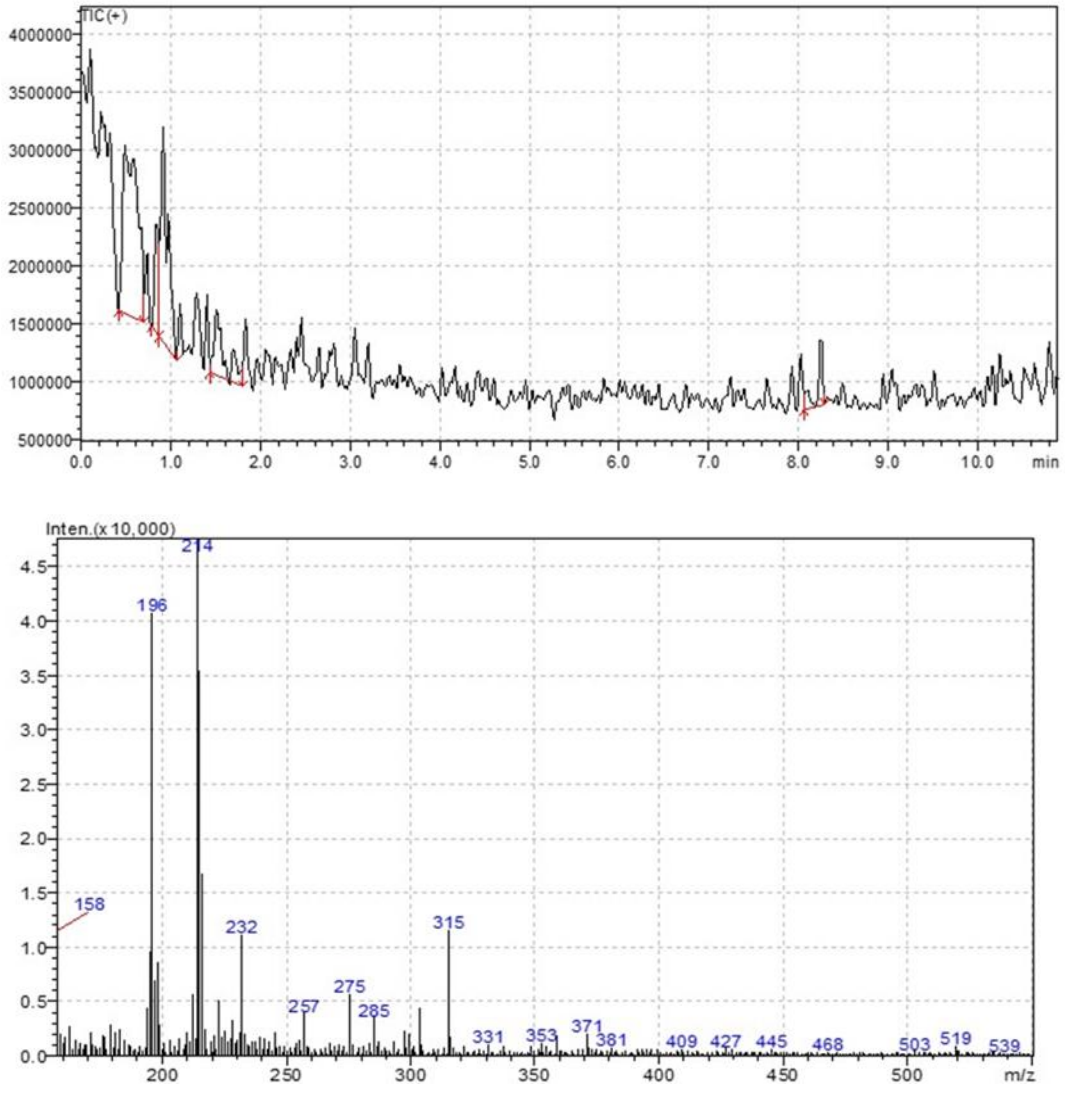

b). Top: Time dependence of the TIC (+), the spectrum of the raw data

Bottom: The signal was integrated from t = 7.00 to 12.00 min

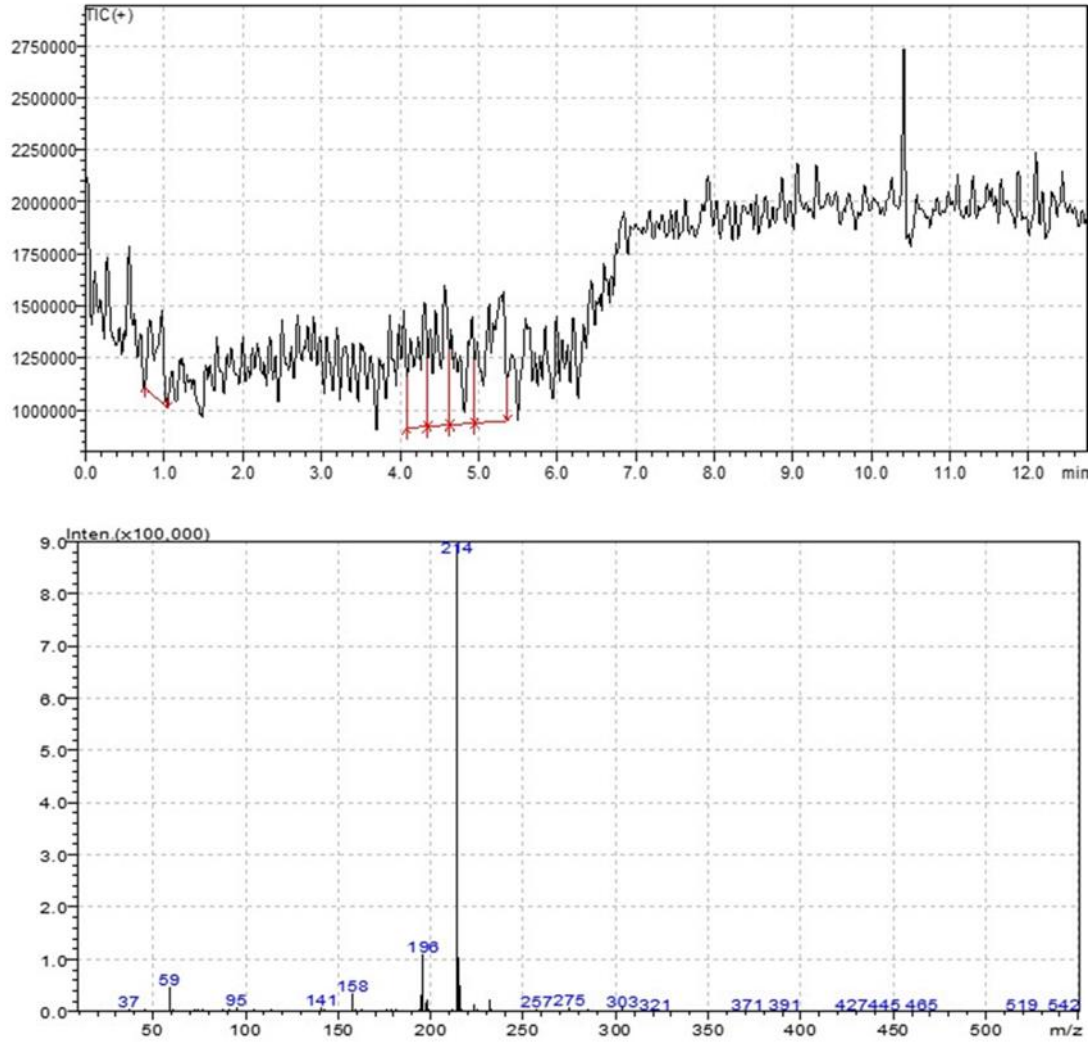

c). Top: Time dependence of the TIC (+), the spectrum of the raw data

Bottom: The signal was integrated from t = 0.00 to 11.00 min

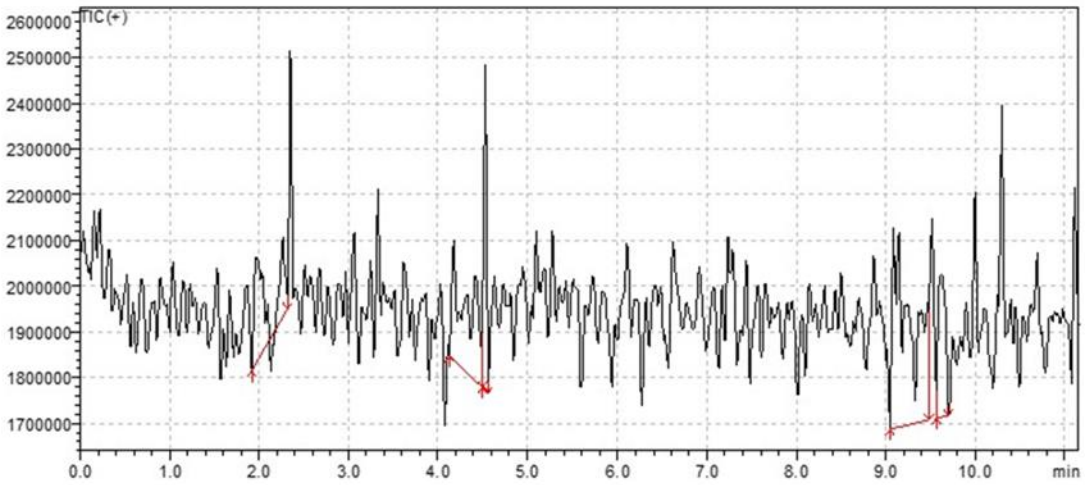

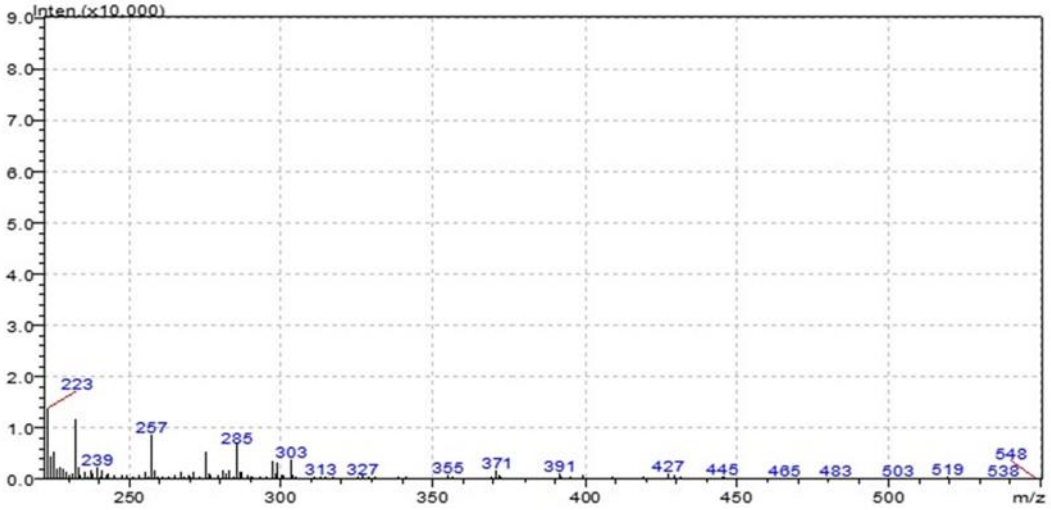

The mixture of calibration solution and EDTA·2Na solution was pumped directly to the low-resolution MS for analysis. Only positive ion mode was applied.

Figure 3.4.3.3. 3 Three MS spectra of the mixture of calibration solution and EDTA·2Na solution, and all the measurements were carried out under positive ion mode.

a). Top: Time dependence of the TIC (+), the spectrum of the raw data

Bottom: The signal was integrated from t = 0.50 to 15.00 min

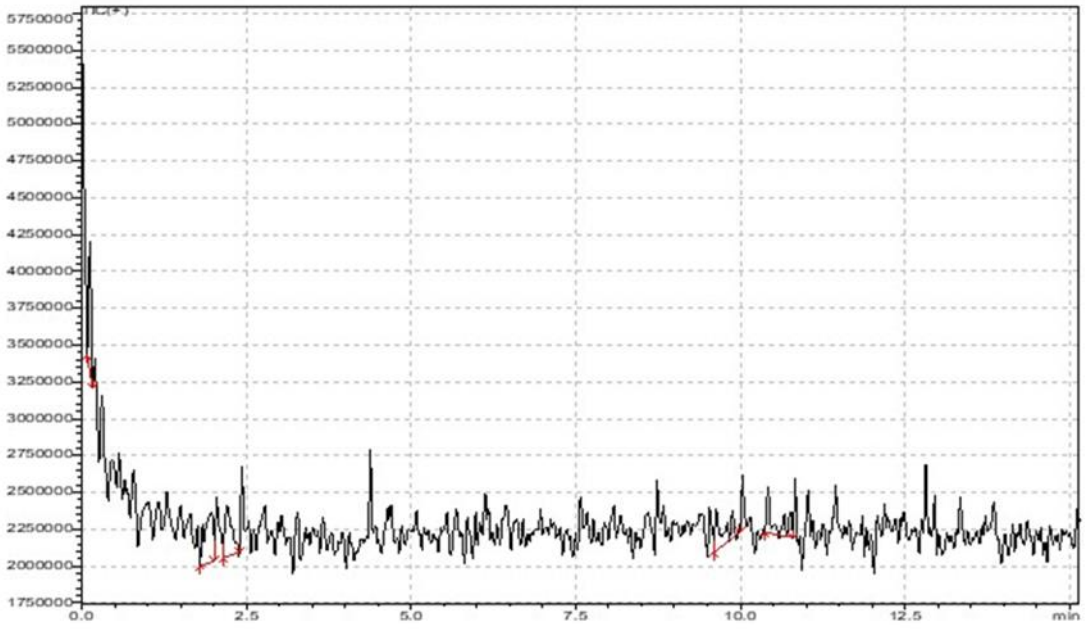

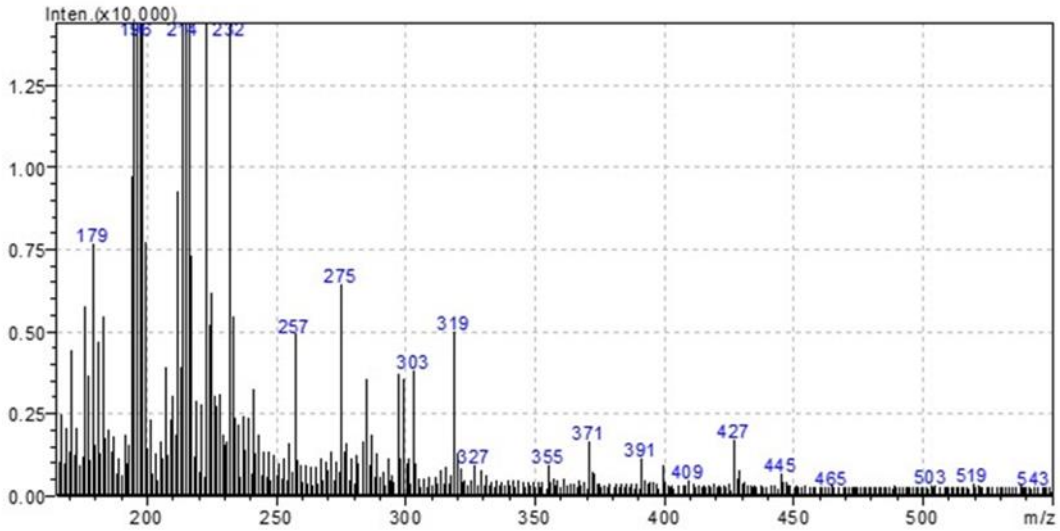

b). Top: Time dependence of the TIC (+), the spectrum of the raw data

Bottom: The signal was integrated from t = 0.50 to 11.00min

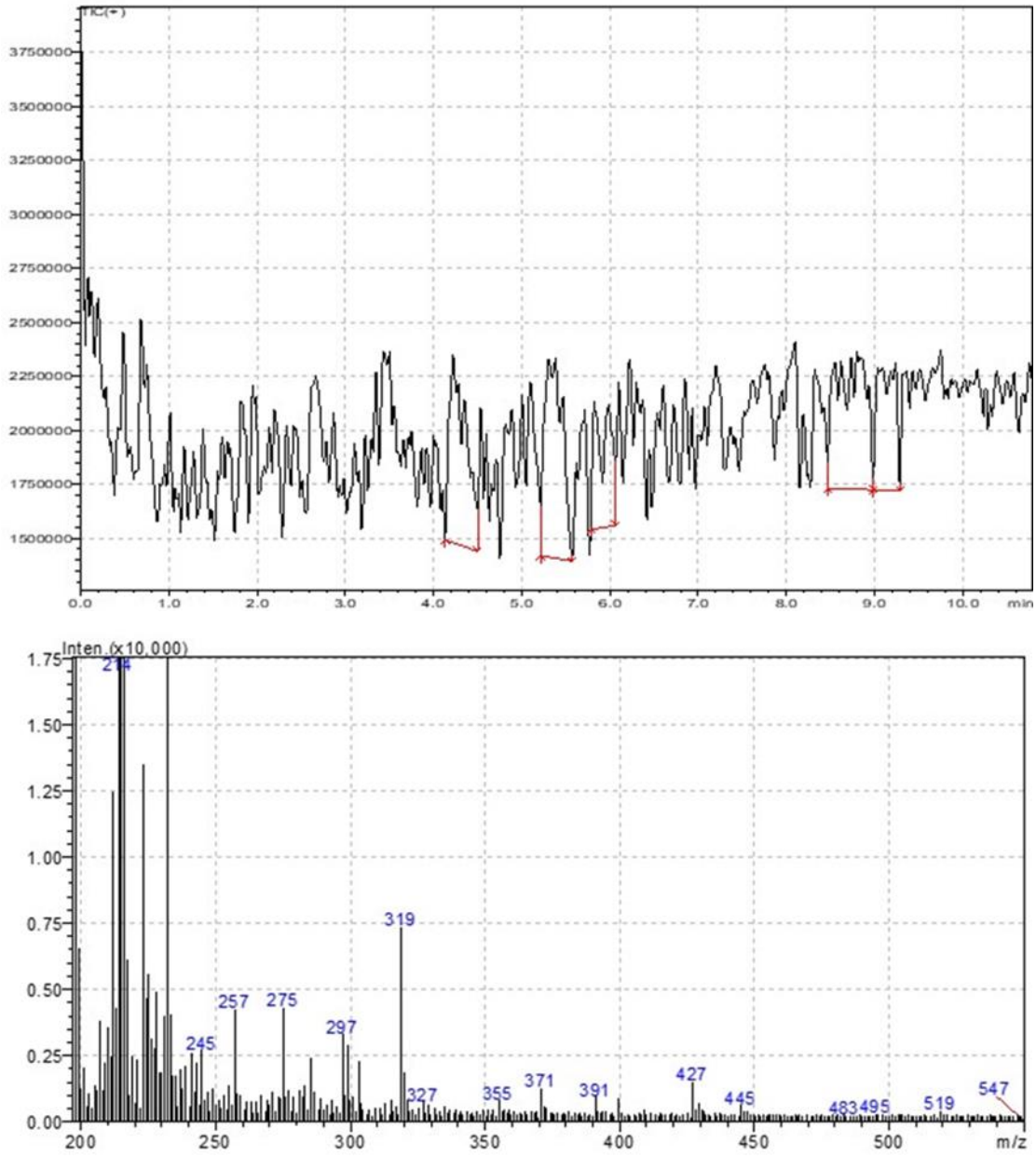

c). Top: Time dependence of the TIC (+), the spectrum of the raw data

Bottom: The signal was integrated from t = 0.50 to 10.00min

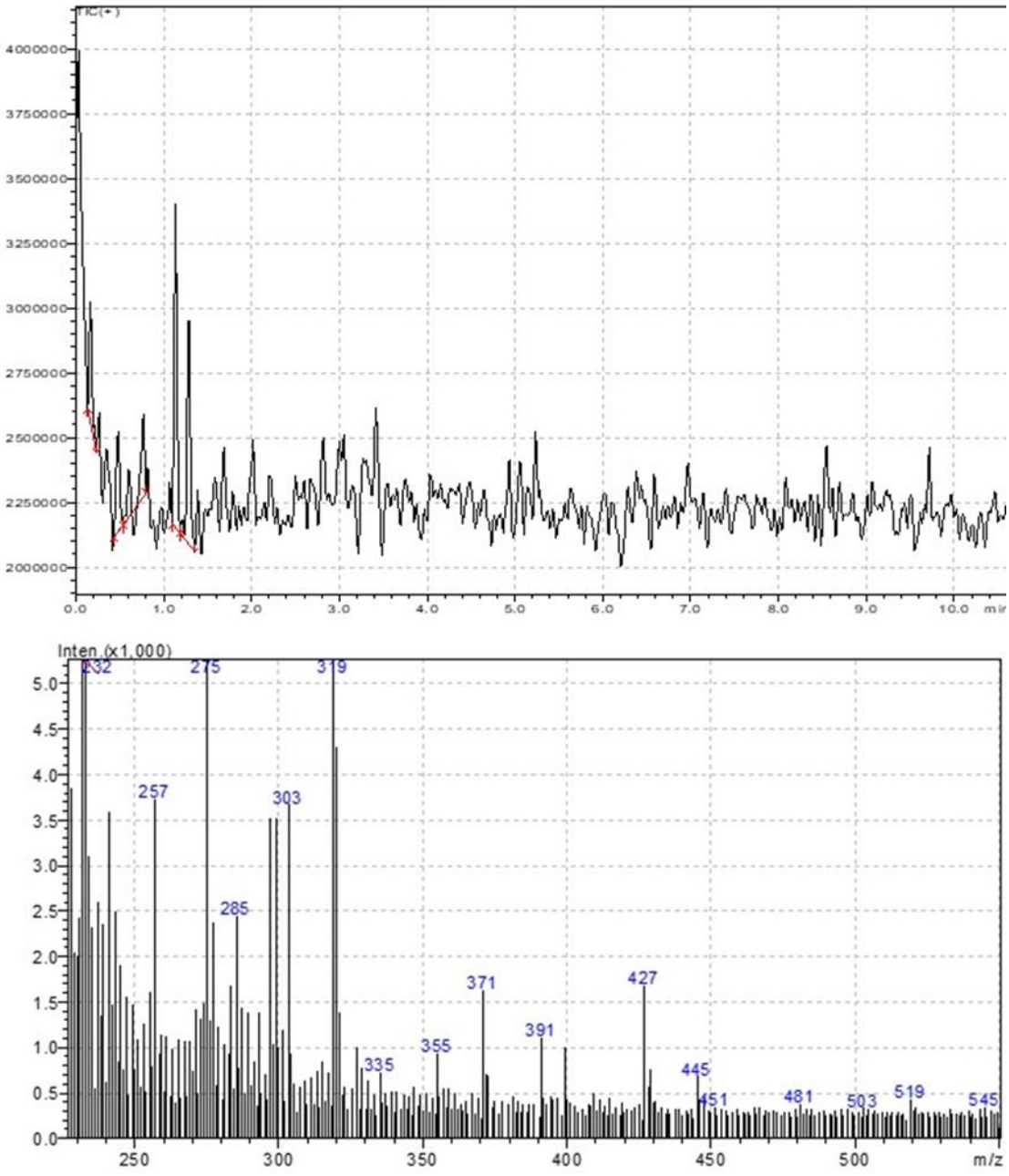

Figure 3.4.3.3. 4 MS spectra of the plasma produced through the LA of shark vertebral halves, m/z: 355 ($^{64}Zn^{2+}$) and 371 ($^{40}Cu^{2+}$) were selected.

NWN6, diameter = 11.2 mm, total length = 1029 mm. The ablation started at T = 1.00 min and stopped at T = 10.25 min. The average energy of the laser pulse was 192 mJ (200-176 mJ). The moving speed of the sample stage during the ablation processes was 0.551 mm/sec.

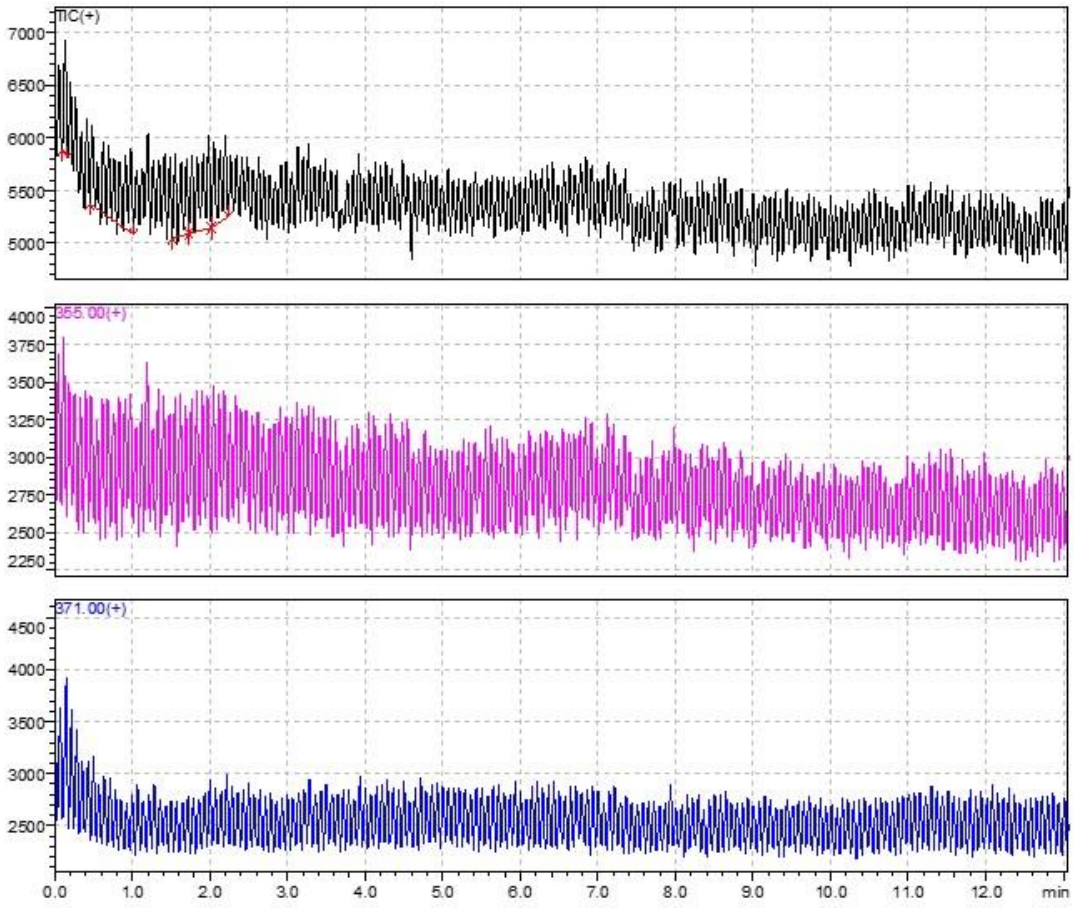

Table 3.4.3.3. 1 Every three peaks were chosen to be integrated to obtain the intensity values of m/z 355 and m/z 371.

Average Time = $(T_1 + T_2)/2$.

TIME Range	T_1	T_2	Average Time	Time-1.00 min	Distance (mm)	m/z 355	m/z 371
[1.083->1.300]	1.083	1.300	1.1915	0.1915	0.105517	2927	2549
[1.300->1.517]	1.300	1.517	1.4085	0.4085	0.225084	2926	2504
[1.517->1.733]	1.517	1.733	1.6250	0.6250	0.344375	2917	2493

[1.733->1.933]	1.733	1.933	1.8330	0.8330	0.458983	2980	2515
[1.933->2.150]	1.933	2.150	2.0415	1.0415	0.573867	2960	2606
[2.150->2.367]	2.150	2.367	2.2585	1.2585	0.693434	2955	2624
[2.367->2.583]	2.367	2.583	2.4750	1.4750	0.812725	2914	2585
[2.583->2.800]	2.583	2.800	2.6915	1.6915	0.932017	2847	2546
[2.800->3.017]	2.800	3.017	2.9085	1.9085	1.051584	2872	2520
[3.017->3.233]	3.017	3.233	3.1250	2.1250	1.170875	2909	2546
[3.233->3.433]	3.233	3.433	3.3330	2.3330	1.285483	2916	2580
[3.433->3.650]	3.433	3.650	3.5415	2.5415	1.400367	2867	2590
[3.650->3.867]	3.650	3.867	3.7585	2.7585	1.519934	2782	2567
[3.867->4.083]	3.867	4.083	3.9750	2.9750	1.639225	2828	2595
[4.083->4.300]	4.083	4.300	4.1915	3.1915	1.758517	2830	2613
[4.300->4.517]	4.300	4.517	4.4085	3.4085	1.878084	2826	2597
[4.517->4.733]	4.517	4.733	4.6250	3.6250	1.997375	2775	2577
[4.733->4.950]	4.733	4.950	4.8415	3.8415	2.116667	2773	2608
[4.950->5.150]	4.950	5.150	5.0500	4.0500	2.231550	2763	2600
[5.150->5.367]	5.150	5.367	5.2585	4.2585	2.346434	2754	2596
[5.367->5.583]	5.367	5.583	5.4750	4.4750	2.465725	2797	2576
[5.583->5.800]	5.583	5.800	5.6915	4.6915	2.585017	2785	2589
[5.800->6.017]	5.800	6.017	5.9085	4.9085	2.704584	2772	2583
[6.017->6.233]	6.017	6.233	6.1250	5.1250	2.823875	2796	2579
[6.233->6.450]	6.233	6.450	6.3415	5.3415	2.943167	2833	2591
[6.450->6.667]	6.450	6.667	6.5585	5.5585	3.062734	2821	2562
[6.667->6.883]	6.667	6.883	6.7750	5.7750	3.182025	2855	2585
[6.883->7.083]	6.883	7.083	6.9830	5.9830	3.296633	2824	2553
[7.083->7.300]	7.083	7.300	7.1915	6.1915	3.411517	2851	2560
[7.300->7.517]	7.300	7.517	7.4085	6.4085	3.531084	2765	2505
[7.517->7.733]	7.517	7.733	7.6250	6.6250	3.650375	2736	2501
[7.733->7.950]	7.733	7.950	7.8415	6.8415	3.769667	2730	2516
[7.950->8.167]	7.95	8.167	8.0585	7.0585	3.889234	2783	2505
[8.167->8.383]	8.167	8.383	8.2750	7.2750	4.008525	2726	2512
[8.383->8.600]	8.383	8.600	8.4915	7.4915	4.127817	2749	2503
[8.600->8.800]	8.600	8.800	8.7000	7.7000	4.242700	2734	2515
[8.800->9.017]	8.800	9.017	8.9085	7.9085	4.357584	2690	2516
[9.017->9.233]	9.017	9.233	9.1250	8.1250	4.476875	2669	2512
[9.233->9.450]	9.233	9.450	9.3415	8.3415	4.596167	2695	2477
[9.450->9.667]	9.450	9.667	9.5585	8.5585	4.715734	2675	2502
[9.667->9.883]	9.667	9.883	9.7750	8.7750	4.835025	2648	2507
[9.883->10.100]	9.883	10.100	9.9915	8.9915	4.954317	2656	2471
[10.100->10.300]	10.100	10.300	10.2000	9.2000	5.069200	2630	2497
[10.300->10.517	10.300	10.517	10.4085	9.4085	5.184084	2660	2509
[10.517->10.733]	10.517	10.733	10.625	9.6250	5.303375	2668	2516

Figure 3.4.3.3. 5 The relationship between laser ablation distance in the NIWAWN6 vertebra sample and the intensity of the metal ion

a). $^{40}Ca^{2+}$

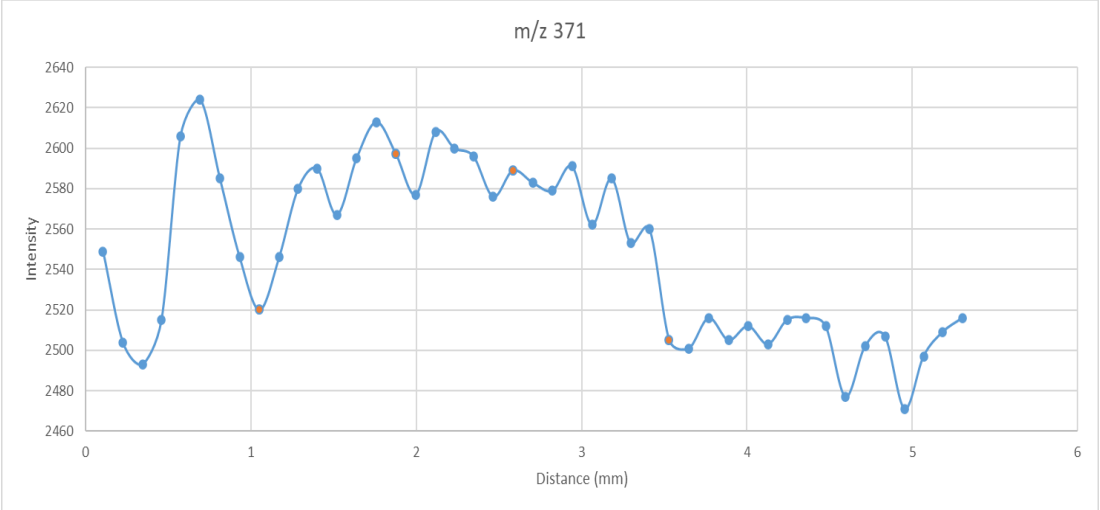

b). $^{64}Zn^{2+}$

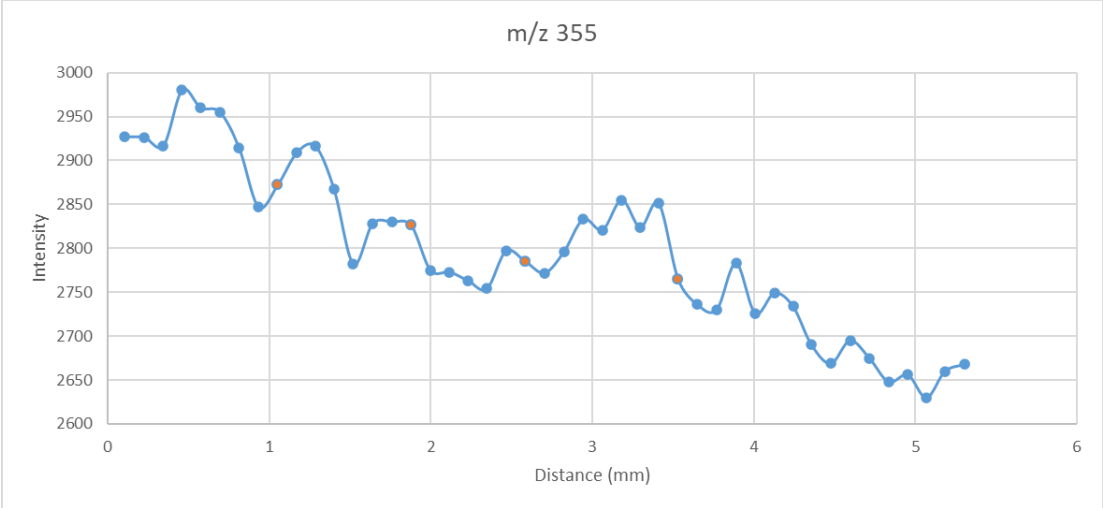

Figure 3.4.3.3. 6 MS spectra of the plasma produced through the LA of shark vertebral halves, m/z: 355 ($^{64}Zn^{2+}$) and 371 ($^{40}Cu^{2+}$) were selected.

J18, diameter = 14.7, total length = 1220 mm. The ablation started at T = 2.48 min and stopped at T = 16.40 min. The average energy of the laser pulse was 214 mJ (178-231 mJ). The moving speed of the sample stage during the ablation processes was 0.656 mm/sec.

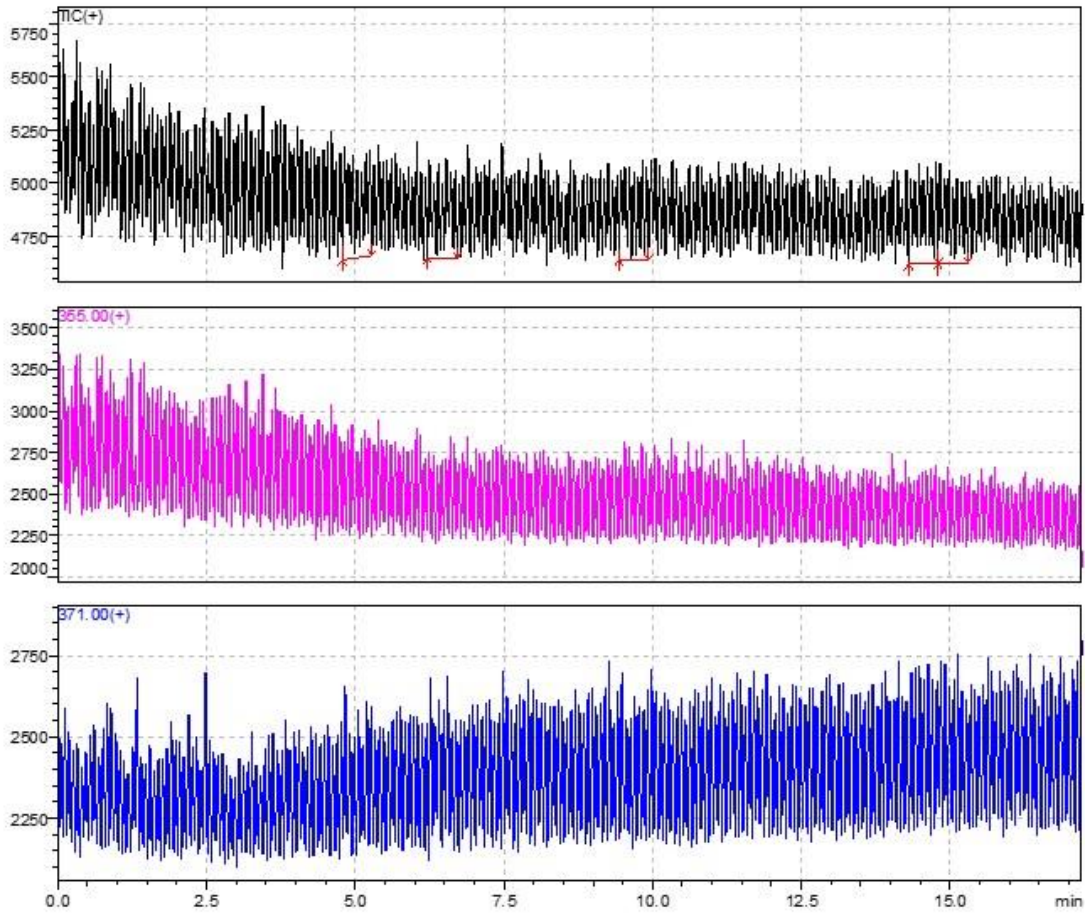

Table 3.4.3.3. 2 Every three peaks were chosen to be integrated to obtain the intensity values of m/z 355 and m/z 371.

Time Range	T_1	T_1	Average Time	Time-2.38 mins	Distance (mm)	m/z 355	m/z 371
[2.633->2.850]	2.633	2.850	2.7415	0.3615	0.237144	2679	2293
[2.850->3.067]	2.850	3.067	2.9585	0.5785	0.379496	2697	2262
[3.067->3.283]	3.067	3.283	3.1750	0.7950	0.521520	2671	2295

[3.283->3.483]	3.283	3.483	3.3830	1.0030	0.657968	2700	2282
[3.483->3.700]	3.483	3.700	3.5915	1.2115	0.794744	2639	2322
[3.700->3.917]	3.700	3.917	3.8085	1.4285	0.937096	2626	2332
[3.917->4.133]	3.917	4.133	4.0250	1.6450	1.079120	2618	2335
[4.133->4.350]	4.133	4.350	4.2415	1.8615	1.221144	2579	2326
[4.350->4.567]	4.350	4.567	4.4585	2.0785	1.363496	2569	2332
[4.567->4.783]	4.567	4.783	4.6750	2.2950	1.505520	2573	2326
[4.783->5.000]	4.783	5.000	4.8915	2.5115	1.647544	2553	2363
[5.000->5.200]	5.000	5.200	5.1000	2.7200	1.784320	2538	2356
[5.200->5.417]	5.200	5.417	5.3085	2.9285	1.921096	2546	2376
[5.417->5.633]	5.417	5.633	5.5250	3.1450	2.063120	2530	2359
[5.633->5.850]	5.633	5.850	5.7415	3.3615	2.205144	2508	2380
[5.850->6.067]	5.850	6.067	5.9585	3.5785	2.347496	2509	2371
[6.067->6.283]	6.067	6.283	6.1750	3.7950	2.489520	2489	2371
[6.283->6.500]	6.283	6.500	6.3915	4.0115	2.631544	2442	2402
[6.500->6.700]	6.500	6.700	6.6000	4.2200	2.768320	2513	2386
[6.700->6.917]	6.700	6.917	6.8085	4.4285	2.905096	2488	2382
[6.917->7.133]	6.917	7.133	7.0250	4.6450	3.047120	2466	2399
[7.133->7.350]	7.133	7.350	7.2415	4.8615	3.189144	2464	2394
[7.350->7.567]	7.350	7.567	7.4585	5.0785	3.331496	2484	2413
[7.567->7.783]	7.567	7.783	7.6750	5.2950	3.473520	2466	2396
[7.783->8.000]	7.783	8.000	7.8915	5.5115	3.615544	2436	2421
[8.000->8.200]	8.000	8.200	8.1000	5.7200	3.752320	2499	2401
[8.200->8.417]	8.200	8.417	8.3085	5.9285	3.889096	2441	2409
[8.417->8.633]	8.417	8.633	8.5250	6.1450	4.031120	2434	2402
[8.633->8.850]	8.633	8.850	8.7415	6.3615	4.173144	2434	2414
[8.850->9.067]	8.850	9.067	8.9585	6.5785	4.315496	2448	2411
[9.067->9.283]	9.067	9.283	9.1750	6.7950	4.457520	2434	2428
[9.283->9.500]	9.283	9.500	9.3915	7.0115	4.599544	2440	2419
[9.500->9.717]	9.500	9.717	9.6085	7.2285	4.741896	2479	2391
[9.717->9.917]	9.717	9.917	9.8170	7.4370	4.878672	2480	2394
[9.917->10.133]	9.917	10.133	10.025	7.6450	5.015120	2468	2438
[10.133->10.350]	10.133	10.350	10.2415	7.8615	5.157144	2466	2413
[10.350->10.567]	10.350	10.567	10.4585	8.0785	5.299496	2441	2398
[10.567->10.783]	10.567	10.783	10.6750	8.2950	5.441520	2457	2405
[10.783->11.000]	10.783	11.000	10.8915	8.5115	5.583544	2438	2423
[11.000->11.217]	11.000	11.217	11.1085	8.7285	5.725896	2422	2418
[11.217->11.433]	11.217	11.433	11.3250	8.9450	5.867920	2443	2423
[11.433->11.633]	11.433	11.633	11.5330	9.1530	6.004368	2465	2423
[11.633->11.850]	11.633	11.850	11.7415	9.3615	6.141144	2435	2454
[11.850->12.067]	11.850	12.067	11.9585	9.5785	6.283496	2426	2429
[12.067->12.283]	12.067	12.283	12.1750	9.795	6.425520	2445	2417

[12.283->12.500]	12.283	12.500	12.3915	10.0115	6.567544	2419	2425
[12.500->12.717]	12.500	12.717	12.6085	10.2285	6.709896	2412	2424
[12.717->12.933]	12.717	12.933	12.8250	10.4450	6.851920	2417	2430
[12.933->13.133]	12.933	13.133	13.0330	10.6530	6.988368	2421	2423
[13.133->13.350]	13.133	13.35	13.2415	10.8615	7.125144	2389	2438
[13.350->13.567]	13.350	13.567	13.4585	11.0785	7.267496	2388	2430
[13.567->13.783]	13.567	13.783	13.6750	11.2950	7.409520	2405	2427
[13.783->14.000]	13.783	14.000	13.8915	11.5115	7.551544	2379	2443
[14.000->14.217]	14.000	14.217	14.1085	11.7285	7.693896	2396	2442
[14.217->14.433]	14.217	14.433	14.3250	11.9450	7.835920	2403	2447
[14.433->14.633]	14.433	14.633	14.5330	12.1530	7.972368	2414	2467
[14.633->14.850]	14.633	14.850	14.7415	12.3615	8.109144	2403	2482
[14.850->15.067]	14.850	15.067	14.9585	12.5785	8.251496	2387	2478
[15.067->15.283]	15.067	15.283	15.1750	12.7950	8.393520	2377	2464
[15.283->15.500]	15.283	15.500	15.3915	13.0115	8.535544	2374	2445
[15.500->15.717]	15.500	15.717	15.6085	13.2285	8.677896	2392	2472
[15.717->15.933]	15.717	15.933	15.8250	13.4450	8.819920	2380	2456
[15.933->16.150]	15.933	16.150	16.0415	13.6615	8.961944	2345	2467
[16.150->16.350]	16.150	16.350	16.2500	13.8700	9.098720	2372	2468
[16.350->16.567]	16.350	16.567	16.4585	14.0785	9.235496	2373	2458
[16.567->16.783]	16.567	16.783	16.6750	14.2950	9.377520	2355	2468
[16.783->17.000]	16.783	17.000	16.8915	14.5115	9.519544	2348	2470

Figure 3.4.3.3. 7The relationship between laser ablation distance in the J18 vertebra sample and the intensity of metal ion

a). $^{40}Ca^{2+}$

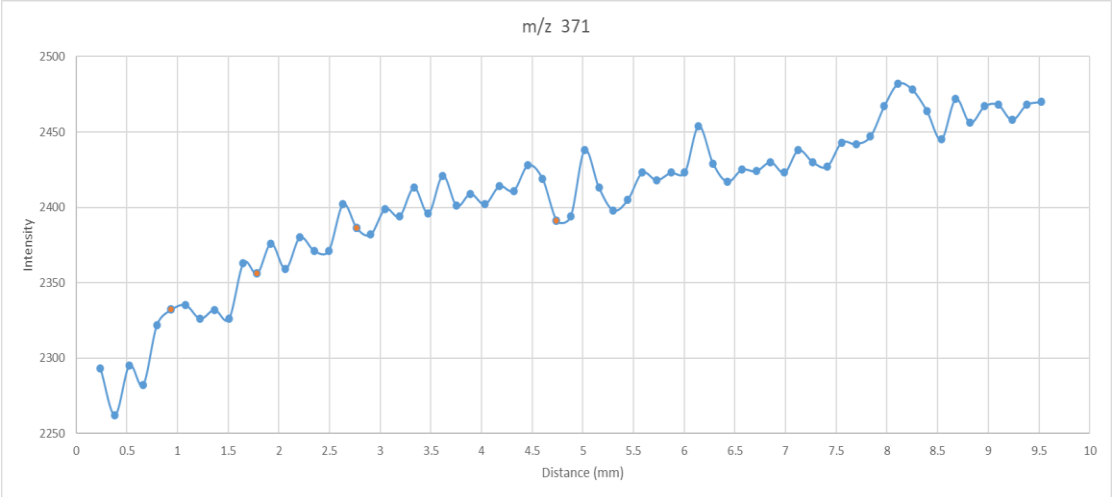

b). $^{64}Zn^{2+}$

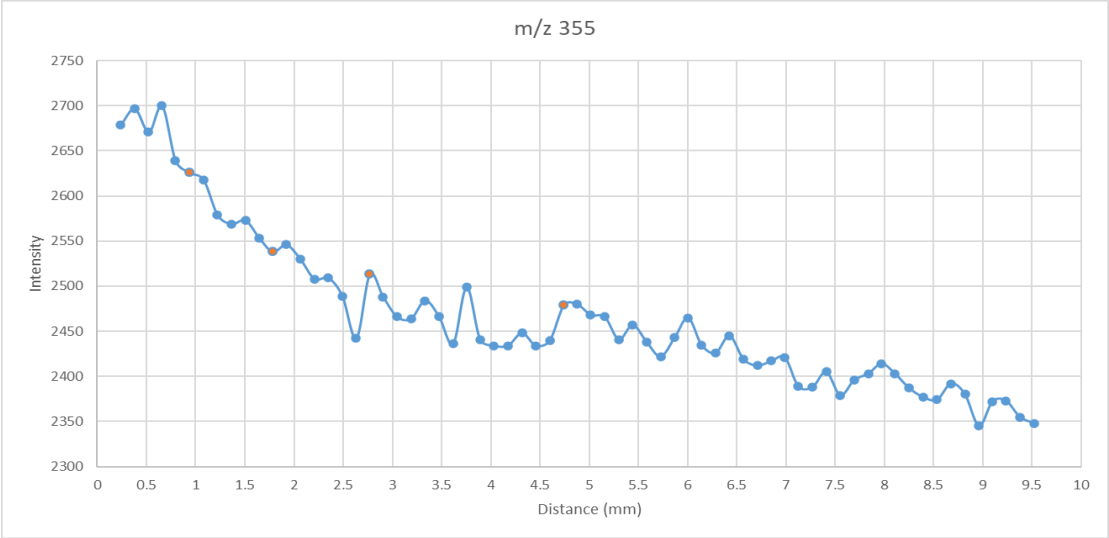
m/z 355
Intensity
2750
2700
2650
2600
2550
2500
2450
2400
2350
2300
0
0.5
1
1.5
2
2.5
3
3.5
4
4.5
5
5.5
6
6.5
7
7.5
8
8.5
9
9.5
10
Distance (mm)

Figure 3.4.3.3. 8 MS spectra of the plasma produced through the LA of shark vertebral halves, m/z: 355 ($^{64}Zn^{2+}$) and 371 ($^{40}Cu^{2+}$) were selected.

MF7 The ablation started at T = 0.00 min and stopped at T = 11.60 min. The average energy of the laser pulse was 260 mJ (279-241 mJ). The moving speed of the sample stage during the ablation processes was 0.655 mm/sec.

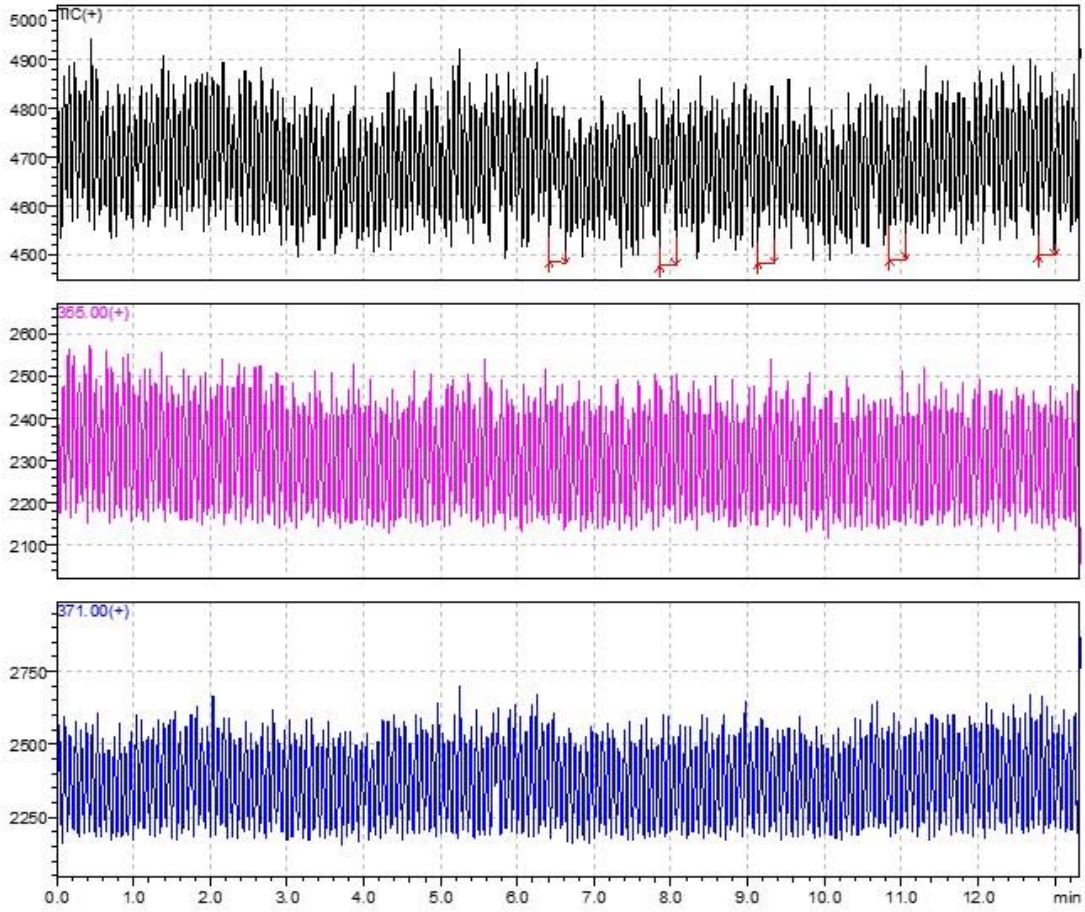

Table 3.4.3.3. 3 Every three peaks were chosen to be integrated to obtain the intensity values of m/z 355 and m/z 371.

Time Range	T1	T2	Average Time	Distance	m/z 355	m/z 371
[0.183->0.400]	0.183	0.400	0.2915	0.190933	2334	2386
[0.400->0.617]	0.400	0.617	0.5085	0.333068	2330	2382
[0.617->0.833]	0.617	0.833	0.7250	0.474875	2355	2360
[0.833->1.033]	0.833	1.033	0.9330	0.611115	2338	2357
[1.033->1.250]	1.033	1.250	1.1415	0.747683	2322	2369
[1.250->1.467]	1.250	1.467	1.3585	0.889818	2331	2402
[1.467->1.683]	1.467	1.683	1.5750	1.031625	2312	2392
[1.683->1.900]	1.683	1.900	1.7915	1.173433	2310	2414
[1.900->2.117]	1.900	2.117	2.0085	1.315568	2312	2403

[2.117->2.333]	2.117	2.333	2.2250	1.457375	2318	2384
[2.333->2.550]	2.333	2.550	2.4415	1.599183	2320	2373
[2.550->2.767]	2.550	2.767	2.6585	1.741318	2315	2366
[2.767->2.967]	2.767	2.967	2.8670	1.877885	2313	2386
[2.967->3.183]	2.967	3.183	3.0750	2.014125	2286	2381
[3.183->3.400]	3.183	3.400	3.2915	2.155933	2302	2382
[3.400->3.617]	3.400	3.617	3.5085	2.298068	2294	2375
[3.617->3.833]	3.617	3.833	3.7250	2.439875	2283	2363
[3.833->4.050]	3.833	4.050	3.9415	2.581683	2299	2360
[4.050->4.267]	4.050	4.267	4.1585	2.723818	2288	2356
[4.267->4.467]	4.267	4.467	4.3670	2.860385	2292	2391
[4.467->4.683]	4.467	4.683	4.5750	2.996625	2296	2386
[4.683->4.900]	4.683	4.900	4.7915	3.138433	2289	2400
[4.900->5.117]	4.900	5.117	5.0085	3.280568	2284	2394
[5.117->5.333]	5.117	5.333	5.2250	3.422375	2309	2405
[5.333->5.550]	5.333	5.550	5.4415	3.564183	2295	2384
[5.550->5.767]	5.550	5.767	5.6585	3.706318	2296	2413
[5.767->5.983]	5.767	5.983	5.8750	3.848125	2289	2395
[5.983->6.183]	5.983	6.183	6.0830	3.984365	2293	2394
[6.183->6.400]	6.183	6.400	6.2915	4.120933	2305	2421
[6.400->6.617]	6.400	6.617	6.5085	4.263068	2297	2391
[6.617->6.833]	6.617	6.833	6.7250	4.404875	2286	2360
[6.833->7.050]	6.833	7.050	6.9415	4.546683	2277	2361
[7.050->7.267]	7.050	7.267	7.1585	4.688818	2283	2378
[7.267->7.483]	7.267	7.483	7.3750	4.830625	2283	2362
[7.483->7.700]	7.483	7.700	7.5915	4.972433	2289	2367
[7.700->7.900]	7.700	7.900	7.8000	5.109000	2311	2363
[7.900->8.117]	7.900	8.117	8.0085	5.245568	2304	2394
[8.117->8.333]	8.117	8.333	8.2250	5.387375	2292	2381
[8.333->8.550]	8.333	8.550	8.4415	5.529183	2295	2387
[8.550->8.767]	8.550	8.767	8.6585	5.671318	2294	2371
[8.767->8.983]	8.767	8.983	8.8750	5.813125	2283	2393
[8.983->9.200]	8.983	9.200	9.0915	5.954933	2292	2386
[9.200->9.400]	9.200	9.400	9.3000	6.091500	2319	2369
[9.400->9.617]	9.400	9.617	9.5085	6.228068	2295	2381
[9.617->9.833]	9.617	9.833	9.7250	6.369875	2290	2384
[9.833->10.050]	9.833	10.050	9.9415	6.511683	2273	2367
[10.050->10.267]	10.050	10.267	10.1585	6.653818	2276	2362
[10.267->10.483]	10.267	10.483	10.3750	6.795625	2282	2382
[10.483->10.700]	10.483	10.700	10.5915	6.937433	2280	2411
[10.700->10.917]	10.700	10.917	10.8085	7.079568	2281	2391

Figure 3.4.3.3. 9 The relationship between laser ablation distance in the MF7 vertebra sample and the intensity of metal ion

a). $^{40}Ca^{2+}$

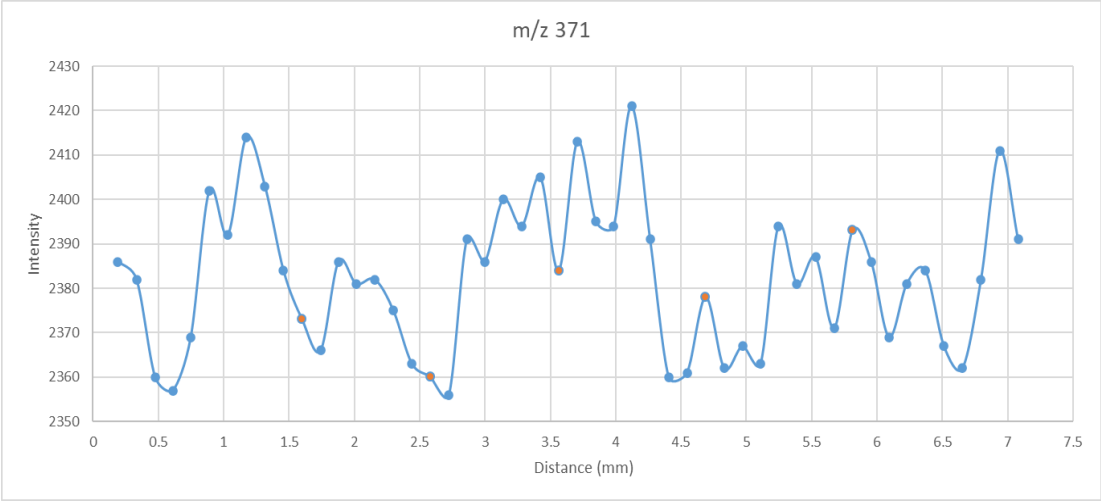

b). $^{64}Zn^{2+}$

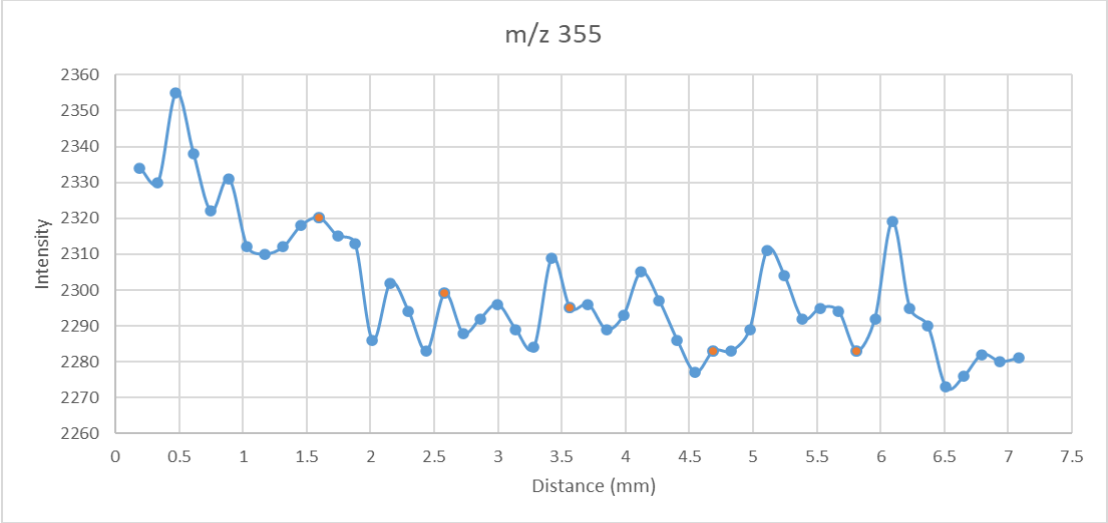

3.4.3.3 Discussion

The opaque bands in shark vertebrae are calcium rich because sharks grow more slowly in cold environments, whereas translucent bands contain less calcium due to the faster growth rates in warm temperatures. The LA-FC-ESI-MS of vertebrae should show the spatial features of the sample, thus, the calcium and variations in other elements in the bands can be detected. Shark vertebrae were ablated by laser and examined by MS under negative and positive ion mode. A burette was filled with 0.1%

formic acid solution to form a liquid film on the glass slide. Many noise signals appeared under negative polarity, and several signals were detected in positive ion mode. Mineral compounds that are composed of shark vertebrae are barely soluble in formic acid solution. To enhance the ionisation of the ESI technique for metal ions. Ethylenediaminetetraacetic acid (EDTA) is a chelating agent that can bind various metal ions, therefore, it is a better option than formic acid. Signals of EDTA·2Na were difficult to detect using the MS. According to other studies, the pH of EDTA is usually adjusted by using a weak base, such as ammonium acetate. Under positive mode, several peaks, such as $[H_5L]^+$ (m/z 293), Na-EDTA (315), Na_2-EDTA (337), Na_3-EDTA (359), Na_4-EDTA (381), Na_5-EDTA (403), and EDTA fragmentation losses of multiple CO or CO_2 in combination with H_2O were detected. The spectrum of EDTA·2Na solution (Fig. 3.4.3.3.1, a) showed m/z peaks at 315 and 359, therefore, Na-EDTA and Na_3-EDTA existed in our solution. Theoretically, under negative mode, $[H_3L]^-$ (291), Na_2-EDTA (335), Na_3-EDTA (357), and fragments of EDTA lose multiple CO_2, H_2O, and CH_2O_2 (Beck, 2021). Nevertheless, none of the relative peaks appeared in the spectrum of our EDTA·2Na solution.

As previously noted, calcium ion is rich in the shark vertebral structure and is one of the main study targets. Before analyzing vertebral samples, a calcium nitrate solution was prepared as a standard solution to establish the mass spectrum of $^{40}Ca^{2+}$ion in EDTA·2Na solution. EDTA·2Na and the calcium solution were mixed in 1:1 ratio. An attempt was made to measure the mass spectrum of the EDTA·2Na and calcium nitrate mixture without balancing the pH, whereby no peaks related to $^{40}Ca^{2+}$ ion or complexed ions were detected. Therefore, 0.1M NaOH was used to attain a pH of around 5. In Figure 3.4.3.3.2, the peak m/z 371 refers to Ca_2-EDTA, which occurred in all three spectra, and the Ca-EDTA peak with m/z 331 appeared as shown in Fig. 3.4.3.3.2 a.

Calibration solution (ICP-OES Wavelength Calibration Solution: 50mg/L Al, As, Ba, Cd, Co, Cr, Cu, Mn, Mo, Ni, Pb, Se, Sr, Zn and 500mg/L K in 5% HNO_3, Agilent Technologies) contains multiple ions that were mixed with pH-adjusted EDTA·2Na and then analyzed by MS. In the resulting spectra (Fig. 3.4.3.3.3), a cluster of peaks

appeared, some of which could be identified as metal-EDTA peaks. Other peaks at 355 m/z and 371 m/z were identified as ^{64}Zn-EDTA and $^{40}Ca_2$-EDTA peaks, respectively, while 427 m/z may correspond to ^{138}Ba ions, and 519 m/z may be a $^{59}Co_3$-EDTA signal.

One of the main goals of this project is to use the LA-FC-ESI-MS method to determine the age of sharks. Consequently, mass peaks at 355 and 371, which are related to Zn-EDTA and Ca_2-EDTA, were selected. The variation in the concentration of $^{64}Zn^{2+}$ and $^{40}Ca^{2+}$ ions along with the corpus calcareum was based on the spectra from Figure 3.4.3.3.4, 3.4.3.3.6 and 3.4.3.3.8. To improve the signal to noise evident in the spectra three cycles from the spectrum were integrated. The cycles were produced due to the compression pulse from the peristaltic pump, which evidently affected the efficiency of the ionization process. The average time was calculated by using the upper and lower limits of the time range. Depending on the ablation starting time, the MS signal has some time delay due to the transit time through the capillary tubes and pump. (Figure 3.4.3.3.4, Table 3.4.3.3.1). Ablation distance related to the ablation time was also calculated by using the ablation speed divided by the total ablation distance. Distance is more closely related to peak intensity than the ablation, hence, it was used to plot the graphs. The orange points labeled in the plots refer to the bumps that are somehow related to the age bands in the vertebrae.

The order of the TBL(total body length) and DOV (diameter of the vertebra) of the samples was NWN6 < MF7 < J18. Five bumps were observed in the middle-sized vertebra sample (MF7), while the smallest sample (NWN6) and the largest sample both had four bumps. The $^{40}Ca^{2+}$ and $^{64}Zn^{2+}$ plot of J18 did not show obvious concentration variations along the distance. The oscillations in the calcium concentration plots of the other two vertebral samples were clearer and showed some correlation to the vertebral age bumps.

According to a recent study, it has been discovered that there is generally a higher concentration of zinc in the intermedialia compared to the corpus calcareum due to larger cell composition and lower levels of calcification (Raoult et al., 2018). Prebirth marks also suggest that prenatal zinc accumulation is significant. Based on mass spectra

we have obtained, the mass intensity of zinc was low in the intermedialia of vertebrae of school sharks. The Zn:Ca ratio was not effective in identifying metal ion accumulation patterns in the vertebrae, unlike other elements. Therefore, our project analyzed the raw data for zinc and calcium ions independently. It was also known that zinc accumulation patterns varied within and between species, with external temperature, diet, and environment as possible factors affecting the distribution. Additionally, it was also noted that zinc concentration in the corpus calcareum was either undetectable or much lower than in the intermedialia of a few shark species, except for Port Jackson sharks. In summary, it may be challenging to determine growth based on spatial analysis of zinc distribution.

In the LA-ICP-MS method for analyzing shark vertebrae, the ablation process is typically carried out in a chamber filled with Ar gas. Because the molecular mass of both ^{40}Ar and ^{40}Ca is 40, ^{43}Ca is instead used as the target for detection and Ca determination. However, in our specific LA-FC-ESI-MS process, we placed the samples on an open-air stage and did not use a carrier gas. As a result, we measured ^{40}Ca ions rather than ^{43}Ca. Since ^{40}Ca is the most abundant calcium isotope (natural abundance 96.9%), its concentration is much higher than that of ^{43}Ca (natural abundance 0.135%). This means that detecting ^{40}Ca should be a more effective method. To confirm the accuracy of the variation in the concentration of $^{64}Zn^{2+}$ and $^{40}Ca^{2+}$ ions found in the mass spectrum, a metal composition scan is required. At the time of writing of this work a comparative scanning electron microscope EDX scan was pending (due to a machine breakdown the delay in obtaining this was indeterminate).

Excluding ^{40}Ca and ^{64}Zn, several elements from vertebral samples, such as ^{55}Mn, ^{86}Sr, and ^{137}Ba, have been analyzed in other articles to determine a shark's age. The mass spectra of the mixed calibration solution we used did not show what ^{55}Mn, ^{86}Sr, or other elements looked like. To ascertain the related peaks of those elements in EDTA solution, single element standard calibration solutions need to be prepared. Obtaining more element profiles would help in identifying the aging bands from vertebrae. Visual observation of the oscillations in calcium concentration obtained from the experiment

indicates that age analysis was not practical. The reasons for this will be discussed later in this thesis.

3.4.4 NIRS

3.4.4.1 Introduction

Near-infrared spectroscopy (NIRS) is a rapid, real-time continuous infrared spectroscopic technique that measures light absorption intensity changes within tissue samples. NIRS is commonly applied in fields such as agriculture, pharmacy, and commerce, and researchers a decade ago began using it to determine the age of teleosts. Although the chemical compositions of teleost otoliths and shark vertebrae are distinct, NIRS inspired Rigby and colleagues (Rigby et al., 2016) to apply the technique to sharks. The whole vertebral centrum was scanned, and statistical methods were applied to analyze the raw data further. The statistical results of wavelengths from the absorption spectra were strongly related to the sharks' ages. The NIRS technique is not an age validation method, but it can work as an age verification model because known ages are needed to establish the calibration model. Additionally, NIRS can determine the ages of deep-water sharks with low calcified vertebrae; therefore, the growth bands have low contrast. So far, the ages of four different shark specimens have been accurately predicted using NIRS.

Rigby et al. have published several papers regarding near-infrared spectroscopy NIRS analyses of shark vertebrae. NIRS, a rapid technique, was employed to determine the ages of shark species from Australia, which assisted with assessing the shark population and predicting their habitat behaviors (Rigby et al., 2016). Vertebrae and dorsal fin spines were often the analyte targets when estimating the essential biological parameter of shark age. Some species, such as deep-water specimens, have poorly calcified vertebral structures with bands that have low resolutions and are difficult to count. Therefore, a method was developed to investigate the chemical compositions of vertebrae with the aid of data from the near-infrared spectrum and multivariate statistical analysis.

One of the disadvantages of the assay NIRS technique is that it must be coupled with the age reading method to produce the calibration model. The advantages of NIRS are that subjectivity and reader bias can be avoided when interpreting the results. However, NIRS is a secondary method, as the calibration mode was constructed by calibrating the spectra against a main reference (Rigby et al., 2016).

Wedding et al. identified the ages of snapper using near-infrared spectroscopy with a 12500 to 3597 cm^{-1} range. For each sample, 32 scans were taken at 8 cm^{-1} resolution. Sample exposure to surrounding light was minimized to limit their interactions with external light. Partial least squares calibration models were established between the referenced data and the experimental results of the ages of otolith fish (Wedding et al., 2014).

Rigby and Wedding have described the entire dried vertebral centrums of piked spurdog (S. megalops) and Philippine spurdog (S. montalbani) sharks, which were scanned at 8 cm^{-1} resolution, and the raw spectrum of one vertebra was generated in 16 s. The wave number range of a Fourier transform near-infrared spectroscopy (FT-NIR) spectrophotometer is 12500 to 3600 cm^{-1} (Rigby et al., 2014).

Two years later, Rigby used a NIRS approach to examine the whole vertebral centra of Sphyrna mokarran and Carcharhinus sorrah sharks. Vertebral centra were examined using a NIRS spectrometer at 8 cm^{-1} resolution over a 12500 to 3600 cm^{-1} wavenumber range (which converts to wavelengths of 800 to 2778 nm) using ATR so the near-infrared beam could sample the centrum (Rigby et al., 2016). Partial least squares regression was used to produce a calibration model. Cross-validation was used to ensure the accuracy of the calibration model; cross-validation involved removing a group of samples from the whole set, and the calibration model was created using the remaining targets (Rigby et al., 2016).

Age data obtained by counting bands were labeled as vert-age, whereas NIRS-age refers to the results of the NIRS process. Partial least squares regression was used to produce a calibration model. Cross-validation was used to ensure the accuracy of the calibration model; cross-validation involved moving a group of samples from the whole

set, and the calibration model was created using the remaining targets (Rigby et al., 2016).

Inspired by the NIRS method of studying shark vertebrae, we will use a similar procedure with the mid-IR ATR and FT-IR NIR/mid-IR transmission instruments to analyze vertebral samples. Using data from journals, we obtained basic setup information to use FT-IR to study shark vertebrae, such as wavenumber range, number of scans, and sample positioning. The wavelength range of near-infrared spectroscopy is 12800–4000 cm^{-1} (780–2500 nm) (Rigby et al., 2016), but the common mid-IR is only sensitive enough to detect 4000–400 cm^{-1}. It is reasonable to use the FT-IR method, even though there is a variation in the wavelength range. Both ATR (Bruker alpha, diamond ATR) and NIR transmission using a Thermo Scientific iS50R were employed. Regardless, NIRS is not an age validation method, so the traditional age determination process must be used to establish a complete age prediction model. The IR experiments were performed in an attempt to see correlations with the scans obtained with LA-FC-ESI-MS.

3.4.4.2 Method

Part 1. Bruker Alpha Spectrometer

Half of the vertebral samples were placed face down on the diamond of the IR instrument (BRUKER, ALPHA). t. Specific areas, that is, A, B, and C on the corpus calcareum of the vertebrae, along with Areas D, E, and F on the centrum of the vertebrae, were analyzed. In the case of the large vertebral samples, marks were left on the back of the samples due to the compression mechanism. However, small samples were easily damaged if too much pressure was applied. The OPUS 8.1 program was used to accumulate spectra and analyze the raw data. All the samples were measured across a range of 4000 to 400 wave numbers, with 48 scans taken per sample at 4 cm^{-1} resolution. Peaks were shown for Areas A, B, and C , whereas only noise was captured around Areas D and E. Area A is the most recent part of the vertebra, B is the intermediate area and Area C is most closely associated with young sharks still in the nursery area.

Comparison A and B could indicate a change associated with age of the cartilagineous material. Comparison of Area C (where the vertebra is growing most rapidly) could indicate compositional effects due to the nursery environment compared to that of B (open ocean) Therefore, the edge of the vertebrae, and not the centrum part, was used for aging studies. Based on this, Areas A, B, and C of all the large and medium samples were measured, but only Areas A and C were measured in the small samples, such as SWS5-C5 and SWS5-A3, due to their size. We attempted to extend the measurement range to 7000–400 cm^{-1}, but no absorbance peaks occurred above 4000 cm^{-1} because the IR instrument is not sensitive within this wave number range. The diameter of each vertebral sample was measured, and Excel was used to plot an integral versus diameter graph.

Part 2. The Is50R FT-IR Spectrometer

The thin section of a shark vertebral was held in a clip and placed on a movable sample holder with x-y-z capabilities. A leaf iris was positioned in front of the sample to control the size of the light source spot, and the background was measured once the iris was adjusted. The TRS-20Mhz mercury cadmium telluride detector (MCT) liquid nitrogen cooled detector was used, while the beam splitter was CaF_2 and the source was white light. The measurement range was from 11700 to 2000 cm^{-1}. The trial samples used were SWL8-2 and SWS5-A4. Following this, eight male and eight female formal vertebral samples were examined, with a total length of the shark (tip of nose to tip of tail) ranging from 300 to 1600 mm.

Figure 3.4.4.2. 1 Setup of FT-IR system.

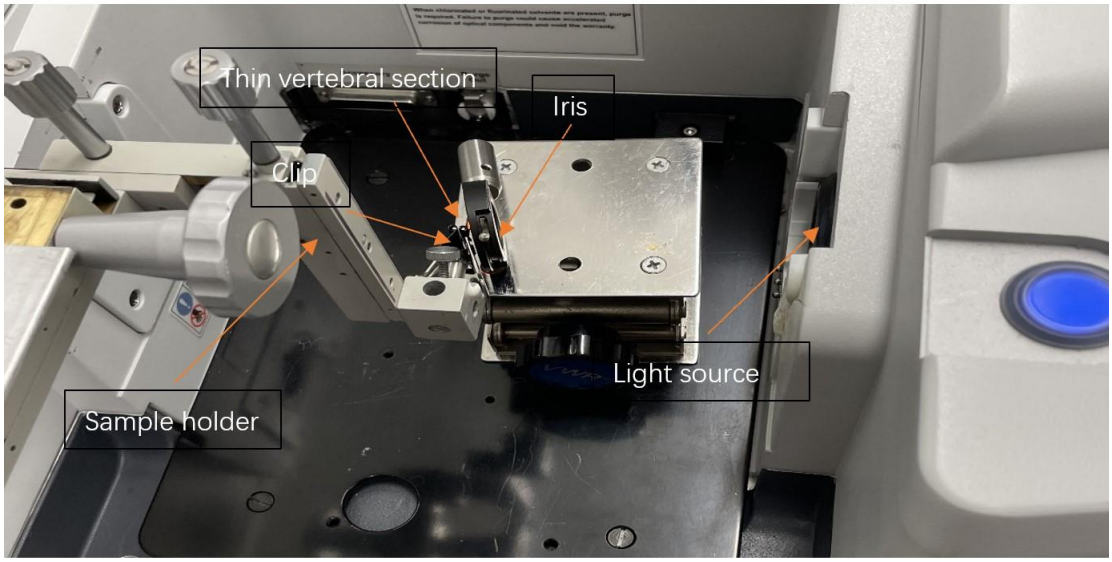

Figure 3.4.4.2. 2 The position of the vertebra section behind the iris.

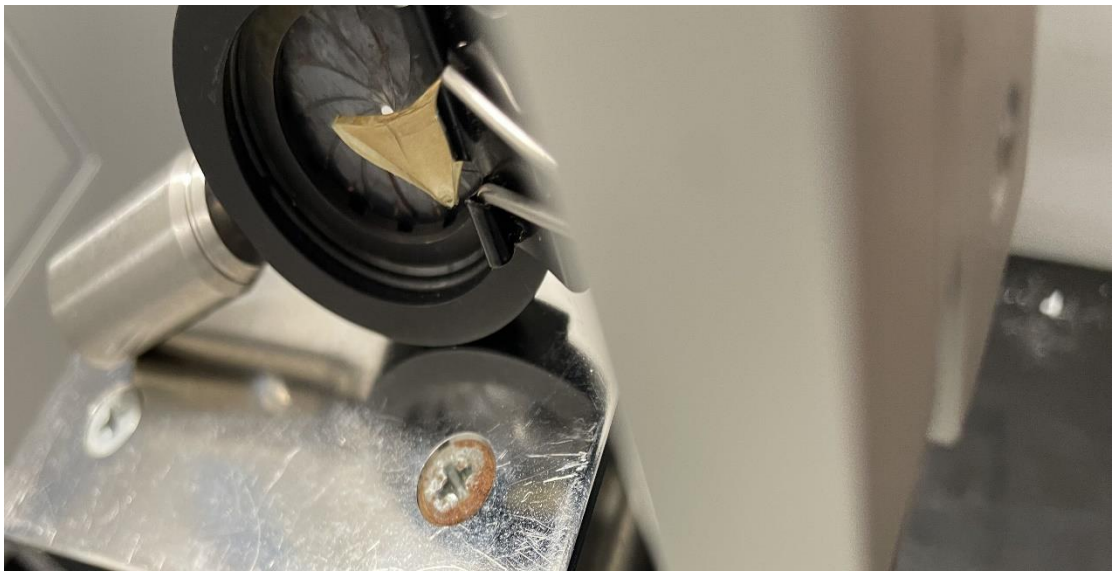

3.4.4.3 Result

Part 1. Bruker Alpha Spectrometer

a). Trial Samples

Both areas, A and C, of small vertebra SWS5-C5 were successfully measured, and the spectrum had similar peak arrangements to other samples. All the samples, not only the SWS5-C5, had similar spectra.

Figure 3.4.4.3. 1 Examined Area A, B, and C of the vertebral sample

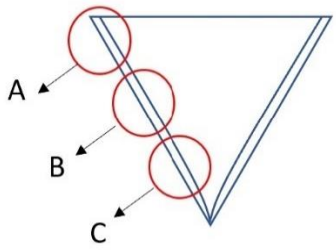

Sample SWL8-6, which is a middle-sized vertebra, was measured with the Bruker Alpha FTIR. During the process, no NIR peaks were found in the spectra of all the selected areas, and only a cluster of noises were shown. This was expected since the ALPHA IR is non-sensitive when the wave number's range is beyond 4000 cm^{-1}. Therefore, the range of the wave number during this process should be set at 4000 to 400 cm^{-1}. To stabilize the signals, vertebral spectra were subtracted from the background spectrum and then normalized. We found that three spectra had similar peak shapes but varied in intensity.

Figure 3.4.4.3. 2 IR spectra of areas A, B, and C of sample SWL8-6

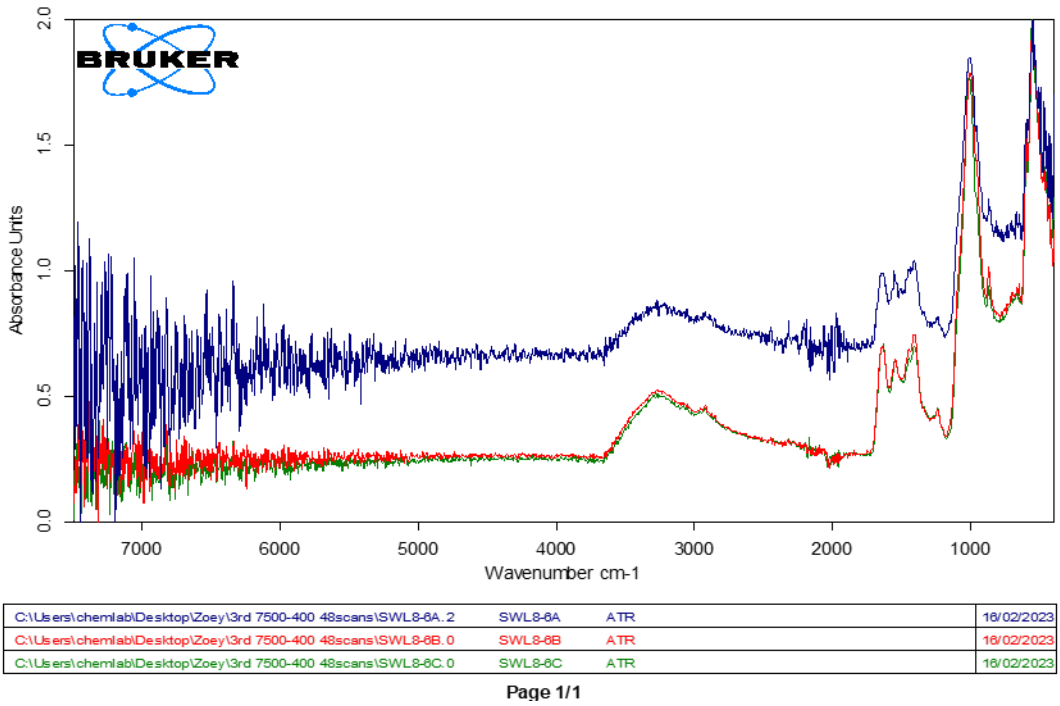

While measuring the large vertebra SWL8-5, the vertebra was repositioned multiple times. Unfortunately, an absorbance signal for Spot B was still not found, and

the intensity of Spot C was relatively poor. It seems that the shape of the sample and the pressure on the vertebral halves are two major factors that affect the measurement of absorbance signals. To solve this problem, polishing and grinding the sample should be considered, as it could potentially enhance the accuracy and reliability of the measurement. This was not attempted.

Figure 3.4.4.3. 3 IR spectra of areas A, B, and C of sample SWL8-5

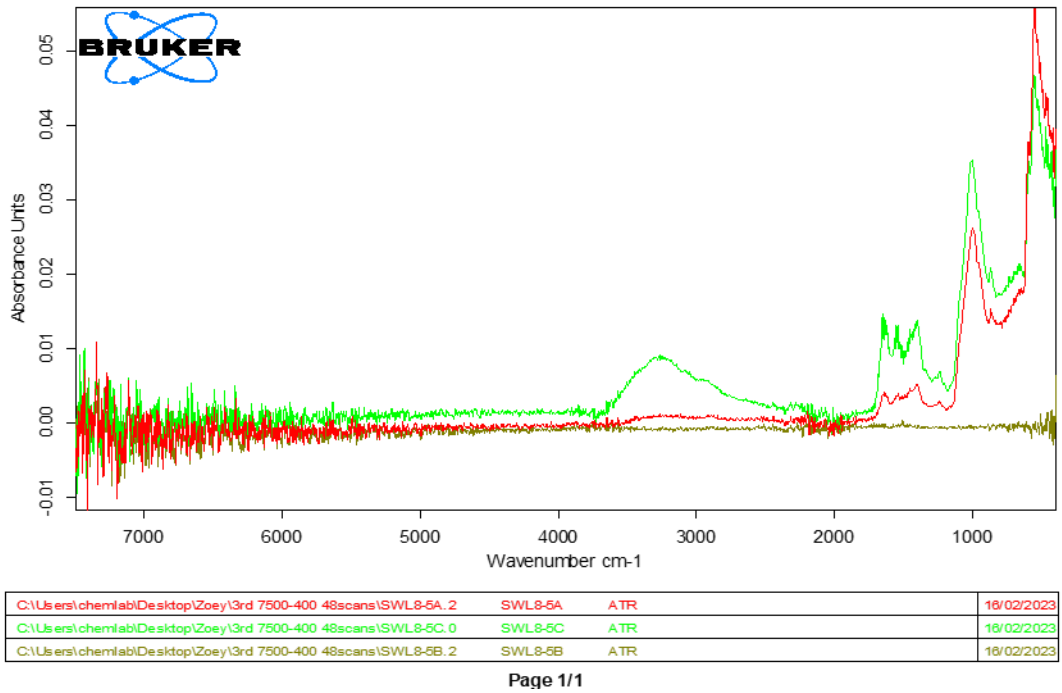

After taking measurements from various spots, it was found that most of them showed similar results within a single vertebra. The samples from all the vertebrae were analyzed in Spot C using FTIR in the wavenumber range of 4000–400 cm^{-1}. The spectral range was divided into 10 areas ranging from 1718.5 to 411.05 cm^{-1}, and integration was performed for each area as indicated in Figure 3.4.4.3. 4.

Figure 3.4.4.3. 4 Integral method of the peaks from the IR spectrum

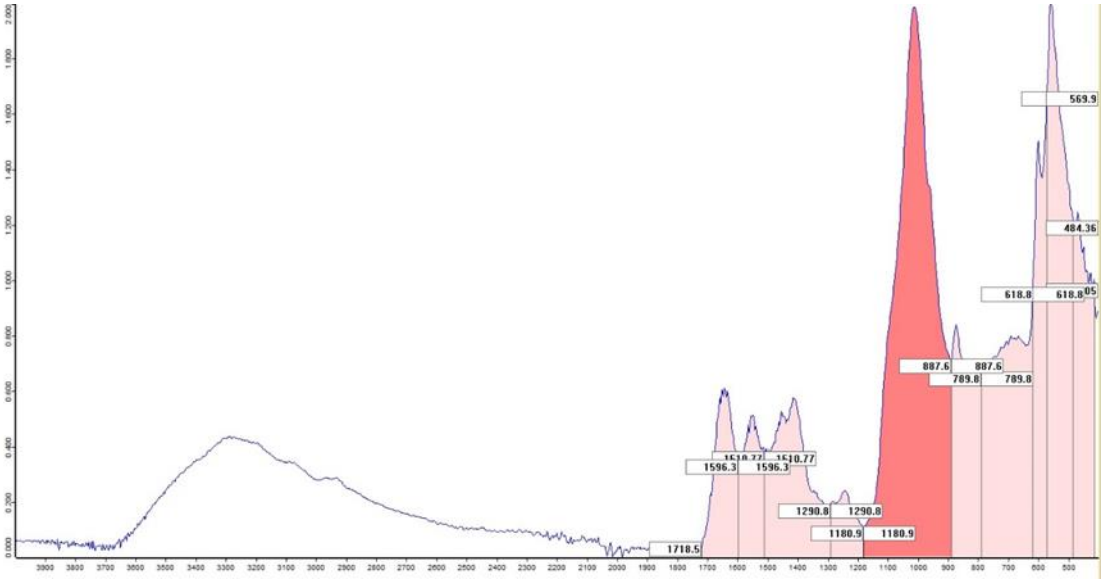

Table 3.4.4.3. 1 Diameter of vertebrae

Area A								
Sample	SWS5-C5	SWS5-A3	SWL8-6	SWS5-D2	SWS5-B6	SWL8-4	SWL7-5	SWSL8-5
Vertebrae Diameter (mm)	5.0	6.0	12.0	12.0	9.0	12.0	15.0	20.0

In analyzing each peak, Peak 5 was found to have the highest value dark red in in Figure 3.4.4.3. 5), and thus the absorbance of the other peaks was divided by that value to normalize the data. First, the normalization data for each peak was obtained through IR software, then this data and the vertebra diameter (as a proxy for age) were used to create 10 scatter graphs. For each peak, three sets of data from measurement spots A, B, and C were plotted in the same graph (Figure 3.4.4.3.5 & Figure 3.4.4.3.6). Diameter values were on the *x*-axis, and integral results were on the *y*-axis. While no obvious pattern was found in the Peak 1–Peak 7 graphs, a minor increase trend was observed in the plots of the Peaks 8–10 graphs. Therefore, we decided to add all the normalization data for Peaks 8, 9, and 10 for Areas A, B, and C (Figure 3.4.4.3.7-Figure 3.4.4.3.9). Among the three regions, Area A's graph had the largest slope and best R^2 value.

Other authors have scanned the whole vertebrae to obtain the IR spectrum, hence, it was reasonable to use the average of Peak 8-10's normalization values from A, B, and

C to plot a scatter graph (Figure 3.4.4.3.10). This graph showed a smaller slope compared to Area A's slope but had a higher R^2 value of 0.6372 > 0.4509.

N = Normalization value

Table 3.4.4.3. 2 Normalization value of each vertebra of each peak at area A

Peak	SWS5-C5 Integral N	SWS5-A3 Integral N	SWL8-6 Integral N	SWS5-D2 Integral N	SWS5-B6 Integral N	SWL8-4 Integral N	SWL7-5 Integral N	SWSL8-5 Integral N
1	0.17	0.18	0.13	0.15	0.17	0.16	0.13	0.07
2	0.14	0.14	0.11	0.11	0.14	0.13	0.10	0.06
3	0.32	0.32	0.27	0.30	0.31	0.32	0.26	0.18
4	0.10	0.12	0.06	0.12	0.10	0.10	0.08	0.06
5	1.00	1.00	1.00	1.00	1.00	1.00	1.00	1.00
6	0.25	0.28	0.26	0.30	0.26	0.25	0.27	0.30
7	0.48	0.58	0.43	0.65	0.51	0.49	0.56	0.62
8	0.24	0.31	0.22	0.34	0.26	0.27	0.31	0.40
9	0.52	0.64	0.48	0.74	0.56	0.58	0.65	0.95
10	0.31	0.47	0.29	0.53	0.36	0.38	0.42	0.66
8+9+10	1.07	1.42	1.00	1.61	1.19	1.23	1.38	2.01

Table 3.4.4.3. 3 Normalization value of each vertebra of each peak at area B

Peak	SWS5-C5 Integral N	SWS5-A3 Integral N	SWL8-6 Integral N	SWS5-D2 Integral N	SWS5-B6 Integral N	SWL8-4 Integral N	SWL7-5 Integral N	SWSL8-5 Integral N
1	-	-	0.20	0.14	0.15	0.20	0.17	-
2	-	-	0.16	0.10	0.12	0.16	0.14	-
3	-	-	0.39	0.28	0.28	0.40	0.33	-
4	-	-	0.14	0.09	0.09	0.15	0.12	-
5	-	-	1.00	1.00	1.00	1.00	1.00	-
6	-	-	0.27	0.25	0.25	0.30	0.32	-
7	-	-	0.47	0.48	0.53	0.58	0.66	-
8	-	-	0.22	0.26	0.29	0.28	0.31	-
9	-	-	0.45	0.51	0.61	0.61	0.68	-
10	-	-	0.29	0.34	0.40	0.45	0.50	-
8+9+10	-	-	0.96	1.11	1.30	1.34	1.50	-

Table 3.4.4.3. 4 Normalization value of each vertebra of each peak at area C

Peak	SWS5-C5 Integral N	SWS5-A3 Integral N	SWL8-6 Integral N	SWS5-D2 Integral N	SWS5-B6 Integral N	SWL8-4 Integral N	SWL7-5 Integral N	SWSL8-5 Integral N
1	0.16	0.17	0.21	0.18	0.18	0.18	0.15	0.17
2	0.12	0.13	0.16	0.13	0.15	0.15	0.12	0.14
3	0.29	0.30	0.40	0.30	0.32	0.35	0.28	0.34
4	0.09	0.08	0.15	0.08	0.10	0.10	0.08	0.10
5	1.00	1.00	1.00	1.00	1.00	1.00	1.00	1.00
6	0.23	0.24	0.27	0.25	0.25	0.25	0.23	0.29
7	0.43	0.44	0.48	0.50	0.53	0.50	0.43	0.54
8	0.22	0.23	0.22	0.25	0.27	0.26	0.23	0.26
9	0.45	0.48	0.48	0.54	0.58	0.56	0.48	0.57
10	0.26	0.28	0.31	0.35	0.39	0.37	0.29	0.41
8+9+10	0.94	0.99	1.01	1.14	1.24	1.19	1.00	1.24

Table 3.4.4.3. 5 Diameter of each sample, Normalization value of each vertebra of peak (8+9+10) at area A, B, and C

Diameter (mm)	5	6	12	12	9	12	15	20
Area A	1.07	1.42	1.00	1.61	1.19	1.23	1.38	2.01
Area B	-	-	0.96	1.11	1.30	1.34	1.50	-
Area C	0.94	0.99	1.01	1.14	1.24	1.19	1.00	1.24
Mean	1.01	1.21	1.03	1.32	1.23	1.19	1.37	1.62

Figure 3.4.4.3. 5 Diameter of the vertebrae (mm) vs. integral normalization data from area A, B, and C

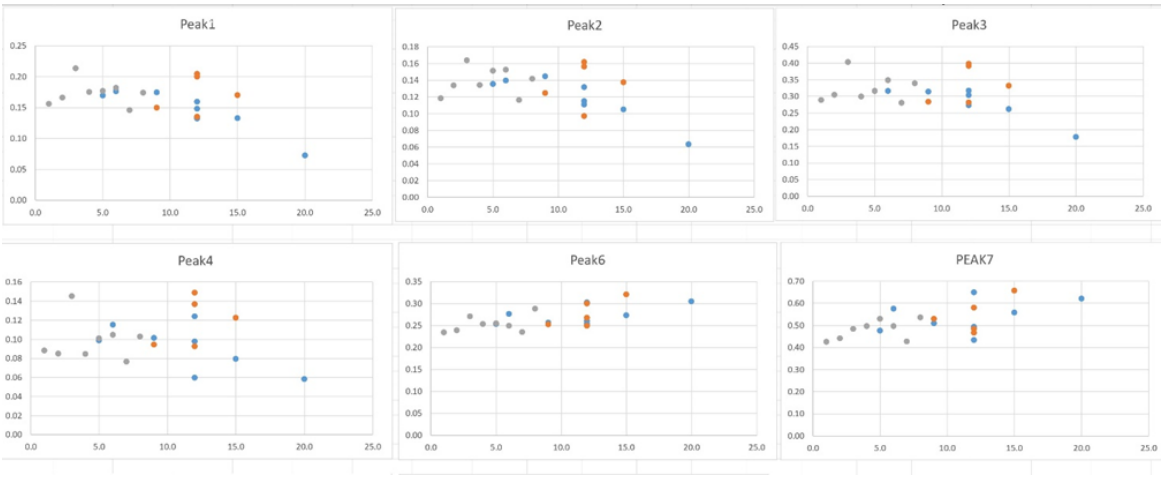

Figure 3.4.4.3. 6 Diameter of the vertebrae vs. integral normalization data from area A, B, and C

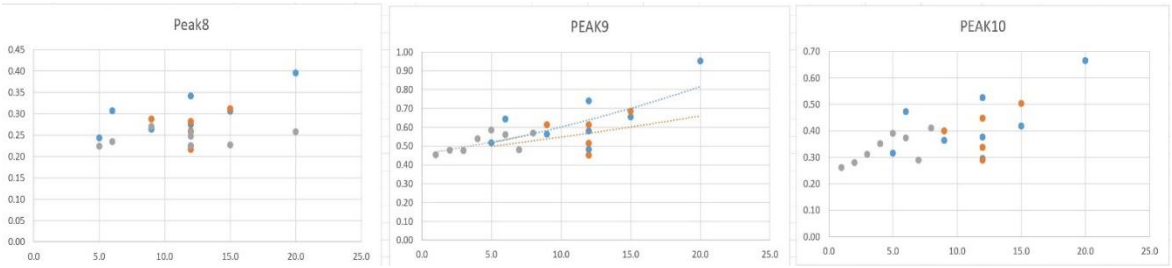

Figure 3.4.4.3. 7 Diameter of the vertebrae (mm) vs. integral normalization value of each vertebra from peak (8+9+10) at area A

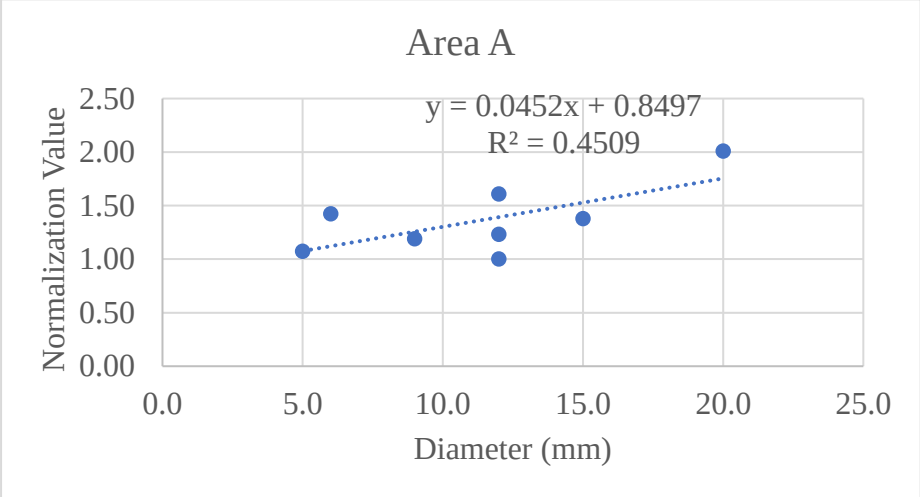

Figure 3.4.4.3. 8 Diameter of the vertebrae (mm) vs. integral normalization value of each vertebra from peak (8+9+10) at area B

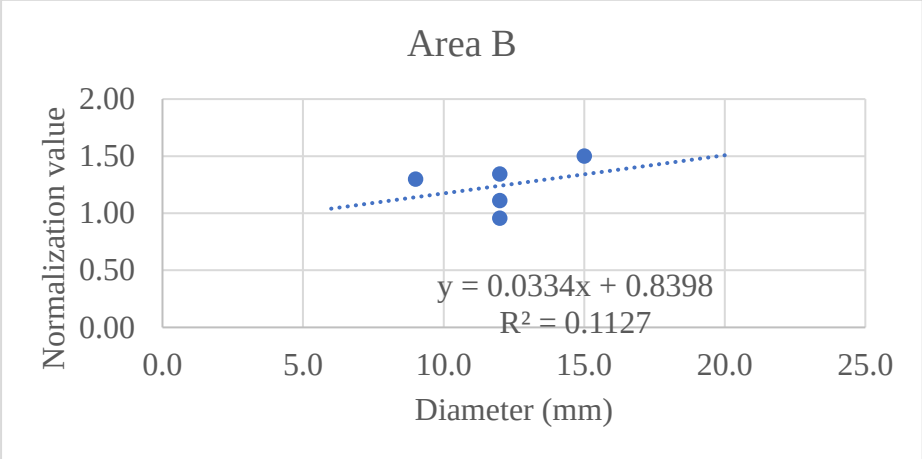

Figure 3.4.4.3. 9 Diameter of the vertebrae (mm) vs. integral normalization value of each vertebra from peak (8+9+10) at area C

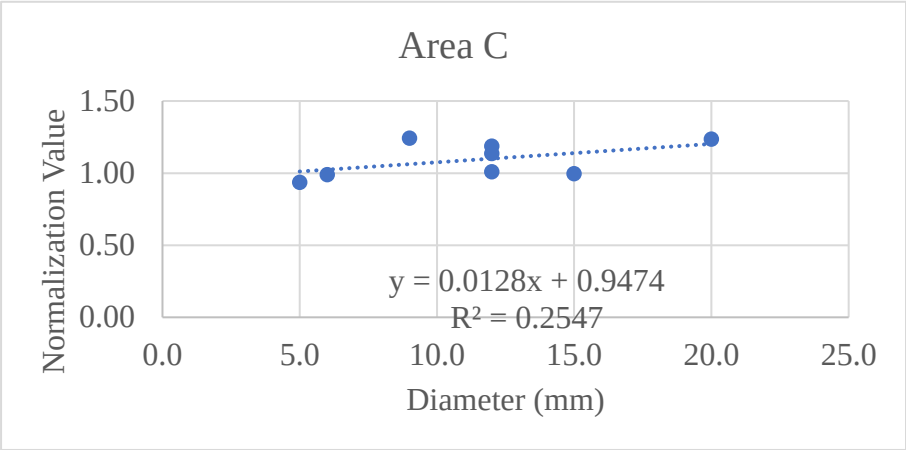

Figure 3.4.4.3. 10 Diameter of the vertebrae (mm) vs. mean value of normalization value of each vertebra from peak (8+9+10)

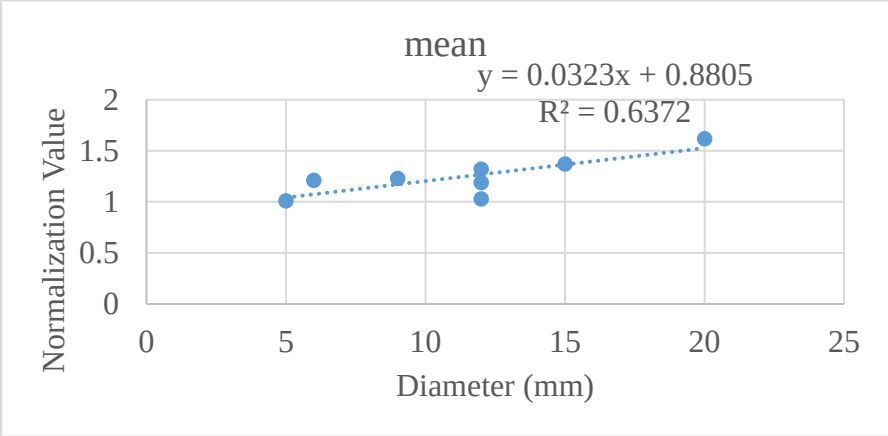

b). Formal vertebral Samples

Seven male and seven female samples were chosen as the formal vertebral test group. Areas A, B, and C of all the large and medium samples were measured, but only Areas A and C were measured in the small samples. Ten peaks from the raw data were integrated first. Then, the absorbance of the other peaks was divided by the highest value (peak 1180.9-887.6 cm^{-1}) to normalize the data. Total body length, diameter of the vertebrae, and the normalization values were used to plot diagrams for further analysis of the data from IR spectra.

Table 3.4.4.3. 6 Total length, diameter, and integral Value (I.V.) of each sample.

Sample (Male)	Length (mm)	Diameter (mm)	1718.5-1596.3 cm^{-1} I.V.	1596.3-1510.77 cm^{-1} I.V.	1510.77-1290.8 cm^{-1} I.V.	1290.8-1180.9 cm^{-1} I.V.	1180.9-887.6 cm^{-1} I.V.
AB3	440	4.00	4.725	3.829	8.523	2.775	27.696
NWN3	1040	11.39	3.981	3.131	7.337	2.355	22.889
SDSOE	1390	15.10	3.550	2.820	6.219	2.015	18.785
MF5	1350	---	3.610	2.972	6.983	2.300	23.667
NWN9	768	---	1.207	0.987	2.163	0.713	8.225
NWN8	907	8.48	1.643	1.319	2.959	1.016	9.542
J17	1500	9.48	2.087	1.616	3.880	1.242	11.514

Table 3.4.4.3. 7 Total length, diameter, and integral Value (I.V.) of each sample.

Sample (Male)	Length mm	Diameter (mm)	887.6-789.8 cm^{-1} I.V.	789.8-618.8 cm^{-1} I.V.	618.8-569.9 cm^{-1} I.V.	569.9-484.36 cm^{-1} I.V.	484.36-411.05 cm^{-1} I.V.
AB3	440	4.00	6.357	12.602	6.476	13.491	8.233
NWN3	1040	11.39	5.549	10.508	5.392	11.510	7.168
SDSOE	1390	15.10	4.625	8.773	4.297	8.981	5.600
MF5	1350	---	5.591	10.795	5.816	12.474	7.862
NWN9	768	---	2.230	4.039	2.031	4.388	2.814
NWN8	907	8.48	2.400	4.917	2.554	5.308	3.484
J17	1500	9.48	2.902	5.809	2.923	6.191	4.026

Figure 3.4.4.3. 11 The IR spectrum of the AB3 vertebral half (edge)

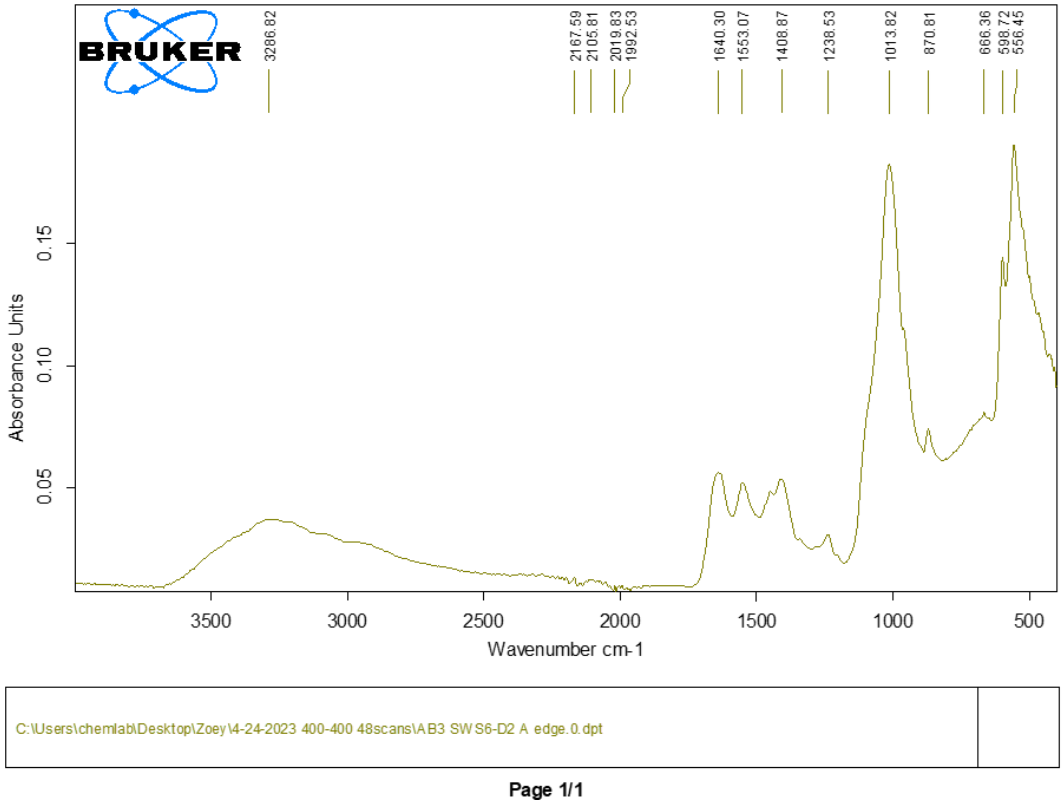

Figure 3.4.4.3. 12 The IR spectrum of the AB3 vertebral half (center)

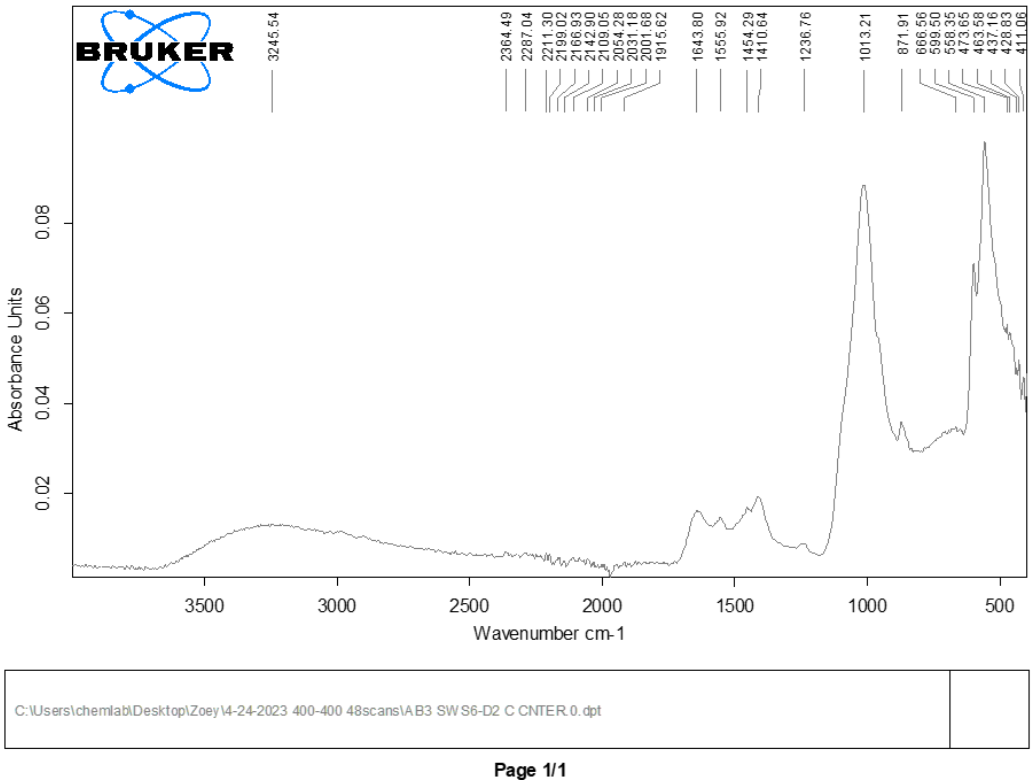

Figure 3.4.4.3. 13 The measurement area 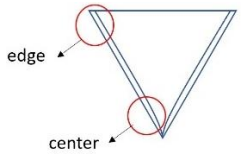

Table 3.4.4.3. 8 Total length, diameter, and normalization Value (N.V.) of male samples. The measurement area was the edge of the vertebral halves.

Sample (Male)	Length mm	Diameter (mm)	1718.5-1596.3 cm^{-1} N.V.	1596.3-1510.77 cm^{-1} N.V.	1510.77-1290.8 cm^{-1} N.V.	1290.8-1180.9 cm^{-1} N.V.	1180.9-887.6 cm^{-1} N.V.
AB3	440	4.00	0.170602	0.138251	0.307734	0.100195	1
NWN3	1040	11.39	0.173926	0.136791	0.320547	0.102888	1
SDSOE	1390	15.10	0.188981	0.150120	0.331062	0.107266	1
MF5	1350	---	0.152533	0.125576	0.295052	0.097182	1
NWN9	768	---	0.146748	0.120000	0.262979	0.086687	1
NWN8	907	8.48	0.172186	0.138231	0.310103	0.106477	1
J17	1500	9.48	0.181258	0.140351	0.336981	0.107869	1

Table 3.4.4.3. 9 Total length, diameter, and normalization Value (N.V.) of male samples

Sample (Male)	Length mm	Diameter (mm)	887.6-789.8 cm^{-1} NV.	789.8-618.8 cm^{-1} N.V.	618.8-569.9 cm^{-1} N.V.	569.9-484.36 cm^{-1} N.V.	484.36-411.05 cm^{-1} N.V.
AB3	440	4.00	0.229528	0.455012	0.233824	0.487110	0.297263
NWN3	1040	11.39	0.242431	0.459085	0.235572	0.502862	0.313164
SDSOE	1390	15.10	0.246207	0.467022	0.228746	0.478094	0.298110
MF5	1350	---	0.236236	0.456120	0.245743	0.527063	0.332193
NWN9	768	---	0.271125	0.491064	0.246930	0.533495	0.342128
NWN8	907	8.48	0.251520	0.515301	0.267659	0.556278	0.365123
J17	1500	9.48	0.252041	0.504516	0.253865	0.537693	0.349661

Figure 3.4.4.3. 14 The total length of shark (mm) vs. normalization value of each peak from the IR spectrum

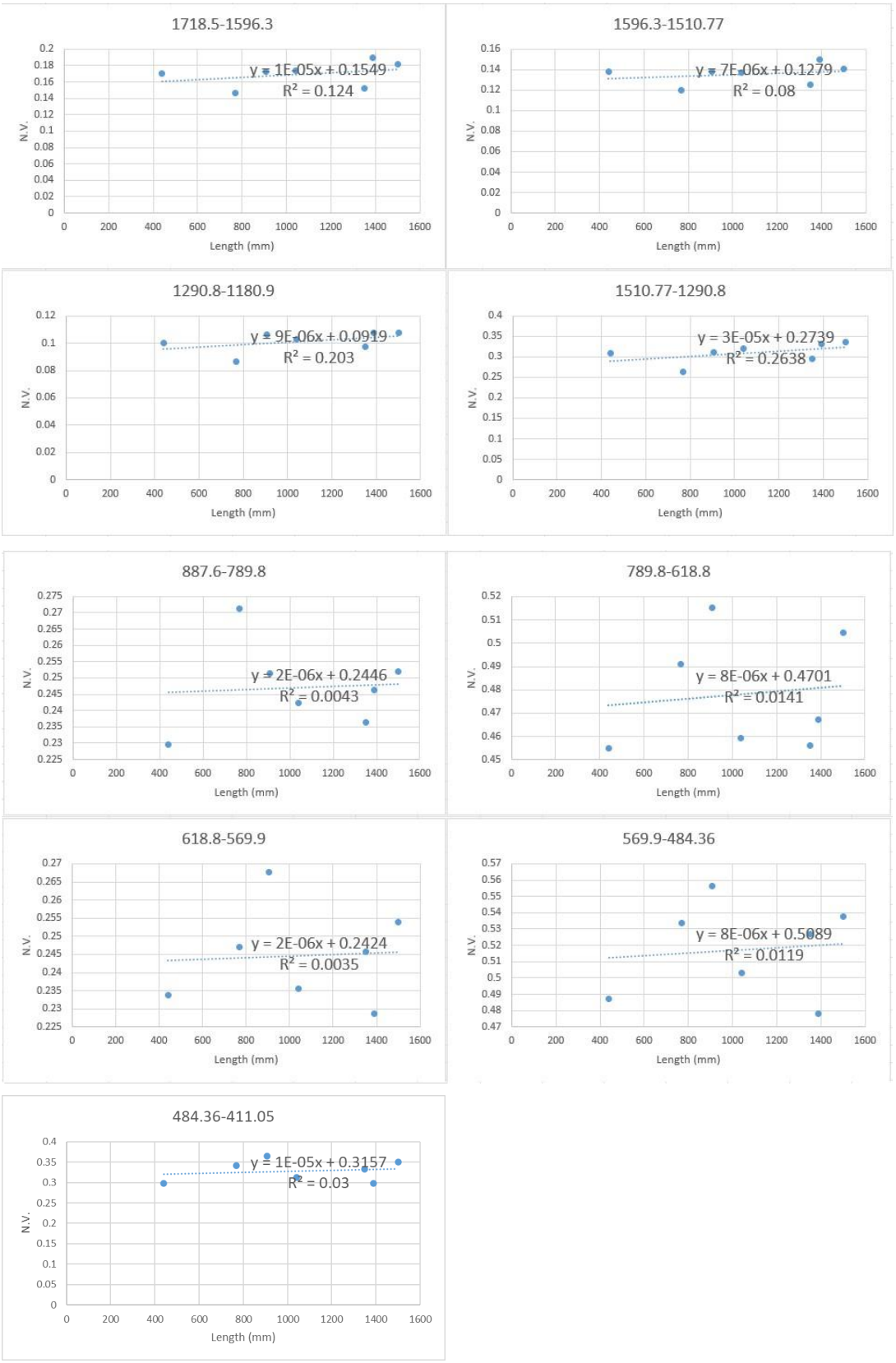

Figure 3.4.4.3. 15 The diameter of vertebrae (mm) vs. normalization value of each peak from the IR spectrum

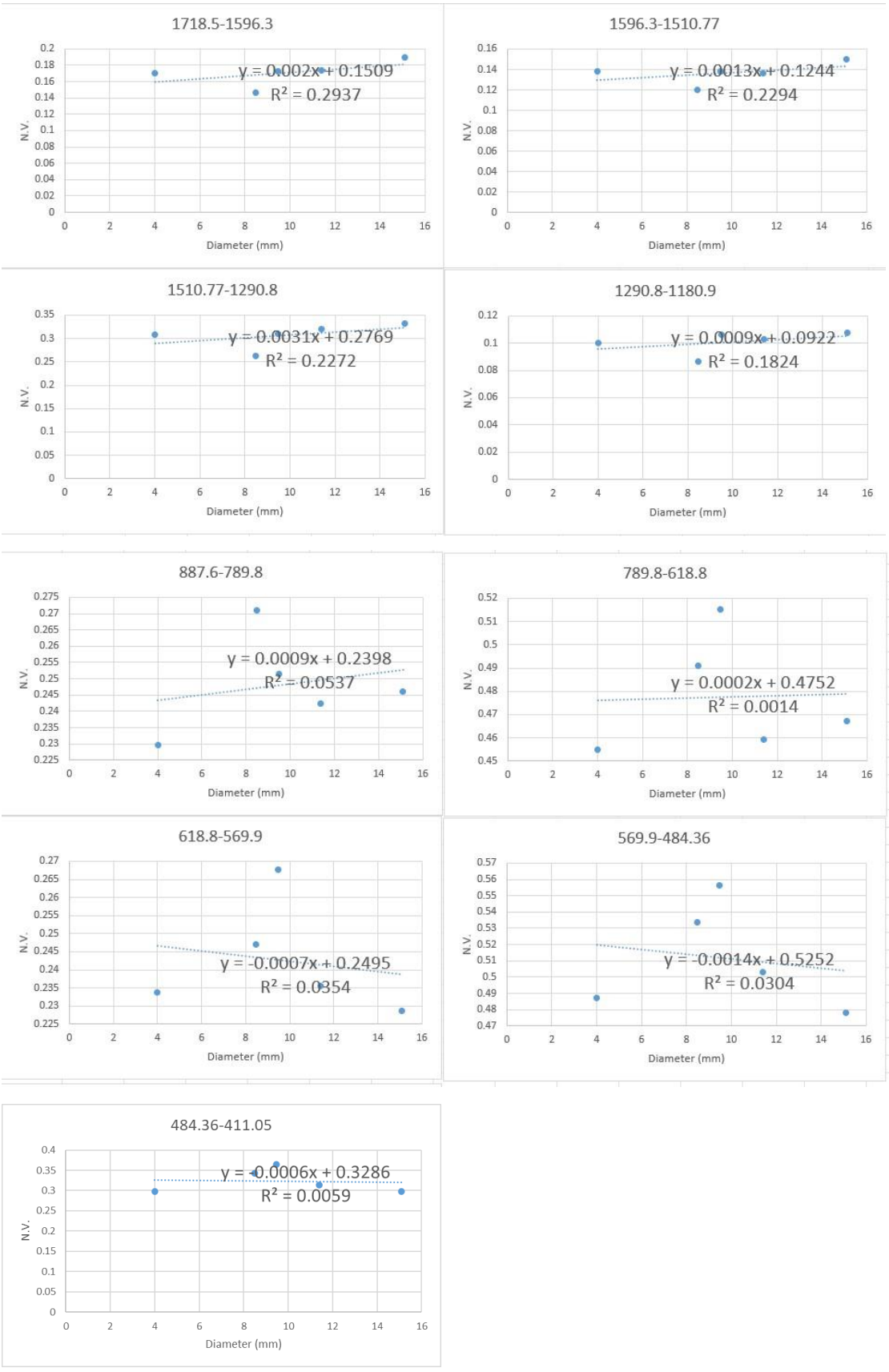

Table 3.4.4.3. 10 Total length, diameter and integral value (N.V.) of female samples

Sample (Female)	Length (mm)	Diameter (mm)	1718.5-1596.3 cm^{-1} I.V.	1596.3-1510.77 cm^{-1} I.V.	1510.77-1290.8 cm^{-1} I.V.	1290.8-1180.9 cm^{-1} I.V.	1180.9-887.6 cm^{-1} I.V.
MK2	880	9.98	2.016	1.601	3.796	1.282	14.598
MF1	1050	---	2.016	1.601	3.796	1.282	14.598
MF8	1125	12.84	2.104	1.703	3.911	1.296	13.273
J28	1610	20.36	6.935	5.264	12.180	3.673	34.619
J19	1590	---	2.679	2.092	5.056	1.618	16.191
AB27	490	4.90	2.808	2.528	10.891	7.523	26.941
LG2	750	7.38	1.447	1.099	2.739	0.941	11.892

Table 3.4.4.3. 11 Total length, diameter and integral value (N.V.) of female samples

Sample (Female)	Length (mm)	Diameter (mm)	887.6-789.8 cm^{-1} I.V.	789.8-618.8 cm^{-1} I.V.	618.8-569.9 cm^{-1} I.V.	569.9-484.36 cm^{-1} I.V.	484.36-411.05 cm^{-1} I.V.
MK2	880	9.98	3.348	6.151	3.424	7.148	4.171
MF1	1050	---	3.348	6.151	3.424	7.148	4.171
MF8	1125	12.84	3.279	6.471	3.423	7.320	4.681
J28	1610	20.36	7.746	15.454	7.884	16.042	9.744
J19	1590	---	3.903	8.434	4.505	9.709	6.401
AB27	490	4.90	7.497	11.444	4.416	8.823	7.167
LG2	750	7.38	2.625	4.608	2.619	5.305	3.099

Figure 3.4.4.3. 16 The IR spectrum of the MK2 vertebral half (edge)

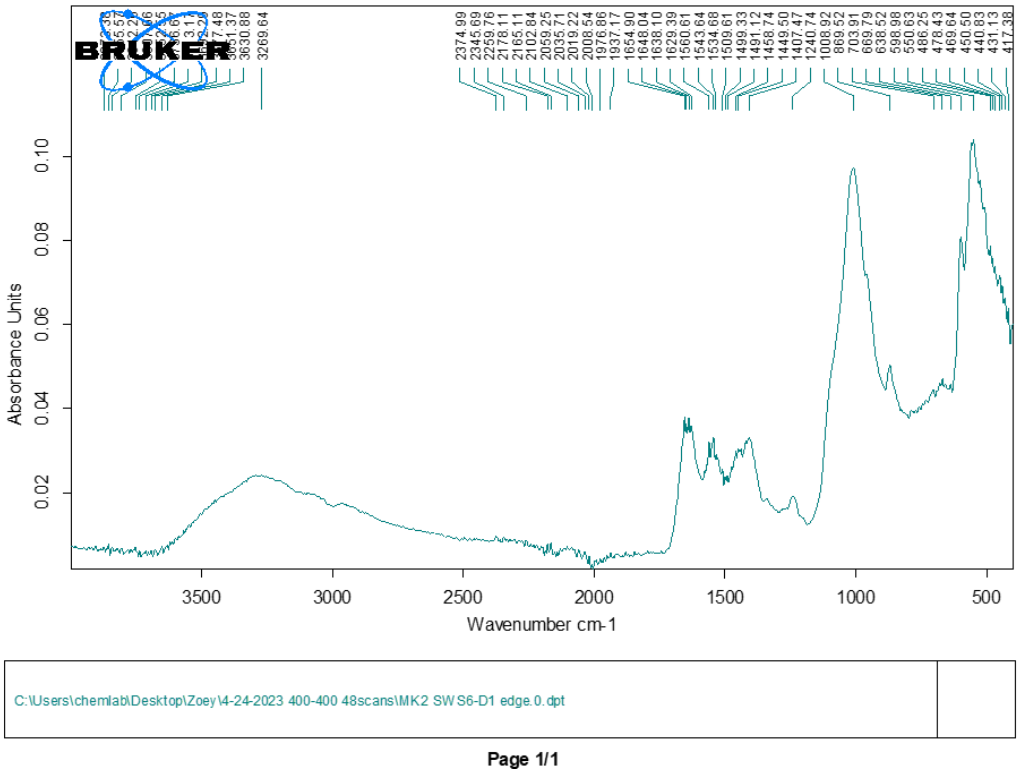

Figure 3.4.4.3. 17 The IR spectrum of the MK2 vertebral half (center)

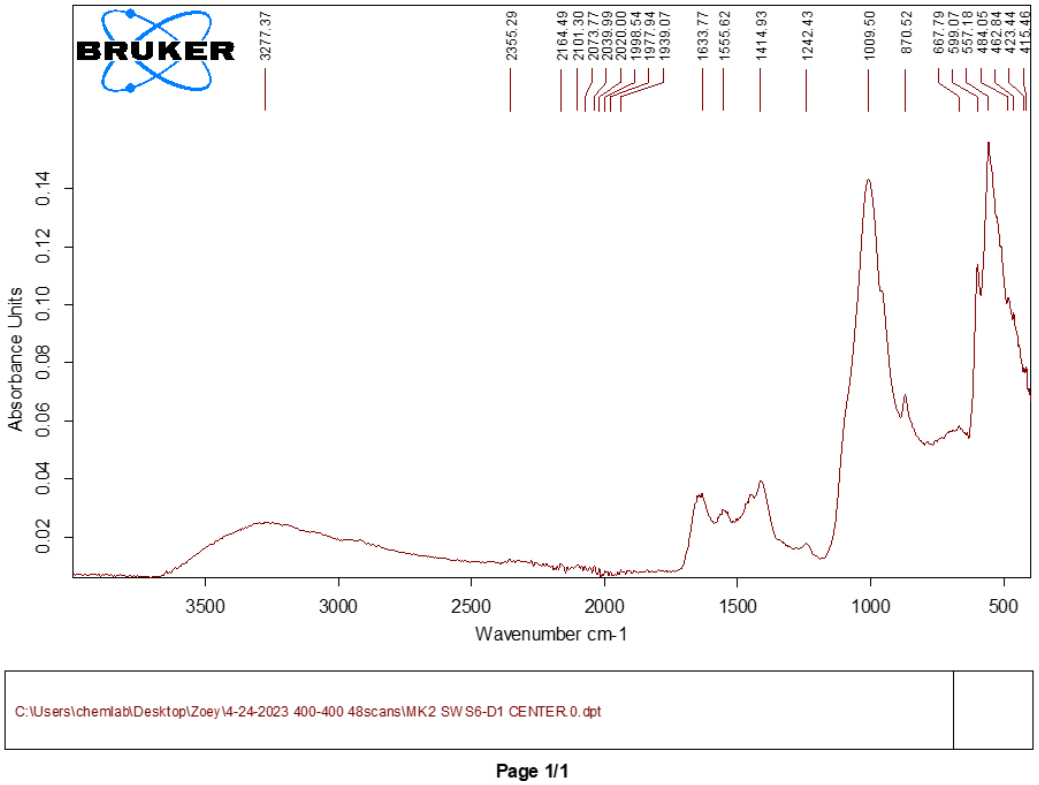

Table 3.4.4.3. 12 Total length, diameter, and normalization Value (N.V.) of female samples. The measurement area was the edge of the vertebral halves.

Sample (Female)	Length mm	Diameter (mm)	1718.5-1596.3 cm^{-1} N.V.	1596.3-1510.77 cm^{-1} N.V.	1510.77-1290.8 cm^{-1} N.V.	1290.8-1180.9 cm^{-1} N.V.	1180.9-887.6 cm^{-1} N.V.
AB27	490	9.98	0.104228	0.093835	0.404254	0.27924	1
MK2	880	---	0.138101	0.109673	0.260036	0.08782	1
MF1	1050	12.84	0.138101	0.109673	0.260036	0.08782	1
MF8	1125	20.36	0.158517	0.128306	0.294658	0.097642	1
J28	1610	---	0.200324	0.152055	0.35183	0.106098	1
J19	1590	4.90	0.165462	0.129208	0.312272	0.099932	1
LG2	750	7.38	0.121678	0.092415	0.230323	0.079129	1

Table 3.4.4.3. 13 Total length, diameter, and normalization Value (N.V.) of female samples. The measurement area was the edge of the vertebral halves.

Sample (Female)	Length mm	Diameter (mm)	887.6-789.8 cm^{-1} N.V.	789.8-618.8 cm^{-1} N.V.	618.8-569.9 cm^{-1} N.V.	569.9-484.36 cm^{-1} N.V.	484.36-411.05 cm^{-1} N.V.
AB27	490	9.98	0.278275	0.42478	0.163914	0.327493	0.266026
MK2	880	---	0.229346	0.421359	0.234553	0.489656	0.285724
MF1	1050	12.84	0.229346	0.421359	0.234553	0.489656	0.285724
MF8	1125	20.36	0.247043	0.487531	0.257892	0.551496	0.352671
J28	1610	---	0.22375	0.446402	0.227736	0.463387	0.281464
J19	1590	4.90	0.24106	0.520907	0.278241	0.599654	0.395343
LG2	750	7.38	0.220737	0.387487	0.220232	0.446098	0.260595

Figure 3.4.4.3. 18 The total length of shark (mm) vs. normalization value of each peak from the IR spectrum

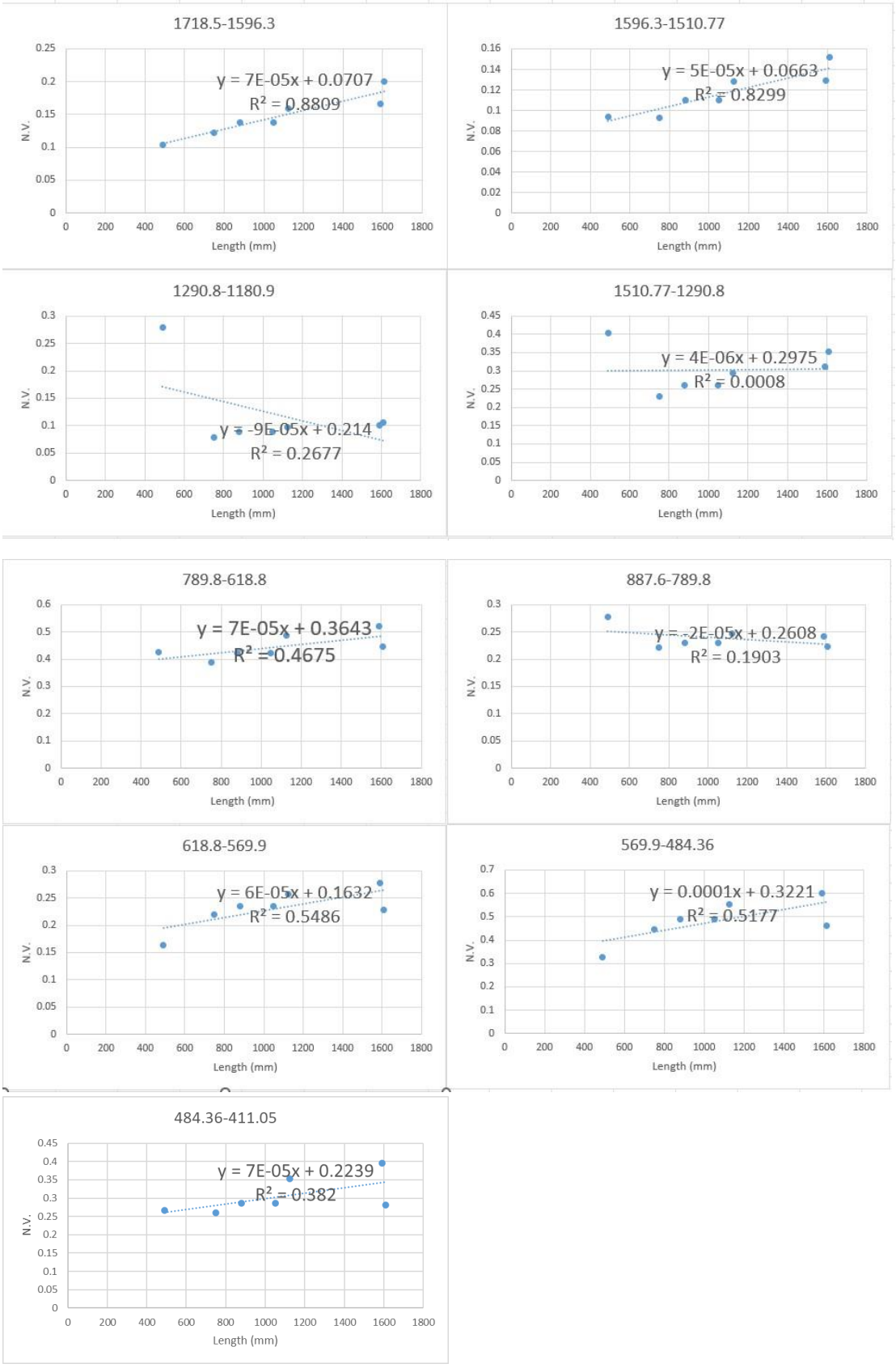

Figure 3.4.4.3. 19 The Diameter of vertebrae (mm) vs. normalization value of each peak from the IR spectrum

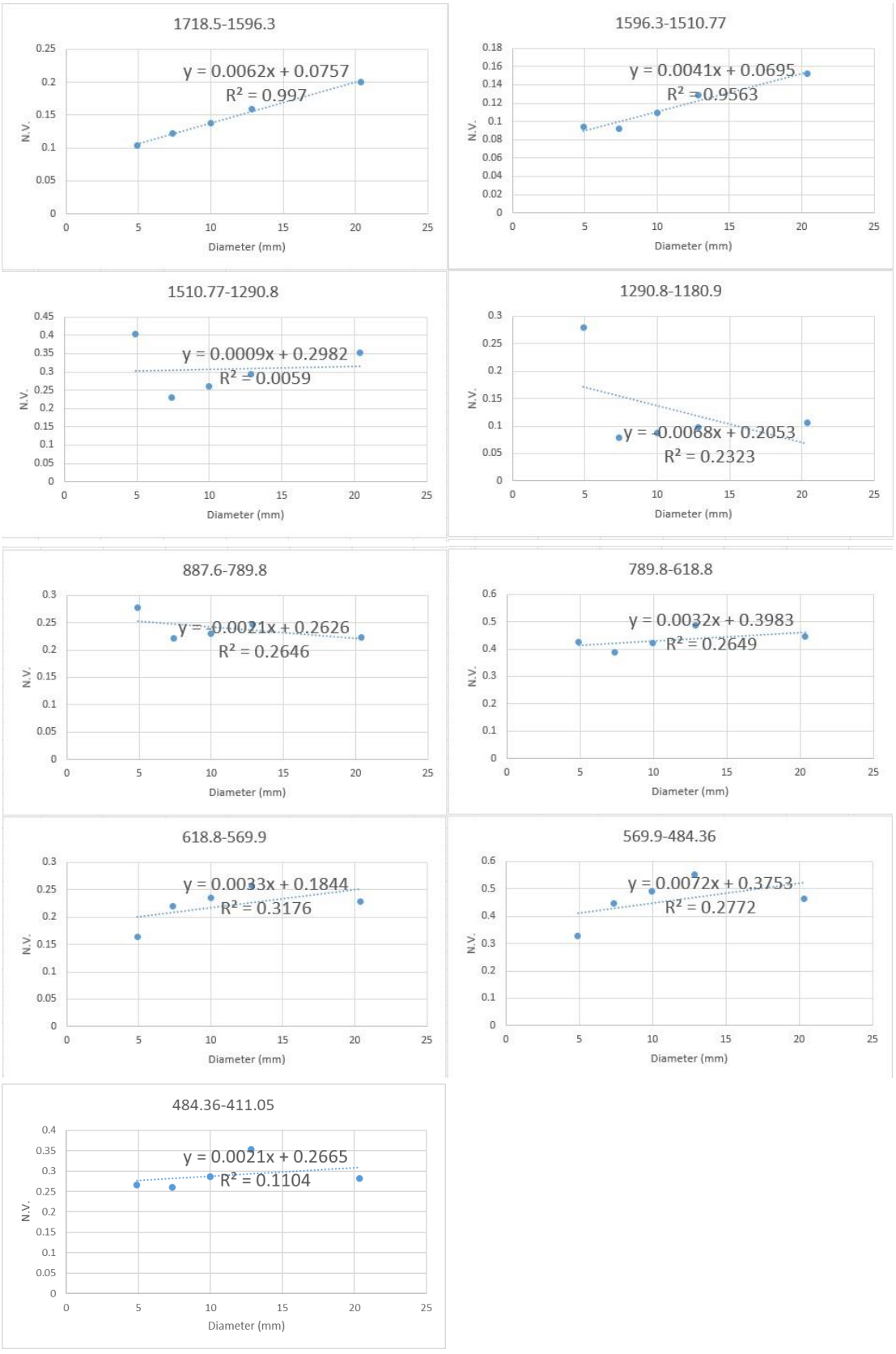

Table 3.4.4.3. 14 Total length, diameter, and normalization Value (N.V.) of male samples. The measurement area was the center of the vertebral halves.

Sample (Male)	Length (mm)	Diameter (mm)	1718.5-1596.3 cm^{-1} N.V.	1596.3-1510.77 cm^{-1} N.V.	1510.77-1290.8 cm^{-1} N.V.	1290.8-1180.9 cm^{-1} N.V.	1180.9-887.6 cm^{-1} N.V.
AB3	440	4.00	0.110859	0.085585	0.222323	0.064851	1
NWN3	1040	11.39	0.129868	0.101419	0.25409	0.076879	1
SDSOE	1390	15.10	0.141249	0.111758	0.287039	0.083738	1
MF5	1350	---	0.102003	0.080906	0.221717	0.062808	1
NWN9	768	---	0.146748	0.12	0.262979	0.086687	1
NWN8	907	8.48	0.068229	0.058333	0.16875	0.071875	1
J17	1500	9.48	0.041796	0.037926	0.118421	0.013932	1

Table 3.4.4.3. 15 Total length, diameter, and normalization Value (N.V.) of male samples. The measurement area was the center of the vertebral halves.

Sample (Male)	Length (mm)	Diameter (mm)	887.6-789.8 cm^{-1} N.V.	789.8-618.8 cm^{-1} N.V.	618.8-569.9 cm^{-1} N.V.	569.9-484.36 cm^{-1} N.V.	484.36-411.05 cm^{-1} N.V.
AB3	440	4.00	0.232312	0.427544	0.240863	0.494514	0.281044
NWN3	1040	11.39	0.242218	0.462936	0.254524	0.52483	0.319748
SDSOE	1390	15.10	0.252815	0.459122	0.245202	0.515673	0.312116
MF5	1350	---	0.242814	0.460466	0.273686	0.561018	0.336011
NWN9	768	---	0.271125	0.491064	0.24693	0.533495	0.342128
NWN8	907	8.48	0.278646	0.668229	0.422917	0.911979	0.593229
J17	1500	9.48	0.268576	0.622291	0.389319	0.859133	0.657895

Figure 3.4.4.3. 20 The total length of shark (mm) vs. normalization value of each peak from the IR spectrum

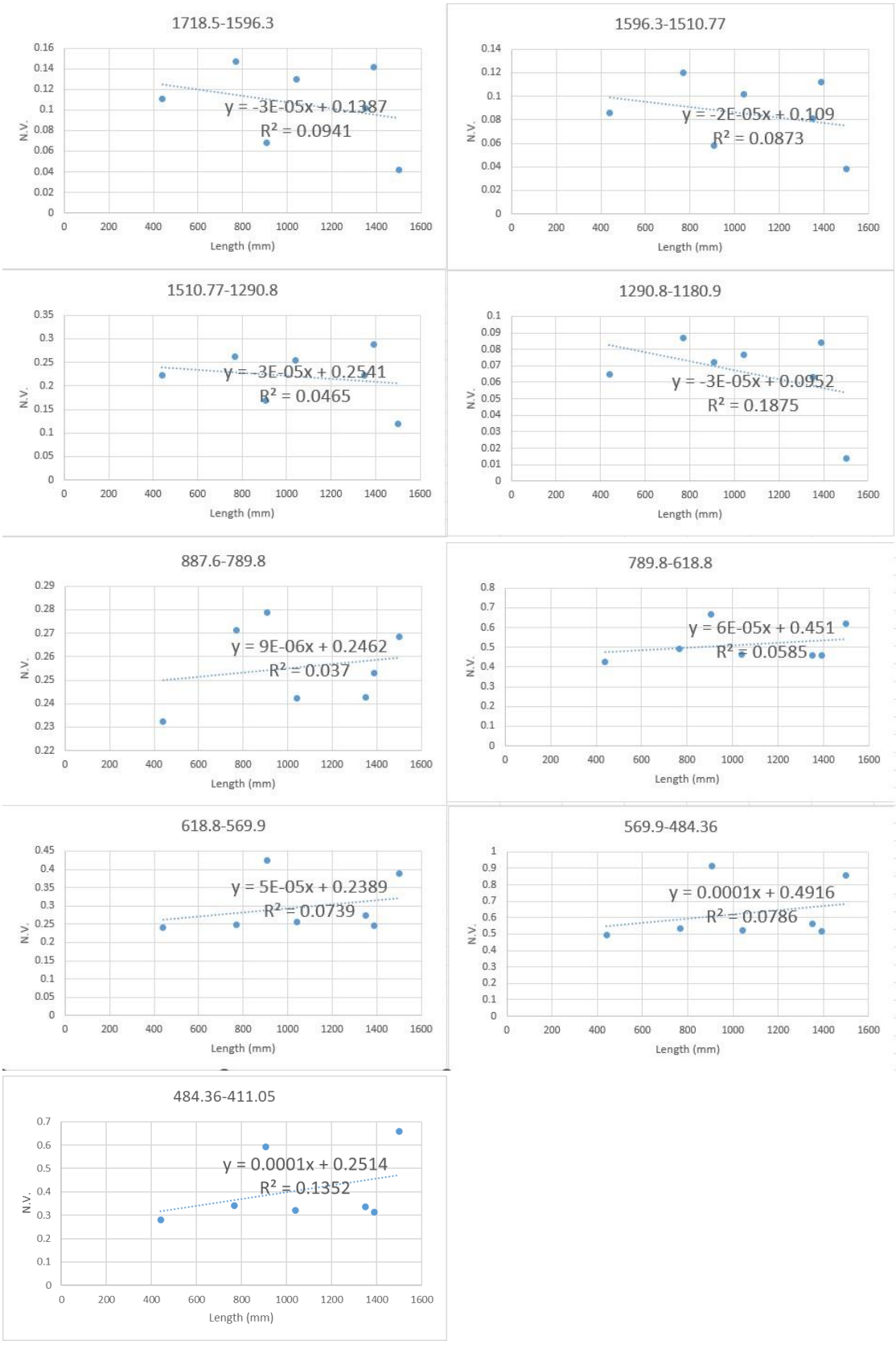

Figure 3.4.4.3. 21 The Diameter of vertebrae (mm) vs. normalization value of each peak from the IR spectrum

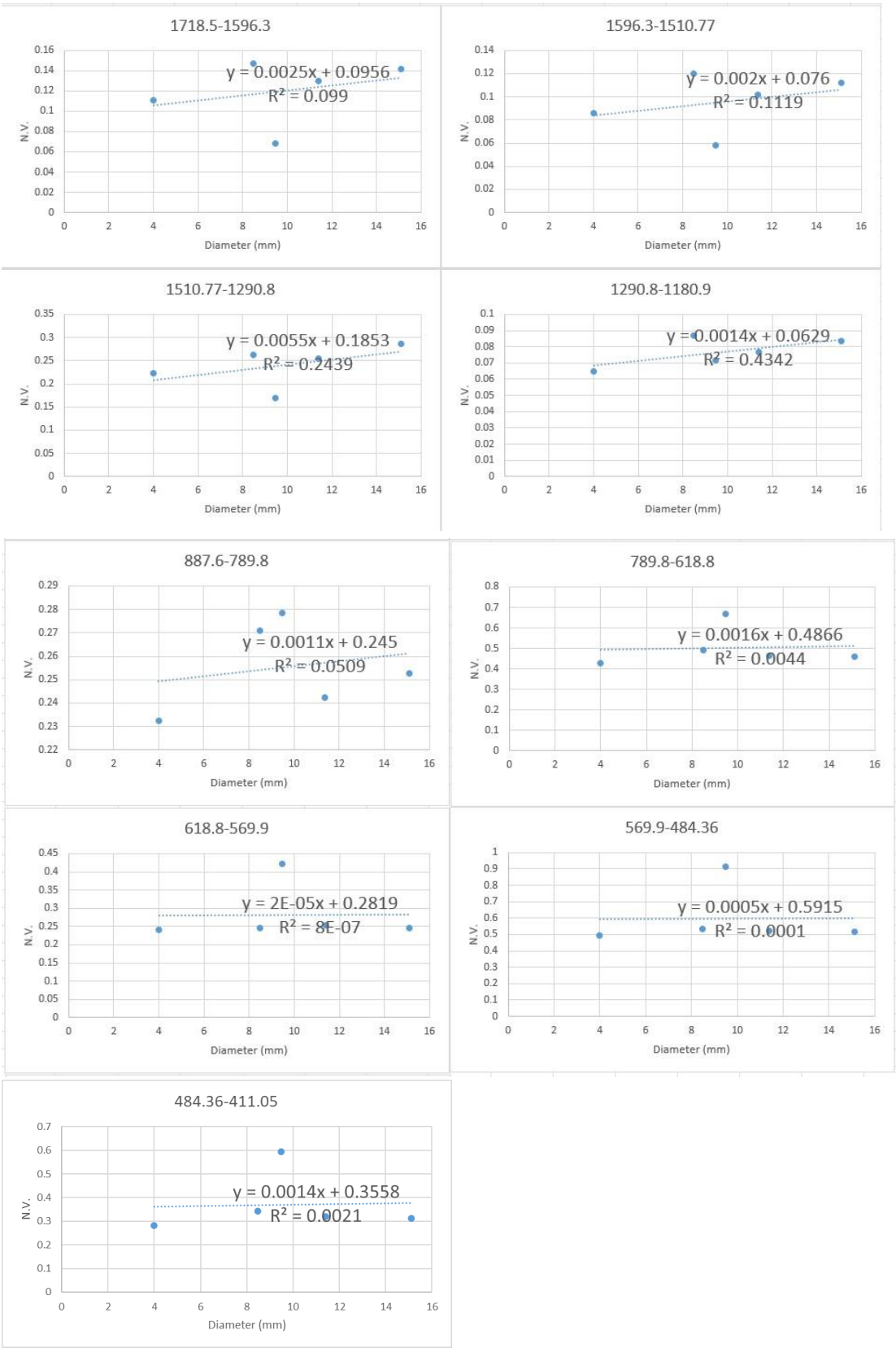

Table 3.4.4.3. 16 Total length, diameter and normalization Value (N.V.) of female samples. The measurement area was the center of the vertebral halves.

Sample (Female)	Length mm	Diameter (mm)	1718.5-1596.3 cm^{-1} N.V.	1596.3-1510.77 cm^{-1} N.V.	1510.77-1290.8 cm^{-1} N.V.	1290.8-1180.9 cm^{-1} N.V.	1180.9-887.6 cm^{-1} N.V.
MK2	880	9.98	0.129868	0.098797	0.256145	0.072616	1
MF1	1050	---	0.099303	0.078776	0.206938	0.063854	1
MF8	1125	12.84	0.08818	0.071486	0.193323	0.058024	1
J28	1610	20.36	0.093193	0.072663	0.215343	0.055051	1
J29	1590	---	0.124089	0.097532	0.261575	0.070505	1
AB27	490	4.90	0.131085	0.10297	0.264903	0.07809	1
LG2	750	7.38	0.128259	0.099757	0.226397	0.073684	1

Table 3.4.4.3. 17 Total length, diameter and normalization Value (N.V.) of female samples. The measurement area was the center of the vertebral halves.

Sample (Female)	Length mm	Diameter (mm)	887.6-789.8 cm^{-1} N.V.	789.8-618.8 cm^{-1} N.V.	618.8-569.9 cm^{-1} N.V.	569.9-484.36 cm^{-1} N.V.	484.36-411.05 cm^{-1} N.V.
MK2	880	9.98	0.247057	0.408646	0.21802	0.476718	0.279384
MF1	1050	---	0.223754	0.410923	0.246554	0.503333	0.286472
MF8	1125	12.84	0.242865	0.482229	0.2951	0.613489	0.364432
J28	1610	20.36	0.255916	0.463857	0.277418	0.601837	0.33933
J29	1590	---	0.26087	0.471994	0.263455	0.570858	0.347904
AB27	490	4.90	0.241821	0.43381	0.242468	0.498957	0.286043
LG2	750	7.38	0.245182	0.43417	0.235466	0.50413	0.30753

Figure 3.4.4.3. 22 The total length of shark (mm) vs. normalization value of each peak from the IR spectrum

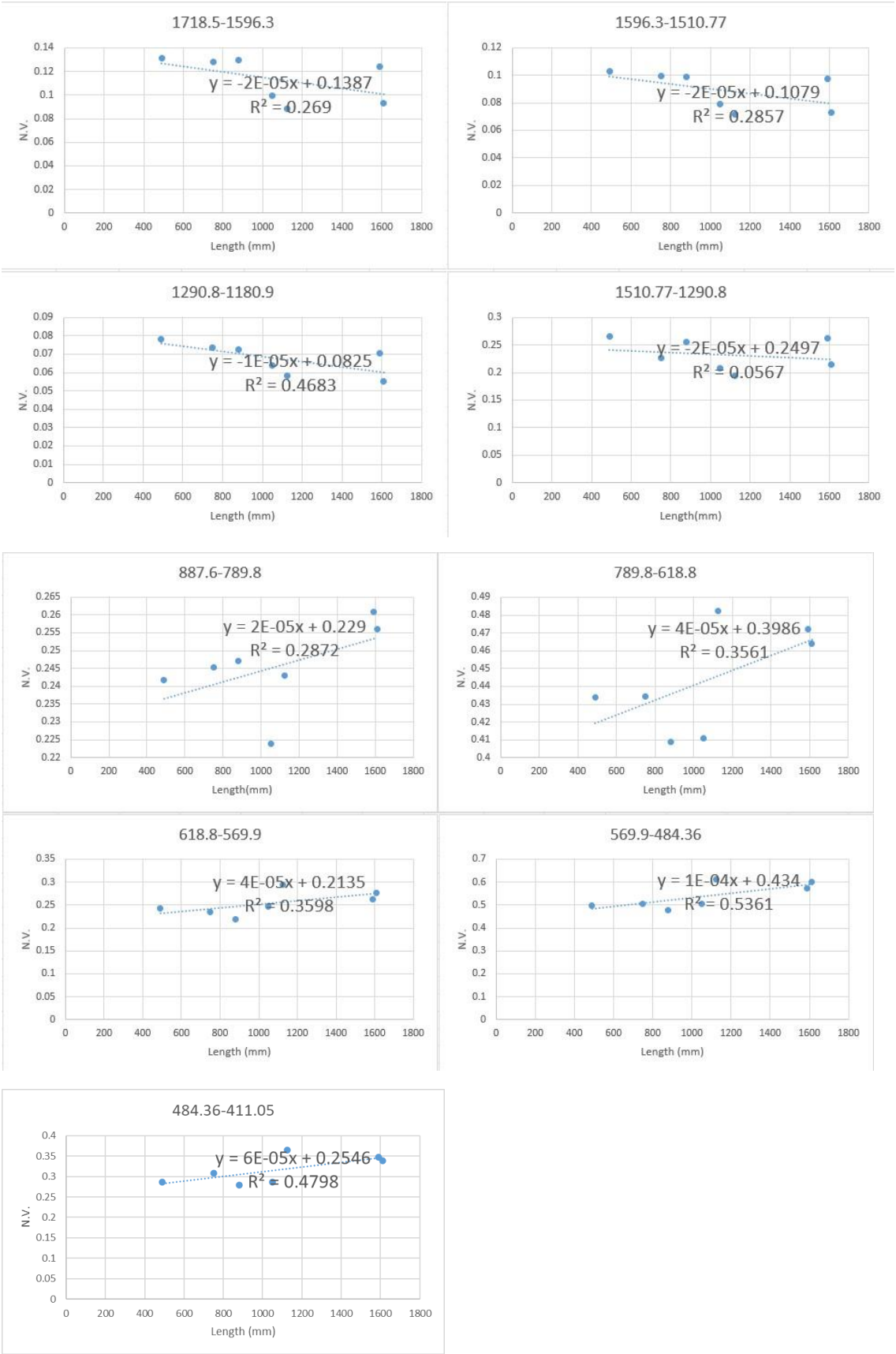

Figure 3.4.4.3. 23 The diameter of vertebrae (mm) vs. normalization value of each peak from the IR spectrum

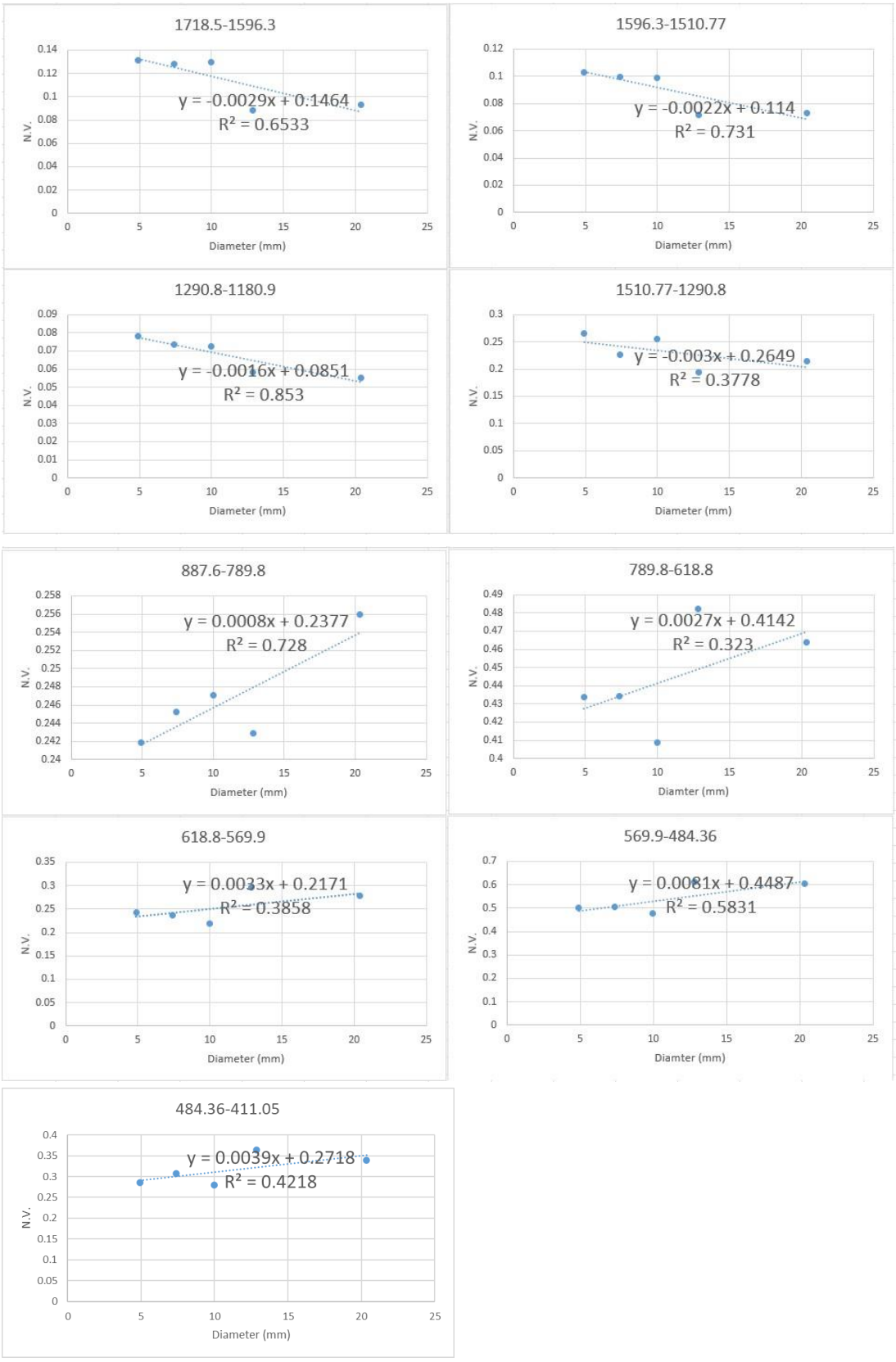

Part 2. iS50R FT-IR

A total of sixteen formal vertebral samples, eight from male sharks and eight from female sharks, were examined. The length of the sharks, measured from the tip of the nose to the tip of the tail, ranged from 300 to 1600 mm. Both edge and center areas of the corpus calcareum from the vertebrae sections were scanned. Seven peaks from the raw FT-IR spectra were chosen to be integrated (Table 3.4.4.3.18). Different peaks were selected as the standard peak to normalize the dataset. First, peak 6033-5456 cm^{-1} was chosen (Table 3.4.4.3.19) because we believed it was related to tightly bound water. Next, the collagen peak 4708-4493 cm^{-1} was selected as the standard peak since it represented the collagen presence and it associated with hydroxyapatite in the vertebrae structure. Total body length, diameter of the vertebrae, and the normalization values were used to plot diagrams for further analysis of the data from IR spectra. R^2 values from the diagrams were compared to identify any trending pattern.

Table 3.4.4.3. 18 Total length and integral value (I.V.) of male samples. The measurement area was the edge of the vertebral halves.

Sample (Male)	Sample (Male)	Length (mm)	8867-7729 cm^{-1} I.V.	7548-6048 cm^{-1} I.V.	6033-5456 cm^{-1} I.V.	5368-4708 cm^{-1} I.V.	4708-4493 cm^{-1} I.V.	4484-4215 cm^{-1} I.V.	4176-3917 cm^{-1} I.V.
J17	FSL1-3	1500	1.8222	14.3061	1.1619	7.8096	0.2739	0.1098	0.6631
MF5	FSL1-2	1350	16.204	100.274	10.876	55.3190	1.291	0.1980	1.764
SDSOE	FSL1-1	1390	3.0231	24.4052	2.3644	13.2481	0.3408	0.3965	0.7354
NWN3	FSS-A5	1040	1.8004	12.6820	0.9629	6.2297	0.2346	0.1048	0.3167
NWN8	FSS-A4	907	0.9134	5.6380	0.4029	2.9568	0.0874	0.0510	0.1178
NWN9	FSS-A3	768	0.9788	3.8162	0.2466	1.8253	0.0741	0.0184	0.0450
NWS1	FSS-A2	600	1.3775	3.9250	0.8551	1.0621	0.0932	0.3111	0.0444
AB3	FSS-A1	440	1.0163	2.7482	0.2641	2.4617	0.1370	0.2291	0.3627

Figure 3.4.4.3. 24 FT-IR spectra of all male vertebral samples and each spectrum is the addition spectra of different area spectra (e.g., center, edge, middle…)

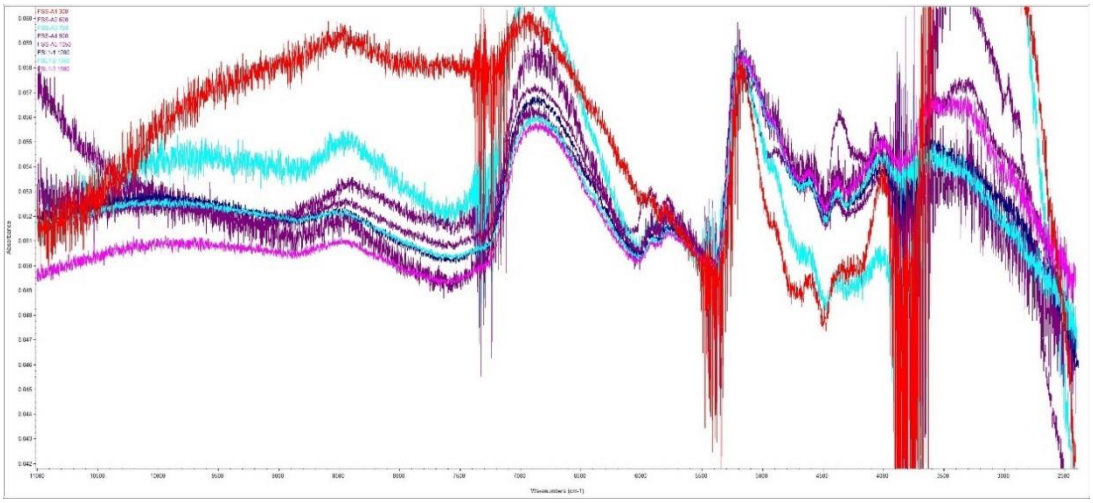

Figure 3.4.4.3. 25 FT-IR spectra of all male vertebral samples, and the measurement areas are a). edge and b). center

a).

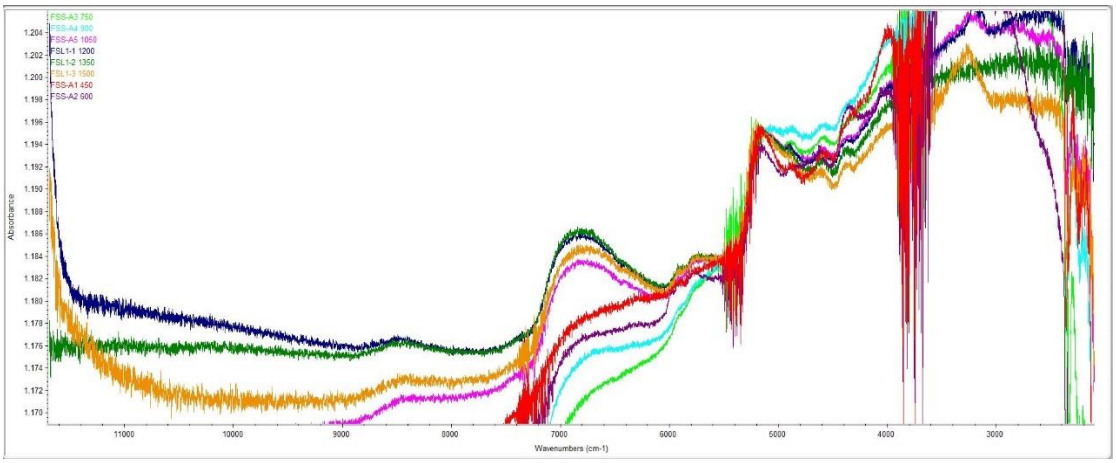

b).

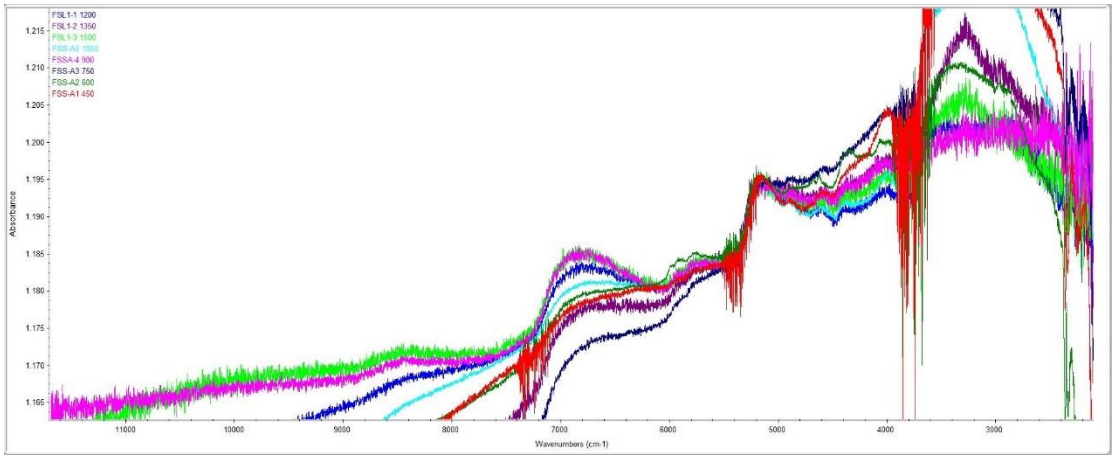

Figure 3.4.4.3. 26 Total length of shark (mm) vs. integral value of each peak from FT-IR spectrum

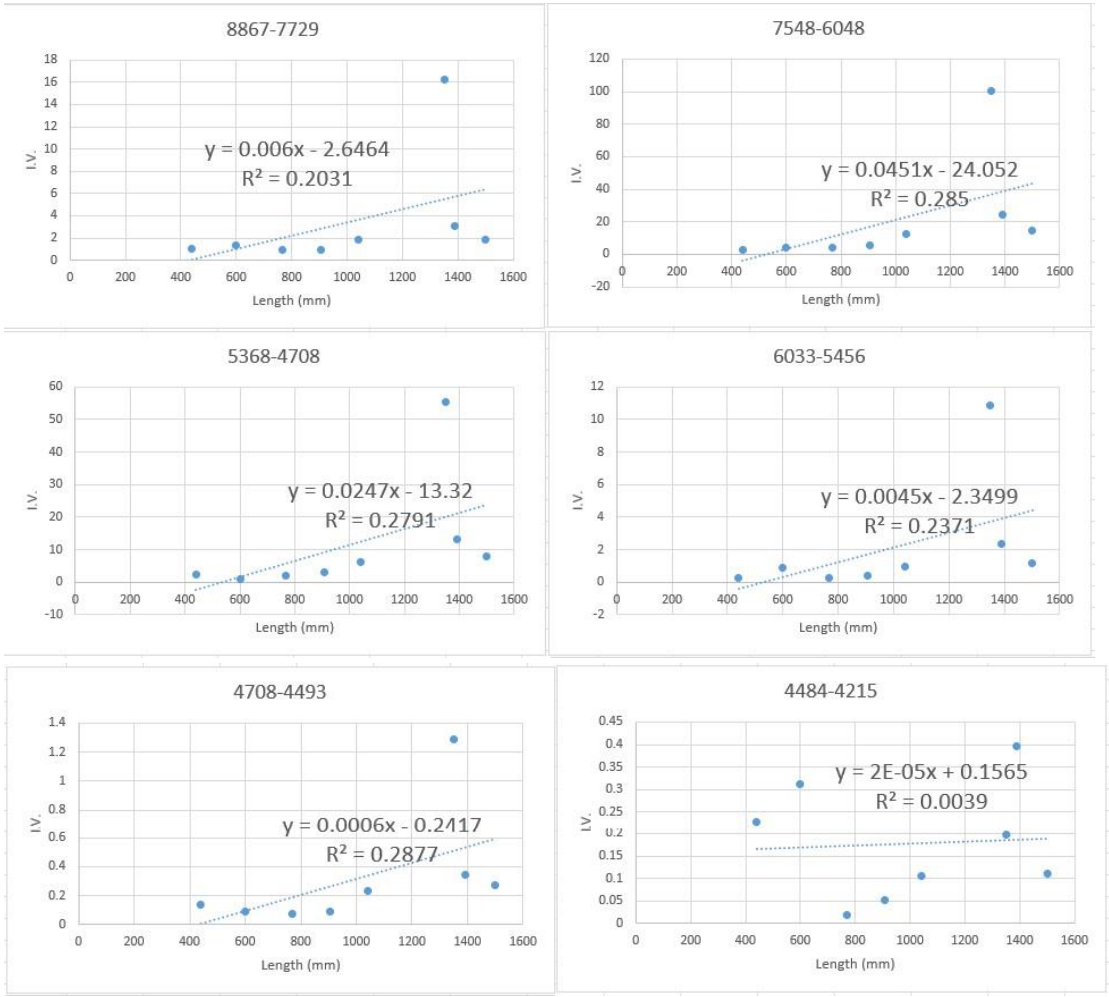

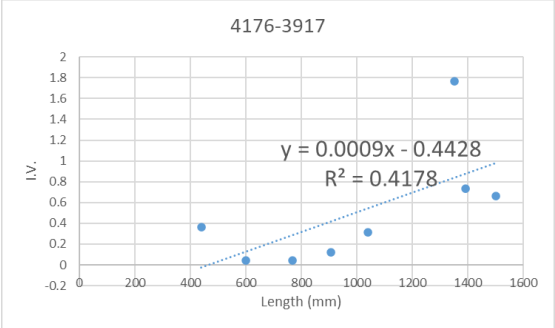

Table 3.4.4.3. 19 Total length and normalization value (N.V.) of male samples. The measurement area was the edge of the vertebral halves.

Sample (Male)	Length (mm)	8867-7729 cm^{-1} N.V.	7548-6048 cm^{-1} N.V.	6033-5456 cm^{-1} N.V.	5368-4708 cm^{-1} N.V.	4708-4493 cm^{-1} N.V.	4484-4215 cm^{-1} N.V.	4176-3917 cm^{-1} N.V.
J17	1500	1.568293	12.31268	1	6.721405	0.235735	0.094500	0.570703
MF5	1350	1.489886	9.219750	1	5.086337	0.118702	0.018205	0.162192
SDSOE	1390	1.278591	10.32194	1	5.603155	0.144138	0.167696	0.311030
NWN3	1040	1.869768	13.17063	1	6.469727	0.243639	0.108838	0.328902
NWN8	907	2.267064	13.99355	1	7.338794	0.216927	0.126582	0.292380
NWN9	768	3.969181	15.47526	1	7.401865	0.300487	0.074615	0.182482
NWS1	600	1.610923	4.590106	1	1.242077	0.108993	0.363817	0.051924
AB3	440	3.848164	10.40591	1	9.321090	0.518743	0.867474	1.373343

Figure 3.4.4.3. 27 Total length of shark (mm) vs. normalization value of each peak from FT-IR spectrum

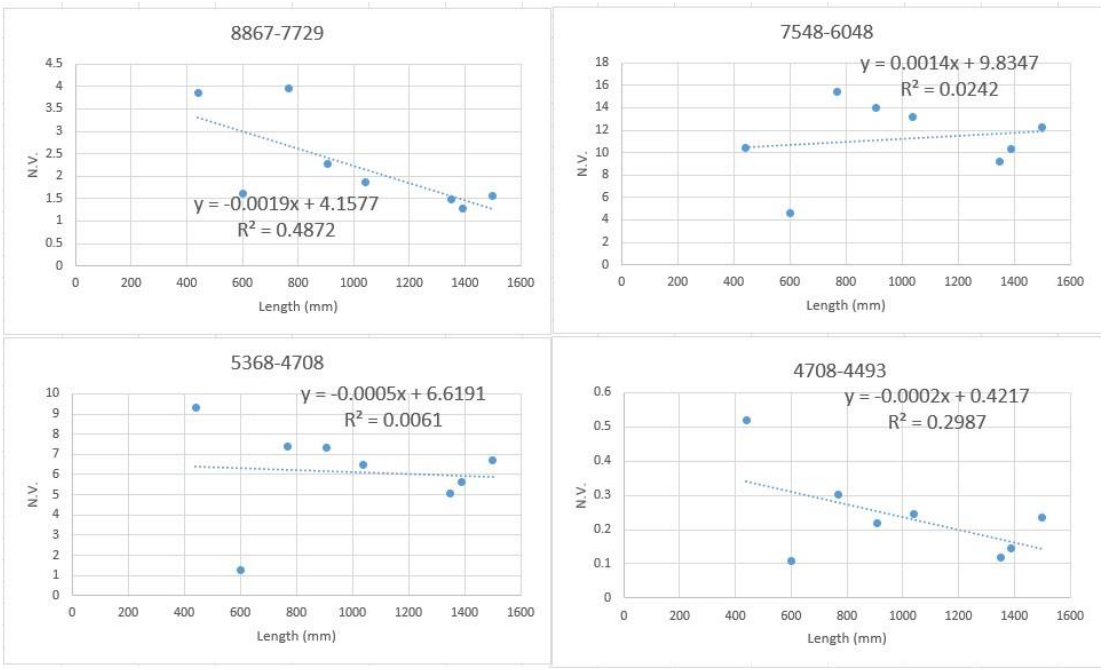

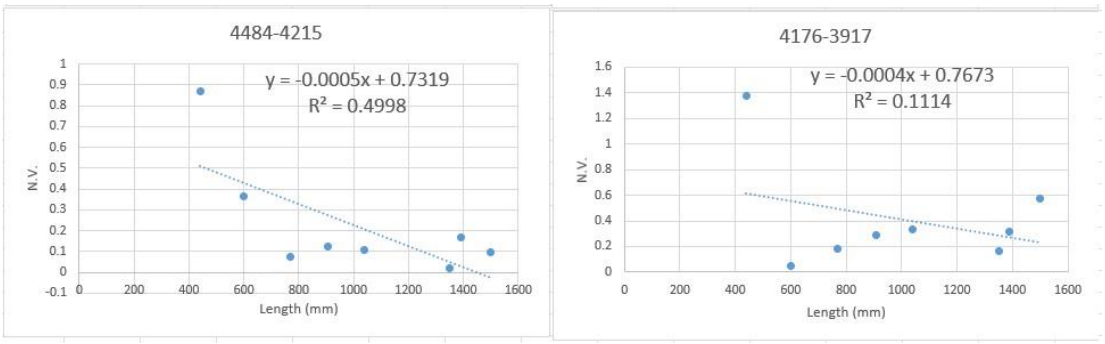

Table 3.4.4.3. 20 Total length and integral value (I.V.) of female samples. The measurement area was the edge of the vertebral halves.

Sample (Female)	Sample (Female)	Length (mm)	8867-7729 cm^{-1} I.V.	7548-6048 cm^{-1} I.V.	6033-5456 cm^{-1} I.V.	5368-4708 cm^{-1} I.V.	4708-4493 cm^{-1} I.V.	4484-4215 cm^{-1} I.V.	4176-3917 cm^{-1} I.V.
NWS12	FSS-B1	334	1.9149	8.1720	1.3776	4.8011	0.2184	0.0957	0.1626
AB27	FSS-B2	450	0.3057	1.7683	0.1086	1.8416	0.1065	0.0875	0.3678
LG2	FSS-B3	750	0.3208	3.6588	0.2129	2.1365	0.0536	0.0353	0.1094
MK2	FSS-B4	900	0.9741	10.1278	0.6842	4.0334	0.0426	0.0139	0.1215
MF1	FSL1-4	1050	0.8291	5.0186	0.7080	2.9383	0.0859	0.1187	0.0392
MF8	FSL1-5	1200	1.5693	12.3630	0.8760	6.2478	0.1990	0.1447	0.2793
J28	FSL1-6	1500	4.6814	32.3801	1.8895	12.1107	0.3537	0.3670	0.3176
J19	FSL2-1	1650	3.1710	31.9030	2.1790	20.8270	0.8760	0.7140	0.5220

Figure 3.4.4.3. 28 FT-IR spectra of all female vertebral samples and each spectrum is the addition spectra of different area spectra (e.g., center, edge, middle…)

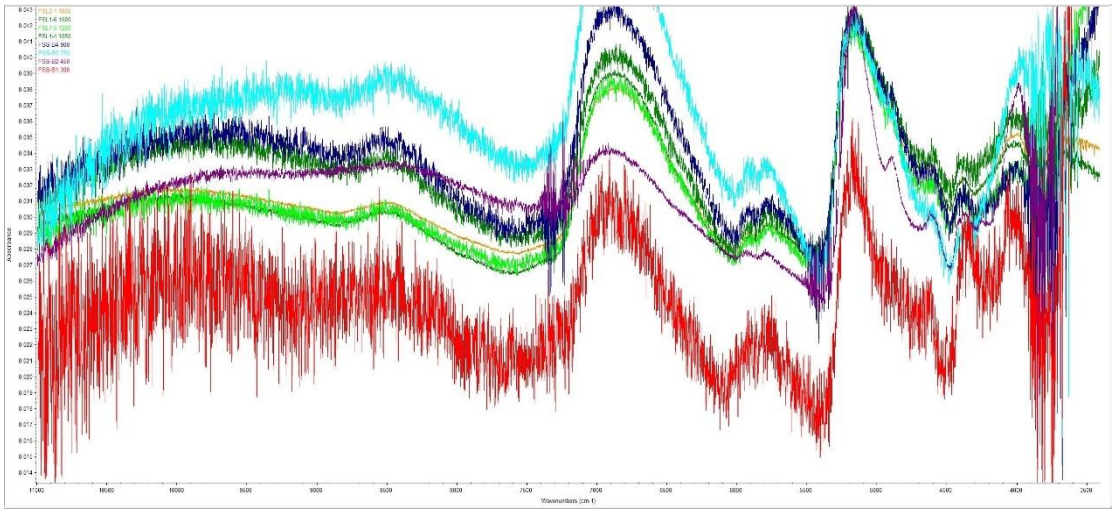

Figure 3.4.4.3. 29 FT-IR spectra of all male vertebral samples, and the measurement

areas are a). edge and b). center

a).

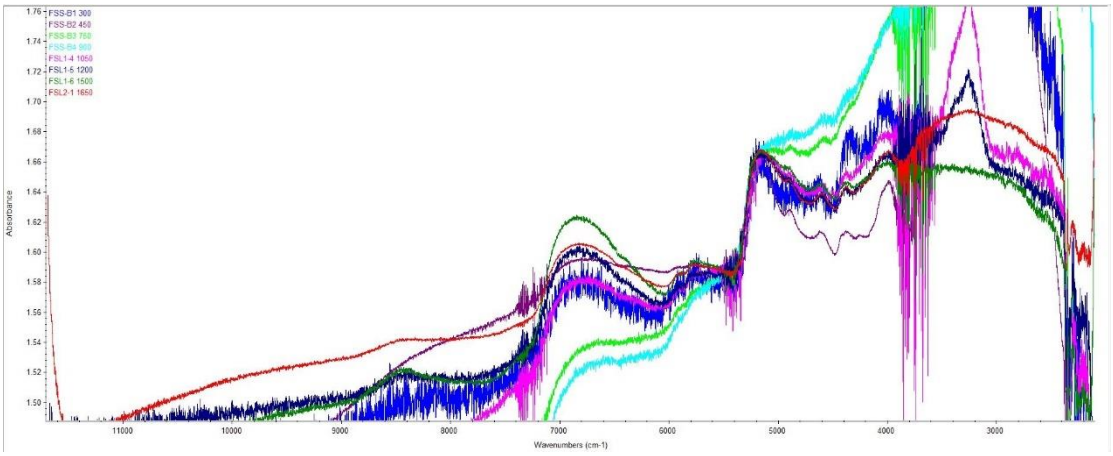

b).

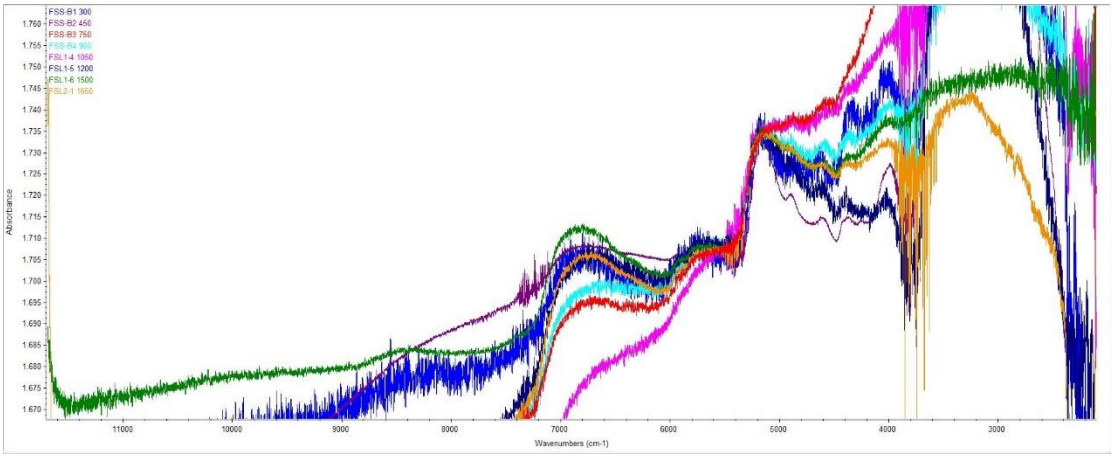

Figure 3.4.4.3. 30 Total length of shark (mm) vs. integral value of each peak from FT-IR spectrum

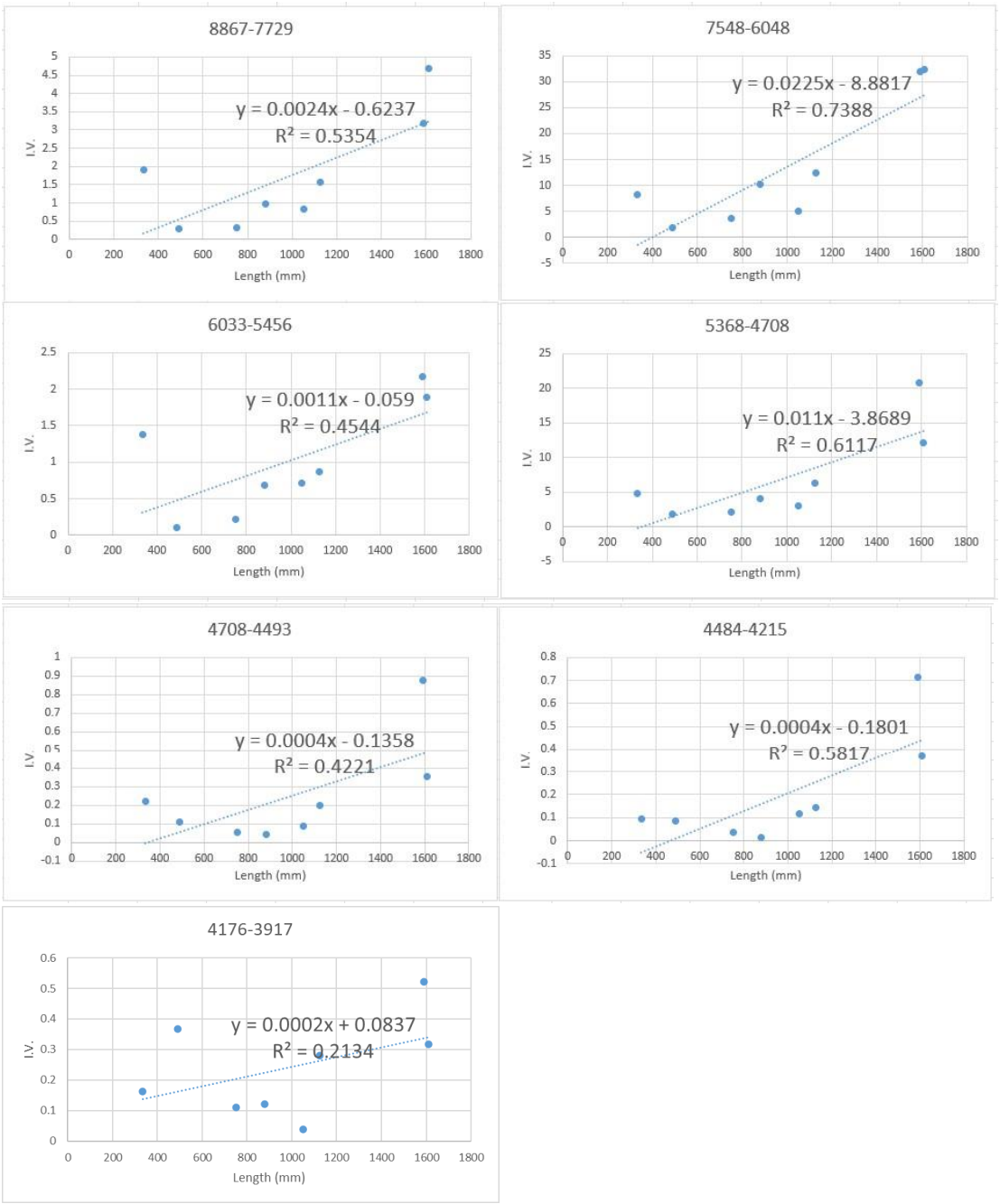

Table 3.4.4.3. 21 Total length and normalization value (N.V.) of female samples. The measurement area was the edge of the vertebral halves.

Sample (Female)	Length (mm)	8867-7729 cm^{-1} N.V.	7548-6048 cm^{-1} N.V.	6033-5456 cm^{-1} N.V.	5368-4708 cm^{-1} N.V.	4708-4493 cm^{-1} N.V.	4484-4215 cm^{-1} N.V.	4176-3917 cm^{-1} N.V.
NWS12	334	1.390026	5.932056	1	3.485119	0.158537	0.069469	0.118031
AB27	450	2.814917	16.28269	1	16.95764	0.980663	0.805709	3.38674

LG2	750	1.506811	17.18553	1	10.03523	0.251761	0.165806	0.513856
MK2	900	1.423707	14.8024	1	5.89506	0.062262	0.020316	0.17758
MF1	1050	1.171045	7.088418	1	4.150141	0.121328	0.167655	0.055367
MF8	1200	1.791438	14.11301	1	7.132192	0.227169	0.165183	0.318836
J28	1500	2.477587	17.13686	1	6.409473	0.187192	0.194231	0.168087
J19	1650	1.455255	14.64112	1	9.558054	0.402019	0.327673	0.239559

Figure 3.4.4.3. 31 Total length of shark (mm) vs. normlization value of each peak from FT-IR spectrum

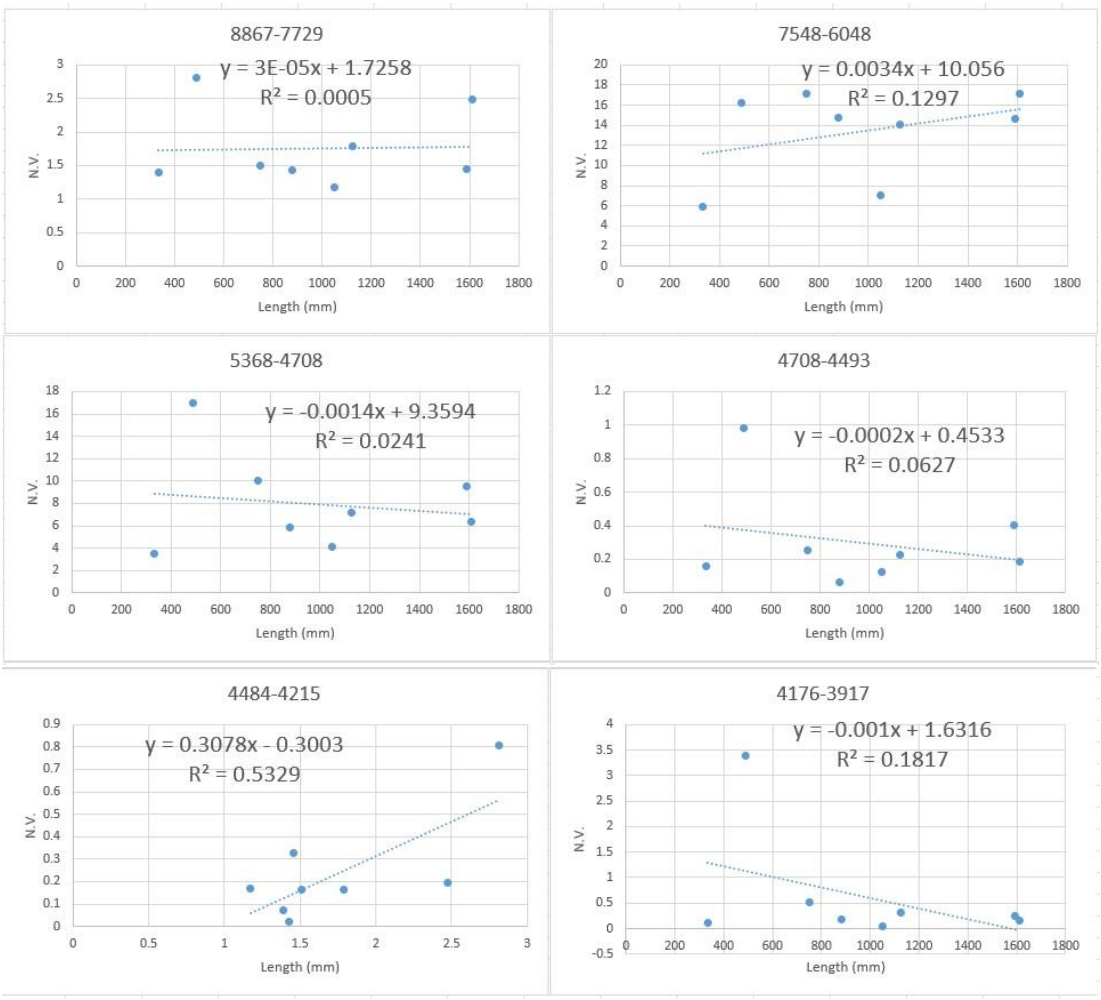

Table 3.4.4.3. 22 Total length and integral value (I.V.) of male samples. The measurement area was the center of the vertebral halves.

Sample (male)	Length (mm)	8867-7729 cm^{-1} I.V.	7548-6048 cm^{-1} I.V.	6033-5456 cm^{-1} I.V.	5368-4708 cm^{-1} I.V.	4708-4493 cm^{-1} I.V.	4484-4215 cm^{-1} I.V.	4176-3917 cm^{-1} I.V.

J17	1500	9.0240	52.1710	4.5430	21.7200	0.6190	1.9220	0.9777
MF5	1350	1.0180	16.5610	1.4900	11.4670	0.3590	0.1490	0.5610
SDSOE	1390	10.184	49.5890	3.8150	31.8480	0.9710	0.8890	1.4450
NWN3	1040	1.9720	12.5270	1.1160	43.3230	0.3920	0.5860	0.6430
NWN8	907	10.3480	99.4760	18.031	38.9870	1.5550	1.2050	3.8080
NWN9	768	1.04180	10.4696	0.8964	4.0501	0.0764	0.0592	0.1633
NWS1	600	0.8613	4.1221	0.5997	2.6922	0.0932	0.4442	0.0410
AB3	440	0.8598	2.8685	0.2336	2.5651	0.1370	0.1011	0.1378

Figure 3.4.4.3. 32 Total length of shark (mm) vs. integral value of each peak from FT-IR spectrum

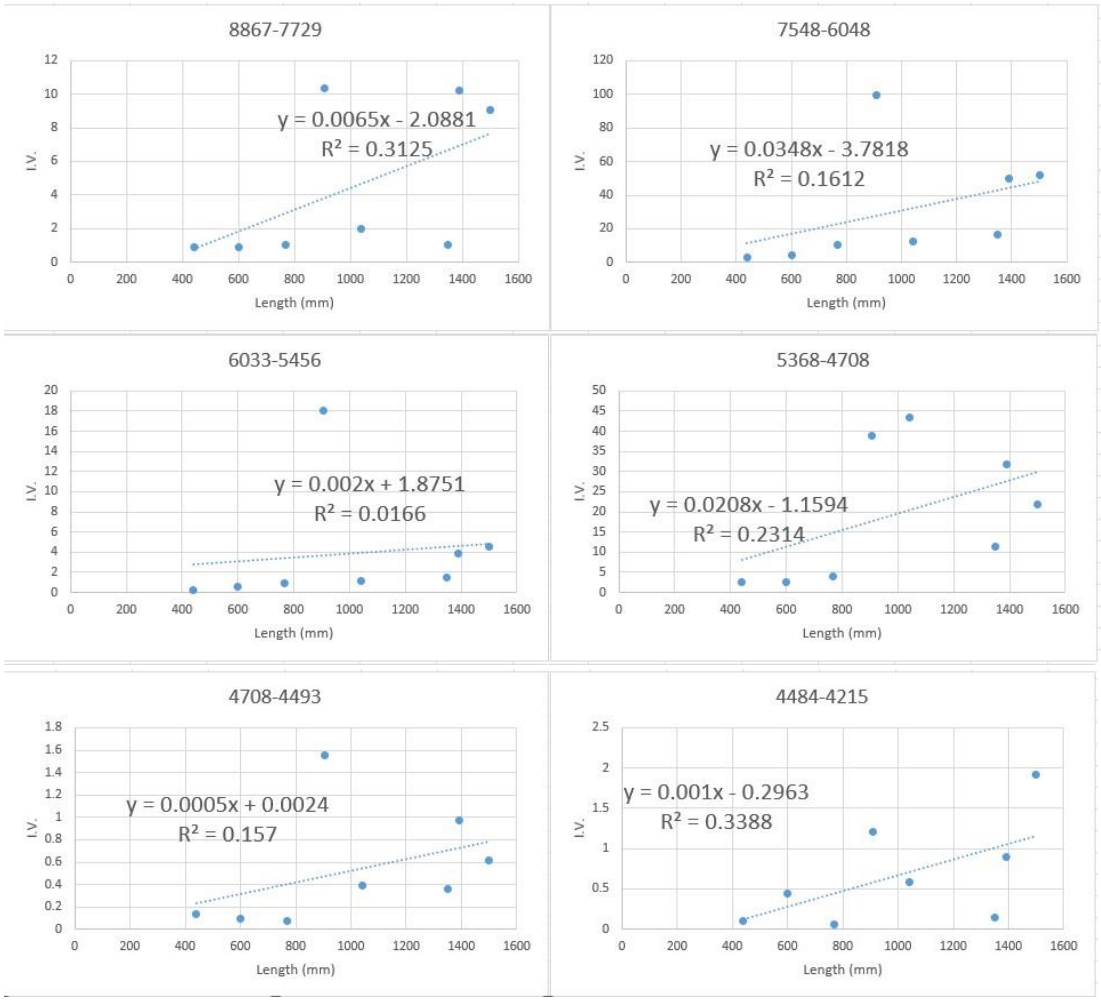

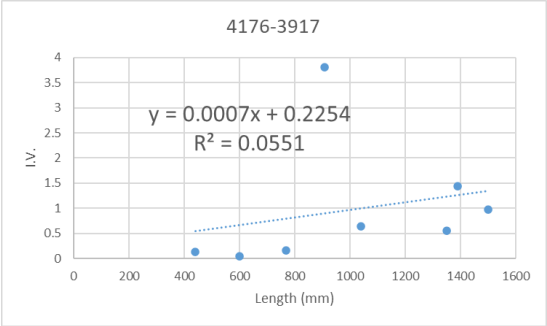

Table 3.4.4.3. 23 Total length and normalization value (N.V.) of male samples. The measurement area was the center of the vertebral halves.

Sample (male)	Length (mm) (male)	8867-7729 cm^{-1} N.V.	7548-6048 cm^{-1} N.V.	6033-5456 cm^{-1} N.V.	5368-4708 cm^{-1} N.V.	4708-4493 cm^{-1} N.V.	4484-4215 cm^{-1} N.V.	4176-3917 cm^{-1} N.V.
J17	1500	1.986353	11.48382	1	4.780982	0.136254	0.423068	0.21521
MF5	1350	0.683221	11.11477	1	7.695973	0.24094	0.1	0.37651
SDSOE	1390	2.669463	12.99843	1	8.3481	0.254522	0.233028	0.378768
NWN3	1040	1.767025	11.22491	1	38.81989	0.351254	0.52509	0.576165
NWN8	907	0.573901	5.516943	1	2.162221	0.08624	0.066829	0.211192
NWN9	768	1.162204	11.67961	1	4.518184	0.08523	0.066042	0.182173
NWS1	600	1.436218	6.873603	1	4.489245	0.155411	0.740704	0.068368
AB3	440	3.680651	12.27954	1	10.98074	0.586473	0.432791	0.589897

Figure 3.4.4.3. 33 Total length of shark (mm) vs. normalization value of each peak from FT-IR spectrum

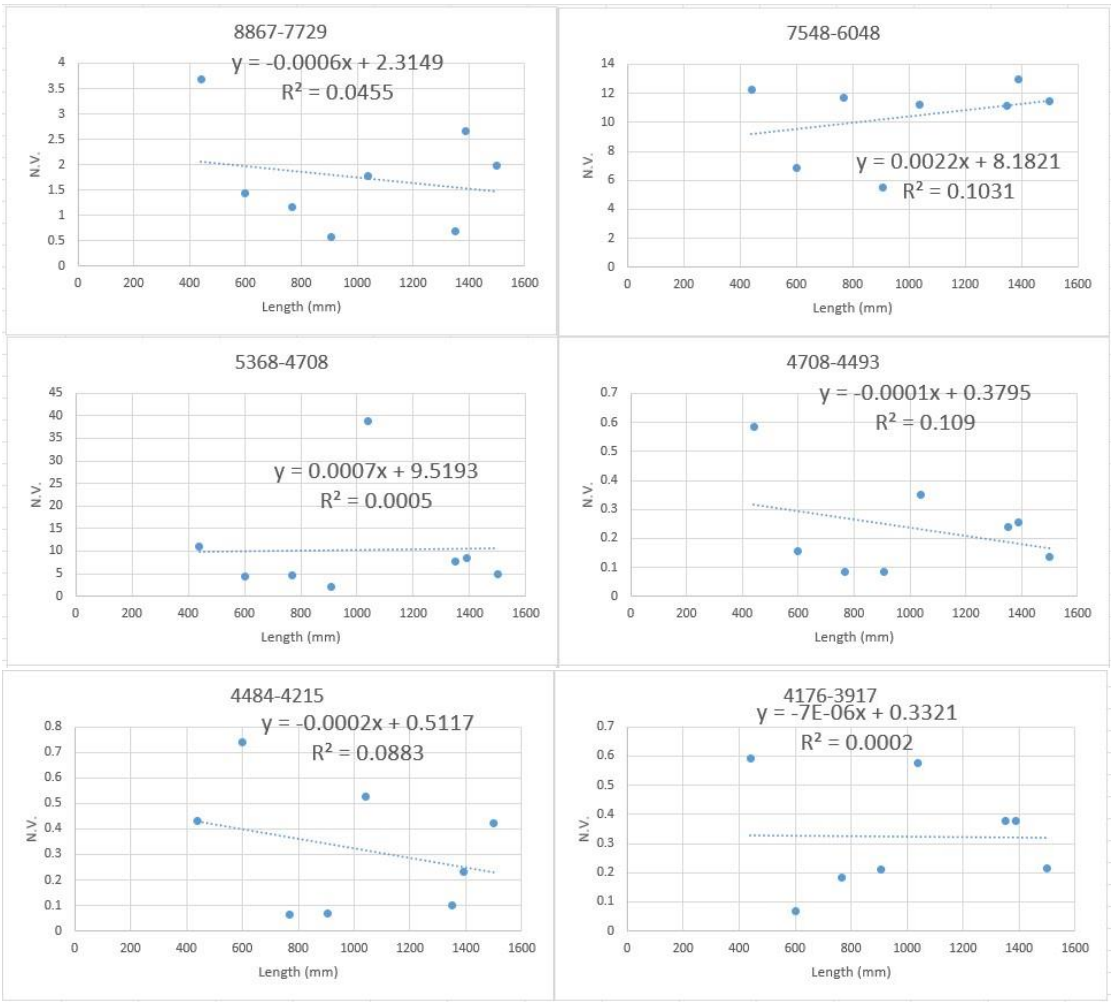

Table 3.4.4.3. 24 Total length and integral value (I.V.) of female samples. The measurement area was the center of the vertebral halves.

Sample (Female)	Length (mm)	8867-7729 cm^{-1} I.V.	7548-6048 cm^{-1} I.V.	6033-5456 cm^{-1} I.V.	5368-4708 cm^{-1} I.V.	4708-4493 cm^{-1} I.V.	4484-4215 cm^{-1} I.V.	4176-3917 cm^{-1} I.V.
NWS12	334	2.5958	7.2498	1.7587	4.3654	0.1795	0.8253	0.4686
AB27	450	0.3606	1.6574	0.1401	2.3906	0.1107	0.133	0.2109
LG2	750	2.0209	13.0269	1.3449	5.3783	0.2464	0.1578	0.012
MK2	900	2.5789	17.0921	1.8898	8.0697	0.4598	0.2584	0.3444
MF1	1050	1.6574	9.0792	0.5794	4.6727	0.1641	0.1944	0.0723
MF8	1200	3.8400	20.9300	2.3390	10.234	0.4290	0.6560	0.8300
J28	1500	8.5340	111.129	9.0720	59.147	1.8040	1.0530	1.2970
J19	1650	2.1585	15.6954	0.9288	6.4047	0.1568	0.2573	0.2828

Figure 3.4.4.3. 34 Total length of shark (mm) vs. integral value of each peak from FT-IR spectrum

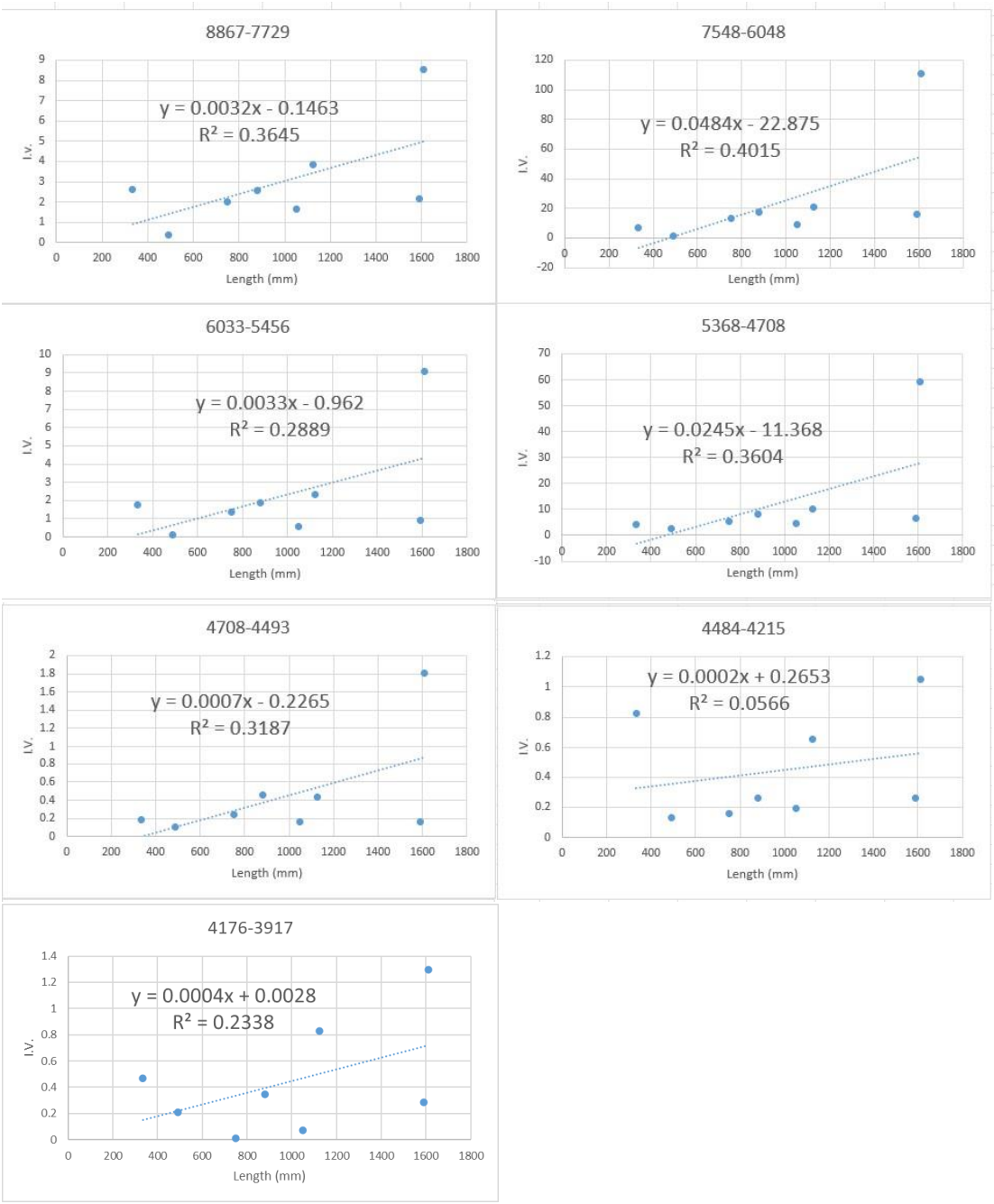

Table 3.4.4.3. 25 Total length and normalization value (N.V.) of female samples. The measurement area was the center of the vertebral halves.

Sample (Female)	Length (mm)	8867-7729 cm^{-1} N.V.	7548-6048 cm^{-1} N.V.	6033-5456 cm^{-1} N.V.	5368-4708 cm^{-1} N.V.	4708-4493 cm^{-1} N.V.	4484-4215 cm^{-1} N.V.	4176-3917 cm^{-1} N.V.
NWS12	334	1.475977	4.122249	1	2.482174	0.102064	0.469267	0.266447

AB27	450	2.573876	11.83012	1	17.06353	0.79015	0.949322	1.505353
LG2	750	1.50264	9.686148	1	3.999033	0.183211	0.117332	0.008923
MK2	900	1.364642	9.044396	1	4.270134	0.243306	0.136734	0.182242
MF1	1050	2.860545	15.67000	1	8.064722	0.283224	0.33552	0.124784
MF8	1200	1.641727	8.948268	1	4.375374	0.183412	0.280462	0.354853
J28	1500	0.940697	12.24967	1	6.519731	0.198854	0.116071	0.142967
J19	1650	2.323966	16.89858	1	6.895672	0.16882	0.277024	0.304479

Figure 3.4.4.3. 35 Total length of shark (mm) vs. integral value of each peak from FT-IR spectrum

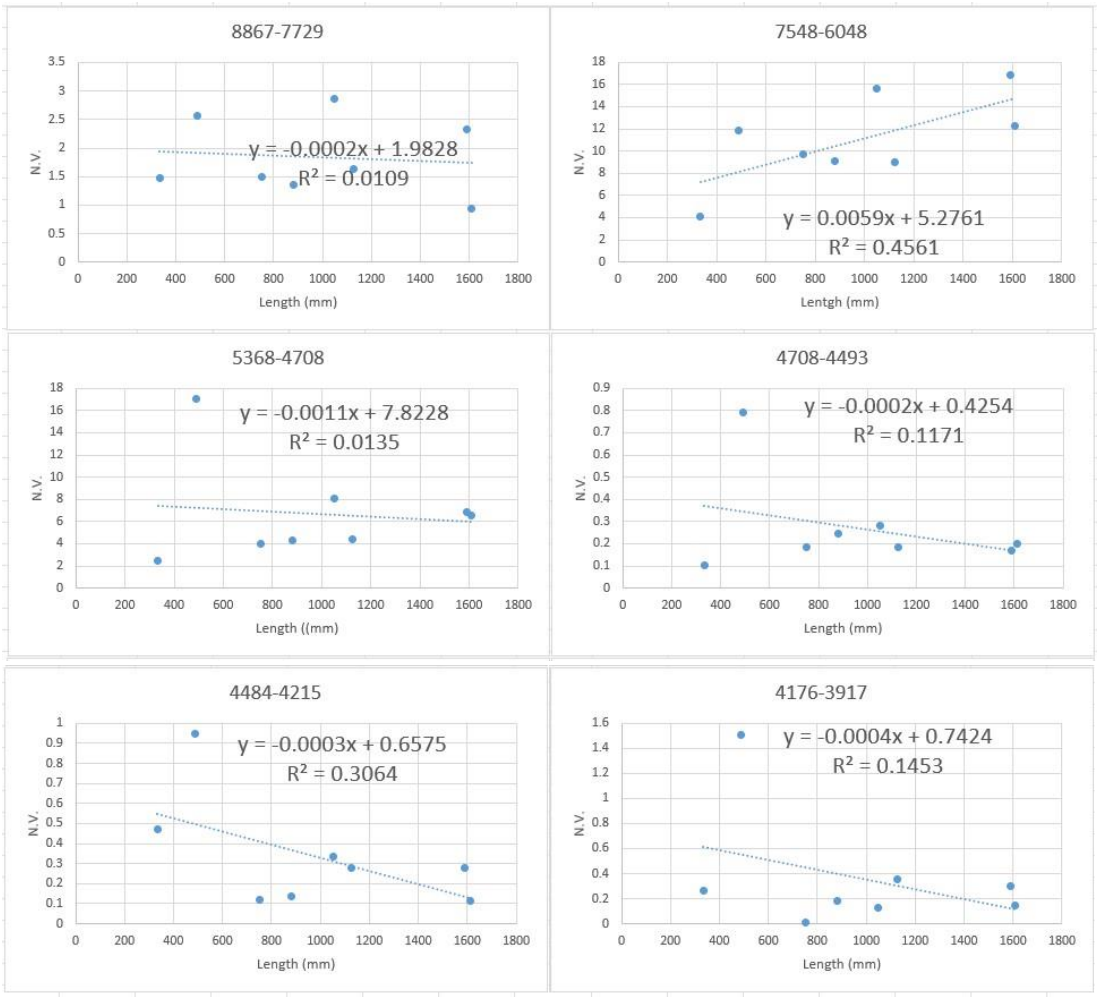

Table 3.4.4.3. 26 Total length, diameter and normalization Value (N.V.) of male samples. The measurement area was the edge of the vertebral halves. The collagen peak was used as the standard to normalize other peaks.

Sample (male)	Length (mm)	8867-7729 cm^{-1} N.V.	7548-6048 cm^{-1} N.V.	6033-5456 cm^{-1} N.V.	5368-4708 cm^{-1} N.V.	4708-4493 cm^{-1} N.V.	4484-4215 cm^{-1} N.V.	4176-3917 cm^{-1} N.V.
J17	1500	6.652793	52.23111	4.242059	28.5126	1	0.400876	2.420957
MF5	1350	12.55151	77.67157	8.424477	42.84973	1	0.153369	1.366383
SDSOE	1390	8.870599	71.6115	6.937793	38.87353	1	1.163439	2.157864
NWN3	1040	7.674339	54.05797	4.104433	26.55456	1	0.446718	1.349957
NWN8	907	10.4508	64.50801	4.60984	33.83066	1	0.583524	1.347826
NWN9	768	13.20918	51.50067	3.327935	24.63293	1	0.248313	0.607287
NWS1	600	14.78004	42.11373	9.174893	11.39592	1	3.337983	0.476395
AB3	440	7.418248	20.05985	1.927737	17.96861	1	1.672263	2.647445

Table 3.4.4.3. 27 Diameter of male samples

Sample (male)	Diameter (mm)
J17	---
MF5	---
SDSOE	15.10
NWN3	11.39
NWN8	9.48
NWN9	8.48
NWS1	5.99
AB3	4.00

Figure 3.4.4.3. 36 Total length of shark (mm) vs. integral value of each peak from FT-IR spectrum

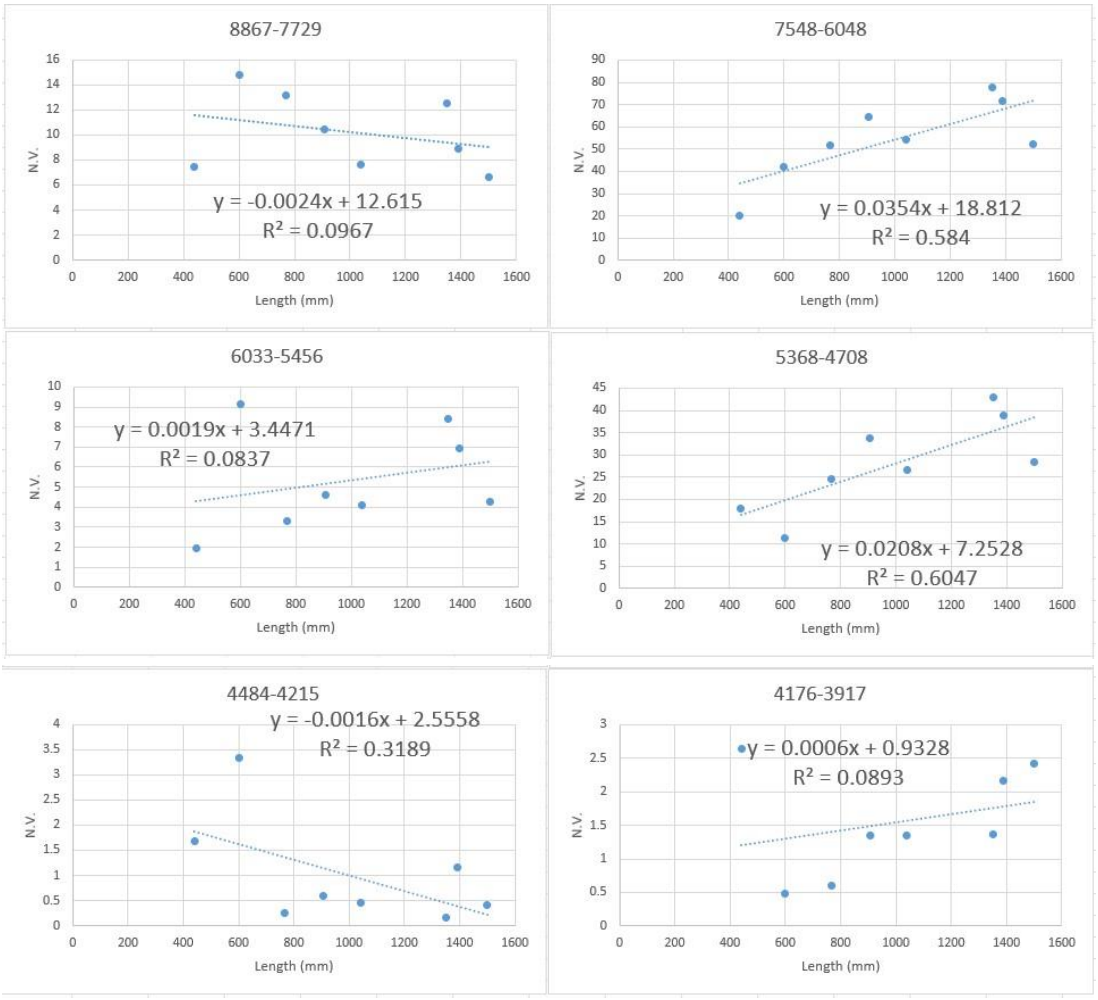

Figure 3.4.4.3. 37 Total length of shark (male) vs. diameter of shark vertebra

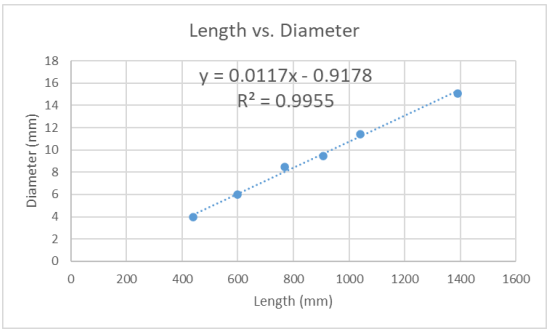

Figure 3.4.4.3. 38 Diameter of shark vertebra (mm) vs. integral value of each peak from FT-IR spectrum

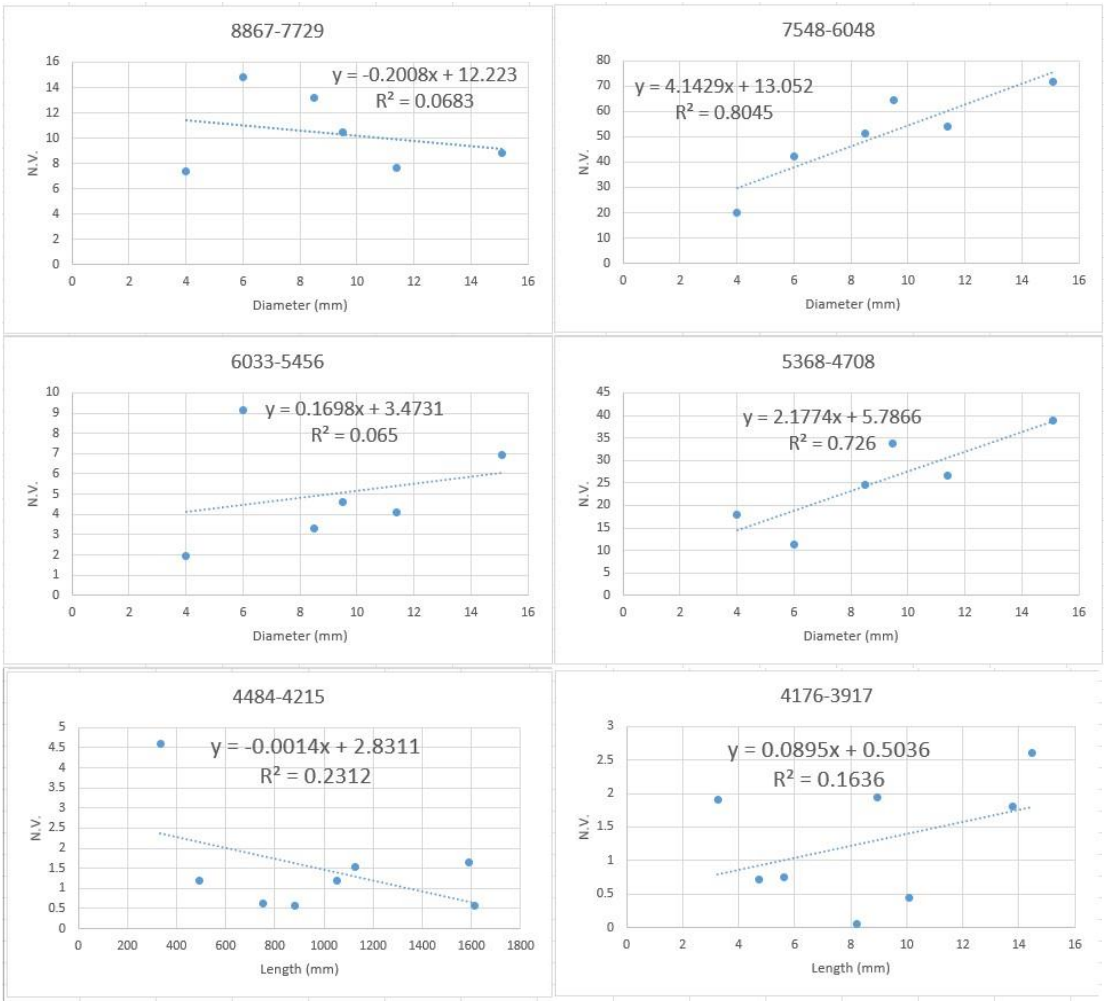

Table 3.4.4.3. 28 Total length, diameter and normalization Value (N.V.) of female samples. The measurement area was the edge of the vertebral halves.

Sample (Female)	Length (mm)	8867-7729 cm^{-1} N.V.	7548-6048 cm^{-1} N.V.	6033-5456 cm^{-1} N.V.	5368-4708 cm^{-1} N.V.	4708-4493 cm^{-1} N.V.	4484-4215 cm^{-1} N.V.	4176-3917 cm^{-1} N.V.
NWS12	334	8.767857	37.41758	6.307692	21.98306	1	0.438187	0.744505
AB27	490	2.870423	16.60376	1.019718	17.29202	1	0.821596	3.453521
LG2	750	5.985075	68.26119	3.972015	39.86007	1	0.658582	2.041045
MK2	880	22.8662	237.7418	16.06103	94.68075	1	0.326291	2.852113
MF1	1050	9.651921	58.42375	8.242142	34.20605	1	1.381839	0.456345
MF8	1125	7.88593	62.12563	4.40201	31.39598	1	0.727136	1.403518
J28	1610	13.23551	91.54679	5.342098	34.24003	1	1.037602	0.897936

J19	1590	3.619863	36.41895	2.487443	23.77511	1	0.815068	0.59589

Table 3.4.4.3. 29 Diameter of female samples.

Sample (Female)	Diameter
NWS12	3.1
AB27	4.9
LG2	7.38
MK2	9.98
MF1	---
MF8	12.84
J28	20.36
J19	---

Figure 3.4.4.3. 39 Total length of shark (mm) vs. integral value of each peak from FT-IR spectrum

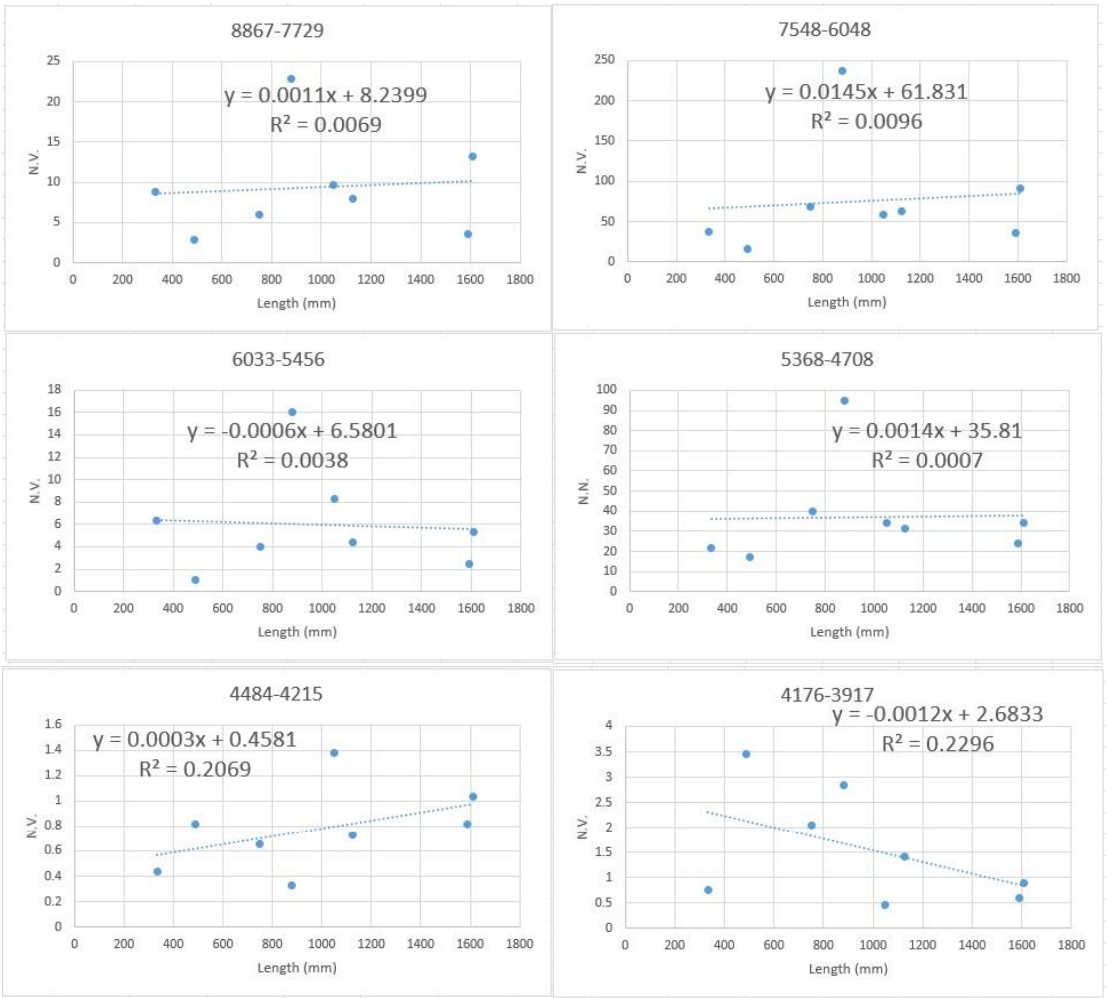

Figure 3.4.4.3. 40 Total length of shark (female) vs. diameter of shark vertebra

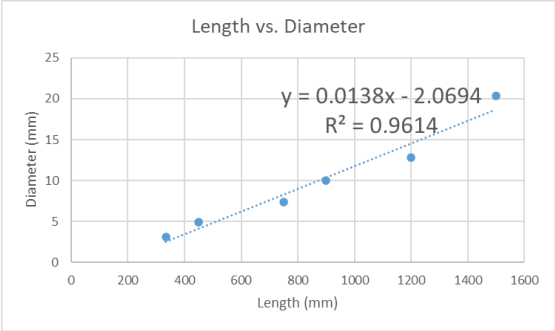

Figure 3.4.4.3. 41 Diameter of shark vertebra (mm) vs. integral value of each peak from FT-IR spectrum

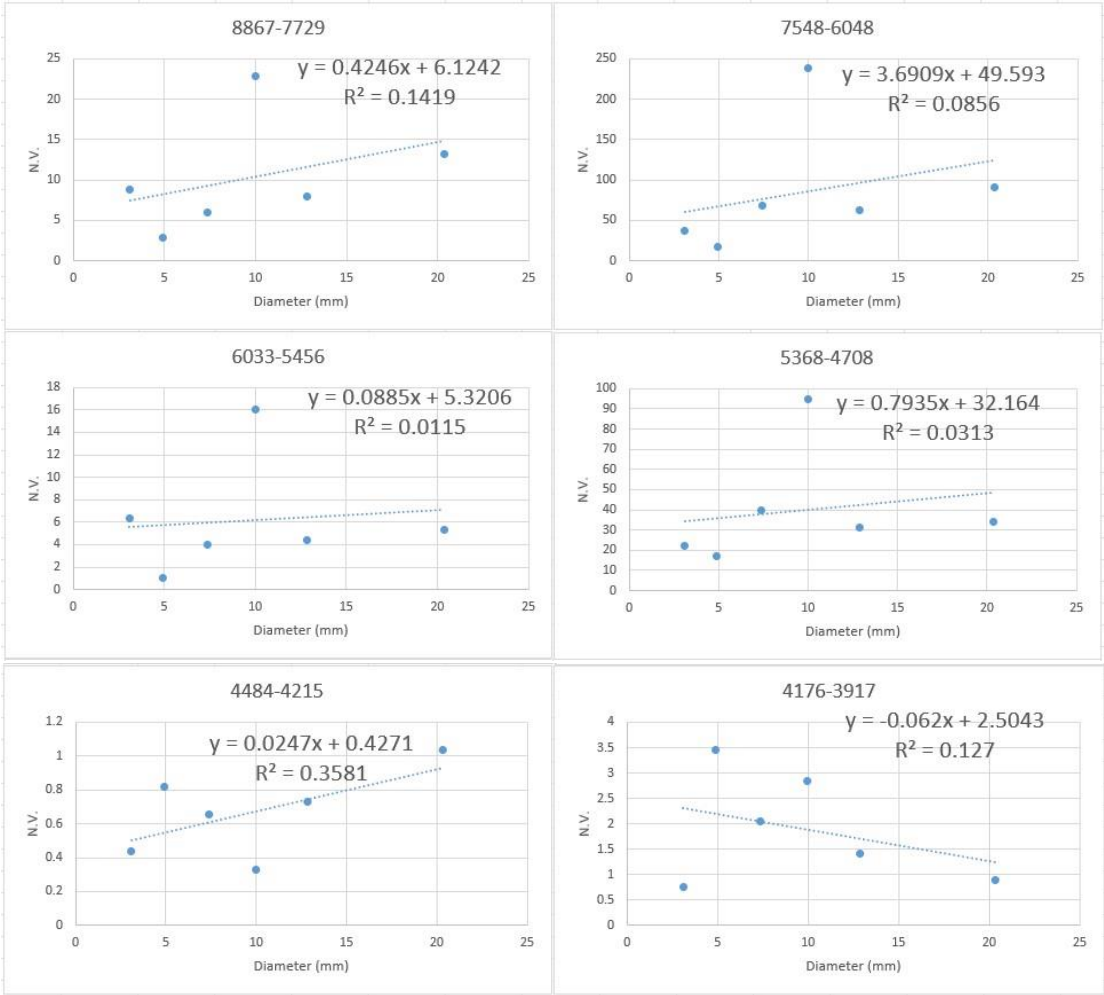

Table 3.4.4.3. 30 Total length and normalization Value (N.V.) of male samples. The measurement area was the center of the vertebral halves.

Sample (male)	Length (mm)	8867-7729 cm^{-1} N.V.	7548-6048 cm^{-1} N.V.	6033-5456 cm^{-1} N.V.	5368-4708 cm^{-1} N.V.	4708-4493 cm^{-1} N.V.	4484-4215 cm^{-1} N.V.	4176-3917 cm^{-1} N.V.
J17	1500	14.57835	84.28271	7.339257	35.08885	1	3.105008	1.579483
MF5	1350	2.835655	46.13092	4.150418	31.9415	1	0.415042	1.562674
SDSOE	1390	10.48816	51.07003	3.928939	32.79918	1	0.915551	1.488157
NWN3	1040	5.030612	31.95663	2.846939	110.5179	1	1.494898	1.640306
NWN8	907	6.654662	63.9717	11.5955	25.07203	1	0.77492	2.448875
NWN9	768	13.63613	137.0366	11.73298	53.01178	1	0.774869	2.137435
NWS1	600	9.241416	44.22854	6.434549	28.88627	1	4.766094	0.439914
AB3	440	6.275912	20.93796	1.705109	18.72336	1	0.737956	1.005839

Figure 3.4.4.3. 42 Total length of shark (mm) vs. integral value of each peak from FT-IR spectrum

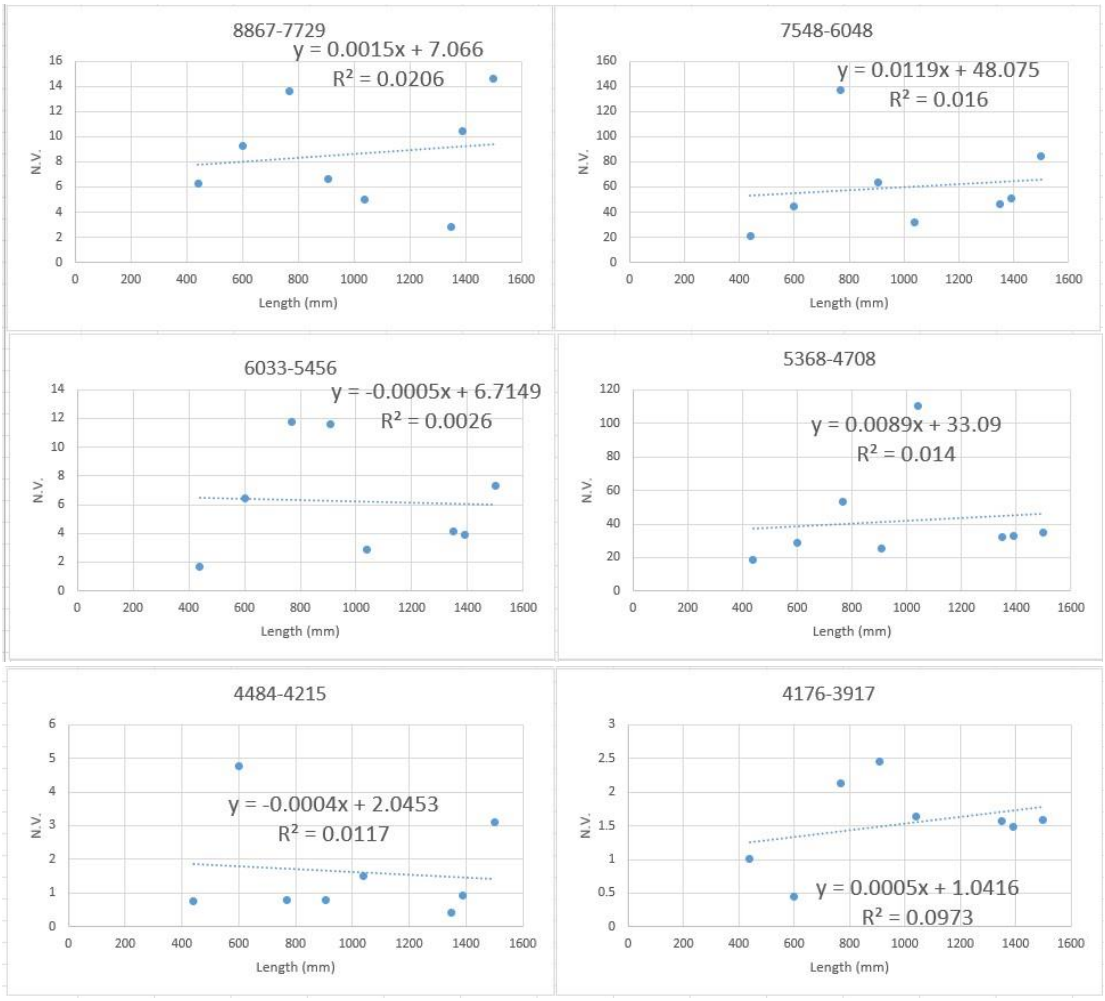

Figure 3.4.4.3. 43 Diameter of shark vertebra (mm) vs. integral value of each peak from FT-IR spectrum

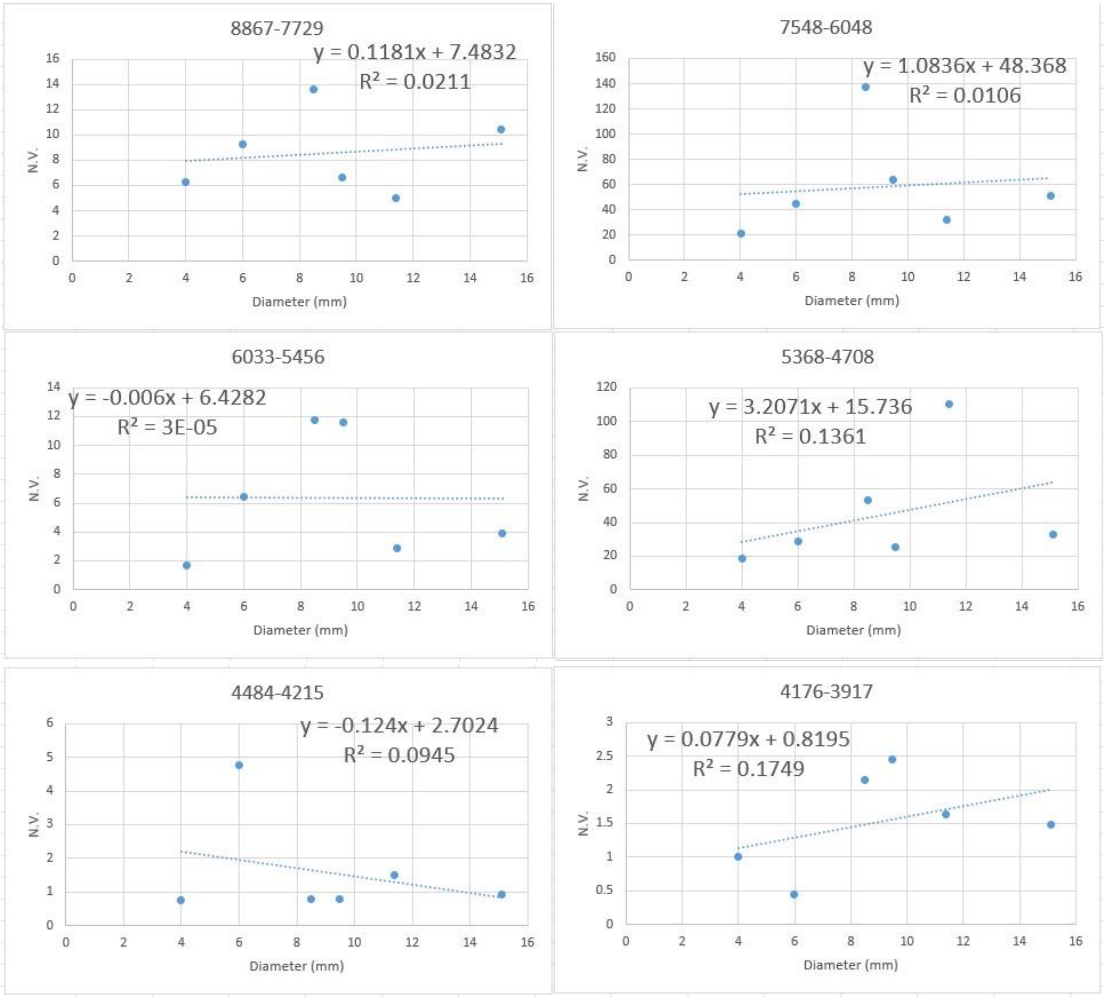

Table 3.4.4.3. 31 Total length and normalization Value (N.V.) of female samples. The measurement area was the center of the vertebral halves.

Sample (female)	Length (mm)	8867-7729 cm^{-1} N.V.	7548-6048 cm^{-1} N.V.	6033-5456 cm^{-1} N.V.	5368-4708 cm^{-1} N.V.	4708-4493 cm^{-1} N.V.	4484-4215 cm^{-1} N.V.	4176-3917 cm^{-1} N.V.
NWS12	334	14.46128	40.38886	9.797772	24.31978	1	4.597772	2.610585
AB27	490	3.257453	14.972	1.265583	21.5953	1	1.201445	1.905149
LG2	750	8.201705	52.86891	5.458198	21.82752	1	0.640422	0.048701
MK2	880	5.608743	37.1729	4.110048	17.55046	1	0.561983	0.749021
MF1	1050	10.09994	55.32724	3.530774	28.47471	1	1.184644	0.440585
MF8	1125	8.951049	48.78788	5.452214	23.85548	1	1.529138	1.934732
J28	1610	4.730599	61.60144	5.028825	32.78659	1	0.583703	0.718958
J19	1590	13.76594	100.0982	5.923469	40.8463	1	1.640944	1.803571

Figure 3.4.4.3. 44 Total length of shark (mm) vs. integral value of each peak from FT-IR spectrum

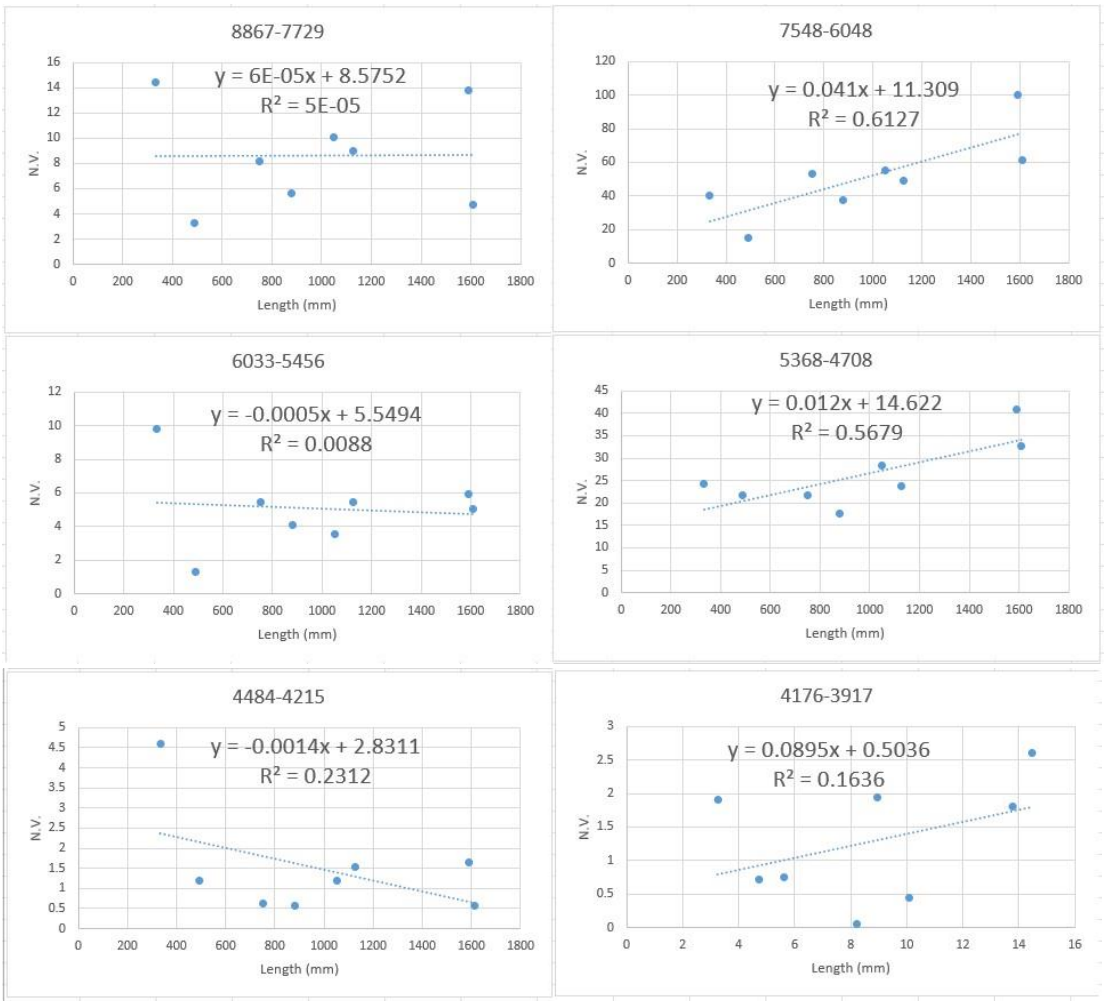

Figure 3.4.4.3. 45 Diameter of shark vertebra (mm) vs. integral value of each peak from FT-IR spectrum

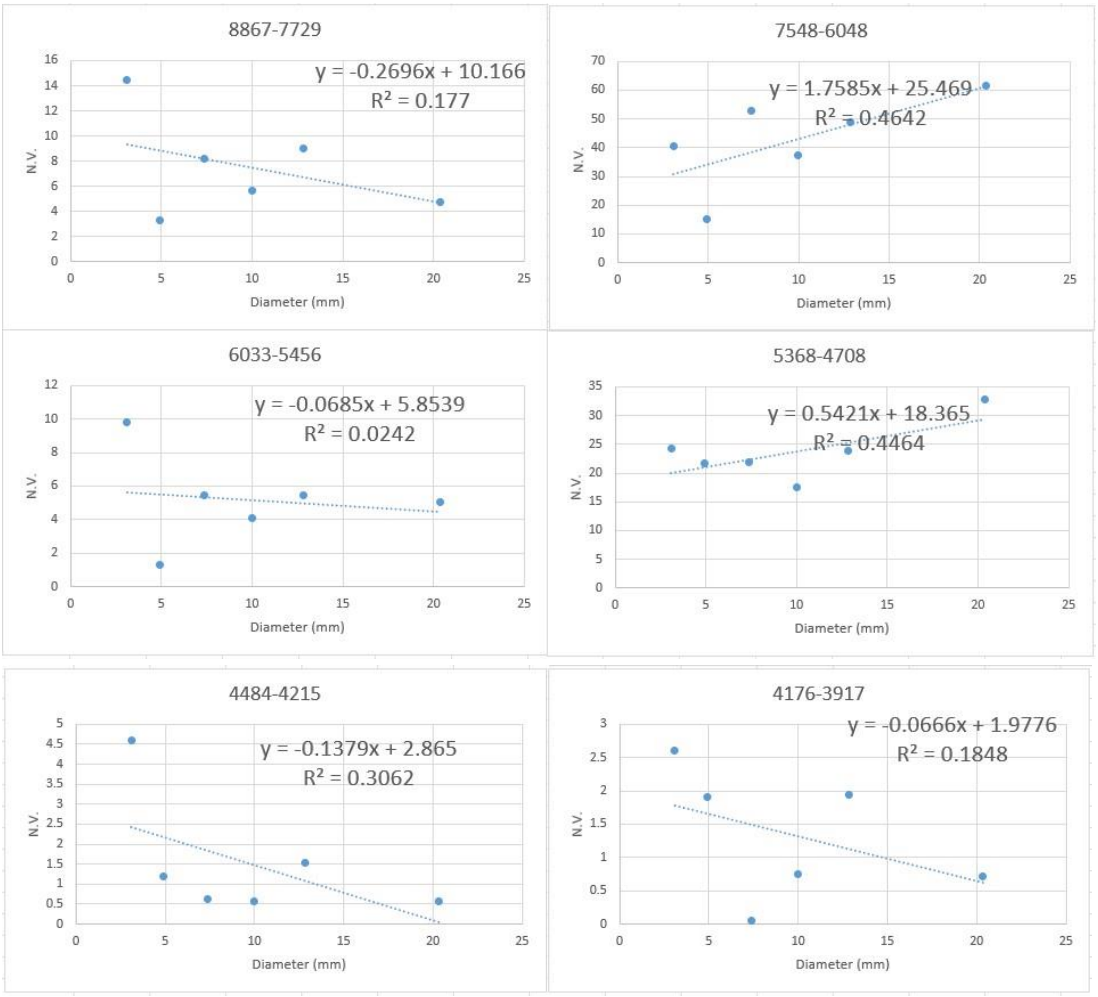

Table 3.4.4.3. 32 R^2 comparison of FTIR plots

Total Body Length vs. Integral value, without normalization								
			Water		Water	collagen		
Sex	Area	8867-7729 cm^{-1} N.V.	7548-6048 cm^{-1} N.V.	6033-5456 cm^{-1} N.V.	5368-4708 cm^{-1} N.V.	4708-4493 cm^{-1} N.V.	4484-4215 cm^{-1} N.V.	4176-3917 cm^{-1} N.V.
Male	Edge	0.2031	0.285	0.2371	0.2791	0.2877	0.0039	0.4178
Female	Edge	0.5354	0.7388	0.4544	0.6117	0.4221	0.5817	0.2134
Male	Center	0.3125	0.1612	0.0166	0.2314	0.157	0.3388	0.0551
Female	Center	0.3645	0.4015	0.2889	0.3604	0.3187	0.0566	0.2338
Total Length vs. Normalization value (The standard peak was the peak with largest integral value, not water peak or collagen peak)								
			Water		Water	collagen		
Sex	Area	8867-	7548-	6033-	5368-	4708-	4484-	4176-

		7729 cm^{-1} N.V.	6048 cm^{-1} N.V.	5456 cm^{-1} N.V.	4708 cm^{-1} N.V.	4493 cm^{-1} N.V.	4215 cm^{-1} N.V.	3917 cm^{-1} N.V.
Male	Edge	0.4872	0.0242	N	0.0061	0.2987	0.4998	0.1114
Female	Edge	0.0005	0.1297	N	0.0241	0.0627	0.5329	0.1817
Male	Center	0.0455	0.1031	N	0.0005	0.109	0.0883	0.0002
Female	Center	0.0109	0.4561	N	0.0135	0.1171	0.3064	0.1453

Table 3.4.4.3. 33 R^2 comparison of FTIR plots

Total Length vs. Normalization value (with collagen peak)								
			Water		Water	collagen		
Sex	Area	8867-7729 cm^{-1} N.V.	7548-6048 cm^{-1} N.V.	6033-5456 cm^{-1} N.V.	5368-4708 cm^{-1} N.V.	4708-4493 cm^{-1} N.V.	4484-4215 cm^{-1} N.V.	4176-3917 cm^{-1} N.V.
Male	Edge	0.0967	0.584	0.0837	0.6047	N	0.3189	0.0893
Female	Edge	0.0069	0.0096	0.0038	0.0007	N	0.2069	0.2296
Male	Center	0.0206	0.016	0.0026	0.014	N	0.0117	0.0973
Female	Center	5.00E-05	0.6127	0.0088	0.5679	N	0.2312	0.1636

Table 3.4.4.3. 34 R^2 comparison of FTIR plots

Diameter vs. Normalization value (with collagen peak)								
			Water		Water	collagen		
Sex	Area	8867-7729	7548-6048	6033-5456	5368-4708	4708-4493	4484-4215	4176-3917
Male	Edge	0.0683	0.8045	0.065	0.726	N	0.2202	0.0072
Female	Edge	0.1419	0.0856	0.0115	0.0313	N	0.3581	0.127
Male	Center	0.0211	0.0106	3.00E-05	0.1361	N	0.0945	0.1749
Female	Center	0.177	0.4642	0.0242	0.4464	N	0.3062	0.1848

3.4.4.4 Discussion

Part 1. Infrared Analysis

The wave number range of the near IR analysis is narrower than that of mid IR method, but unlike near -IR measurements, peaks from IR measurement can be assigned to specific chemical compounds. The vertebral centra is comprised of calcified cartilage, which consists of $Ca_{10}(PO_4)_6(OH)_2$ (calcium phosphate mineral

hydroxyapatite) and a matrix of proteins. According to the reference data (Bērziņa-Cimdiņa & Borodajenko, 2012), the PO_4^{3-} group appear at 460, 560–600, 960, 1020–1120, 1040, and 1000–1100 cm^{-1}. The two most intense peaks, 1004 and 555 cm^{-1}, in the vertebral spectra refer to the PO_4^{3-} function group.

Absorbance peaks were integrated, and the ratios of integrated peaks were required. The intensity of the absorbance relies on the applied pressure and measuring area, which vary because they are manually controlled. Hence, for one vertebrae sample, the intensity of certain peaks in each spectrum might be different, but the integral ratio of peaks should be similar among the spectra.

During the cutting process, RO water was used to prevent burning, which would have contaminated the vertebral samples. Samples were taken from the fridge and kept in the fume hood to reach room temperature. To eliminate the impurities, vertebral halves and sections were rinsed with MILLI-Q water and immersed in MILLI-Q water for a few seconds. The wet samples were then left in the fume hood to air dry for around 2 hr. Before the IR analysis, the samples were weighed (M_1). Next, the samples were placed in a vacuum chamber under low pressure for overnight drying. The weight of the dried samples was recorded (M_2), and the IR spectra of the vertebral halves were taken. Later, the samples were replaced in the vacuum chamber and the weight of the vertebrae was recorded after 4 hr to ensure that the overnight vacuum samples were completely dry. This step was taken to double-check that the overnight vacuum samples were bone dry.

According to the data, the weight differences between M_1 and M_2 for SWL8-5 and SWL8-6 were 0.2597 and 0.0852 g, respectively, indicating that both samples were dried. The IR spectra further support this, as they showed that vertebrae absorb MILLI-Q water during cleaning, and the absorbance intensity corresponding to water absorption in the range of 3500–3000 cm^{-1} is higher in the wet sample spectra. Additionally, two CH peaks occurred in the range between 2900 to 2800 cm^{-1} in the wet vertebral spectra rather than the dry sample spectra. Moreover, it is important to be aware that the drying process of the sample can affect the IR analysis.

The ΔMs of SWL8-5 and SWL8-6 were 0.0081 and 0.0029 g, respectively, which represents a very small difference in mass, suggesting that after the overnight vacuum treatment vertebrae were completely dried. Furthermore, the spectra of SWL8-5 and SWL8-6 showed peaks around 1000, 550, and 470 cm^{-1} that were signed as PO_4^{3-} from the hydroxyapatite compound. The peak around 470 cm^{-1} became more obvious once the vertebral samples were dried.

The ratio of PO_4^{3-} in different areas (A, B, and C) of the two vertebral samples were calculated, and the average ratios were also derived. The ratio of the individual areas or the average ratio of the vertebral halves was found to be larger in SWL8-5 than in SWL8-6. It is worth noting that the diameter of SWL8-5 is larger than SWL8-6, suggesting that there is a direct relationship between the PO_4^{3-} peak ratio and the diameter of the vertebrae. The surface of the SWL8-5 half was uneven, hence, only noise was captured in Area A under both dry and wet conditions. Signals of CO_3^{2-} ions that substitute for phosphate ions can appear in the range of 1650 to 870 cm^{-1}. Phosphate groups in hydroxyapatite are usually substituted with carbonate due to calcium deficiency in biological hydroxyapatite.

Table 3.4.4.3. 35 Mass and mass changes of samples

Sample	Diameter (mm)	M1(g)	M2(g)	ΔM(g)	M3(g)	ΔM'(g)
SWL8-5	20.0	1.8120	1.5523	0.2597	1.5442	0.0081
SWL8-6	12.0	0.4897	0.4035	0.0852	0.4006	0.0029

Table 3.4.4.3. 36 Intensity of PO_4^{3-} peak of sample SWL8-6

Area C			
Peak PO_4^{3-}	Wavelength (nm)	Abs. intensity	Normalization
1	1007	0.09374	0.84
2	556	0.11125	1
3	468	0.06842	0.61
Area B			
Peak PO_4^{3-}	Wavelength (nm)	Abs. intensity	Normalization
1	1005	0.13826	0.84

2	551	0.16485	1.00
3	466	0.12002	0.73
Area A			
Peak PO_4^{3-}	Wavelength (nm)	Abs. intensity	Normalization
1	999	0.06212	0.78
2	550	0.07964	1.00
3	467	0.05902	0.74

Average ratio P1: P2: P3 = 0.82: 1: 0.69

Table 3.4.4.3. 37 Intensity of PO_4^{3-} peak of sample SWL8-5

Area C			
Peak	Wavelength (nm)	Abs. intensity	Normalization
1	1007	0.08702	0.90
2	559	0.09657	1.00
3	469	0.06920	0.72
Area B			
Peak	Wavelength (nm)	Abs. intensity	Normalization
1	1005	0.02282	0.75
2	551	0.03038	1.00
3	470	0.02487	0.82

Average ratio P1: P2: P3 = 0.83: 1: 0.77

For the analysis of the formal sample data set, only the center and edge areas of the vertebrae halves were considered. The same integral methods were used as before, where 10 peak regions were integrated. The dominant peak region selected was 1180.9 -887.6 cm^{-1}, as it had the largest intensity and may be related to the PO_4^{3-} functional group through hydroxyapatite. Because the shark's total body length (TBL) and vertebrae diameter are two factors that are strongly correlated with the age of the shark, they were used to plot different graphs with integration values to test whether IR spectra could be used to determine the shark's age.

Female and male sharks have different growth rates, and female sharks are usually larger than male sharks but with slower growth rates. However, the school shark species is an exception, which means females and males have similar growth rates based on the length at age data. The mature year range is 12–17 years for males at 125–135 cm and

13–15 years for females at 140 cm (Francis & Mulligan, 1998). Although their growth rates are the same, female and male samples still need to be analyzed separately due to different levels of maturity, body length, and other elements.

It appears that all the peak spectra had the same shape pattern. It is not possible to determine the metal ion composition of the vertebrae using IR. However, it was important to keep the sample dry during the measurement because the spectra of dry and wet samples were found to be distinct.

As previously stated, the total body length (TBL) and diameter of shark vertebrae (DOV) are two parameters that correspond to shark aging. If a close relationship between TBL or DOV and peak intensity can be found, the spectrum can be used to determine the shark's age. There are also open questions around the growth rate at maturity where the sharks stop growing in length, but may increase in girth. The top edge of the corpus calcareum of the male vertebrae was first measured, and two variables TBL and DOV were used to plot graphs with a normalized intensity value (NV) of nine peaks. The TBL versus NV plots showed that the largest coefficient of determination, R^2, was 0.2638 at the peak range of 1510.77–1290.8 cm^{-1}. Among the DOV versus NV graphs, the peak area of 1718.5 to 1596.3 cm^{-1} was found to be more correlated with vertebrae size, in which R^2 was 0.2937. However, the R^2 value for both kinds of plots was low, thus, it can be concluded that the IR spectrum of the top edge area of the vertebrae cannot independently determine age.

For the female vertebrae samples, in both the length and diameter plot series, peak regions of 1718.5–1596.3 and 1596.3–1510.77 cm^{-1} were found to be highly correlated to length and diameter, with R^2 values above 0.8. However, the PO_4^{3-} group in biological HAp is generally substituted with a carbonate due to calcium deficiency, hence, these two peak regions might refer to the absorbed CO_3^{2-} groups that substitute for phosphate ions. Additionally, the TBL graphs showed that peak regions 789.8–618.8, 618.8–569.9, and 569.9–484.36 cm^{-1} were moderately related to body length because the R^2 values were around 0.5. However, the DOV graphs did not show the same results.

The center of the corpus calcareum of the male vertebrae was also examined, and

no obvious linear pattern was found in the TBL plots. However, the diameter was found to have some correlation to the peak region 1290.8–1180.9 cm^{-1}, based on an R^2 value of 0.4342 from the graph. In contrast, the TBL graphs of female corpus calcareum centers showed different patterns, in which regions 1290.8–1180.9, 569.9–484.6, and 484.36–411.05 cm^{-1} were all correlated with TBL. The R^2 values from the DOV were much higher, and most of the regions showed a linear relationship with vertebrae size.

In summary, it appears that peak regions from female shark samples are more likely to be correlated with either body length or vertebrae size, suggesting a possible relationship with shark aging. Surprisingly, no obvious linear relationship was discovered through plotting results for either male or female sharks, which means that peaks from the IR spectrum are not suitable for determining the age of New Zealand school shark species.

Part 2. Fourier Transform-IR

Near-infrared spectroscopy (NIRS) is a secondary technique that needs to be calibrated with a primary method to establish a reliable model (Rigby et al., 2016). Articles on the NIRS analysis of vertebrae determination emphasize that it is difficult to discern the relationship between the spectral areas and a specific chemical compound. Rigby has denied the possibility of finding correlations between peaks and specific chemical molecules. It is possible that hydroxyapatite (HAp), the essential growth chemical compound in the cartilage of shark vertebrae, may be related to the chemical changes, but the other components in the organic matrix were still not clear. In NIR analysis, CO_3^{2-} and OH are strongly absorbing groups, which makes the calcium hydroxyapatite detectable in NIR measurement. For the NIRS analysis, three main spectral regions, which correlate with various groups, C=C, CH, -CH_3, -CH_2 -NH_2, -$CONH_2$, and -CONH, were found between 9200 and 4000 cm-1. The absorbance intensity of other chemical components, such as water, proteoglycan, and collagen, can also be captured by the NIR spectra.

The second derivative, Savitzky-Golay, has been used in other research to smooth the raw spectra (Ailavajhala et al., 2020). However, in this study, after calculating the

first or second derivative, no spectral peaks were obtained, hence, no further analysis could be conducted.

Regarding the molecules found in the spectra of the vertebrae, phosphate mineral and hydroxyapatite are commonly detected, as mineralization increases with age in many chondrichthyans. Of the dry shark vertebral samples, hydroxyapatite is reported to account for 39% to 55%, water accounts for 26% to 53%, and collagen accounts for 17% to 27% (Rigby et al., 2018). Accordingly, using pure hydroxyapatite as a reference spectrum can be helpful in FT-IR analysis (Rigby et al., 2016). The opaque and translucent bands with various ratios of the mineral and organic matrix are used for age determination. Collagen fibers, water, and proteoglycan are also present in the range of 5400 to 3800 cm^{-1}. However, it is important to note that a single portion of the spectrum cannot be used to determine age by itself.

The size of the sample is also important, as the NIRS spectra are correlated with both age- and size-related chemical changes in the structure. Completed dry samples may yield more accurate analysis results.

It is important to highlight that while non-destructive, vertebrae halves were used in the mid IR method, but thin sections were used for the NIR measurements as the NIR measurements were made in transmission mode and too thick a sample led to too much light lost from scattering, and hence insufficient transmitted light to make a reliable measurement . The FT-IR spectrum of biological hydroxyapatite contains both loosely and tightly bound water. The water absorption that appeared at 7000 cm^{-1} was proven to be inversely related to donor age. To clarify, the tissue mineral density of female donors is directly correlated with age, and tissue mineral density increases as collagen cross-linking bound water increases and collagen bound water decreases (Ailavajhala et al., 2020). The information about loosely and tightly bound water is helpful in understanding the relationship between water and collagen in this study.

The spectral peaks of biological HAp at 5200 and 7000 cm^{-1} were found to be correlated to loosely bound water, while the peak at 4608 cm^{-1} was assigned as the collagen peak. At 5200 cm^{-1}, there is tightly bound water. Loosely bound water is

associated with the water bound to the surface of the collagen and mineral compounds, which can be removed through an evaporative process. Tightly bound water refers to water that is within the collagen fiber or the mineral complex, which is harder to remove (Ailavajhala et al., 2020).

Before any statistical processes, the raw spectra were examined by stacking the spectra of different samples together along with the peak at 5400 cm^{-1}, which served as a rough normalization. In the addition spectrum of the male sharks (Figure 3.4.4.3.24), patterns around the water peak of 7000–6000 cm^{-1} showed that this peak was inversely correlated with the TBL of the samples. The peak at 7000–6000 cm^{-1} of J17 (TBL = 1500 mm) had the lowest absorbance, while that of AB3 (TBL= 440 mm) had the highest absorbance. However, when examining the spectra of the edge area, it was found that J17 had the largest absorbance and AB3 had the lowest absorbance at the same peak. Additionally, in the edge area and center area spectra of females, the relationship between the absorbance at the 7000–6000 cm^{-1} peak and TBL was unclear. It is difficult to determine the true relationship between the 7000–6000 cm^{-1} peak and vertebrae size by only examining the raw data, hence, integration processes were applied.

There was a direct relationship between the TBL and the DOV for both males (R^2 = 0.9955) and females (R^2 = 0.9614). The NZ school sharks grew in portion of the length of the body. Little notable information was shown by the plots of TBL versus IV peaks from the male vertebral top edge spectra. The R^2 value for the 4176–3917 cm^{-1} peak region from the vertebral edge was 0.4178, indicating a direct relationship with TBL. The R^2 values for the 8867–7729 and 4484–4215 cm^{-1} peak regions from the vertebral center spectra were both around 0.3 and believed to be indirectly related to TBL. We assumed that normalization methods could help us find more details. The water peak at 6033–5456 cm^{-1} was used as the standard peak. The R^2 values for the 8867–7729 cm^{-1} and 4484–4215 cm^{-1} peak regions from the edge spectra were 0.4872 and 0.4998, respectively, indicating an indirect relationship with TBL. None of the peak regions from the vertebral center area were closely associated with the size of the shark.

All the peak regions, except for the 4176–3917 cm^{-1} peak of TBL versus IV of the female vertebral edge, were directly related to TBL since all the R^2 values were around and above 0.5. Peak regions from the IV of the female vertebral center were less correlated with TBL, and the 7548–6048 cm^{-1} peak region plot had the largest R^2 value of 0.4015. The R^2 values from the normalization plots became much smaller, and the 4708–4493 cm^{-1} peak region from the edge spectra was the only region directly related to TBL with an R^2 value of 0.5392. Other peak areas did not show any signs of being associated with TBL. Among the vertebral center graphs, the 7548–6048 cm^{-1} peak region graph had the highest R^2 value of 0.4561, and other peak regions were not closely related to TBL.

Rather than using the water peak region as the standard normalization, the collagen region 4708–4493 cm^{-1} was used for the normalization process, which was believed to produce more important details. The R^2 values for the peak regions NV (normalization value) of male vertebra edge versus TBL plots were 0.584 and 0.6074 for 7548–6048 and 5368–4708 cm^{-1}, respectively. The 7548–6048 cm^{-1} peak region had an R^2 value of 0.8045, and the 5368–4708 cm^{-1} peak region had an R^2 value of 0.726, showing a closer direct linear relationship at the NV (male vertebra center) versus DOV plots. For the vertebral edge of female samples, no obvious relationship pattern was found between peak regions and TBL or vertebra diameter.

Linear trendlines from the TBL and DOV graphs of the male vertebral center area were flat, and no particular trend patterns were discovered. In the TBL graphs of the female vertebral center, only two water peak regions, 7548–6048 (R^2 = 0.6127) and 5368–4708 cm^{-1} (R^2 = 0.5679), showed obvious linear trends. While the R^2 values of these two peak regions in the DOV plots were smaller, a direct relationship between the vertebral size and the IV of the peak areas was still evident.

In summary, the peak regions from the female vertebral top edges showed a clear linear association with the length of the sharks. However, normalization processes did not generate better results, and peak regions showed a less consistent relationship between the NV and body length or vertebra diameter. Water peak regions from the

edge of male vertebrae and the center of female vertebrae corresponded to the size of the sample. Hence, it is not clear that peak areas are closely related to the shark's size. Therefore, FT-IR is not a reliable method for identifying the age of NZ school sharks.

This is in contrast to studies elsewhere, which may reflect differences in school shark behaviour compared to those used for the other studies. Unfortunately, the results obtained here indicate that mineralization appears to reflect environmental conditions at the time the vertebrae are growing rather than long term cumulative mineralization effects.

3.4.5 Fluorescence spectrophotometry (FS)

3.4.5.1 Introduction

Fluorescence spectrophotometry (FS) is a highly sensitive and selective process that collects the fluorescence emissions of a sample excited by a particular wavelength of light. FS is popular in various research fields such as biology, chemistry, and biochemistry. Proteins, amino acids, and even small molecules can be measured and quantified using FS. Luciano and colleagues reviewed the application of FS in biological tissue, such as in sharks' cartilage and dental tissues as well as human tissue. Age can be identified by analyzing the structure and composition of the vertebrae. Hydroxyapatite crystals and collagen are generated and remodeled during a shark's lifetime (Tovar-Ávila et al., 2009). Therefore, we assume that FS can be applied to study the structural and chemical properties of vertebrae, which can help us analyze shark growth and aging. There is insufficient information about this method in the shark age determination study, but logically, the method is worth trying. In this method we are trying to image the growth bands in order to count them. Under normal illumination the age bands can be indistinct, so this approach was trialed in an attempt to enhance the contrast. The fluorescent probes used either could potentially substitute for Ca^{2+} (in the case of Samarium) or bind to the metal ions (benzoyl acid, naphthylamide sulfonate).

3.4.5.2 Method

Four Vertebral samples were immersed in different solutions: samarium (S), a

mixture of samarium and methanol (SM), a solution consisting of samarium and benzoyl acid (SB), and naphthylamide sulfonate (NS), respectively. The wavelength fluorescing range of samarium oxide is 230–560 nm, and that of 4-amino-1,8-naphthalimide is between 460 nm to 600 nm according to the reference. The vertebral sections were placed in the fluorescence spectrometer (Shimadzu RF-6000). Two dimensional scans were performed. The excitation wavelength (Ex) scan started from 200.0 and ended at 600 nm, whereas the emission wavelength (Em) was from 250 to 800 nm. The data interval was 5.0 nm for Ex and 2.0 nm for Em. The scan speed was 12,000 nm/min, scan sensitivity was low, and the bandwidths of both Ex and Em were 3.0 nm.

3.4.5.3 Result & Discussion

Nothing was found in either of the vertebral spectra, although the sample emitted a green light under UV light at 365 nm. Lanthanide solutions of samarium and GSP21(a naphthalimide complex solution) were also analyzed by FS with the same settings, but there was no useful information on the spectrum.

To improve the fluorescence of the stained vertebra, we decided to place sample (S) in the GSP21 solution. The (S) sample was placed in the lanthanide and GSP21 for 5 mins, then rinsed with a small amount of MILLI-Q water, and finally submerged in MILLI-Q water for approximately 10 minutes. A paper towel was used to dry the vertebral section a little, and then the sample was allowed to dry completely and labeled. After the vertebral section was completely dried, it was observed under UV light at 365 nm, and the sample was luminous green. Therefore, (S) was examined through FS to obtain the intensity information, but unfortunately, no noticeable result was identified.

3.4.6 Staining

3.4.6.1 Introduction

Staining methods are commonly used in biology, botany, and other scientific fields due to their low costs and simple processes (Pérez-Rojas et al., 2020). Staining techniques highlight the target component or structure in tissue samples, making them

easily visualized. Since 1979, staining approaches have been employed in elasmobranch research. However, Goldman pointed out that each staining technique produces results specific to the species, so there is no standard procedure for all elasmobranch species (Pérez-Rojas et al., 2020). Alizarin Red S, crystal violet, and silver nitrate are popular choices for staining. Nuri mentioned that silver nitrate is the most efficient method for staining R. clavata, R. miraletus, and R. rhinobatos, but it is not a suitable approach for R. asterias, T. marmorata, or G. altavela. Hammerhead, lemon, smooth dogfish, blue, and sandbar sharks have been stained using Alizarin Red S, cobalt nitrate, and silver nitrate (Hoenig & Brown, 1988). Durate stated that cobalt nitrate is an appropriate staining method for contrasting concentric increments in the whole vertebrae of a school shark, Galeorhinus galeus, and modified Hoenig's procedure (Duarte et al., 2001).

In 1988, Hoenig et al. presented a simple and effective method of vertebrae staining to identify the ages of hammerhead sharks, lemon sharks, dogfish, blue sharks, and sandbar sharks. Elasmobranch vertebrae contained abundant calcium, so the calcium phosphate in vertebrae could be stained. Hoenig et al. stated that better results were achieved staining cobalt nitrate compared to staining Alizarin Red S and silver nitrate. Silver nitrate staining technique decreased the band resolution due to the generation of silver grain. With the Alizarin Red S staining method, much longer immersion time was required (Hoenig & Brown, 1988).

In 2001, Pedro et al. evaluated different methods of chemically staining shark vertebrae. Modified cobalt staining, which can produce consistent replicate readings and better optical resolutions of the age bands, was considered the most efficient way to determine the ages of school sharks (Galeorhinus galeus) from Azores (Duarte et al., 2001).

Four techniques, Alizarin Red S staining, silver nitrate staining, cobalt nitrate staining, and deep-coned vertebrae, were carried out in the lab (Duarte et al., 2001). Unlike the deep-coned method, other methods are highly related to the calcium salt in the vertebrae, which improved the contrast in shark bands on the edge of vertebrae. The

cobalt nitrate method from Hoenig was adjusted to analyze the school shark samples since the original technique did not work properly. The new cobalt nitrate method was not tested with other shark species, so further analysis is required to determine other sharks' ages using their vertebrae. The deep-coned vertebrae method was not able to generate countable rings in the school shark vertebrae because the corpus calcareum is rich in minerals.

The vertebrae were placed in a 5% cobalt nitrate solution for a few minutes until the bands turned pink, and then the samples were rinsed with distilled water. Then, samples were dried with paper towels before being immersed in a 10% solution of hypochlorite for several seconds. Once the vertebrae rings became darker, they were cleaned with distilled water again. Stained samples were stored in a 70% ethanol solution (Duarte et al., 2001). Normally, from the center to the edge of the vertebrae, the distance between rings decreased, which was apparent in the results (Hoenig & Brown, 1988).

Our study subjects are school sharks from the South Pacific Ocean near New Zealand, so J. M. Hoenig's nitrate procedure may not work for our experiment. Pedro's modified protocol is more suitable for our study because Pedro's research used the same shark species as our research, although the sharks in Pedro's research were not captured near New Zealand.

In 2020, Pérez-Rojas et al. used various staining agents and methods, such as Alizarin Red S, methylene blue, crystal violet, basic fuchsin, acid fuchsin, Bismarck brown Y, light green, silver nitrate, and Dahl staining, to visualize the age bands in the vertebrae of batoids and sharks (Alopias pelagicus, Carcharhinus falciformis, Sphyrna lewini, Sphyrna corona, and Mustelus lunulatus) (Pérez-Rojas et al., 2020). The sexes and body lengths of the sharks captured from the Colombian Pacific were recorded since the age bands were related to the individuals' sizes. The thickness of the vertebral sections greatly impacted the visualization of the growth bands. According to the data, Bismarck brown Y was the best analyzing method for Alopiac pelagicus, whereas crystal violet provided the best visualized results for Carcharhinus falciformis and

Sphyrna corona sharks. For the determination of Mustelus lunulatus's growth bands, light green staining was the most suitable option (Pérez-Rojas et al., 2020).

Their results confirmed that the staining process is related to species. It is worth trying different staining methods to choose the best staining option for New Zealand's school sharks.

3.4.6.2 Method

Cobalt(II) nitrate at a concentration of 3.6% was obtained by dissolving 0.6122 g of 99% pure cobalt(II) nitrate hexahydrate (ARCROS ORGANICS CAS:10026-22-9) in 20 mL of RO water. The vertebral samples from school sharks (SWL8-2, SWL8-3, SWS5-C4, SWS5-C6, SWL8-1, SWS5-D1 part1, SWS5-D1 part2) were then immersed in the cobalt(II) nitrate solution for several minutes until the bands became pink and visible. The stained samples were rinsed with RO water and then transferred to 10% sodium hypochlorite (diluted with 13.5% sodium hypochlorite [ECOCHEM], with RO water). The vertebral rings were darkened and contrasted, after which the samples were transferred to RO water to terminate the reaction. Damage to the structure of the sample's surface was caused when SWL8-1 was immersed in bleach without being first rinsed with water.

The stained samples were then observed under the direct and reflected light of the microscope to identify the visible rings. Indirect light from above the sample was used, whereas the direct light was under the sample stage. Based on the result images, visible growth bands could only be detected when the sample was immersed in the cobalt nitrate solution for a sufficient time, and when no saw marks were present on the sample.

3.4.6.3 Result

Seven thin vertebral sections were stained with the cobalt nitrate solution by following the procedure mentioned above. Stained sections were placed on a glass slide and observed under indirect and direct light using a microscope (OPTIKA, MICROSCOPES, ITALY). Photos of sections were captured using an iPhone 12.

Table 3.4.6.3. 1 Immersion time of vertebral samples

Sample	In cobalt nitrate (time, s)	In bleach (time, s)
SWL8-2	158	10
SWL8-3	355	52
SWS5-C4	570	13
SWS5-C6	420	4.0
SWL8-1	770	---
SWS5-D1 part1	454	30
SWS5-D1 part2	438	60

Figure 3.4.6.3. 1 Sample SWL8-2 Indirect light: The immersion time was not long enough, so no visible mark at the edge of the shark vertebra appeared.

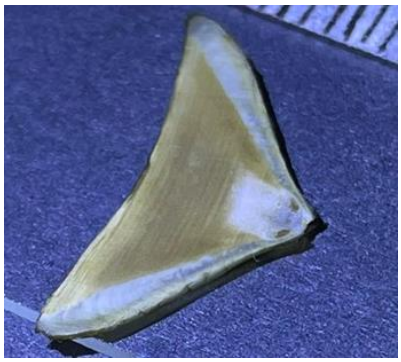

Figure 3.4.6.3. 2 Sample SWS5-D1, part 1. Indirect light: Both growth marks and saw marks were shown.

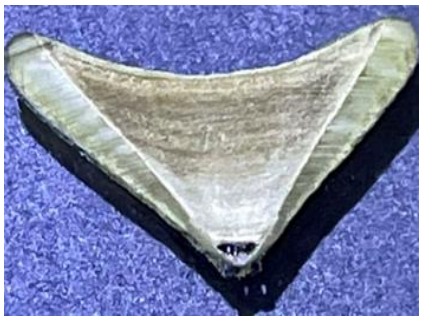

Figure 3.4.6.3. 3 Sample SWS5-D1, part 2

a). Direct light: Both growth marks and saw marks were shown.

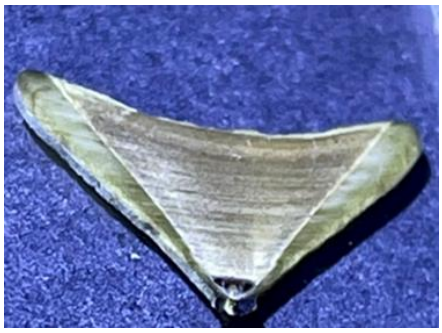

b). Indirect light: Image was too dark, and both growth marks and saw marks were shown.

3.4.6.4 Discussion

It was difficult to observe stain marks on the corpus calcareum of cobalt nitrate stained vertebral sample SWL8-2 due to insufficient immersion time in the solution. Therefore, one of the crucial factors in the staining method is the immersion time, which depends on the thickness and size of the sample. Thinner and larger samples require longer soaking durations, typically ranging from 7 to 10 minutes for sections from small vertebrae and above 10 min for large vertebral samples. Two parts of sample SWS5-D1 were immersed in the cobalt nitrate solution for long enough for the rings to be contrasted. However, both the growth bands and saw marks were emphasized, indicating the importance of the vertebral cutting position. It can be challenging to differentiate between ring and saw marks when they are at the same position, leading to false counting. Therefore, vertebral samples should be sagittally sectioned, following

the trend in most shark aging studies (Geraghty et al., 2012). Sections cannot be cut dorsoventrally through the center of the vertebra. Infant and juvenile school shark samples of smaller sizes are less difficult to stain because they have fewer growth rings and larger distances between bands. However, as body size increases, the spacing between growth bands towards the edge of the centra declines, and narrowly spaced bands accumulate around the outer region of the corpus calcareum (Duarte et al., 2001). Counting the vertebrae in adult sharks is a challenge due to the narrow spacing between growth bands and represents a common issue for long-lived specimens (Cailliet et al., 1983). School sharks are one of the elasmobranchs characterized by longevity and slow growth. According to Duarte's experimental results, the maximum age counted age is 11, at which the total body length (TBL) of sharks is around 150 cm. It is questionable whether the staining method can accurately determine the ages of sharks that are older than 11 years or longer than 150 cm TBL.

The microscope method faced a similar issue to the cobalt nitrate approach in that it was difficult to visualize the growth bands around the peripheral region in the large vertebral samples. As a result, for more precise evaluation of the ages of large sharks, more complicated techniques such as X-ray micro CT, or potentially laser ablation, are required.

Based on our observations, the lanthanide staining method did not highlight the growth bands in the vertebral sample. Under UV light, not only the bands, but also the entire vertebral sample stained with GSP21 turned fluorescent green. The stained samples were further analyzed through the fluorescence spectrum, but the band contrasts could not be visualized. We assumed that the bands and the rest of the vertebra would show different intensities on the fluorescence spectrum, but there were no obvious changes in the fluorescence intensity along the emission wavelength exhibited. Consequently, the lanthanide staining method did not work as a way to determine the age of school sharks from New Zealand.

3.4.7 Light Micoscopy

3.4.7.1 Introduction

Modern microscopes usually have an integrated light source. Several common kinds of light sources are used in microscopy, such as halogen lamps, incandescent lamps, arc lamps, and light-emitting diodes (LEDs). Incandescent lamps were commonly used in the past, but they have mostly been replaced by halogen lamps, which offer brighter and more consistent illumination. LEDs have become popular because of their high energy efficiency and low heat generation, making them an environmentally friendly choice. Illuminating samples using a microscope light produces precise, high-resolution images. Light transmitted by the sample under the microscope can in principle be used to examine the elasmobranch vertebrae.

The age and growth characteristics of shark species were studied, usually because of overfishing. The whole vertebral samples of Mustelus lenticulatus sharks from New Zealand were placed under oblique light to visualize the growth bands, and the bands could be visualized through both direct and indirect light (Francis & Maolagáin, 2000). Corsso has analyzed the vertebrae of R. lalandii and R. porosus sharks from the Atlantic (Corsso et al., 2021), and Bishop et al. have studied the characteristics of the mako shark (Isurus oxyrinchus) from New Zealand. They did not use the whole vertebrae to carry out the analysis directly. In Corsso's and Bishop's studies, vertebral centrum samples were sliced using an Isomet saw combined with diamond blades along the mid-sagittal axis into 0.30–0.35 mm and 0.6 mm sections, respectively. The fine-grained 0.6 mm sections were used to make the retention of the vertebral focus possible, which is vital for precisely measuring the birth band radius and the vertebral radius (Bishop et al., 2006). Light is easier to transmit with thin sections, so in our research, we will cut vertebrae into thin sections when using a microscope with a fiber-optic light.

To increase the contrast of the growth bands, vertebral sections were put into mineral oil immediately after they were cut (Corsso et al., 2021). Francis has stated that the bleaching process improves the contrast of the growth increments. Similarly, samples from Corsso's experiment were observed under a microscope with both direct

and indirect light, and images were obtained using a digital camera. However, Bishop only applied reflected light to the samples immersed in 70% ethanol and placed on a black background.

A band pair consists of one light band and one dark band. To determine the ages of the targets, each band pair was hypothesized to represent one year of growth. Therefore, only the translucent bands were counted to accurately estimate the sharks' ages (Bishop et al., 2006). Previous research has confirmed that two readers are required, so our research will include two people to determine the sharks' ages using the traditional method. The index of average percentage error was utilized to determine the precision of the age calculations between the first and second reads to assess the accuracy of the process (Corsso et al., 2021). Two readers independently counted the growth bands from the vertebral photos, and their results were compared. The primary reader was trained by an experienced professional, and the second reader was taught by the primary reader. The primary reader counted each sample twice, and the second reader counted only once. In the event of a discrepancy of three or more years between the readers' initial counts, they re-read the samples to ensure accuracy (Bishop et al., 2006).

Statistical methods are crucial to the data analysis and the development of the age estimation model. Analysis of covariance (ANCOVA) was used to analyze the differences in shark growth, and the relationship between the growth rate and body length was investigated through linear regressions (Corsso et al., 2021). Moreover, Bishop has used average precent error and coefficient of variation to measure precision. Francis has mentioned that the Von Bertalanffy growth model was also applied in this research to generate the growth curves. The results showed that the total length of a shark is highly correlated with the shark's estimated age.

Ultraviolet (UV) radiation is a subset of the electromagnetic spectrum, and its wavelength is shorter than that of visible light but longer than that of X-ray radiation. UV radiation is applied in the fields of photography, fluorescent dyes, and forensics. In chemistry, UV radiation is often used with a spectrofluorometer, where the sample is

excited by UV light and the fluorescence is detected. In biological research, UV fluorescence is commonly employed to quantify nucleic acids and proteins. Additionally, in environmental chemistry, UV radiation can be a valuable tool for detecting contaminants in water samples. In 1990, Natanson and colleagues studied the age and growth of pacific angel sharks, Squatina californica (Natanson & Cailliet, 1990). Sharks were injected with a fluorescent compound, tetracycline, and then fed thawed squid and mackerel and dissected in a darkroom to prevent the tetracycline from losing its intensity. Samples were observed under a microscope equipped with a short wavelength of 365 nm UV light. The tetracycline in the vertebrae was illuminated by UV radiation, so the ring growth followed the tetracycline mark. Smith used the tetracycline injection method to study band deposition in the vertebrae of leopard sharks (Smith, 1984). Again, sample sections were examined using a microscope under 365 nm UV light.

3.4.7.2 Method

Thin sections of shark vertebrae were observed under different kinds of light sources in various situations. Additionally, some vertebral samples were also immersed in 70% ethanol and observed under various light sources. The following methods were used:

a. Thin vertebral sections were placed on a glass slide, and a UV light source with a wavelength of 365 nm was positioned beneath the glass slide.

b. Thin vertebral sections were directly placed on a UV lamp with a wavelength of 365 nm, and the light source was positioned beneath the samples.

c. Thin vertebral sections were placed on a glass slide and then placed inside a UV box. A UV light source with a wavelength of 365 nm was positioned above the samples.

d. Thin vertebral sections were placed on a piece of black paper. A torch was positioned at the side of the samples, and a small mirror was used to reflect the light onto the

samples.

e. Thin vertebral sections were placed in a plastic multiwell plate, and a UV light source with a wavelength of 365 nm was positioned underneath the cell.

f. Thin vertebral sections were placed in a plastic multiwell plate inside a UV box, and a light source with a wavelength of 365 nm was positioned above the sample.

g. Thin vertebral sections were placed in a plastic multiwell plate with a black background. A torch was placed at the side of the samples, and a small mirror was used to reflect the light onto the samples.

h. Thin vertebral sections were placed on a glass slide on a black background. The microscope's light was positioned at the side of the samples, and a small mirror was used to reflect the light onto the samples.

i. Thin vertebral sections were placed in a plastic multiwell plate on a black background. The microscope's light was positioned at the side of the samples, and a small mirror was used to reflect the light onto the samples.

j. Thin vertebral sections were placed on a glass slide, and the microscope's light was positioned underneath the samples.

k. Thin vertebral sections were placed in a plastic multiwell plate with a black background, and the microscope's light was positioned above the samples.

l. Thin vertebral sections were placed in a plastic multiwell plate, and the microscope's light was positioned underneath the samples.

m. Thin vertebral sections stained with $Co(NO_3)_2$ were placed on a glass slide with a

black background. The microscope's light was positioned at the side of the samples, and a small mirror was used to reflect the light onto the samples.

n. Thin vertebral sections stained with $Co(NO_3)_2$ were placed on a glass slide, and the microscope's light was positioned underneath the samples.

o. Thin vertebral sections stained with $Co(NO_3)_2$ were placed on a black background, and the microscope's light was positioned above the samples.

3.4.7.3 Result

Part 1. Light Filters

The sample was placed on top of the UV light source (254 nm), and a glass wavelength filter was placed between the sample and the camera. In total, nine, long wavelength pass filters with different cutoff wavelengths were used, and while the images did appear to be different, the age bands were still not sufficiently clear to count accurately. It appears that wavelength filters are ineffective in improving shark vertebral image resolution.

Figure 3.4.7.3. 1 UV light images of sample SWL7-1

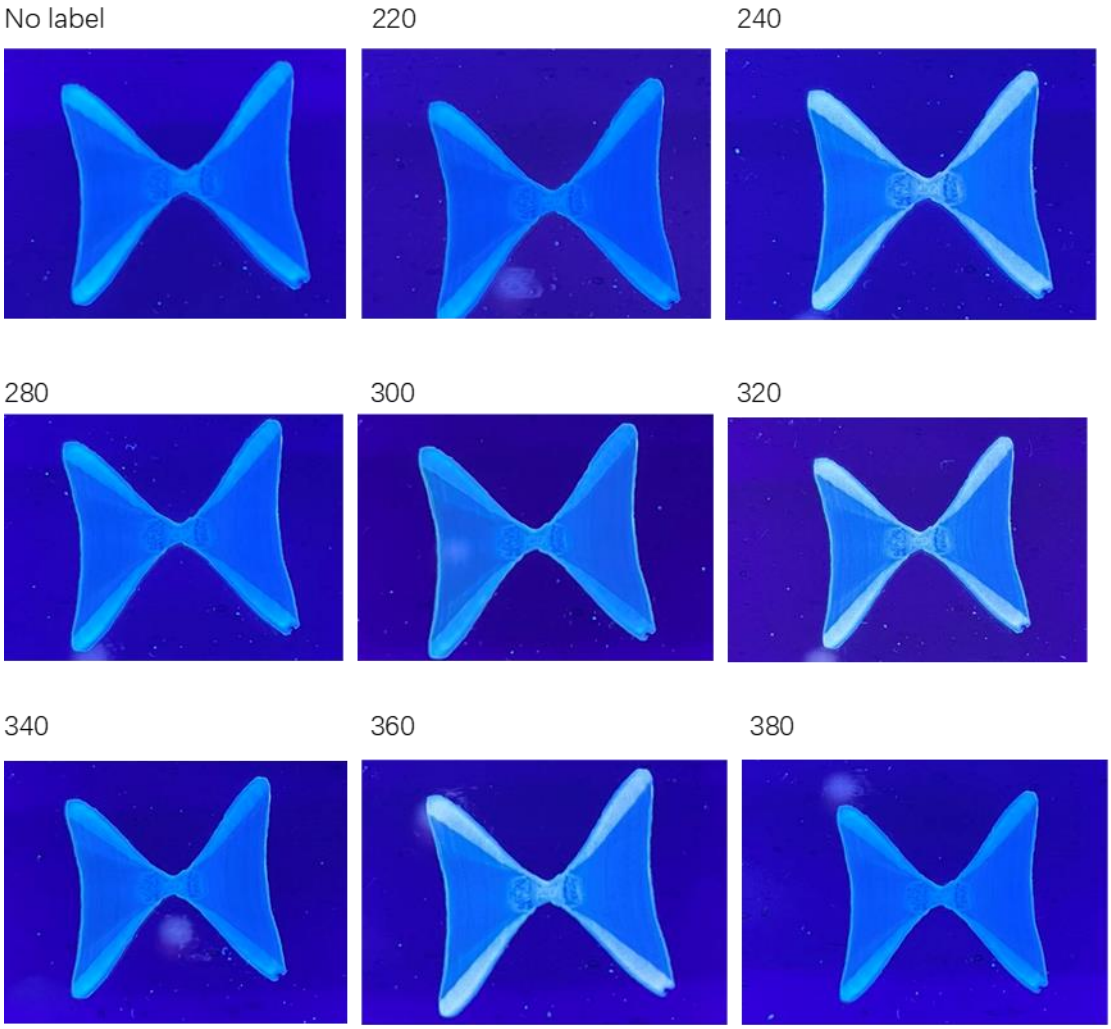

Figure 3.4.7.3. 2 UV light images of sample SWS4-A1

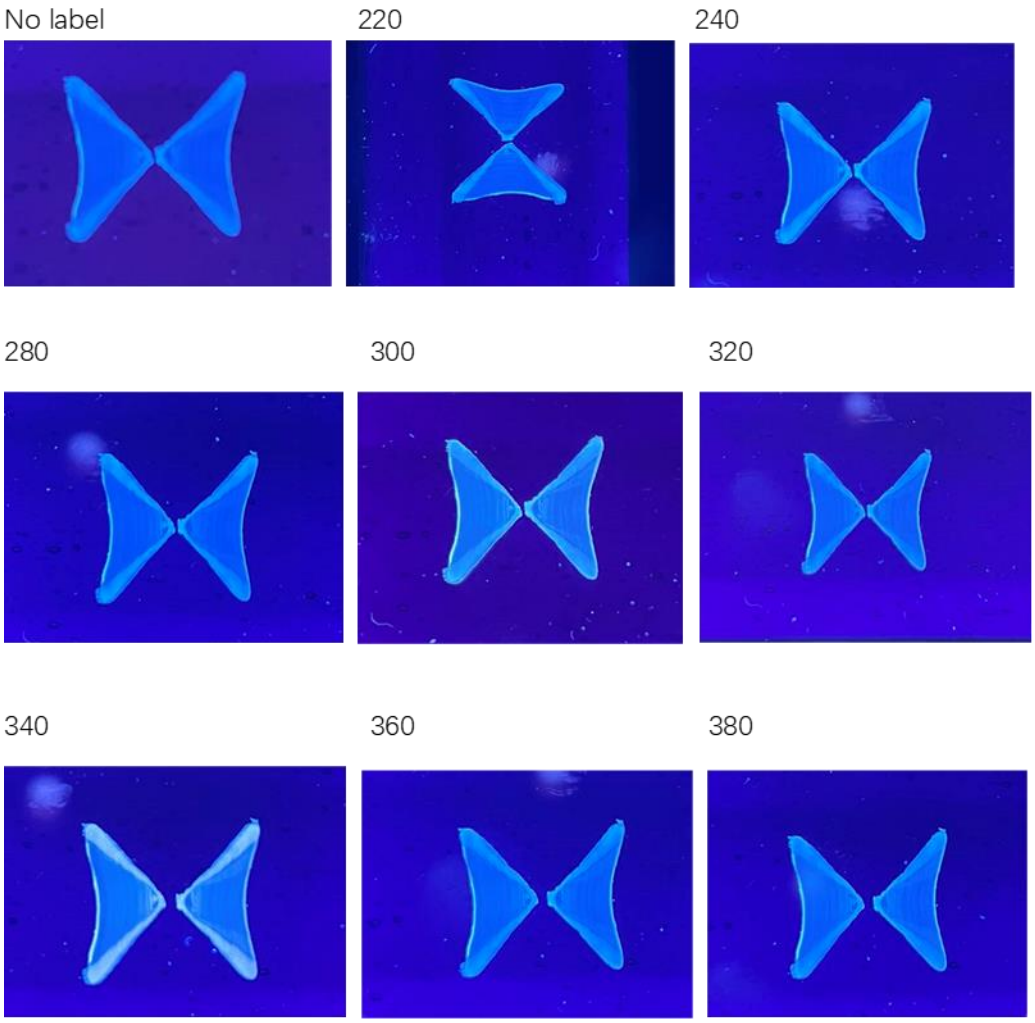

Figure 3.4.7.3. 3 2D Fluorescence spectrum of sample J19-2. The x-axis represents the emission wavelength (nm), and the y-axis represents the excitation wavelength (nm). The different colors represent the levels of intensity (red to blue, high to low).

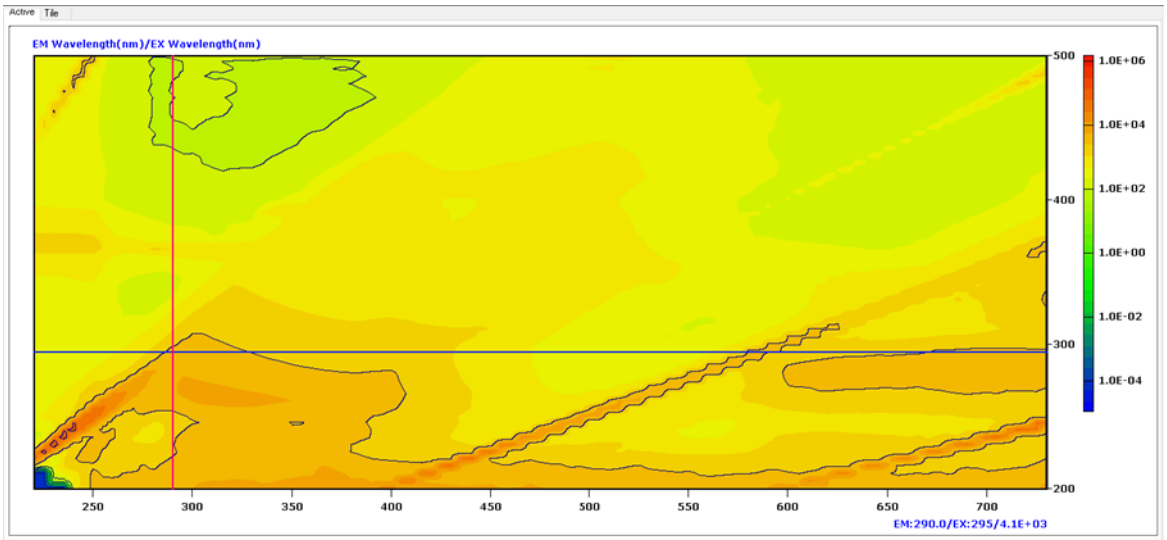

Part 2. Different conditions

Sample 1: MF220422-7_B3

The cutting plane was sagittal, and the cutting position was hourglass (anterior to posterior). The section's thickness was 0.6 mm. All the conditions were labeled based on Section 3.5.7.2.

Figure 3.4.7.3. 4 condition a

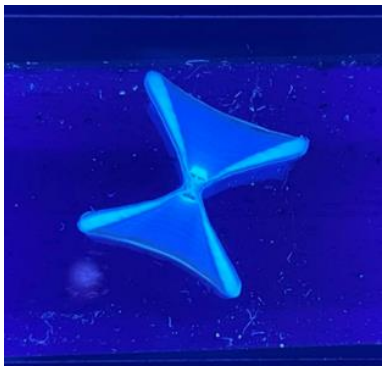

Figure 3.4.7.3. 5 condition b

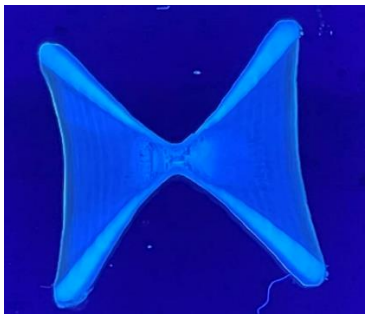

Figure 3.4.7.3. 6 condition k

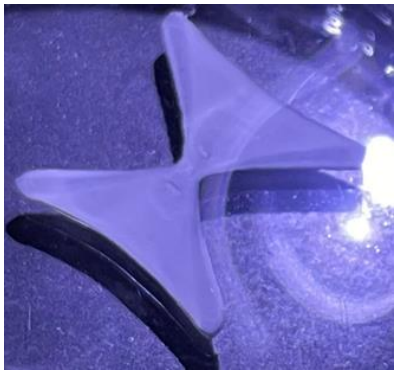

Figure 3.4.7.3. 7 condition I

Figure 3.4.7.3. 8 condition m

Figure 3.4.7.3. 9 condition o

Sample 7: JHARSOEGG18_T3

The cutting plane and position were the same as in Sample 1. The section's thinness was 0.6 mm.

Figure 3.4.7.3. 10 condition a, but the sample was wet.

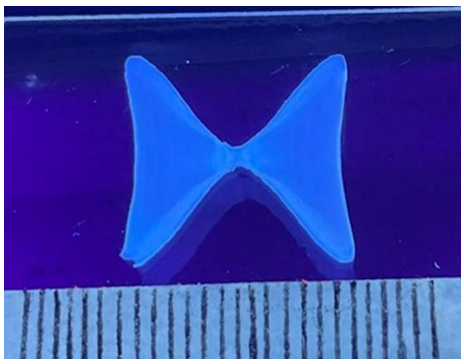

Figure 3.4.7.3. 11 condition b, but the sample was not dried.

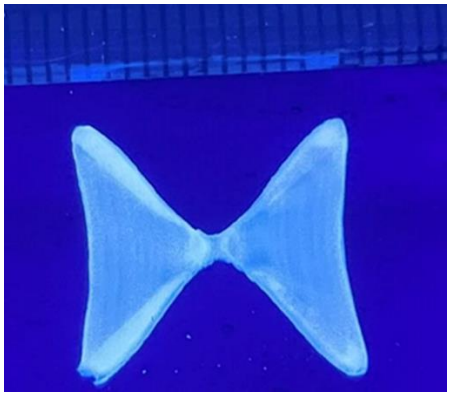

Figure 3.4.7.3. 12 condition c, and the sample was wet.

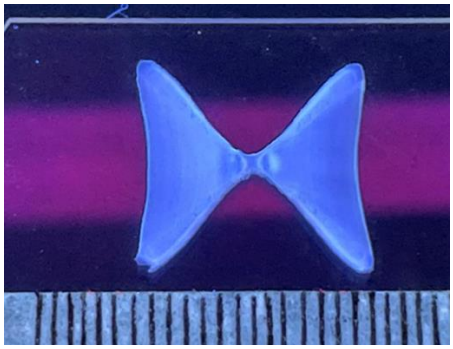

Figure 3.4.7.3. 13 condition e, and the sample was immersed in the 70% ethanol solution.

Figure 3.4.7.3. 14 condition e, and the sample was placed in the 70% ethanol.

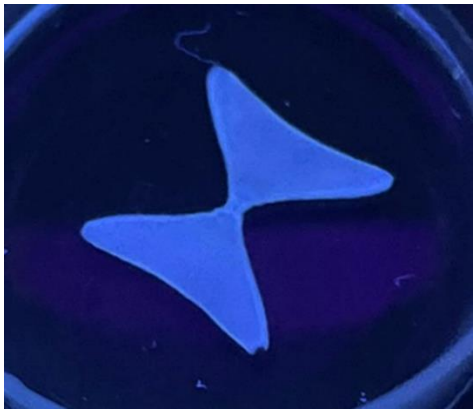

Figure 3.4.7.3. 15 condition f, and the sample was immersed in the 70% ethanol.

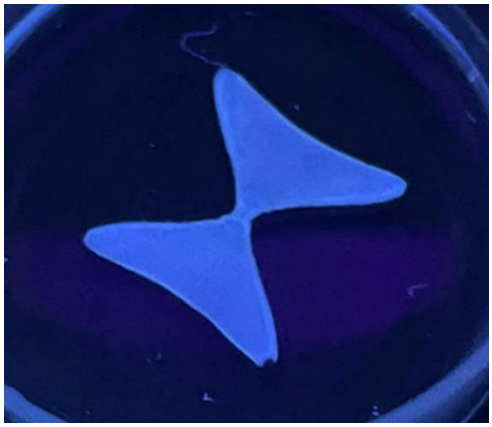

Figure 3.4.7.3. 16 condition g and with 70% ethanol immersion.

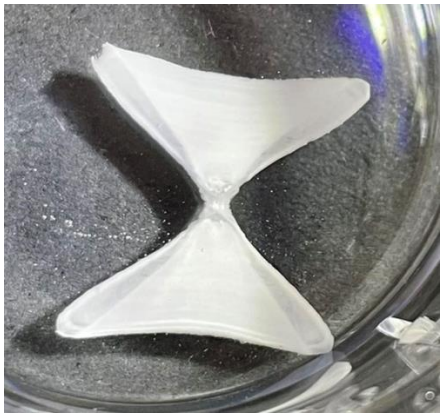

Figure 3.4.7.3. 17 condition i with ethanol immersion.

Figure 3.4.7.3. 18 condition k with ethanol immersion

Figure 3.4.7.3. 19 condition l with ethanol immersion

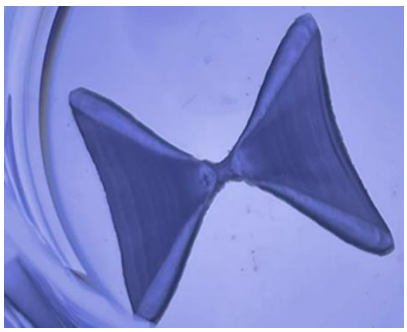

3.4.7.4 Discussion

The thin school shark vertebral sections SWL7-1(JHARSOEGG18_T3) and SWS4-A1 (NIWAWNGG006_T3) were photographed using an iPhone 12 camera under UV light to count the bands. However, the band marks on the corpus calcareum were not clear enough to be identified from the images. As a result, it was assumed that the use of filters might improve the image resolution. For sample SWL7-1, images with wavelengths of 240, 320, and 360 nm showed higher clarity, but not all the marks on the corpus calcareum could be distinguished. For sample SWS4-A1, although photos taken with 300 nm and 340 nm filters had the best resolution, they were still not good enough to be used as age counting photos. Applying filters may slightly enhance the pixel quality, but the issue was not resolved. However, the UV method could be further developed by trying to use a higher quality camera.

Based on the 2D fluorescence spectrum, the most intense emission signal of vertebra falls within the wavelength range of 290 to 395 nm for excitation from about

230nm to 300nm. Therefore, it would be reasonable to use a filter with a wavelength of 300 nm to filter out UV light (λ excitation = 254nm). Additionally, images taken under long wavelength excitation (365nm) UV light showed higher resolution than those taken under short wavelength (254nm) UV light, indicating that the particles in vertebra are large. However, images taken with the 300 nm filter under short wavelength UV light did not show clear growth rings that could be counted to determine the shark's age. It is possible that the emission intensities in the fluorescence spectrum are not caused by the particles in vertebral bands. For this reason, the fluorescence spectrum may not be ideal for directly analyzing vertebral halves to determine the shark's age.

In part 2, a series of tests were conducted on shark vertebrae sections under varying conditions. However, we encountered a setback as the resolution of the images obtained was not high enough to facilitate clear identification of the ageing marks on the corpus calcareum. Nevertheless, we were able to make significant observations on the bands present on the intermedialia. It's important to note that bands on the intermedialia may not necessarily be indicative of the shark's age, as they could be fake ageing bands. Despite this limitation, the images obtained have proven to be a guide in the ageing process.

3.4.8 CT scans

3.4.8.1 Introduction

In micro-computed tomography, also known as X-ray microtomography, X-rays are used to produce cross-sectional images of a subject sample that can be used to reconstruct a 3D model without damaging the sample. Geraghty determined the age of the spinner shark, Carcharhinus brevipinna, from eastern Australia using micro-computed tomography (micro-CT) (Geraghty et al., 2012). Growth bands could be counted by micro-CT scanning 3D images of the whole vertebrae, half samples, cutting sections, and radiograph.

In 2012, Geraghty analyzed age bands in the vertebrae of Carchahinus sharks using micro-computed tomography (microCT) 3D images. A whole vertebra, a half vertebra,

and a cut section were all viewed under microCT (Geraghty et al., 2012). With the microCT method, vertebrae can be nondestructively viewed during measurement without worrying about variables such as width and location. Nevertheless, the high cost of the scan is a non-negligible disadvantage.

Raoult studied strontium distribution in the vertebrae of Sphyrna zygaena, Charcharodon carcharias, Carcharhinus brevipinna, Heterodontus portusjacksoni, Carcharhinus obscurus, and Squatina albipunctata using scanning x-ray fluorescence microscopy (Raoult et al., 2016). Vertebrae were cut dorso-vertically through the center by 0.1 mm increments using a diamond-edged blade into approximately 0.6 mm thick sections. The sections on the film were covered with tape so they would not become dehydrated (Raoult et al., 2016). Both calcium and strontium bands were investigated, but the strontium bands had higher resolutions. The distribution of strontium in the vertebrae was assumed to correlate with changes to salinity in the environment. Strontium peak counts were more closely related to the band counts observed using microscopy, which supports the new aging technique, the strontium-focused elemental method.

Again, thin sections are better for X-ray CT scans than whole and half vertebrae. Although micro-CT is an expensive technique, it promises precise results.

3.4.8.2 Result

Part 1. CT scan

Images obtained at the University of Auckland micro-CT facility (Bruker skyscan microCT) are shown below.

Figure 3.4.8.2. 1 CT false colour images

a) Sample J19

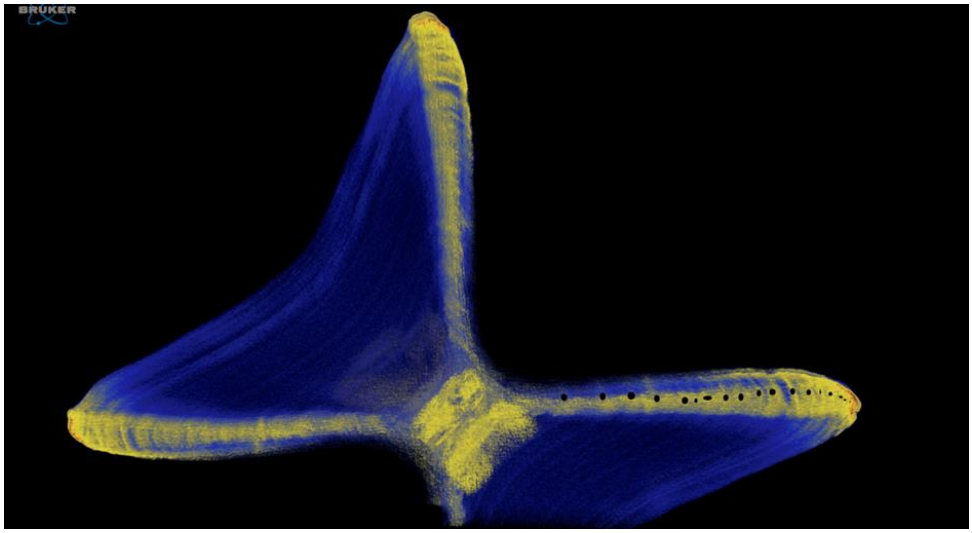

b) Sample MF7

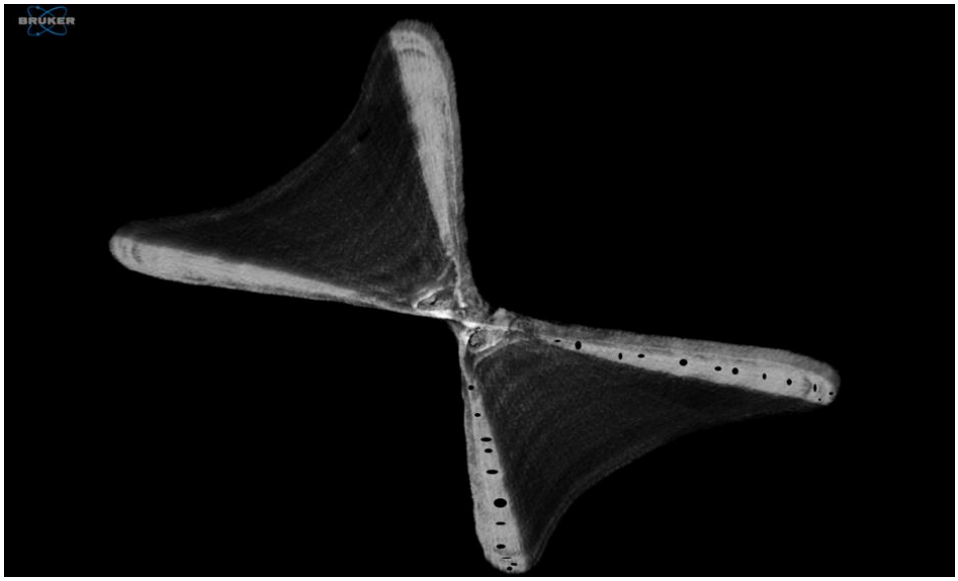

Part 2. Microscope

Figure 3.4.8.2. 2 Light Microscope images of the vertebrae scanned by microCT for comparison

a). Sample J19

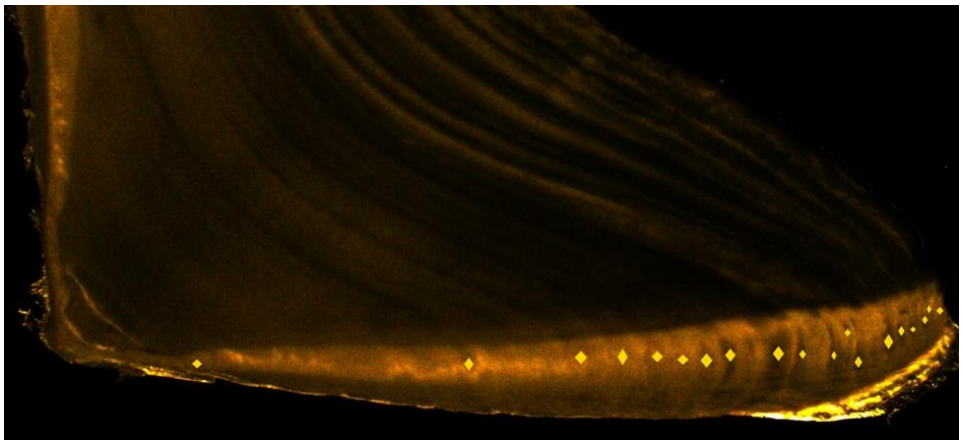

b). Sample MF7

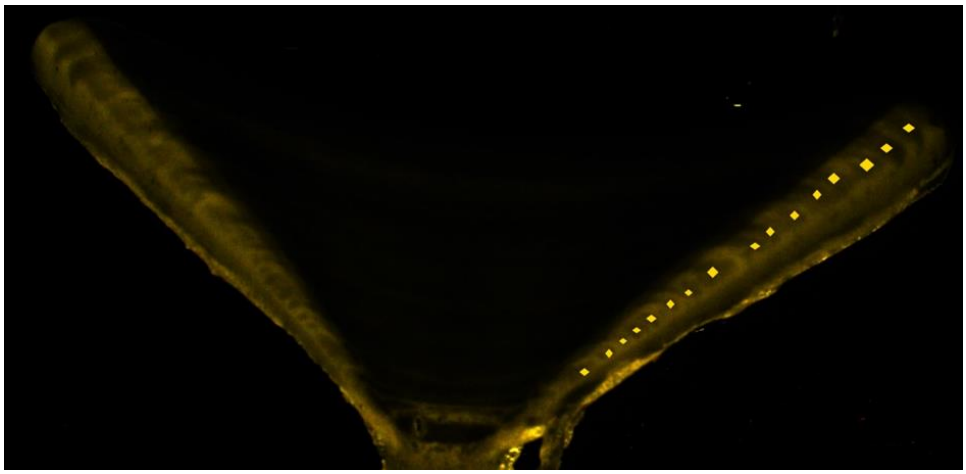

3.4.8.3 Discussion

CT scans of shark vertebral sections or halves revealed more aging bands than the microscope image of the vertebrae section. This means that different reading principles are required to study a CT scan result. Some of the lines shown at the corpus calcareum in the CT picture may not be related to age. If images from a CT scan can be precisely interpreted, this method could be a powerful tool for validating the results from the LA-MS method. It is however, expensive, time consuming and not suitable for extensive data set collection from 100+ individual specimens.

3.5 Summary of School Shark Aging/ Vertebrae Imaging Methods

This study also applied different approaches to identify the growth rings in NZ school shark vertebrae and determine the age of sharks. Bands at the intermedialia of vertebrae could be observed when thin sections of the vertebrae were viewed under different light sources with varying conditions. However, based on the images that were taken, it appears that the age marks on the corpus calcareum were not very clear. Instead, we relied on the rings on the corpus calcareum to determine the age of the sharks. The bands at the intermedialia could only be used as a guide to help with aging.

Based on the observations, it was found that the peak regions from IR spectra and FTIR spectra were correlated with biological hydroxyapatite and water molecules in the samples of the vertebral halves. Diagrams were plotted using the TBL and DOV centrum, with the normalized intensity values of peak areas. It was discovered that the peak regions from the IR spectra of the female shark samples had some correlation with either the TBL or DOV parameter, but no such trends were observed in the male sample spectra. In addition, while the water peak region and collagen peak region from the FT-IR spectra were sometimes directly related to the TBL and DOV, this pattern was not very consistent. As a result, it was not possible to determine the age of the school shark based on the IR and FTIR methods.

In previous NIRS studies, researchers examined approximately 100 vertebral samples (Rigby et al., 2018). It is necessary to have a sufficient number of samples in order to cover the wide range of age vibrations among fish of similar lengths. To enhance the accuracy of the IR and FTIR methods, one feasible solution is to increase the number of samples. With a larger sample size, the R^2 value can be improved, and a clearer correlation pattern might be identified between TBL or DOV and peak regions.

The traditional method of attaining the age of a shark is to count the growth bands found in microscope images of the corpus calcareum. However, our results showed that age bands can also be observed through CT scan images. Although this approach has potential benefits, the number of bands found in CT scans and microscope images do not always correspond. Therefore, a new reading protocol needs to be developed to

accurately read CT scan images.

The difficulty in finding a good method to compare shark age against the information obtained from our new method of LA-FC-ESI-MS imaging meant that no firm comparison could be made at this stage. All existing literature methods gave results that were inconclusive for age determination. Given that age is an important parameter in fishery management for many species, including school sharks, this topic needs to be pursued further and a definitive method developed.

Chapter 4. Conclusion and Future Work

In conclusion, this research has determined the functionality and efficiency of the modified LA-MS method. The important finding in this project is that a film of water or solution on the glass slide can be used to capture the plasma produced by laser ablation, and the atoms and compounds transferred to the solution can then be detected through ESI-MS. The method was trialed on several different sample matrices. Desorption of molecular species with little or no fragmentation was demonstrated by using caffeine deposited on an absorbing graphite sample. Natural products consisting of biopolymers, i.e. wood from different species, were analysed indicating the method may have some application to bio-typing and bio-fingerprinting. Spatial distribution of metal ions in shark vertebra using an ionization enhancing compound (EDTA) indicates that the method may have some versatility in imaging of biological samples.

In terms of the specific applications:

(a) Desorption analysis. The LA-FC-ESI-MS method may be a useful technique similar to MALDI for introducing complex molecules into the ion source of a mass spectrometer. An advantage over MALDI seems to be that little effort is required for sample preparation. The disadvantage would be that only molecules that are soluble in the liquid used for film generation are likely to be captured.

(b) The spectra of wood samples were successfully obtained by applying the LA-FC-ESI-MS method. The mass peak versus intensity diagrams roughly stated the difference between three wood species. However, further analysis is required to be able to use this method to identify and distinguish unknown species.

(c) Aging of shark vertebral samples using our LA-FC-ESI-MS technique. Due to the inconsistent results generated by CT scans and microscope images, the analysis of metal ion composition might be a better way to determine a shark's age. We detected $^{40}Ca^{2+}$ and $^{64}Zn^{2+}$ ions, and observed

that the concentrations of these two ions could be correlated to the bumps in the vertebral samples. To further verify this finding, a scanning electron microscope is required, which could show the composition of the metal ions by EDS scanning the vertebral sample.

The trial apparatus could be improved in the following ways:

The long delay time and the time resolution could be improved by changing from a peristaltic pump to something similar to an HPLC pump. The HPLC pumps have only a small dead volume, and would remove the long delay time evident for the sample to return to baseline. An HPLC pump also would remove the pulsing arising from flow related dynamics affecting the ion concentration (evident in the MS in the shark vertebrae study)

The delivery of water flow onto the slide was also very crude and a flow controlled pump would be advantageous.

The supply of liquid to the film and the liquid flow rate transfer to the MS need to be matched to ensure all analyte is collected, enhancing the sensitivity.

For imaging studies a motorized x,y,z stage would be advantageous to set the laser focus, and to scan accurately in two dimensions, rather than the modified syringe pump drive used to provide 1D motion.

Other mixed solvents e.g. acetonitrile/water need also to be trialed

The system could also be contained in an inert gas enclosure to prevent the effects of oxidation for those samples susceptible to atmospheric oxidation under the energetic conditions of the laser ablation step.

No attempt at establishing detection limits, or quantitative analysis, was performed in this initial work. Because of the ability to add ionization enhancing additives to the liquid film solvent, it would be interesting to establish the sensitivity of the method.

The LA-FC-ESI-MS technique shows considerable promise as a versatile, economical addition to the standard ESI source for analysis of a wide range of sample

matrices, including possibilities associated with MS spatial imaging.

References

Beck, J., & Schmidt, C. (2003). *LC/MS Two Sources are Better Than One - More Choices for Sample Ionization with ESI and APCI*. https://www.agilent.com/Library/applications/lcms06.pdf

Bishop, S., Francis, M. P., Duffy, C. a. J., & Montgomery, J. A. (2006). Age, growth, maturity, longevity and natural mortality of the shortfin mako shark (Isurus oxyrinchus) in New Zealand waters. *Marine and Freshwater Research*, *57*(2), 143. https://doi.org/10.1071/mf05077

Belkind, A., & Gershman, S. (2008, January 1). Plasma cleaning of surfaces. ResearchGate.https://www.researchgate.net/publication/284486745_Plasma_cleaning_of_surfaces

Basile, F., Zhang, S., Shin, Y., & Drolet, B. S. (2010). Atmospheric pressure-thermal desorption (AP-TD)/electrospray ionization-mass spectrometry for the rapid analysis of Bacillus spores. *Analyst*, *135*(4), 797. https://doi.org/10.1039/c0an00071j

Bērziņa-Cimdiņa, L., & Borodajenko, N. (2012). Research of calcium phosphates using Fourier Transform Infrared Spectroscopy. In *InTech eBooks*. https://doi.org/10.5772/36942

Bonta, M., Lohninger, H., Marchetti-Deschmann, M., & Limbeck, A. (2014). Application of gold thin-films for internal standardization in LA-ICP-MS imaging experiments. *Analyst*, *139*(6), 1521. https://doi.org/10.1039/c3an01511d

Bodzon-Kulakowska, A., Drabik, A., Ner, J., Kotlinska, J., & Suder, P. (2014). Desorption electrospray ionisation (DESI) for beginners - how to adjust settings for tissue imaging. *Rapid Communications in Mass Spectrometry*, *28*(1), 1–9. https://doi.org/10.1002/rcm.6755

Banerjee, S., & Zare, R. N. (2019). Influence of Inlet Capillary Temperature on the Microdroplet Chemistry Studied by Mass Spectrometry. *Journal of Physical Chemistry A*, *123*(36), 7704–7709. https://doi.org/10.1021/acs.jpca.9b05703

Beck, S. (2021). Fragmentation behavior of EDTA complexes under different activation conditions. *Journal of Mass Spectrometry*, *56*(7). https://doi.org/10.1002/jms.4775

Cailliet, G. M., Martin, L. K., Kusher, D., Wolf, P., & Welden, B. A. (1983). Techniques for enhancing vertebral bands in age estimation of California elasmobranchs. *Proceedings International Workshop on Age Determination of Oceanic Pelagic Fishes: Tunas, Billfishes, Sharks, NOAA Tech. Rep. NMFS*, *8*, 157–165.

Choi, Y., Im, H., & Jung, K. (1999). Laser ablation of graphite at 355 nm: cluster formation and plume propagation. *International Journal of Mass Spectrometry*, *189*(2–3), 115–123. https://doi.org/10.1016/s1387-3806(99)00060-3

Cremer, P., & Boxer, S. G. (1999). Formation and Spreading of Lipid Bilayers on Planar Glass Supports. *Journal of Physical Chemistry B*, *103*(13), 2554–2559. https://doi.org/10.1021/jp983996x

Canning, J., Petermann, I., & Cook, K. H. (2012). Surface treatment of silicate based glass: basePiranha treatment versus 193nm laser processing. *Third Asia Pacific Optical Sensors Conference*. https://doi.org/10.1117/12.915823

Chen, F., Hu, Z., Parker, R. A., & Laizure, S. C. (2017). Measurement of caffeine and its three primary metabolites in human plasma by HPLC-ESI-MS/MS and clinical application. *Biomedical Chromatography*, *31*(6), e3900. https://doi.org/10.1002/bmc.3900

Coiraton, C., Tovar-Ávila, J., Garcés-García, K. C., Rodríguez-Madrigal, J. A., Gallegos-Camacho, R., Chávez-Arrenquín, D. A., & Amezcua, F. (2019). Periodicity of the growth-band formation in vertebrae of juvenile scalloped

hammerhead shark*Sphyrna lewini*from the Mexican Pacific Ocean. *Journal of Fish Biology*, *95*(4), 1072–1085. https://doi.org/10.1111/jfb.14100

Coiraton, C., & Amezcua, F. (2020). In utero elemental tags in vertebrae of the scalloped hammerhead shark Sphyrna lewini reveal migration patterns of pregnant females. *Scientific Reports*, *10*(1). https://doi.org/10.1038/s41598-020-58735-8

Corsso, J. T., Gadig, O. B. F., Caltabellotta, F. P., Barreto, R., & Motta, F. S. (2021). Age and growth of two sharpnose shark species (Rhizoprionodon lalandii and R. porosus) in subtropical waters of the south-western Atlantic. *Marine and Freshwater Research*, *72*(3), 398. https://doi.org/10.1071/mf19379

Dietemann, P., Edelmann, M. J., Meisterhans, C., Pfeiffer, C., Zumbühl, S., Knochenmuss, R., & Zenobi, R. (2000). Artificial Photoaging of Triterpenes Studied by Graphite-Assisted Laser Desorption/Ionization Mass Spectrometry. *Helvetica Chimica Acta*, *83*(8), 1766–1777. https://doi.org/10.1002/1522-2675(20000809)83:8

Duarte, P., Silva, A. S., Menezes, G. M., & Pinho, M. (2001). Staining techniques for ageing tope shark, Galeorhinus galeus (Linnaeus, 1758), from the Azores : a comparison based on precision analysis. *Research Gate*.

Dreisewerd, K. (2003). The Desorption Process in MALDI. *Chemical Reviews*, *103*(2), 395–426. https://doi.org/10.1021/cr010375i

Durrant, S. F., & Ward, N. (2005). Recent biological and environmental applications of laser ablation inductively coupled plasma mass spectrometry (LA-ICP-MS). *Journal of Analytical Atomic Spectrometry*, *20*(9), 821. https://doi.org/10.1039/b502206a

Dittrich, N., Zuber, J., Rathsack, P., & Otto, M. (2018). Comparison of graphite-assisted laser desorption/ionization and matrix-assisted laser desorption/ionization Fourier transform ion cyclotron resonance mass spectrometry for the analysis of pyrolysis liquids. *International Journal of Mass Spectrometry*, *433*, 31–39. https://doi.org/10.1016/j.ijms.2018.08.002

Diaz, D., & Hahn, D. W. (2020). Plasma chemistry produced during laser ablation of graphite in air, argon, helium and nitrogen. *Spectrochimica Acta Part B: Atomic Spectroscopy*, *166*, 105800. https://doi.org/10.1016/j.sab.2020.105800

El-Aneed, A., Cohen, A., & Banoub, J. (2009). Mass Spectrometry, Review of the Basics: Electrospray, MALDI, and Commonly Used Mass Analyzers. *Applied Spectroscopy Reviews*, *44*(3), 210–230. https://doi.org/10.1080/05704920902717872

Fenselau, C. (1997). Peer Reviewed: MALDI MS and Strategies for Protein Analysis. *Analytical Chemistry*, *69*(21), 661A-665A. https://doi.org/10.1021/ac971831z

Francis, M. P., & Mulligan, K. (1998). Age and growth of New Zealand school shark,Galeorhinus galeus. *New Zealand Journal of Marine and Freshwater Research*, *32*(3), 427–440. https://doi.org/10.1080/00288330.1998.9516835

Francis, M. P., & Maolagáin, C. Ó. (2000). Age, growth and maturity of a New Zealand endemic shark (Mustelus lenticulatus) estimated from vertebral bands. *Marine and Freshwater Research*, *51*(1), 35. https://doi.org/10.1071/mf99012

Germain, C., Girault, C., Aubreton, J., & Catherinot, A. (1993). Laser ablation of graphite targets. *Applied Surface Science*, *69*(1–4), 359–364. https://doi.org/10.1016/0169-4332(93)90534-i

Green, F. M., Salter, T. L., Gilmore, I. S., Stokes, P., & O'Connor, G. (2010). The effect of electrospray solvent composition on desorption electrospray ionisation (DESI) efficiency and spatial resolution. *Analyst*, *135*(4), 731. https://doi.org/10.1039/b924208b

Geraghty, P. T., Jones, A. S., Stewart, J., & Macbeth, W. G. (2012). Micro-computed tomography: an alternative method for shark ageing. *Journal of Fish Biology, 80(5),* 1292–1299. https://doi.org/10.1111/j.1095-8649.2011.03188.x

Griggs, Kathryn (2022) "X-Ray Diffraction and Structural Analysis of Shark Vertebrae," *DePaul Discoveries:* Vol. 11: Iss. 1, Article 9.

Hoenig, J., & Brown, C. A. (1988). A Simple Technique for Staining Growth Bands in

Elasmobranch Vertebrae [Review of *A Simple Technique for Staining Growth Bands in Elasmobranch Vertebrae*]. *Bulletin of Marine Science*, *42(2)*, 334–337.

Heymann, D. (1996). Solubility of Fullerenes $C_{60}$and C_{70}in Seven Normal Alcohols and Their Deduced Solubility in Water. *Fullerene Science and Technology*, *4*(3), 509–515. https://doi.org/10.1080/10641229608001567

Harvey D. J. (1999). Matrix-assisted laser desorption/ionization mass spectrometry of carbohydrates. *Mass spectrometry reviews*, *18*(6), 349–450. https://doi.org/10.1002/(SICI)1098-2787(1999)18:6<349::AID MAS1>3.0.CO;2-H

Hull, M. C., Cambrea, L. R., & Hovis, J. S. (2005). Infrared Spectroscopy of Fluid Lipid Bilayers. *Analytical Chemistry*, *77*(18), 6096–6099. https://doi.org/10.1021/ac050990c

Hare, J. P., Kroto, H. W., & Taylor, R. J. K. (2013). Reprint of: Preparation and UV/visible spectra of fullerenes C60 and C70. *Chemical Physics Letters*. https://doi.org/10.1016/j.cplett.2013.08.068

Hollerbach, A., Ayrton, S. T., Jarmusch, A. K., & Cooks, R. G. (2017). Desorption Electrospray Ionization: Methodology and Applications. https://doi.org/10.1016/b978-0-12-409547-2.12133-x

Junaid, M., Almuqri, E. A., Liu, J., & Zhang, H. (2016). Analyses of the Binding between Water Soluble C60 Derivatives and Potential Drug Targets through a Molecular Docking Approach. *PLOS ONE*, *11*(2), e0147761. https://doi.org/10.1371/journal.pone.0147761

Kroto, H. W., Heath, J. R., O'Brien, S., Curl, R. F., & Smalley, R. E. (1985). C60: Buckminsterfullerene. *Nature*, *318*(6042), 162– 163. https://doi.org/10.1038/318162a0

Kim, J., Kim, G., & Cremer, P. (2001). Investigations of Water Structure at the Solid/Liquid Interface in the Presence of Supported Lipid Bilayers by Vibrational Sum Frequency Spectroscopy. *Langmuir*, *17*(23), 7255–7260.

https://doi.org/10.1021/la0017274

Kaur-Atwal, G., Weston, D. J., Green, P., Crosland, S., Bonner, P. L., & Creaser, C. S. (2007). Analysis of tryptic peptides using desorption electrospray ionisation combined with ion mobility spectrometry/mass spectrometry. *Rapid Communications in Mass Spectrometry*, *21*(7), 1131–1138. https://doi.org/10.1002/rcm.2941

Kern, B., Böttcher, A., & Strelnikov, D. (2016). IR and UV-NIR Absorption Spectroscopy of Matrix-Isolated C70+ and C70–. *Journal of Physical Chemistry A*. https://doi.org/10.1021/acs.jpca.6b06212

Manicke, N. E., Dill, A. L., Ifa, D. R., & Cooks, R. G. (2010). High-resolution tissue imaging on an orbitrap mass spectrometer by desorption electrospray ionization mass spectrometry. *Journal of Mass Spectrometry*, *45*(2), 223–226. https://doi.org/10.1002/jms.1707

Mohan, J. A., TinHan, T. C., Miller, N. R., & David Wells, R. (2017). Effects of sample cleaning and storage on the elemental composition of shark vertebrae. *Rapid Communications in Mass Spectrometry, 31(24),* 2073–2080. https://doi.org/10.1002/rcm.7998

Mohan, J. A., Miller, N. R., Herzka, S. Z., Sosa-Nishizaki, O., Kohin, S., Dewar, H., Kinney, M., Snodgrass, O., & Wells, R. J. D. (2018). Elements of time and place: manganese and barium in shark vertebrae reflect age and upwelling histories. *Proceedings of the Royal Society B: Biological Sciences, 285(1890),* 20181760. https://doi.org/10.1098/rspb.2018.1760

McMillan, M. N., Gillanders, B. M., Semmens, J. M., & Gillanders, B. M. (2018). Natural tags reveal populations of Conservation Dependent school shark use different pupping areas. *Marine Ecology Progress Series*, *599*, 147–156. https://doi.org/10.3354/meps12626

Maher, R., & Emmott, E. (2022). Electrospray ionization: “We taught elephants to fly.” *The Biochemist*, *44*(5), 5–8. https://doi.org/10.1042/bio_2022_127

Natanson, L. J., & Cailliet, G. M. (1990). Vertebral Growth Zone Deposition in Pacific Angel Sharks. Copeia, 1990(4), 1133. https://doi.org/10.2307/1446499

Smith, S. M. (1984). Timing of Vertebral-Band Deposition in Tetracycline-Injected Leopard Sharks. *Transactions of the American Fisheries Society*, *113*(3), 308–313.

Nielen, M., Hooijerink, H., Zomer, P. J., & Mol, J. M. C. (2011). Desorption electrospray ionization mass spectrometry in the analysis of chemical food contaminants in food. *Trends in Analytical Chemistry*, *30*(2), 165–180. https://doi.org/10.1016/j.trac.2010.11.006

Natanson, L. J., Skomal, G. B., Hoffmann, S., Porter, M. E., Goldman, K., & Serra, D. (2018). Age and growth of sharks: do vertebral band pairs record age? *Marine and Freshwater Research*, *69*(9), 1440. https://doi.org/10.1071/mf17279

Oldach, L. (2023). Lumber sleuths. *C&EN Global Enterprise 2023 101 (7), 24-29* DOI: 10.1021/cen-10107-cover

Puretzky, A. A., Geohegan, D. B., Haufler, R. E., Hettich, R. L., Zheng, X., & Compton, R. N. (1996). Laser ablation of graphite in different buffer gases. *Nucleation and Atmospheric Aerosols*. https://doi.org/10.1063/1.44881

Petasch, W., Kegel, B., Schmid, H., Lendenmann, K., & Keller, H. (1997). Low-pressure plasma cleaning: a process for precision cleaning applications. *Surface & Coatings Technology*, *97*(1–3), 176–181. https://doi.org/10.1016/s0257-8972(97)00143-6

Pérez-Rojas, J. G., Torres-Palacios, K., Uribe, A., Navia, A. F., & Mejía-Falla, P. A. (2020). Evaluation of staining techniques for the observation of growth bands in tropical elasmobranch vertebrae. *Scientia Marina*, *84*(4), 343–354. https://doi.org/10.3989/scimar.05045.03a

Pereira, I., Ramalho, R. R. F., Maciel, L. I., De Aguiar, D. V. A., Trindade, Y., Da Cruz, G. F., Vianna, A. M., Medeiros, I., Junior, Da S Lima, G., & Vaz, B. G. (2022). Directly Mapping the Spatial Distribution of Organic Compounds on

Mineral Rock Surfaces by DESI and LAESI Mass Spectrometry Imaging. *Analytical Chemistry*, *94*(40), 13691–13699. https://doi.org/10.1021/acs.analchem.2c01154

Ruoff, R. S., Tse, D. B., Malhotra, R., & Lorents, D. C. (1993). Solubility of fullerene (C60) in a variety of solvents. *The Journal of Physical Chemistry*, *97*(13), 3379–3383. https://doi.org/10.1021/j100115a049

Russo, R. E., Mao, X., Liu, H., Gonzalez, J., & Mao, S. S. (2002). Laser ablation in analytical chemistry-a review. *Talanta, 57*(3), 425–451. https://doi.org/10.1016/s0039-9140(02)00053-x

Russo, R. E., Mao, X., Gonzalez, J. J., Zorba, V., & Yoo, J. S. (2013). Laser Ablation in Analytical Chemistry. *Analytical Chemistry*, *85*(13), 6162–6177. https://doi.org/10.1021/ac4005327

Rigby, C. L., Wedding, B., Grauf, S., & Simpfendorfer, C. A. (2014). The utility of near infrared spectroscopy for age estimation of deepwater sharks. *Deep-Sea Research Part I-Oceanographic Research Papers*, *94*, 184–194. https://doi.org/10.1016/j.dsr.2014.09.004

Rigby, C. L., Wedding, B. B., Grauf, S., & Simpfendorfer, C. A. (2016). Novel method for shark age estimation using near infrared spectroscopy. *Marine and Freshwater Research, 67(5)*, 537. https://doi.org/10.1071/mf15104

Raoult, V., Peddemors, V. M., Zahra, D., Howell, N. A., Howard, D. L., De Jonge, M. D., & Williamson, J. E. (2016). Strontium mineralization of shark vertebrae. *Scientific Reports*, *6*(1). https://doi.org/10.1038/srep29698

Ravi-Kumar, S., Lies, B., Zhang, X., Lyu, H., & Qin, H. (2019). Laser ablation of polymers: a review. *Polymer International*, *68*(8), 1391–1401. https://doi.org/10.1002/pi.5834

St-Onge, L., Sing, R., Béchard, S., & Sabsabi, M. (1999). Carbon emissions following 1.064 μm laser ablation of graphite and organic samples in ambient air. *Applied Physics A*, *69*(S1), S913–S916. https://doi.org/10.1007/pl00006964

Seu, K. J., Pandey, A. P., Haque, F., Proctor, E. A., Ribbe, A. E., & Hovis, J. S. (2007). Effect of Surface Treatment on Diffusion and Domain Formation in Supported Lipid Bilayers. *Biophysical Journal*, *92*(7), 2445–2450. https://doi.org/10.1529/biophysj.106.099721

Scharer, R. M., Patterson III, W. F., Carlson, J. K., & Poulakis, G. R. (2012). Age and Growth of Endangered Smalltooth Sawfish (Pristis pectinata) Verified with LA-ICP-MS Analysis of Vertebrae. *PLoS ONE, 7(10),* e47850. https://doi.org/10.1371/journal.pone.0047850

Sylvester, P. W., & Jackson, S. K. (2016). A Brief History of Laser Ablation Inductively Coupled Plasma Mass Spectrometry (LA–ICP–MS). *Elements*, *12*(5), 307–310. https://doi.org/10.2113/gselements.12.5.307

Saraswati, T. E., Setiawan, U. N. A., Ihsan, M., Isnaeni, I., & Herbani, Y. (2019). The Study of the Optical Properties of C60 Fullerene in Different Organic Solvents. *Open Chemistry, 17*(1), 1198–1212. https://doi.org/10.1515/chem-2019-0117

Shrestha, B. (2021). Ionization sources for imaging mass spectrometry. In *Elsevier eBooks* (pp. 11–22). https://doi.org/10.1016/b978-0-12-818998-6.00002-4

Sims, D. (n.d.). *Oceanic sharks and rays have declined by 71% since 1970 – a global solution is needed*. The Conversation. https://theconversation.com/oceanic-sharks-and-rays-have-declined-by-71-since-1970-a-global-solution-is-needed-154102#:~:text=Worldwide%2C%20oceanic%20shark%20and%20ray,was%20thought%20to%20be%20endangered.

Tovar-Ávila, J., Izzo, C., Walker, T. I., Braccini, J. M., & Day, R. W. (2009). Assessing growth band counts from vertebrae and dorsal-fin spines for ageing sharks: comparison of four methods applied to Heterodontus portusjacksoni. *Marine and Freshwater Research*, *60*(9), 898. https://doi.org/10.1071/mf08206

Tillett, B., Meekan, M., Parry, D., Munksgaard, N., Field, I., Thorburn, D., & Bradshaw, C. (2011). Decoding fingerprints: elemental composition of vertebrae

correlates to age-related habitat use in two morphologically similar sharks. *Marine Ecology Progress Series, 434,* 133–142. https://doi.org/10.3354/meps09222

Towers, M. W., Karancsi, T., Jones, E., Pringle, S. D., & Claude, E. (2018). Optimised Desorption Electrospray Ionisation Mass Spectrometry Imaging (DESI-MSI) for the Analysis of Proteins/Peptides Directly from Tissue Sections on a Travelling Wave Ion Mobility Q-ToF. *Journal of the American Society for Mass Spectrometry*, *29*(12), 2456–2466. https://doi.org/10.1007/s13361-018-2049-0

Taylor, A., Tsikritsis, D., Dexter, A., Burton, A. L., Bunch, J., & Belsey, N. A. (2022). Classification of tablet formulations by desorption electrospray ionisation mass spectrometry and transmission Raman spectroscopy. *Journal of Chemometrics*. https://doi.org/10.1002/cem.3412

Veiko, V. P., Volkov, S. A., Zakoldaev, R. A., Sergeev, M. M., Samokhvalov, A. A., Kostyuk, G. K., & Milyaev, K. (2017). Laser-induced microplasma as a tool for microstructuring transparent media. *Quantum Electronics*, *47*(9), 842–848. https://doi.org/10.1070/qel16377e47850.

Wiseman, J. M., Ifa, D. R., Zhu, Y., Kissinger, C. B., Manicke, N. E., Kissinger, P. T., & Cooks, R. G. (2008). Desorption electrospray ionization mass spectrometry: Imaging drugs and metabolites in tissues. *Proceedings of the National Academy of Sciences of the United States of America*, *105*(47), 18120–18125. https://doi.org/10.1073/pnas.0801066105

Wyszyński, D., Gawlik, J., & Janusz, M. (2013). Application of DPSS Nd: YAG (532nm) laser for precise machining of diamond. http://www.ptzp.org.pl/files/konferencje/kzz/artyk_pdf_2013/e015.pdf

Wedding, B., Forrest, A. K., Wright, C. L., Grauf, S., Exley, P., & Poole, S. (2014). A novel method for the age estimation of Saddletail snapper (Lutjanus malabaricus) using Fourier Transform-near infrared (FT-NIR) spectroscopy.

Marine and Freshwater Research, *65*(10), 894. https://doi.org/10.1071/mf13244

Yu. I. Prylutskyy, V. I. Petrenko, O. I. Ivankov, O. A. Kyzyma, L. A. Bulavin, O. O. Litsis, M. P. Evstigneev, V. V. Cherepanov, A. G. Naumovets, and U. Ritter. (2014.) On the Origin of C_{60} Fullerene Solubility in Aqueous Solution. *Langmuir 30* (14), 3967-3970 DOI: 10.1021/la404976k

Zenobi, R., & Knochenmuss, R. (1998). Ion formation in MALDI mass spectrometry. *Mass Spectrometry Reviews*, *17*(5), 337–366. https://doi.org/10.1002/(sici)1098-2787(1998)17:5

Appendix A: Figures for Section 3.1.3.2

Figure A. 1 MS spectrum of the plasma produced by graphite ablation. (The Q-switch was 45 μs, the average energy of each pulse was 272 mJ, and the distance was 43.6 mm.)

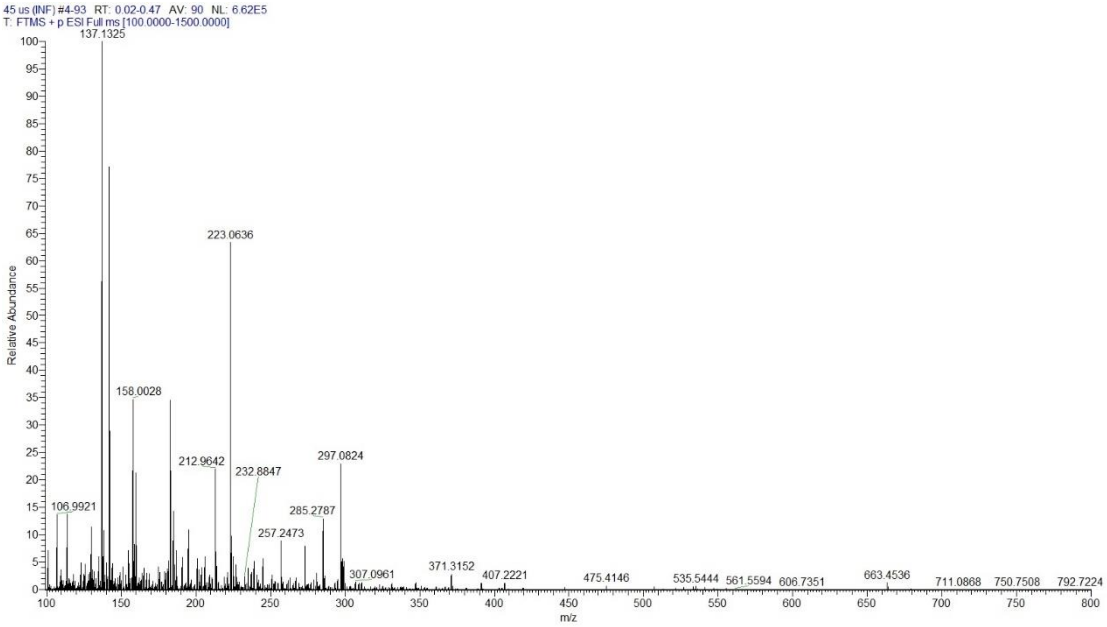

Figure A. 2 MS spectrum of the plasma produced by graphite ablation. (The Q-switch was 60 μs, the average energy of each pulse was 231 mJ, and the distance was 43.6 mm.)

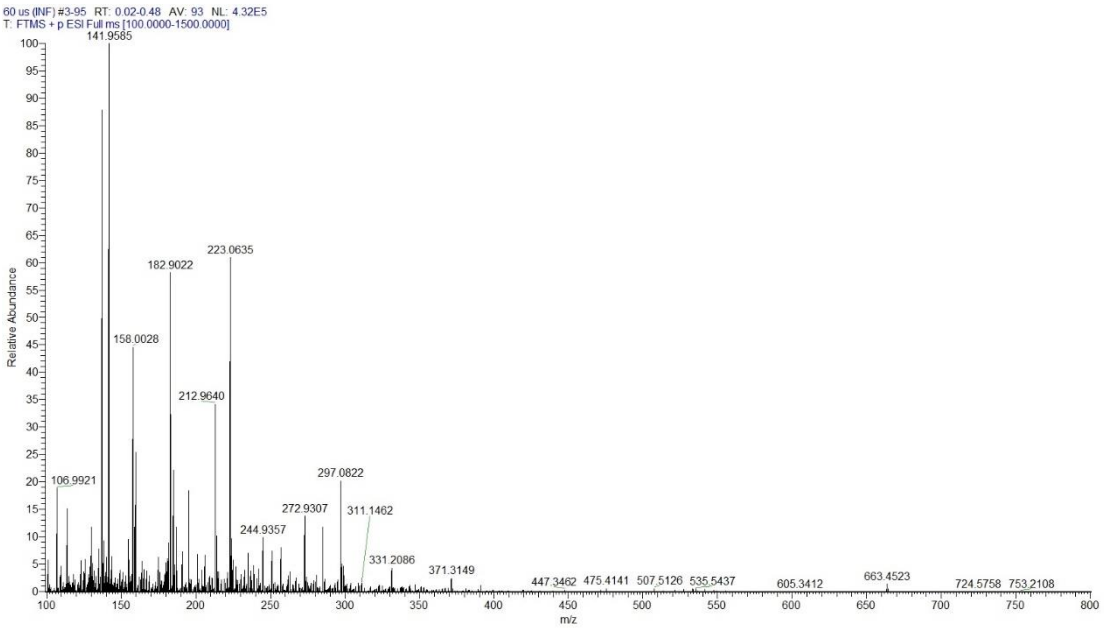

Figure A. 3 MS spectrum of the plasma produced by graphite ablation. (The Q-switch was 75 μs, the average energy of each pulse is 114 mJ, and the distance is 43.6 mm.)

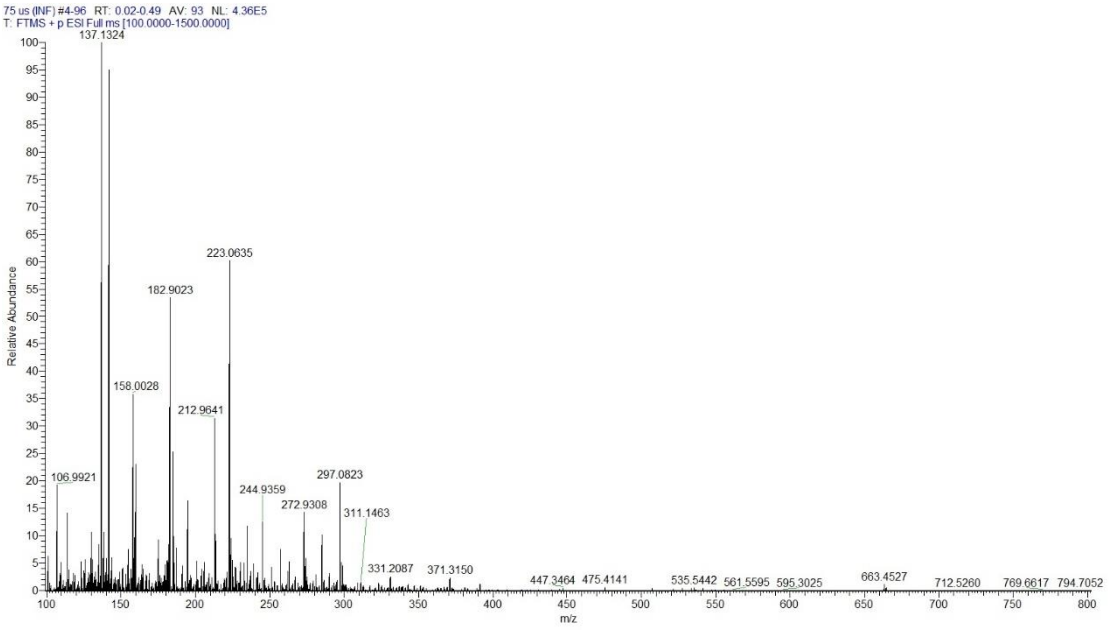

Figure A. 4 MS spectrum of the plasma produced by graphite ablation. (The Q-switch was 135 μs, the average energy of each pulse was 11.1 mJ, and the distance was 43.6 mm.)

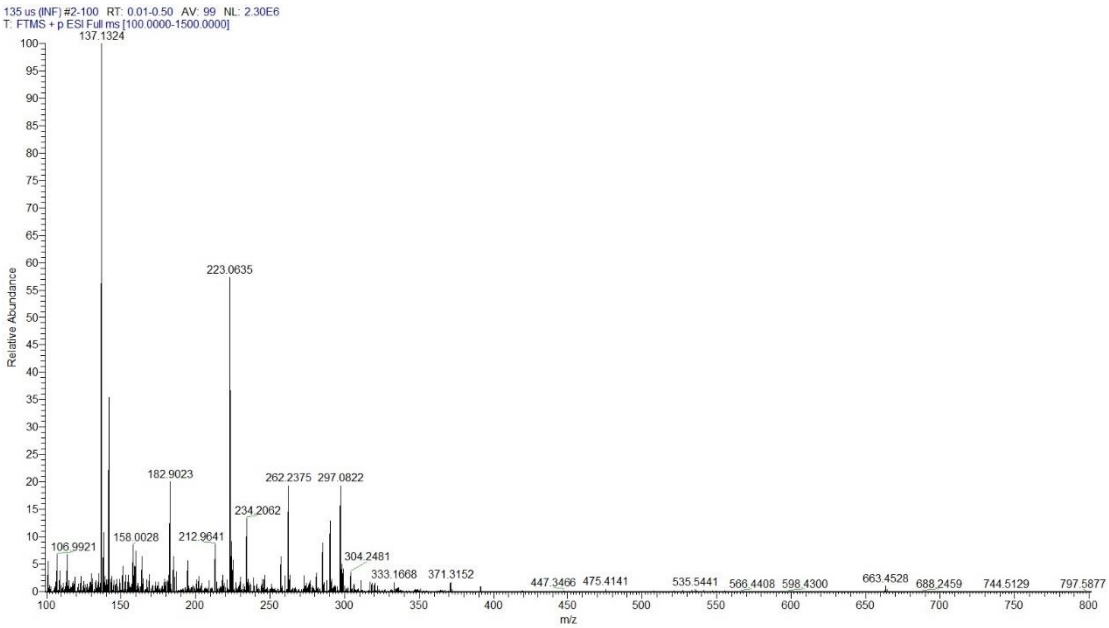

Figure A. 5 MS spectrum of the plasma produced by graphite ablation. (The Q-switch was 150 μs, the average energy of each pulse was 4.88 mJ, and the distance was 43.6 mm.)

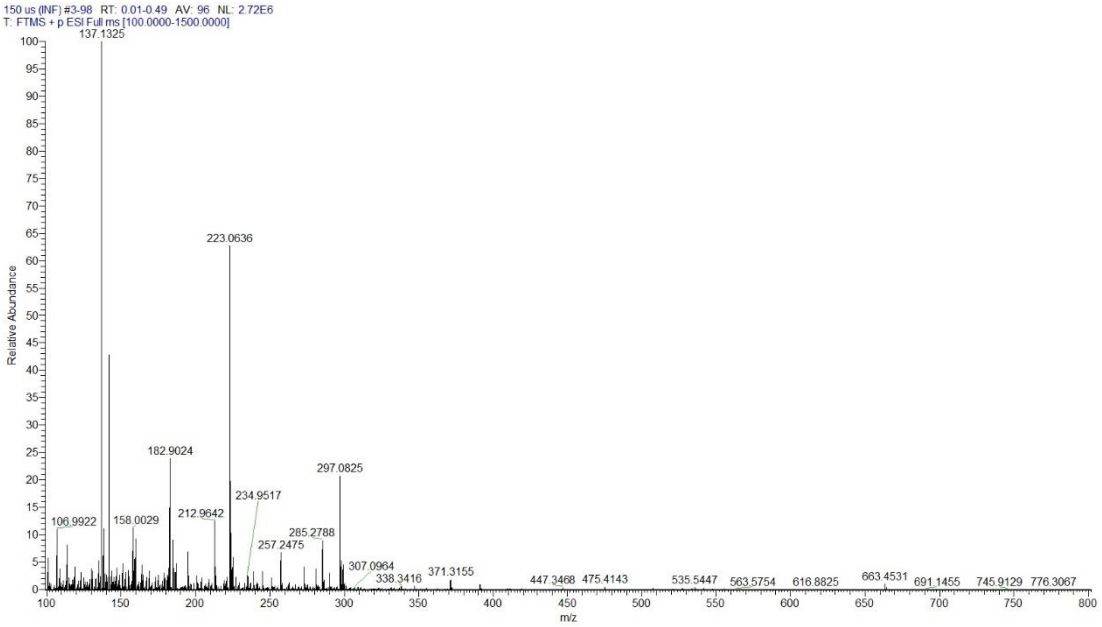

Figure A. 6 MS spectrum of the plasma produced by graphite ablation. (The Q-switch was 45 μs, the average energy of each pulse was 182 mJ, and the distance was 42.7 mm.)

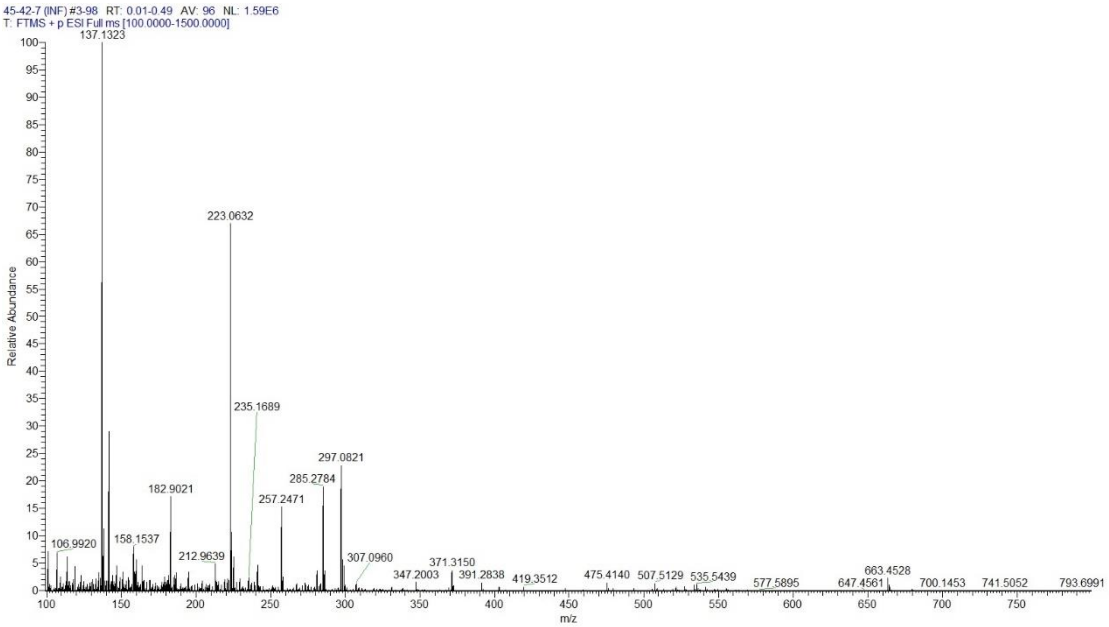

Figure A. 7 MS spectrum of the plasma produced by graphite ablation. (The Q-switch was 60 μs, the average energy of each pulse was 138 mJ, and the distance was 43.6 mm.)

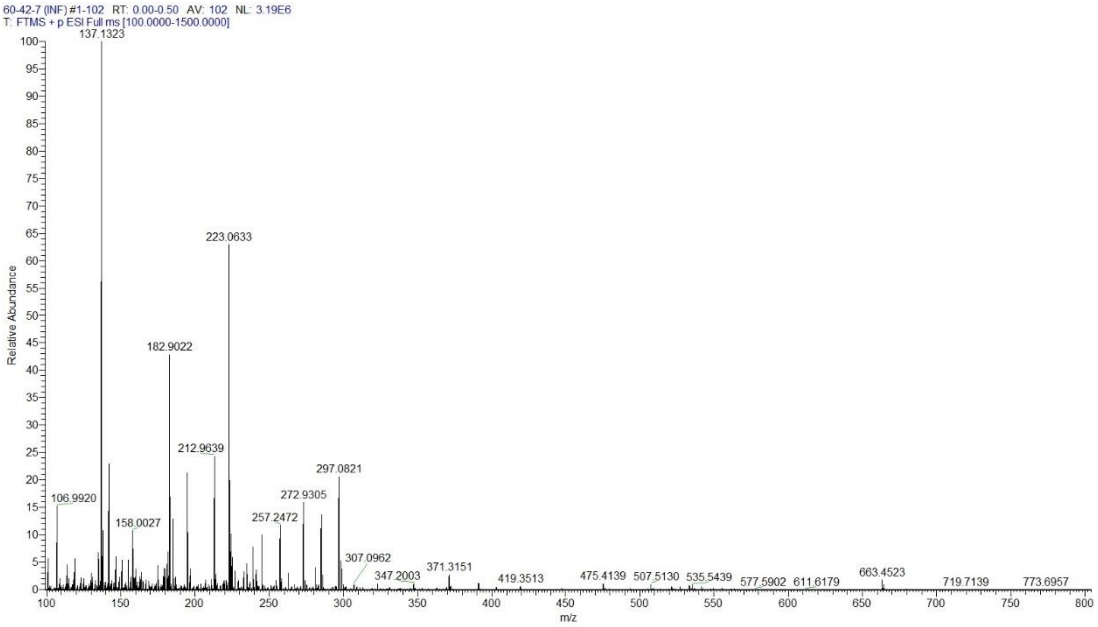

Figure A. 8 MS spectrum of the plasma produced by graphite ablation. (The Q-switch was 150 μs, the average energy of each pulse was 6.19 mJ, and the distance was 43.6 mm.)

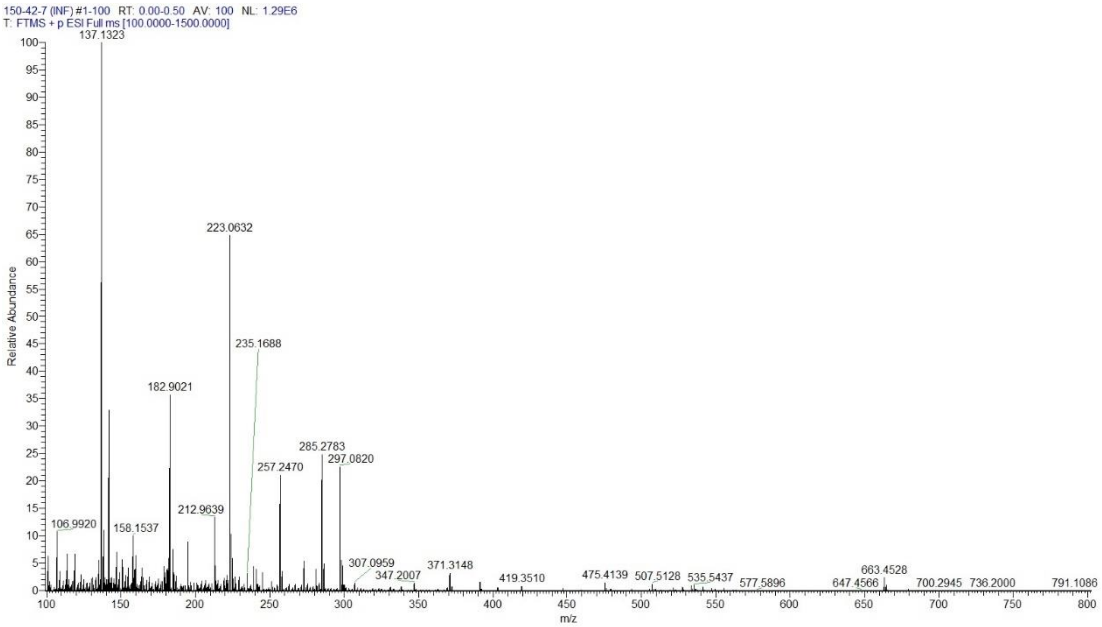

Figure A. 9 MS spectrum of the plasma produced by graphite ablation. (The Q-switch was 45 μs, the average energy of each pulse was 169 mJ, and the distance was 38.2 mm.)

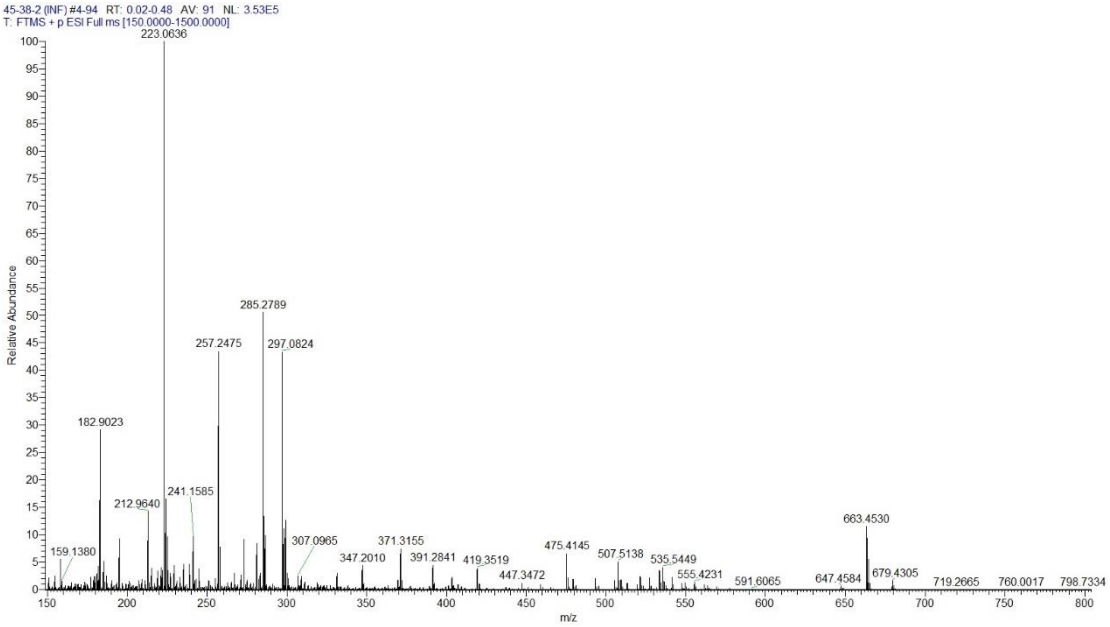

Figure A. 10 MS spectrum of the plasma produced by graphite ablation. (The Q-switch was 60 μs, the average energy of each pulse was 158 mJ, and the distance was 38.2 mm.)

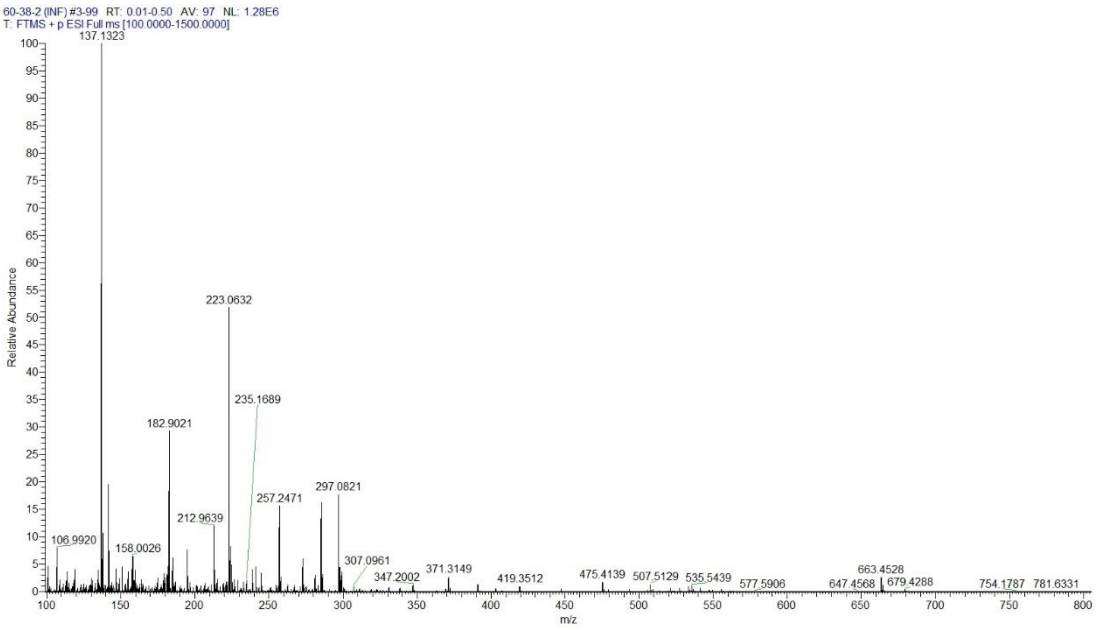

Figure A. 11 MS spectrum of the plasma produced by graphite ablation. (The Q-switch was 150 μs, the average energy of each pulse was 6.25 mJ, and the distance was 38.2 mm.)

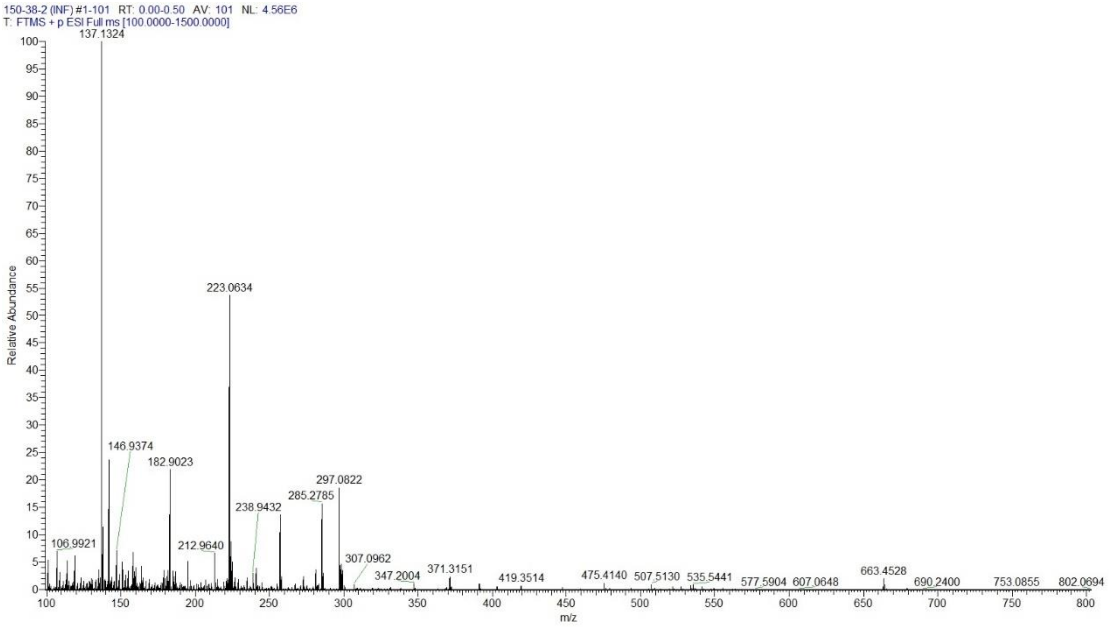

Appendix B: Figure for Section 3.4.4

Figure B. 1 IR spectra of areas A and C of sample SWS5-C5

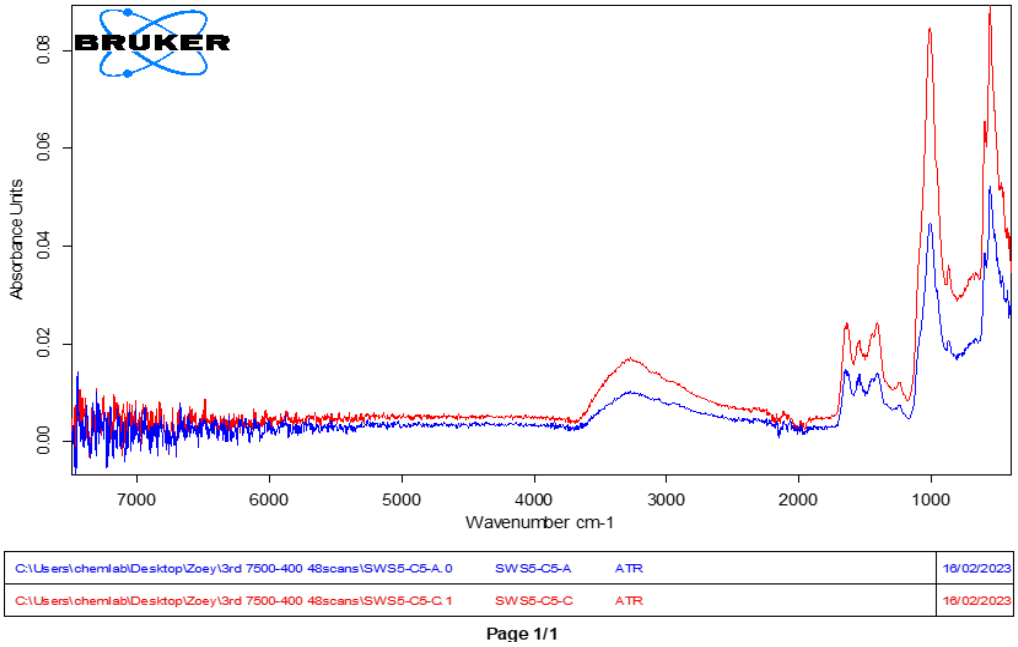

Figure B. 2 IR spectra of areas A, and C of sample SWL7-5

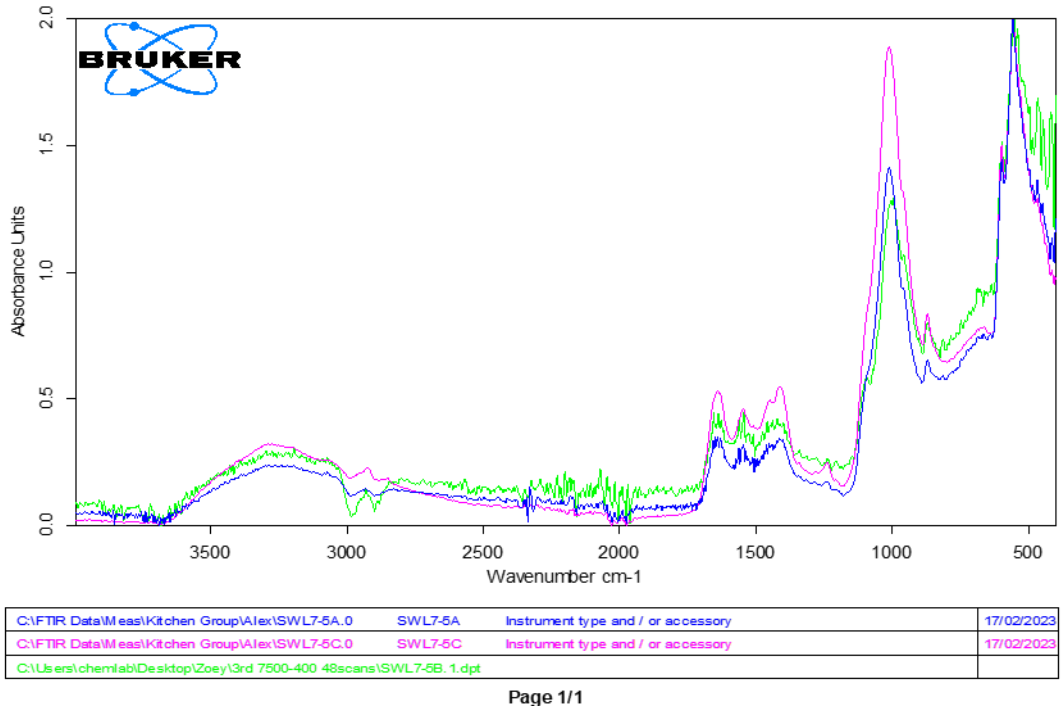

Figure B. 3 IR spectra of areas A, B, and C of sample SWL8-4

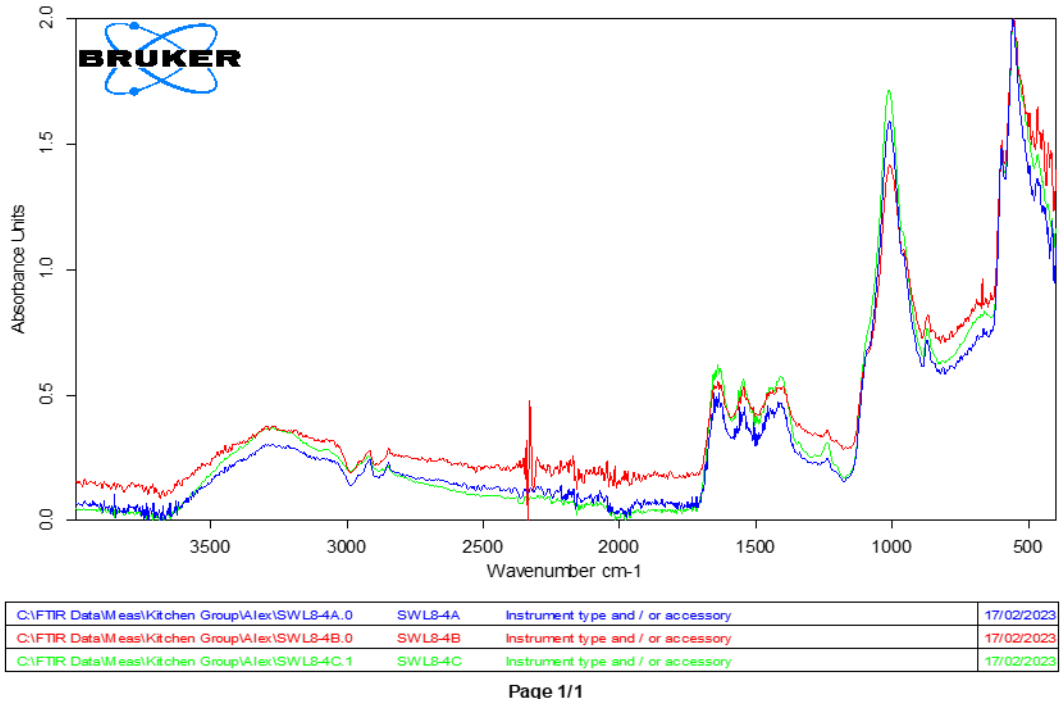

Figure B. 4 IR spectra of areas A, B, and C of sample SWS-B6

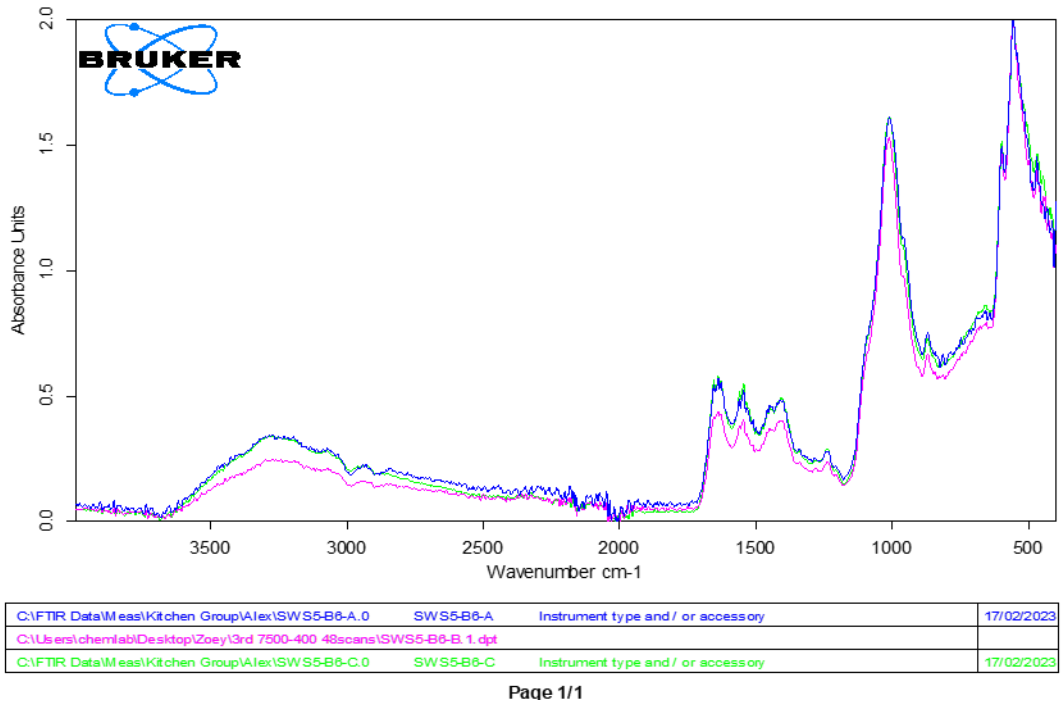

Figure B. 5 IR spectra of areas A, B, and C of sample SWS5-D2

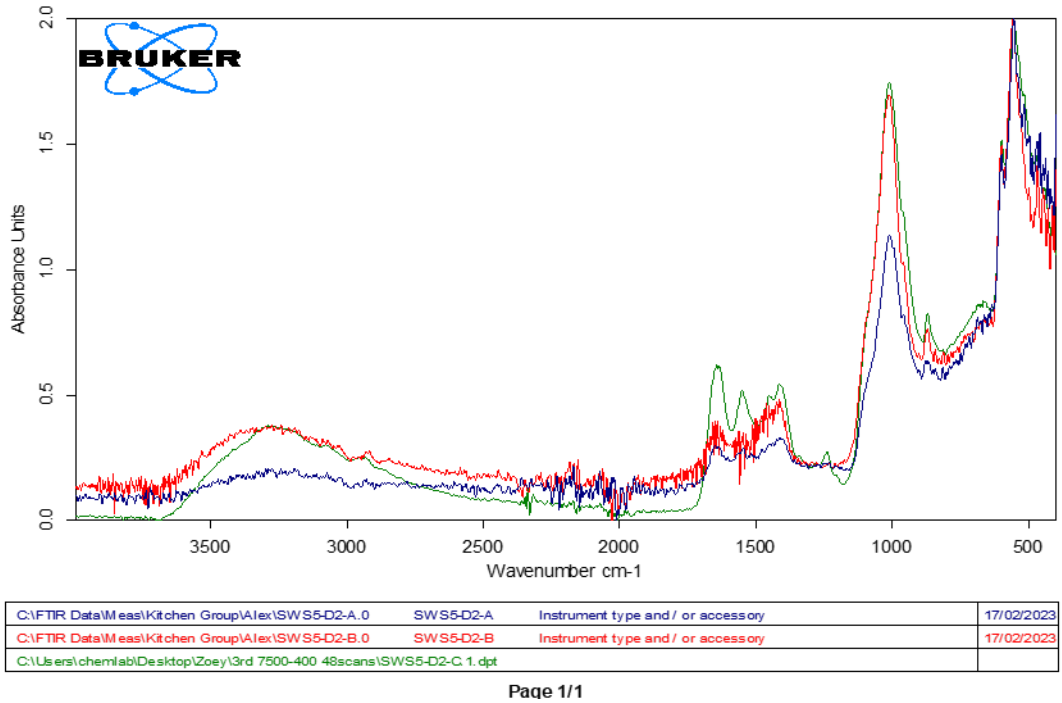

Figure B. 6 The IR spectrum of the NWN3 vertebral half (edge)

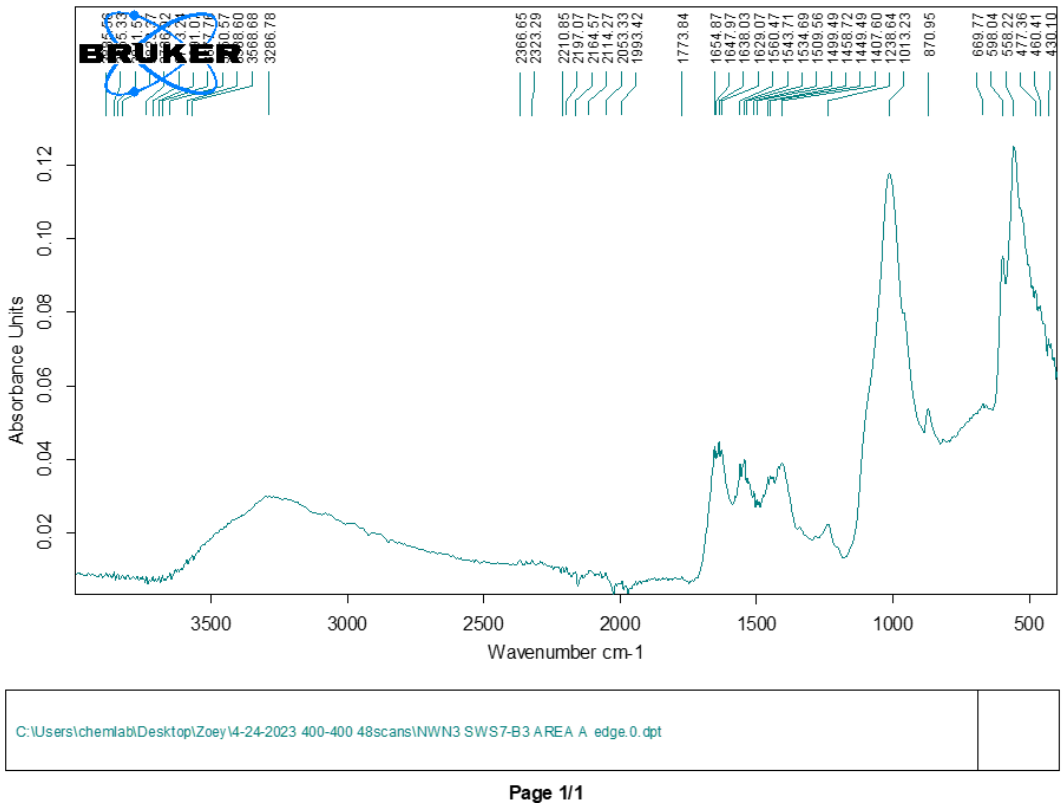

Figure B. 7 The IR spectrum of the NWN3 vertebral half (center)

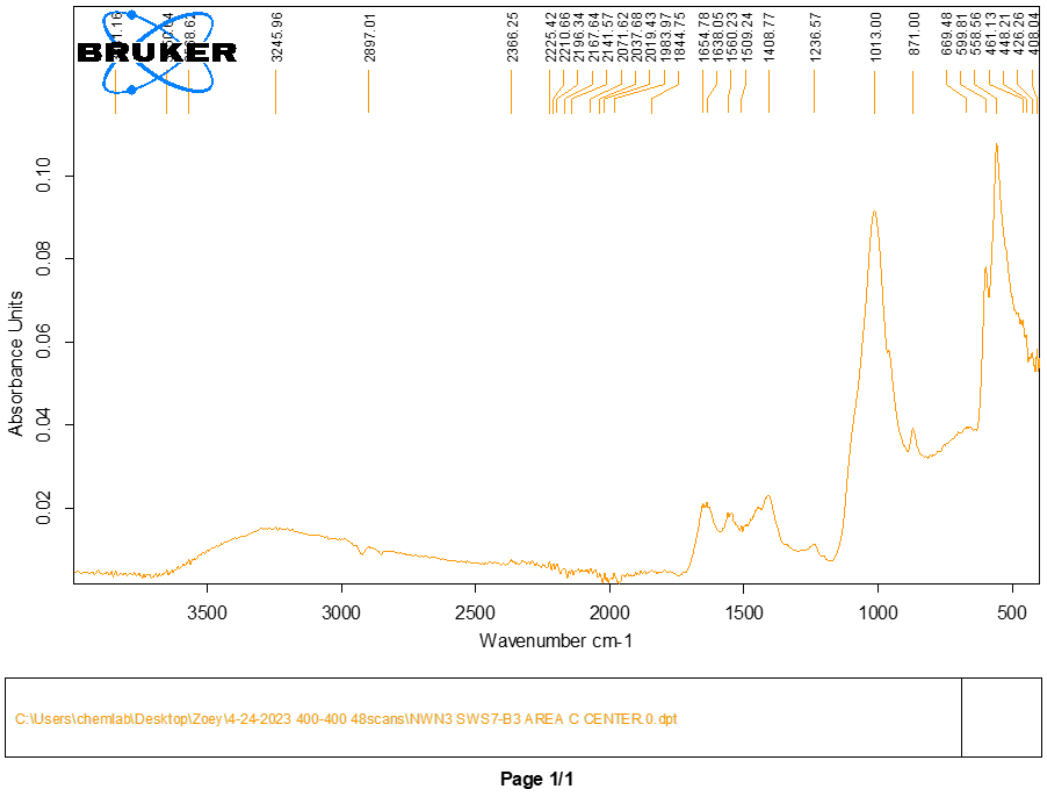

Figure B. 8 The IR spectrum of the SDSOE vertebral half (edge)

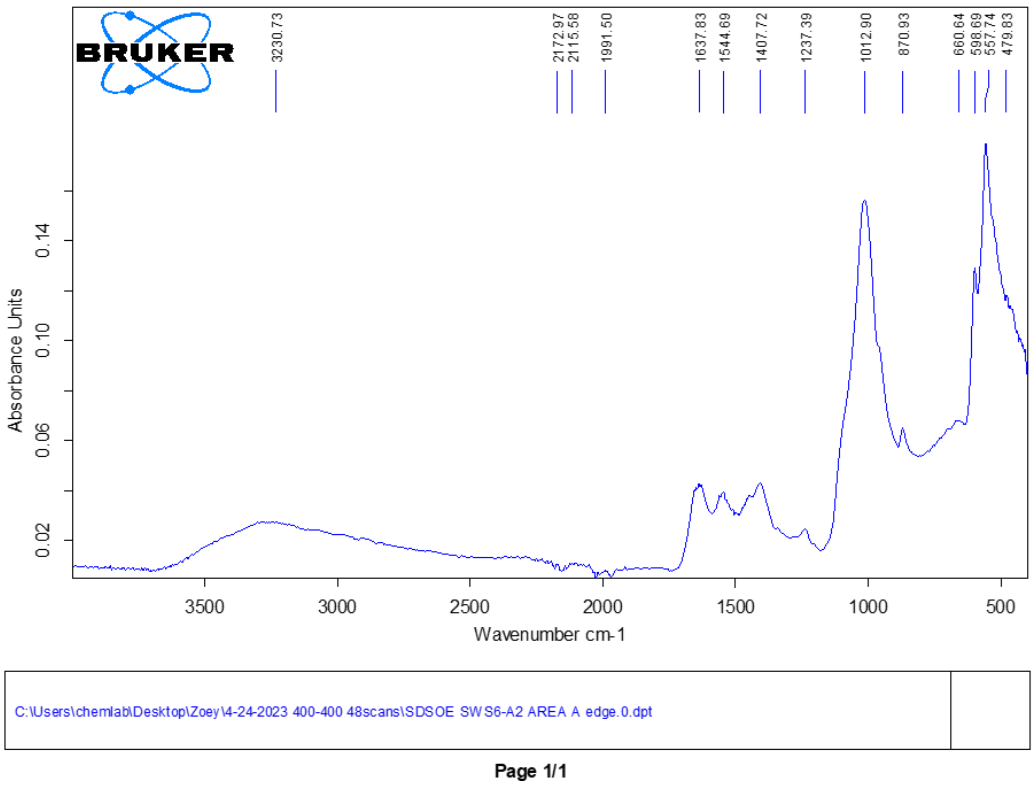

Figure B. 9 The IR spectrum of the SDSOE vertebral half (center)

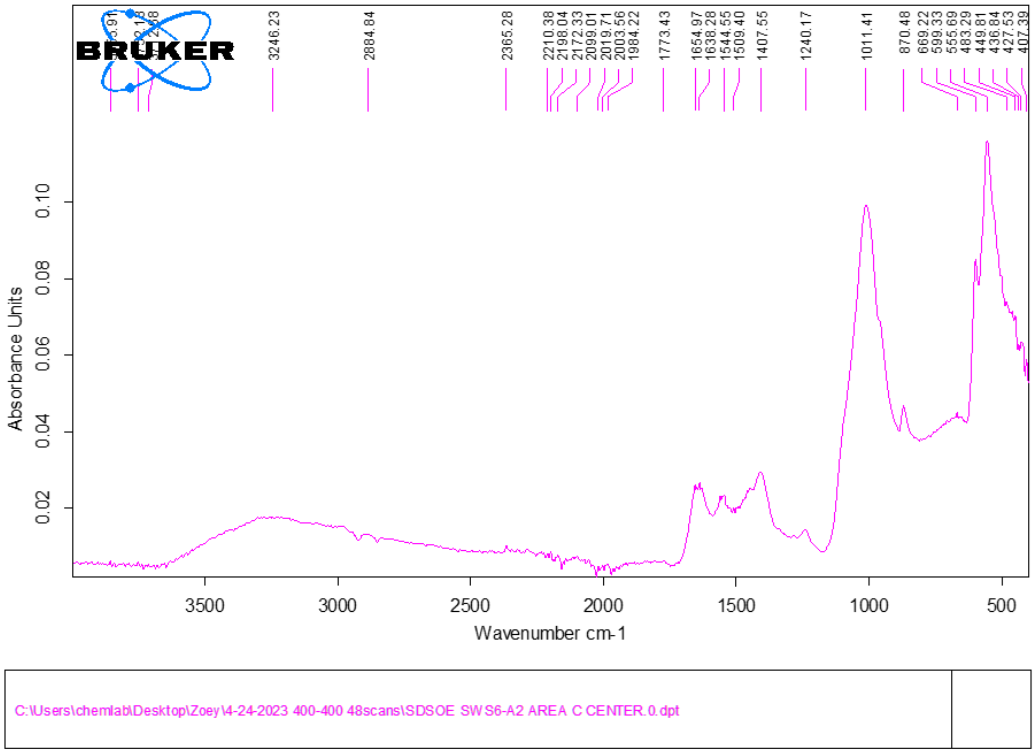

Figure B. 10 The IR spectrum of the MF5 vertebral half (edge)

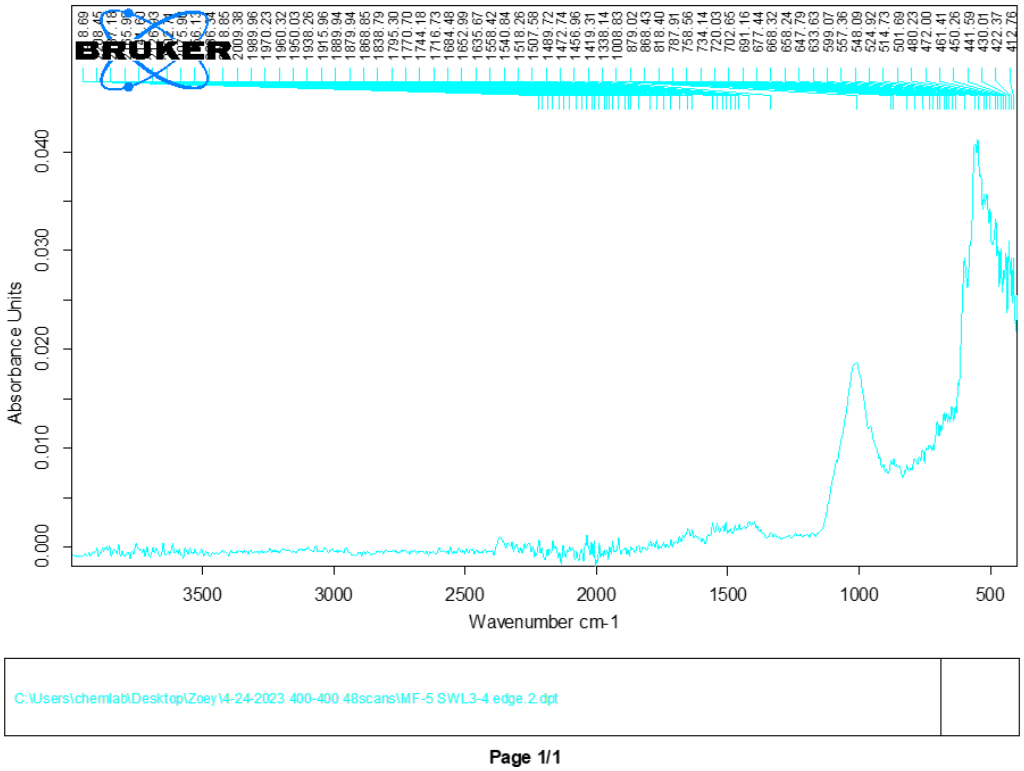

Figure B. 11 The IR spectrum of the MF5 vertebral half (center)

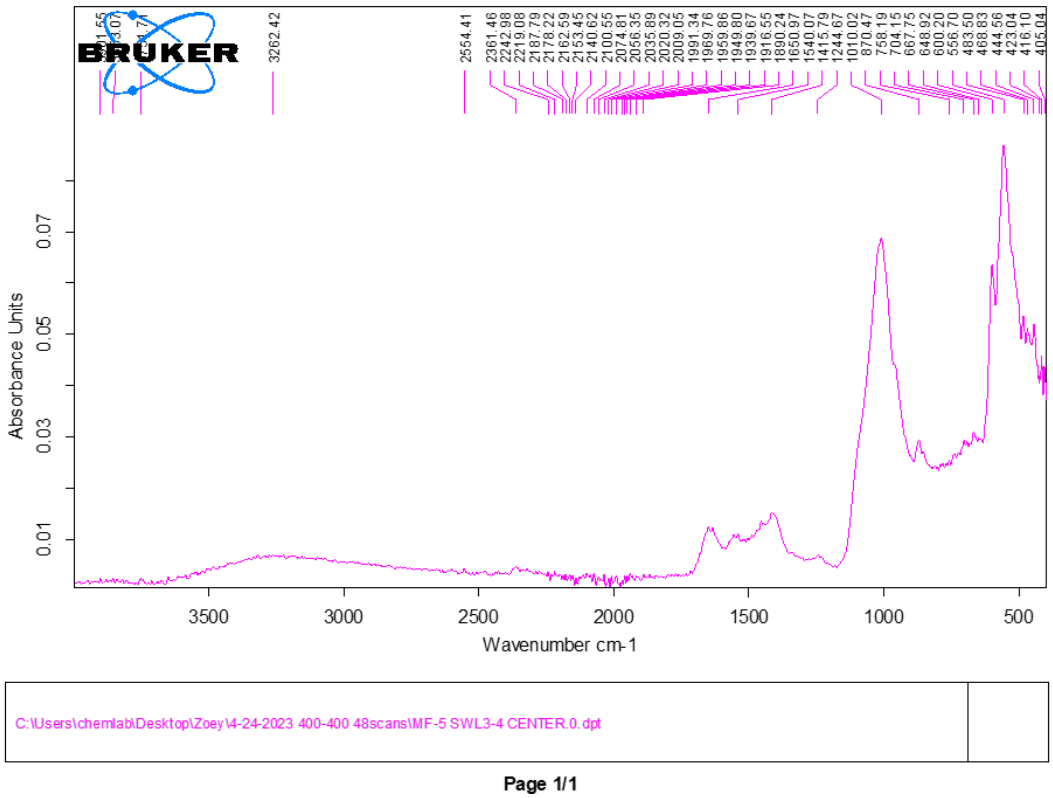

Figure B. 12 The IR spectrum of the NWN9 vertebral half (edge)

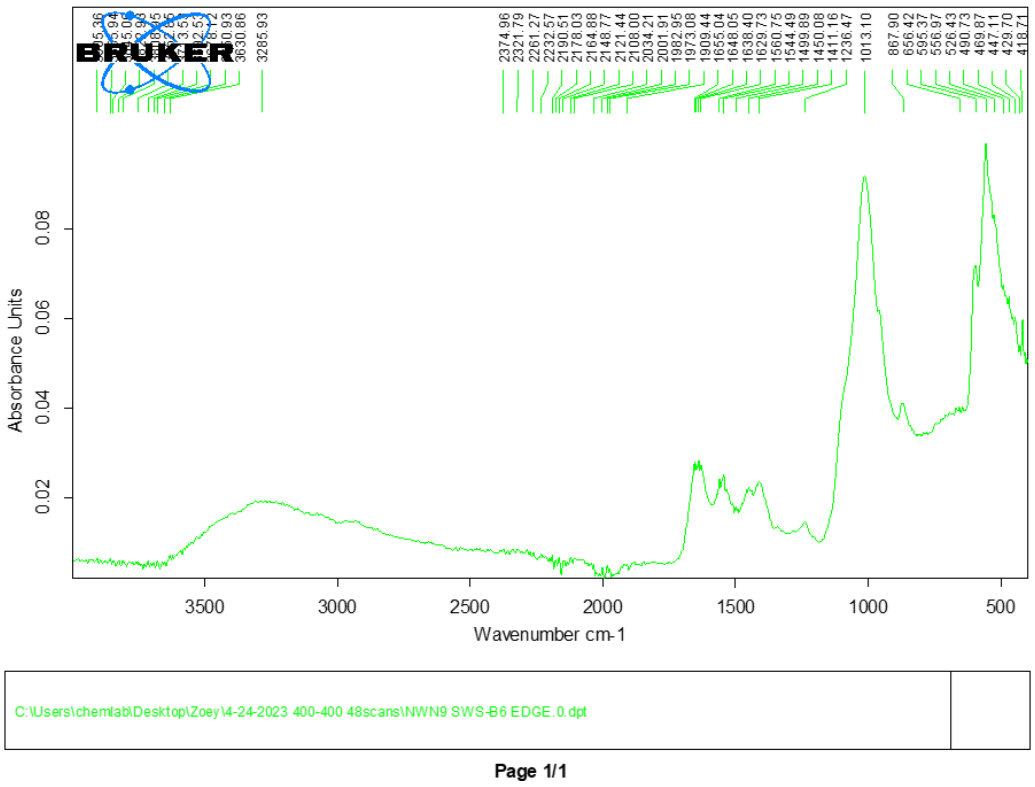

Figure B. 13 The IR spectrum of the NWN9 vertebral half (center)

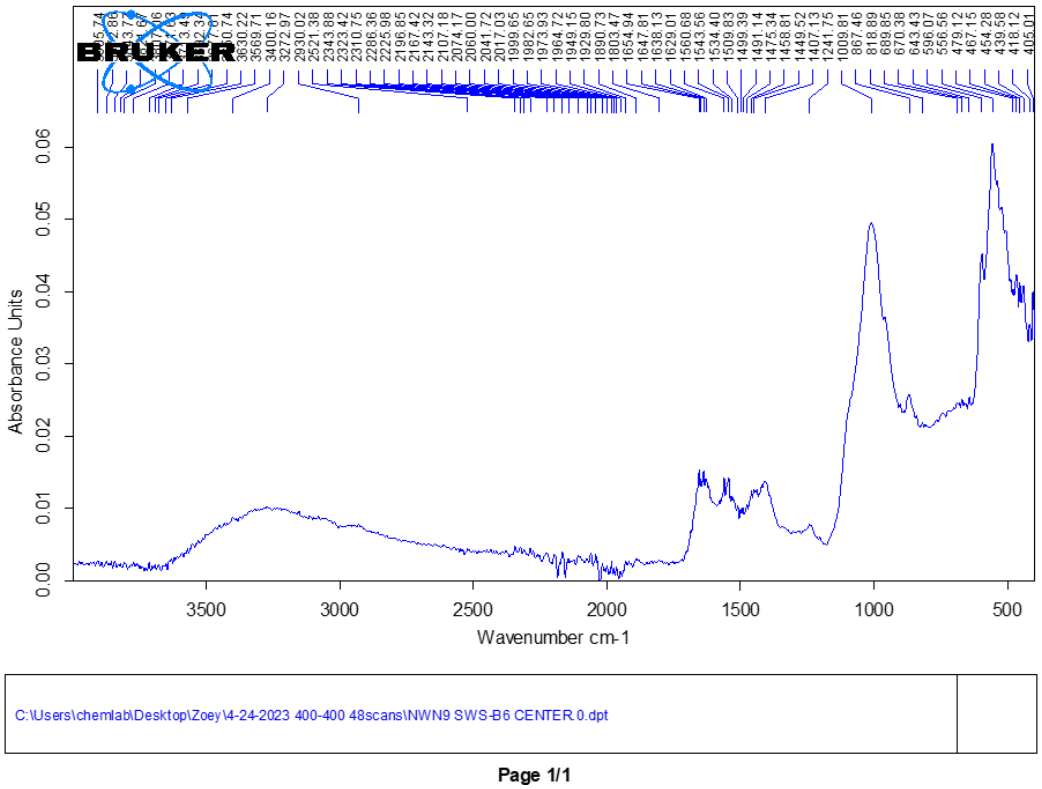

Figure B. 14 The IR spectrum of the NWN8 vertebral half (edge)

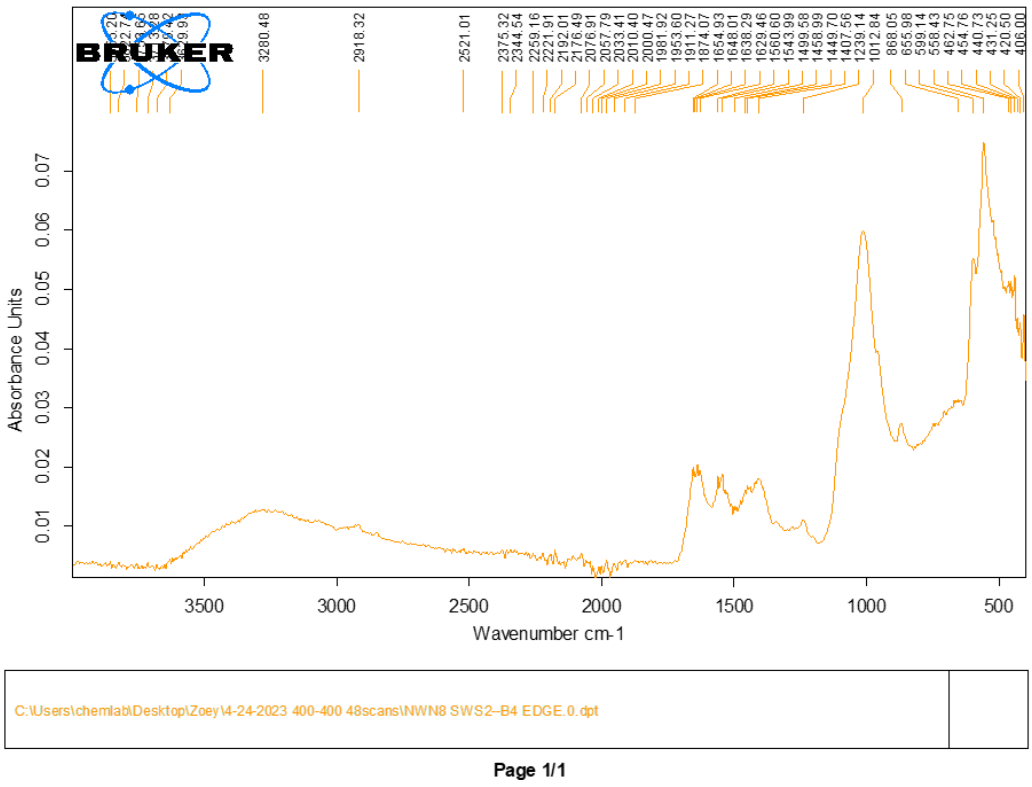

Figure B. 15 The IR spectrum of the NWN8 vertebral half (center)

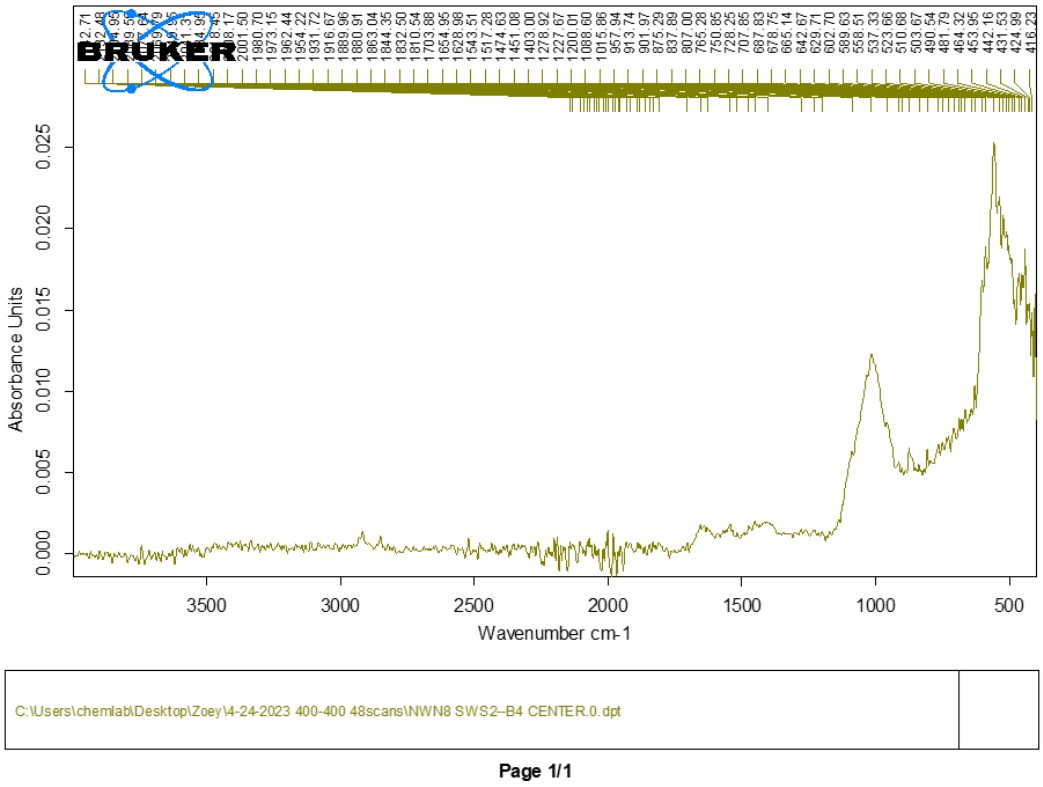

Figure B. 16 The IR spectrum of the J17 vertebral half (edge)

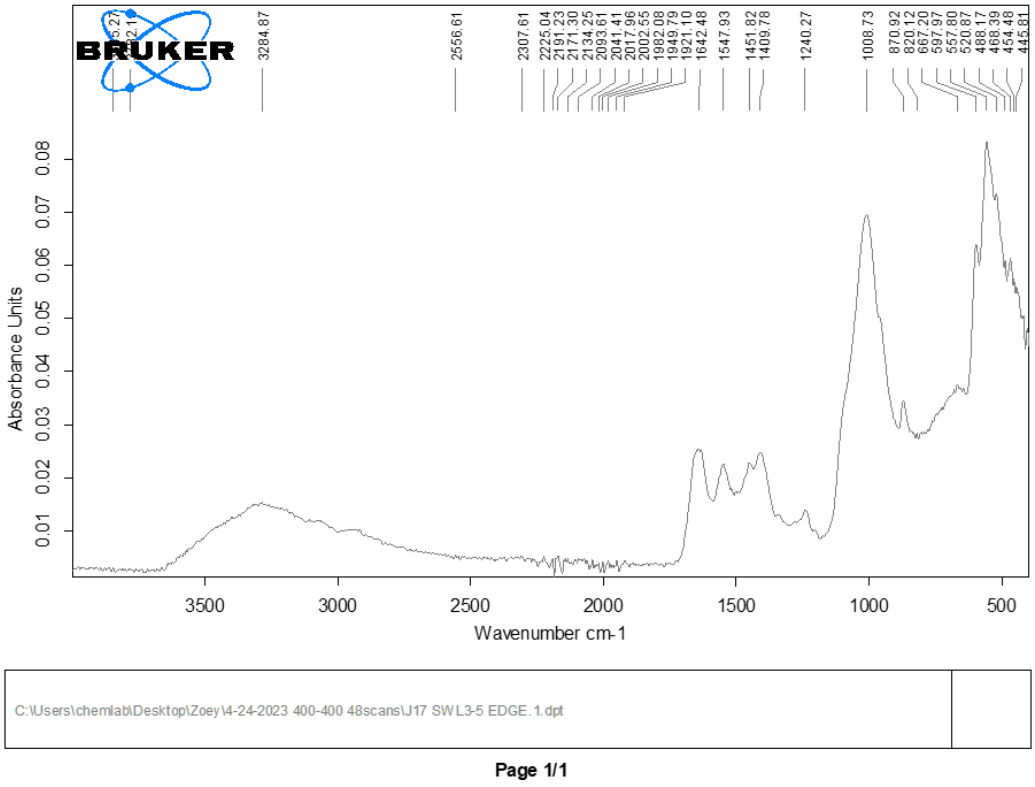

Figure B. 17 The IR spectrum of the J17 vertebral half (center)

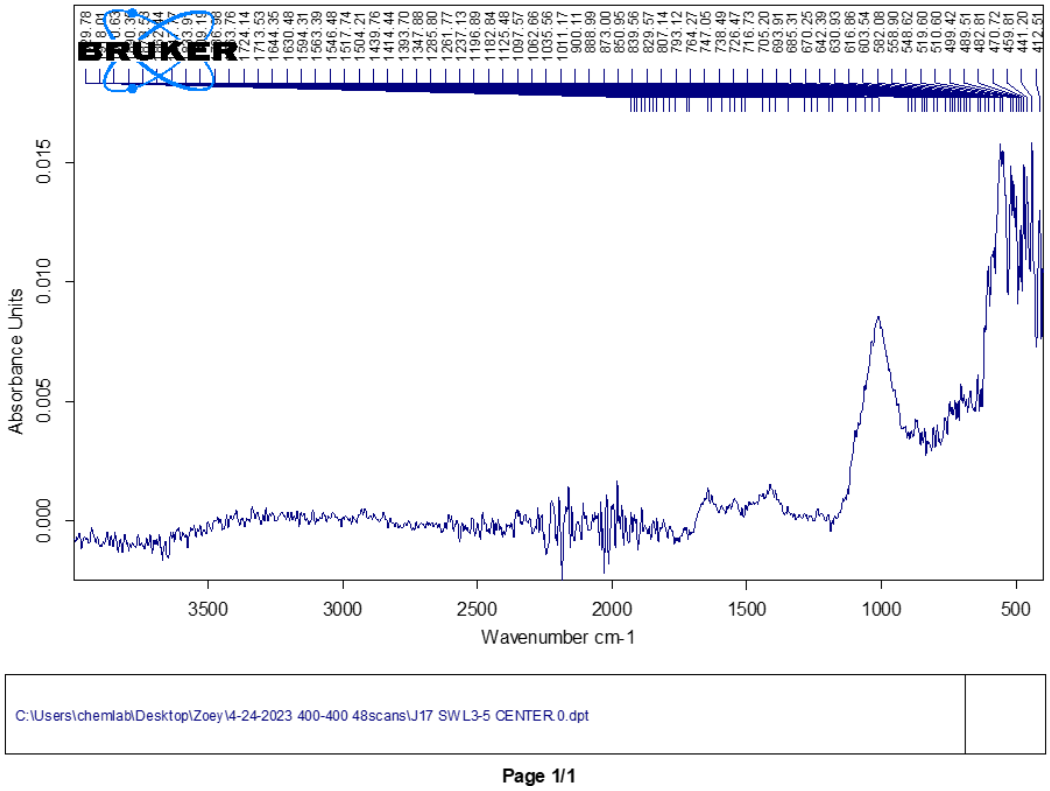

Figure B. 18 The IR spectrum of the MF1vertebral half (edge)

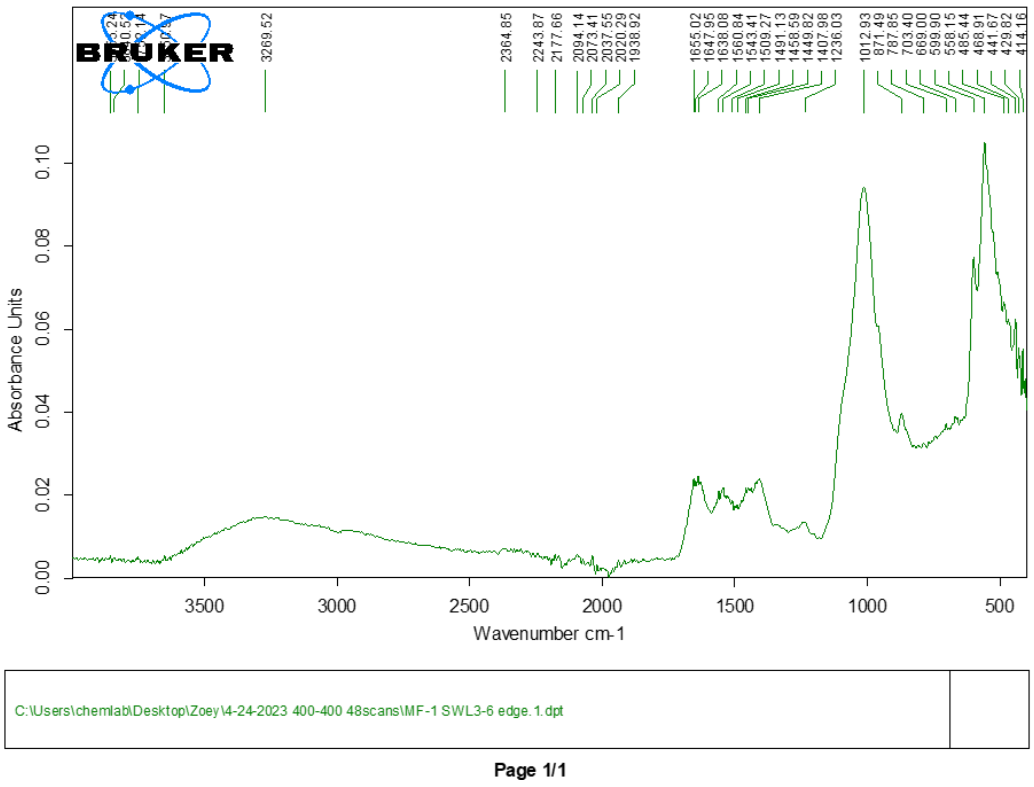

Figure B. 19 The IR spectrum of the MF1vertebral half (center)

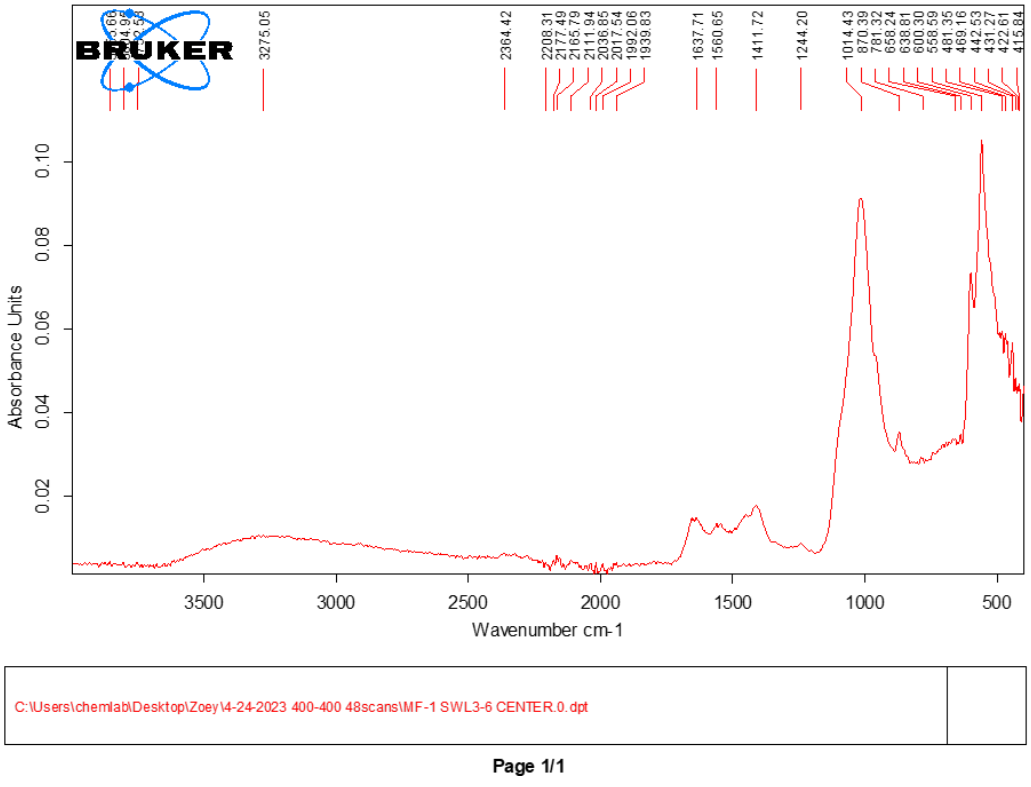

Figure B. 20 The IR spectrum of the MF8 vertebral half (edge)

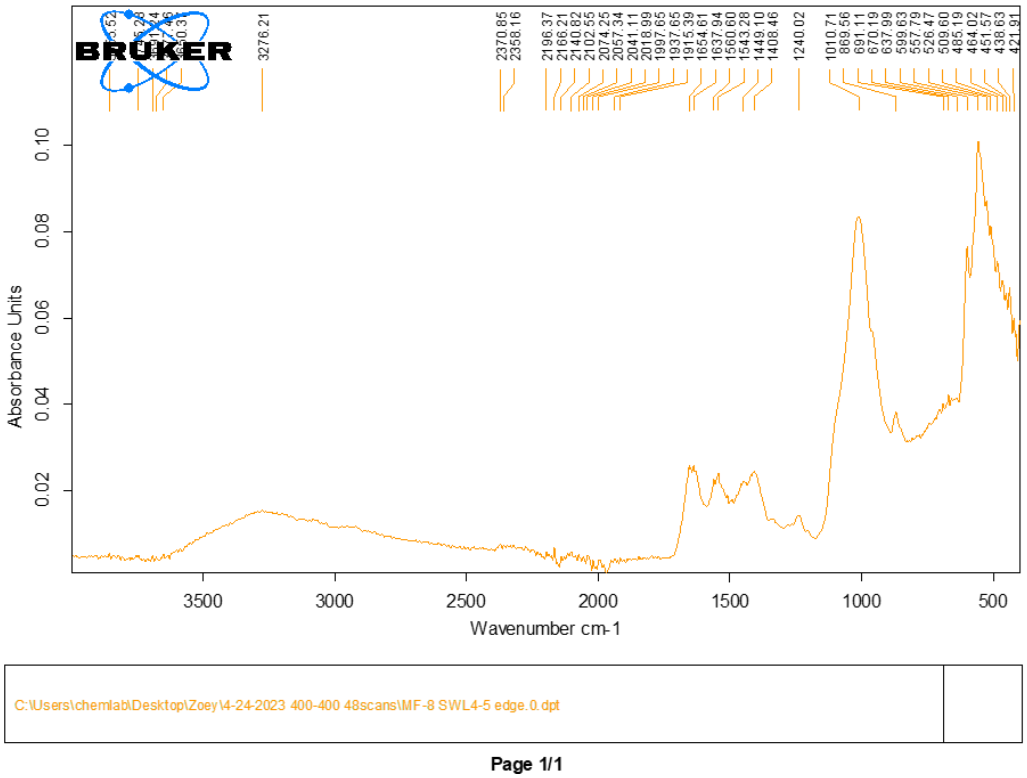

Figure B. 21 The IR spectrum of the MF8 vertebral half (center)

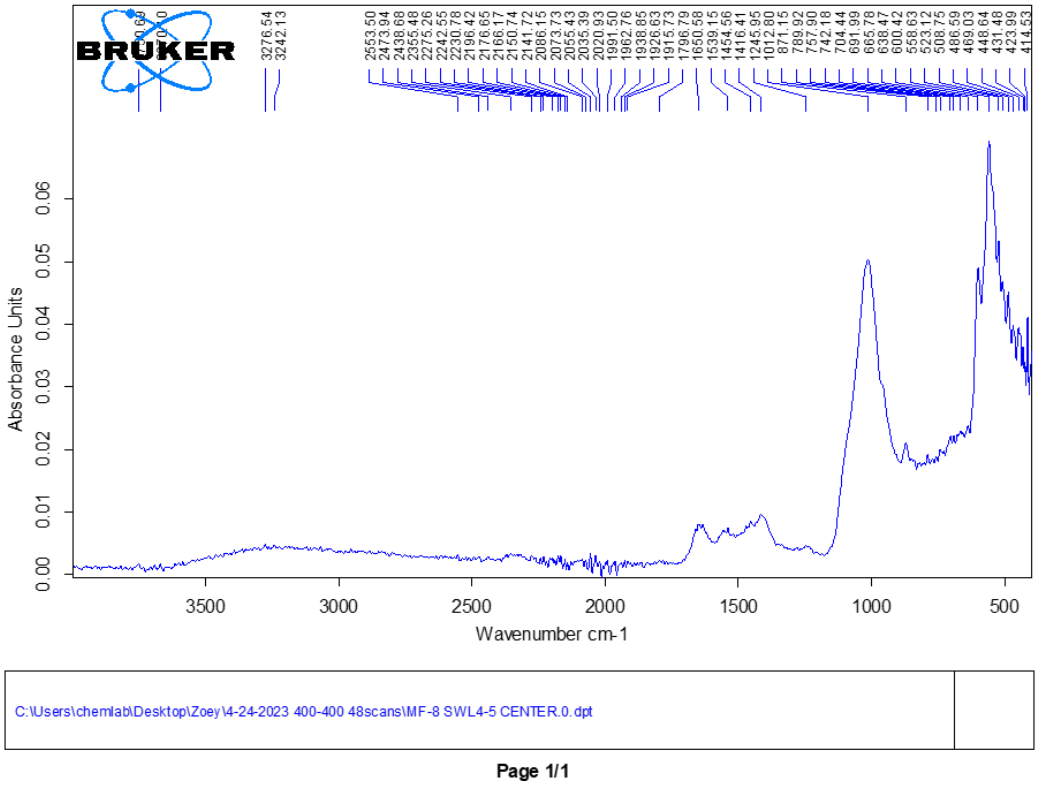

Figure B. 22 The IR spectrum of the J28 vertebral half (edge)

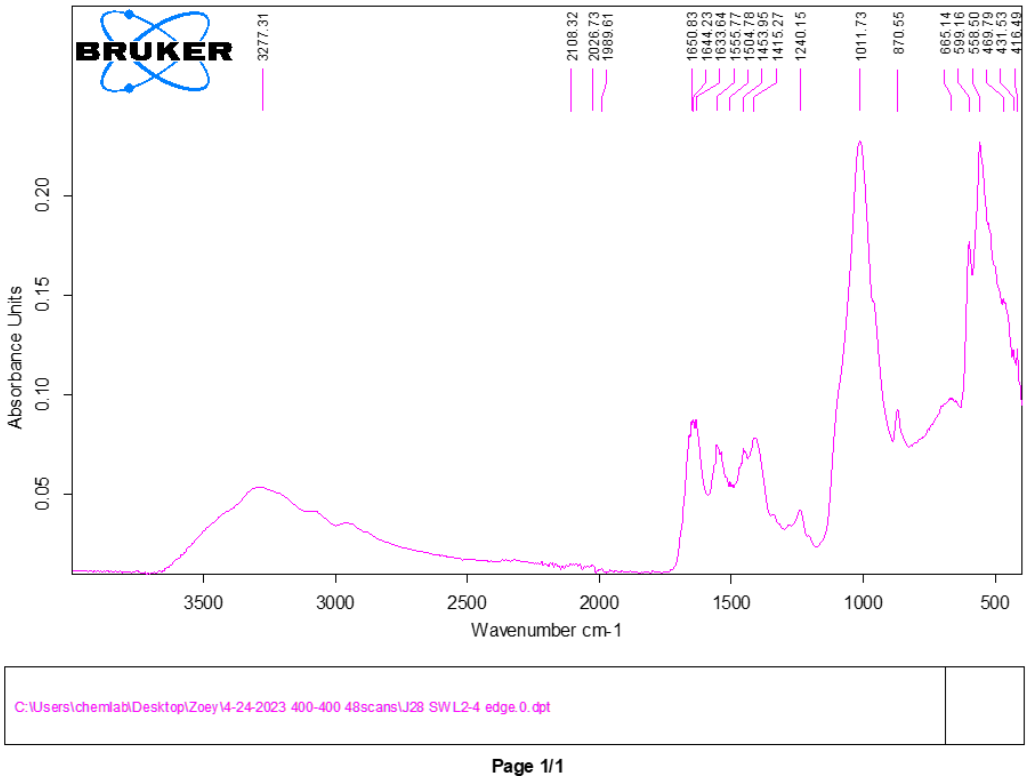

Figure B. 23 The IR spectrum of the J28 vertebral half (center)

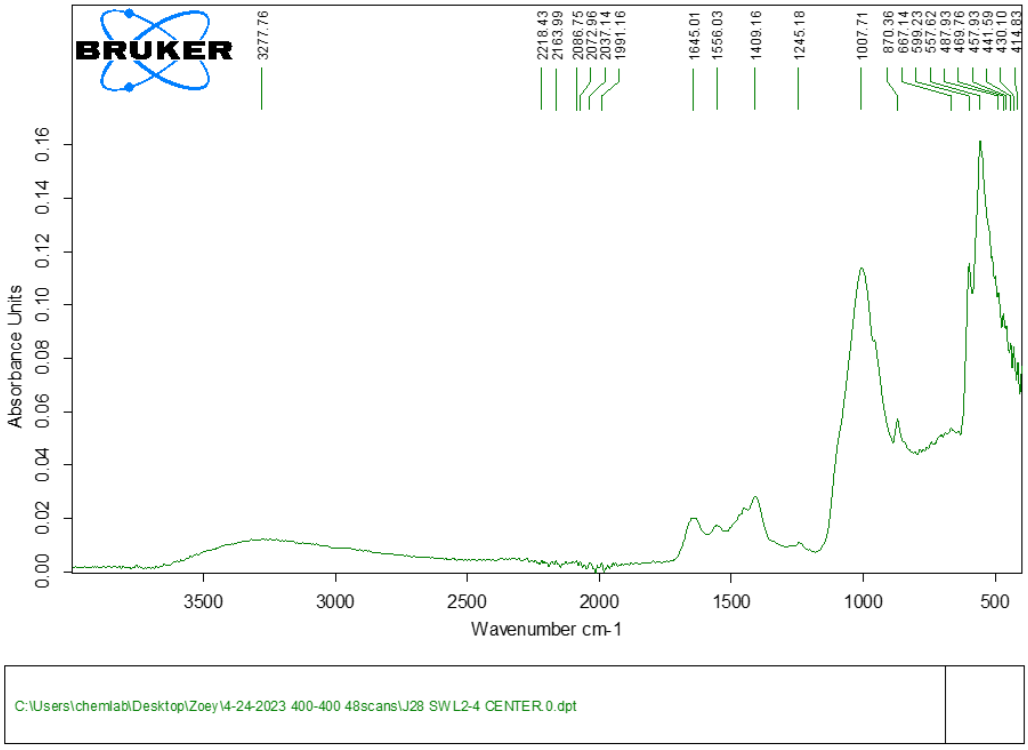

Figure B. 24 The IR spectrum of the J19 vertebral half (edge)

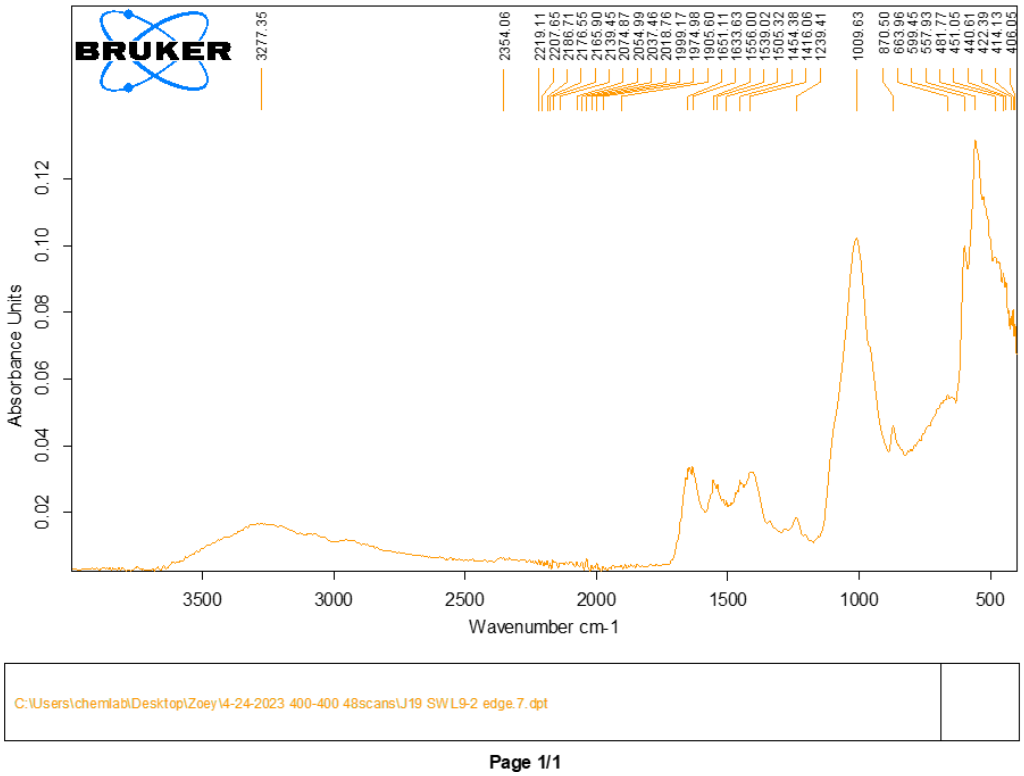

Figure B. 25 The IR spectrum of the J19 vertebral half (center)

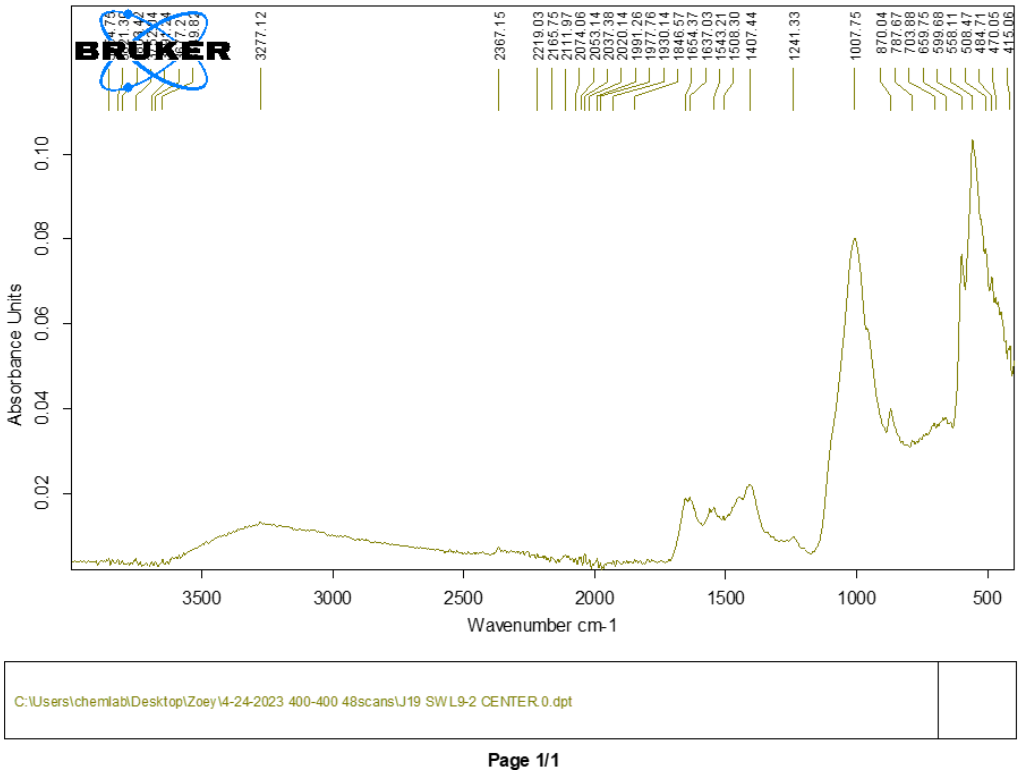

Page 1/1

Figure B. 26 The IR spectrum of the LG2 vertebral half (edge)

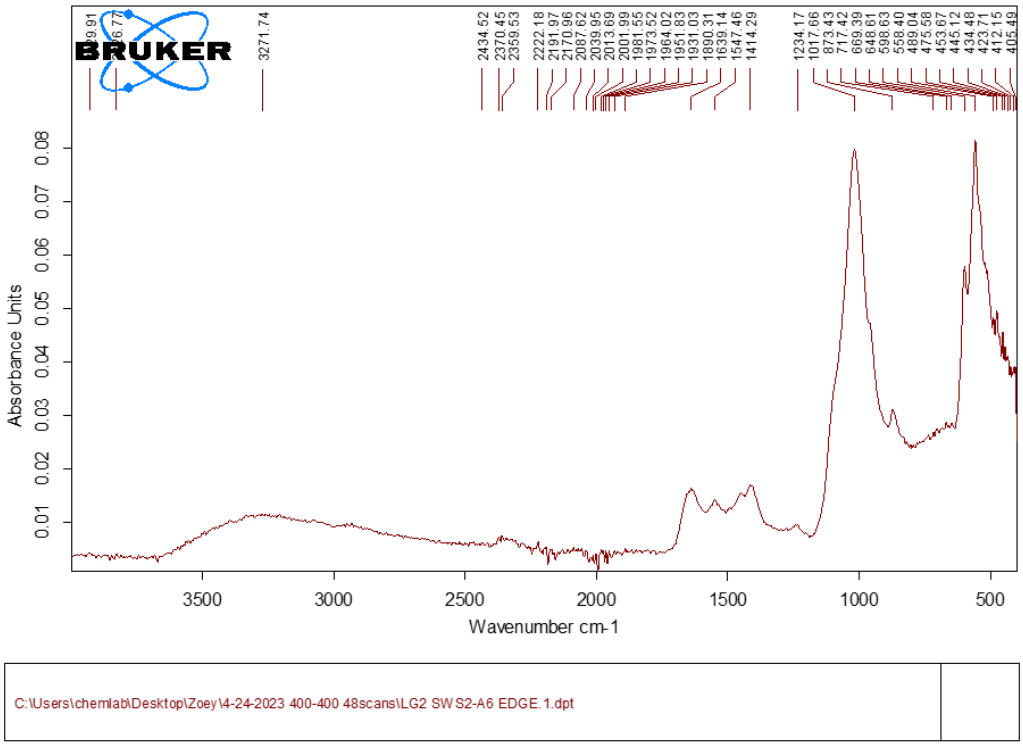

Page 1/1

Figure B. 27 The IR spectrum of the LG2 vertebral half (center)

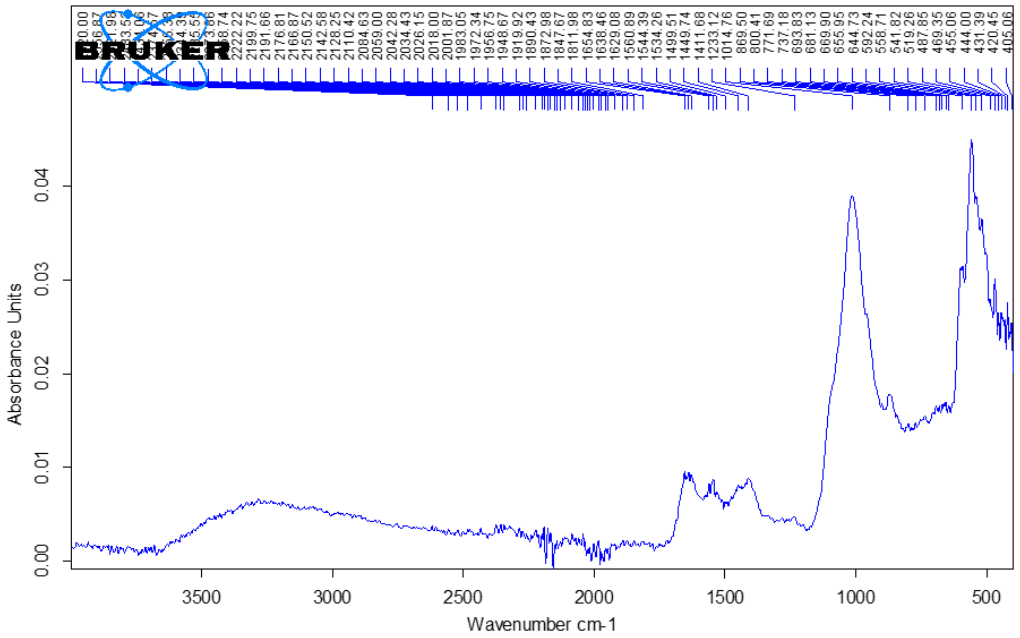

Page 1/1

Appendix C Figures for Section 3.4.5

Figure C. 1 Fluorescence spectrum of sample (S)

Figure C. 2 Fluorescence spectrum of cell (SM)

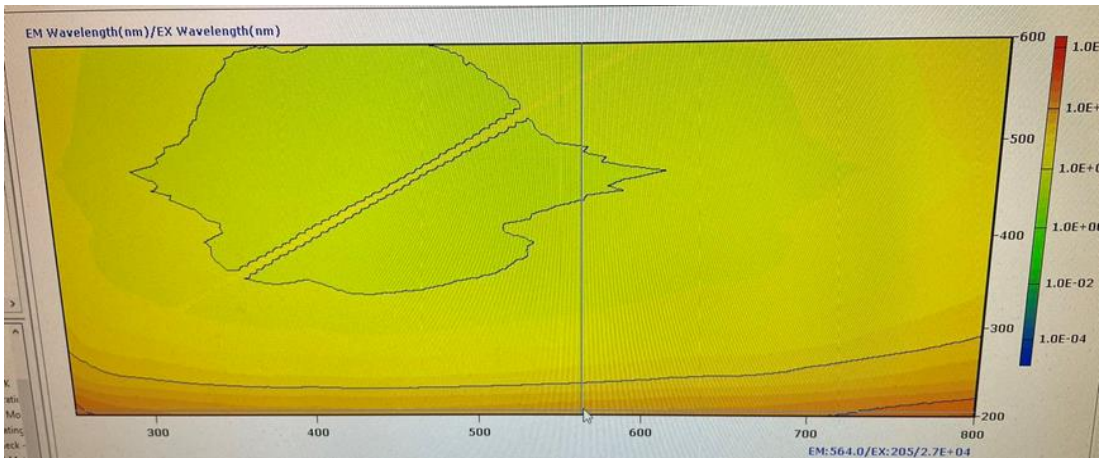

Figure C. 3 Fluorescence spectrum of (SB)

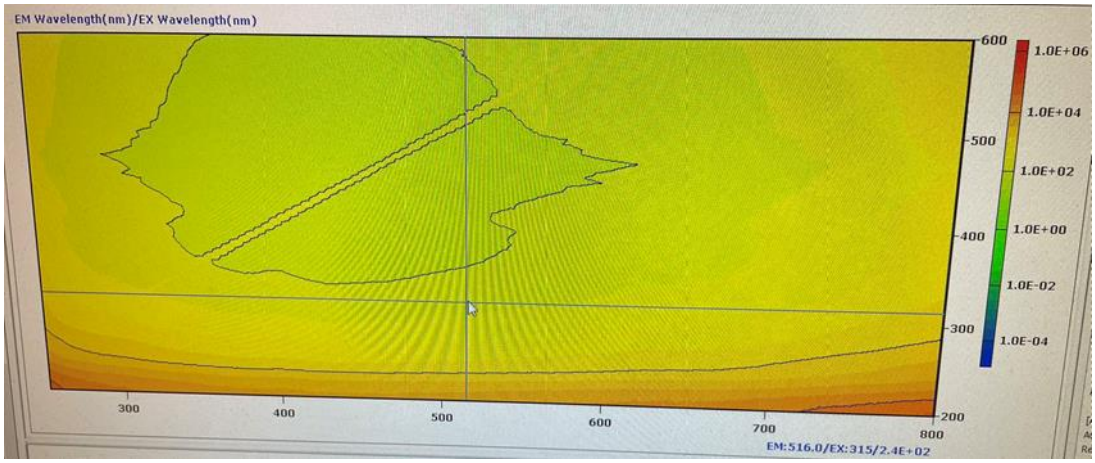

Figure C. 4 Fluorescence spectrum of (NS)

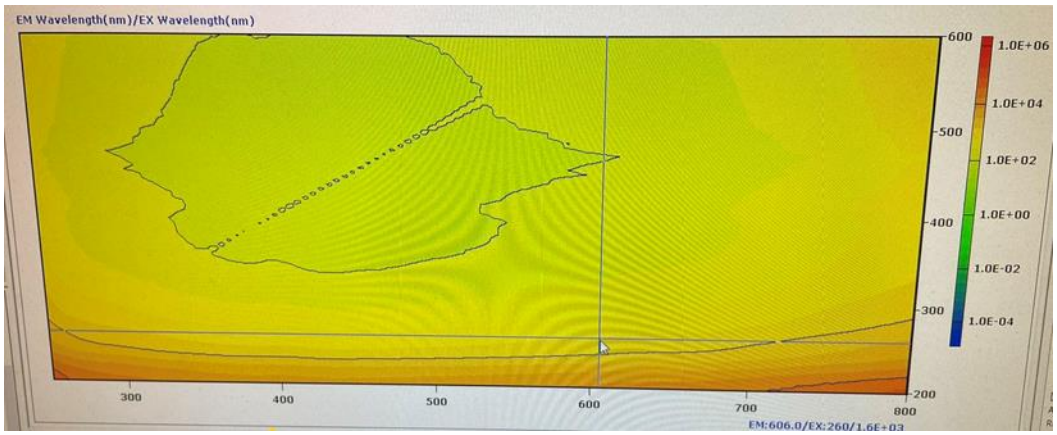

Figure C. 5 Fluorescence spectrum of samarium solution

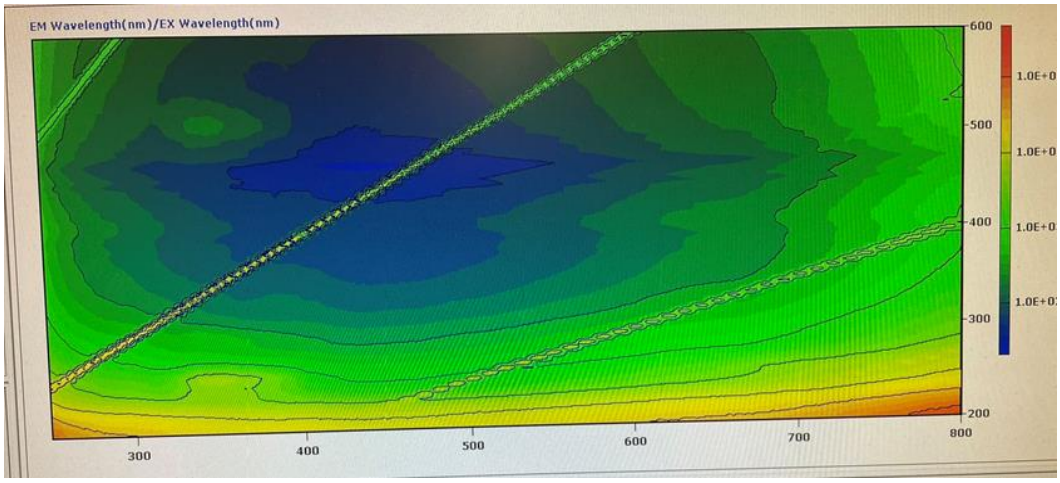

Figure C. 6 Fluorescence spectrum the GSP21 solution

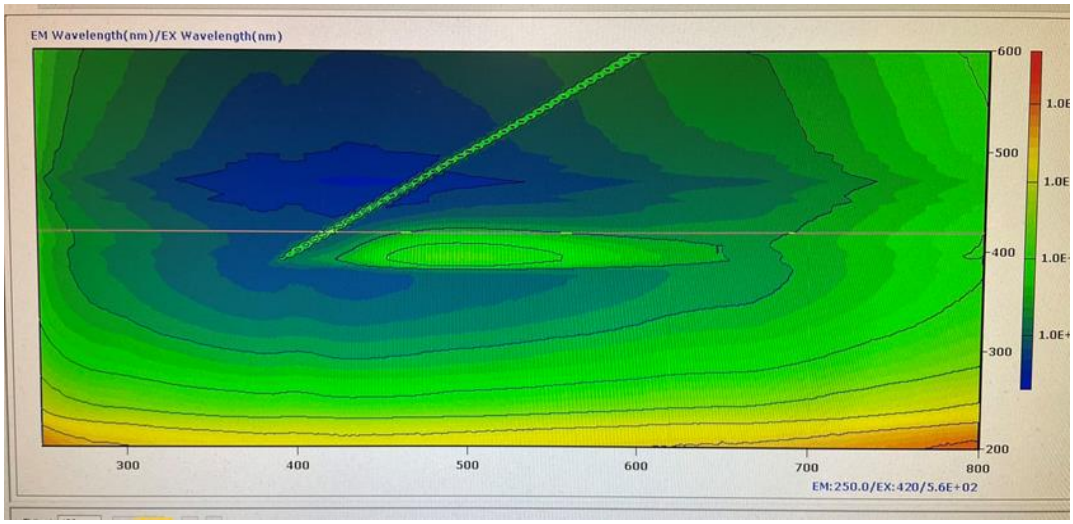

Appendix D Figures for Section 3.4.6

Figure D. 1 Sample SWL8-3

a). Indirect light: Few marks were shown at the edge of the vertebra.

b). Direct light: Few marks were shown.

Figure D. 2 Sample SWS5-C4

a). Direct light.

b). Direct light.

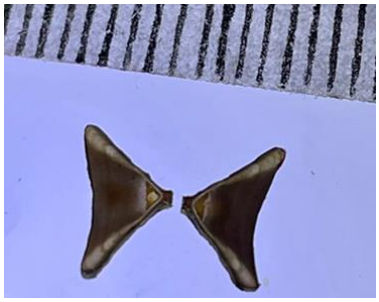

Figure D. 3 Sample SWW5-C6

a). Indirect light: no marks were observed.

b). Direct light.

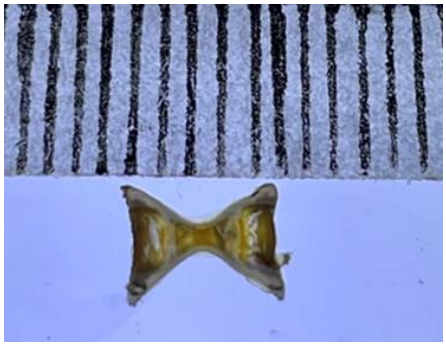

Appendix E Figures for Section 3.4.7

Sample JHARSOEGG-19_B1

The cutting plane and position were the same as in Sample 1. The section's thickness was 0.6 mm.

Figure E. 1 condition a

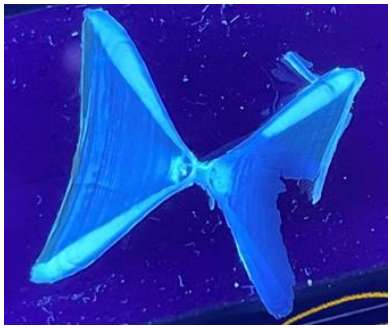

Figure E. 2 condition b

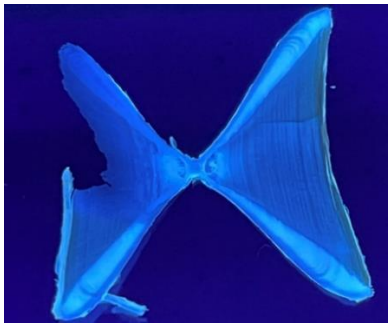

Figure E. 3 condition k

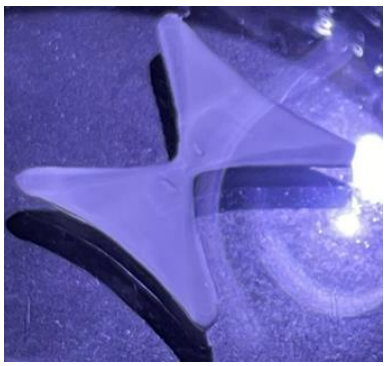

Figure E. 4 condition I

Figure E. 5 condition m

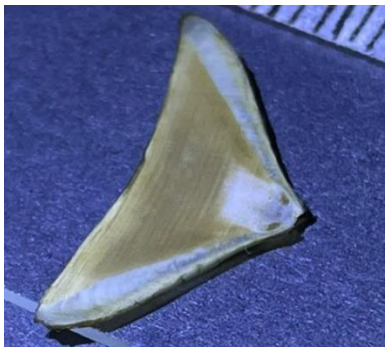

Sample NIWAWNGG013_B3

The cutting plane and position were the same as in Sample 1. The section's thinness was 0.6 mm.

Figure E. 6 condition a

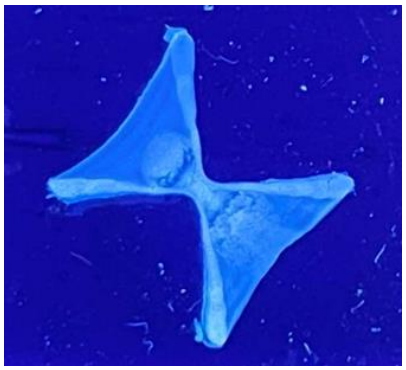

Figure E. 7 condition b

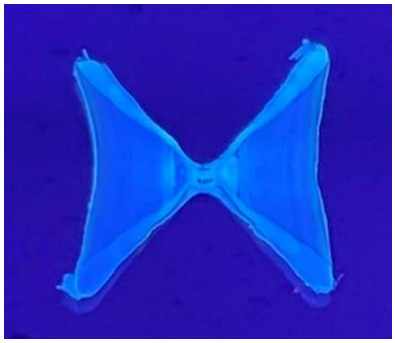

Figure E. 8 condition m

Figure E. 9 condition n

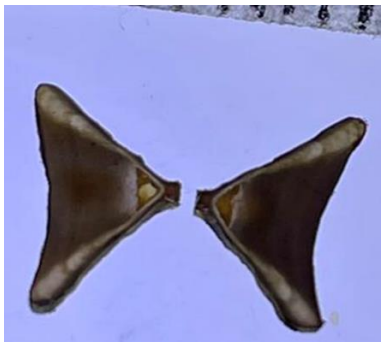

Sample NIWAWNGG013_B2

The cutting plane was mediolateral, and the cutting position was dorsal ventral.

The section’s thinness was 0.6 mm.

Figure E. 10 condition a

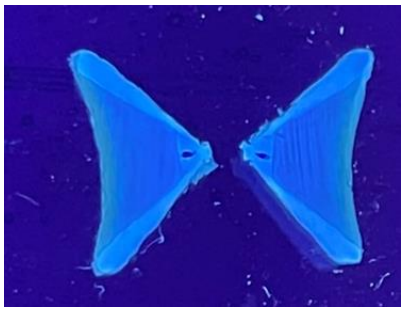

Figure E. 11 condition b

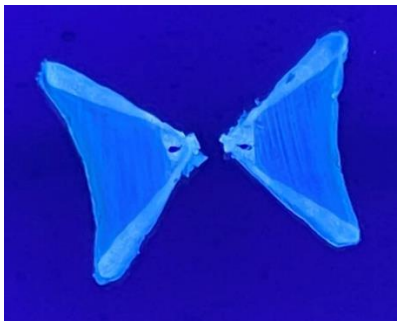

Sample ABKHGG002_B2

The cutting plane and position were the same as in Sample 4. The section's thinness was 0.6 mm.

Figure E. 12 condition a

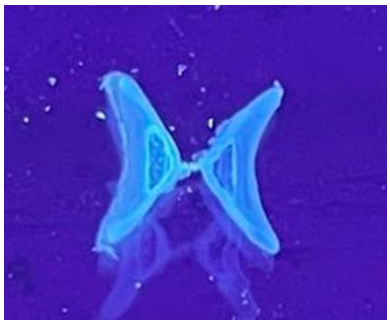

Figure E. 13 condition b

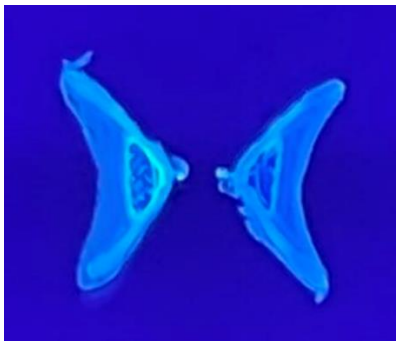

Sample MF220422-7_B2

The cutting plane and position were the same as in Sample 4. The section's thinness was 0.6 mm.

Figure E. 14 condition a

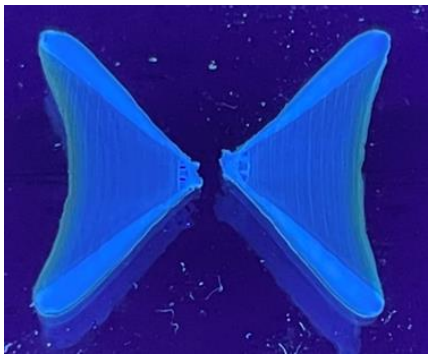

Figure E. 15 condition b

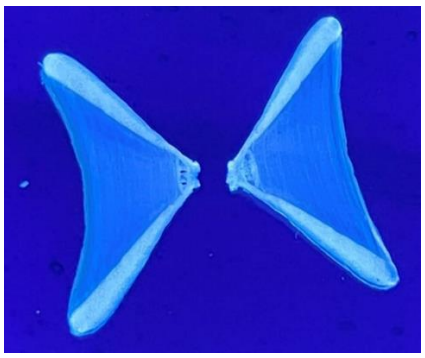

Figure E. 16 condition m

Figure E. 17 condition o

Sample NIWAWNGG006_T3

The cutting plane and the cutting position are the same as Sample 1. The section's thinness is 0.6mm.

Figure E. 18 condition a, but the sample was wet.

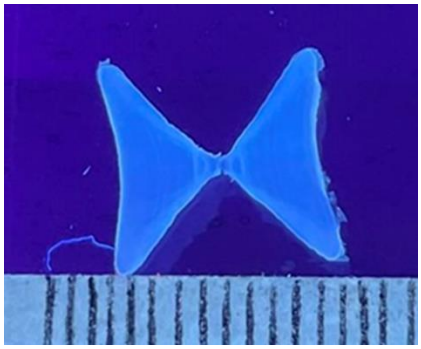

Figure E. 19 condition a, and the sample was dried.

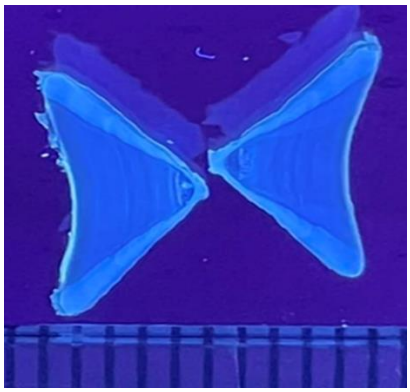

Figure E. 20 condition b, and the sample was wet.

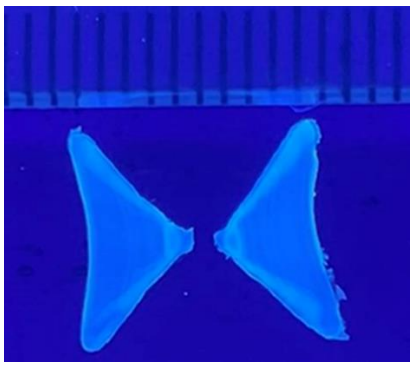

Figure E. 21 condition b, and the sample was dried.

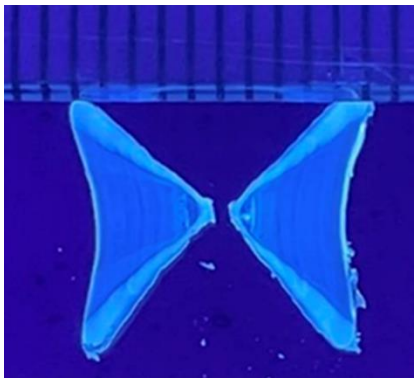

Figure E. 22 condition c, and the sample was wet.

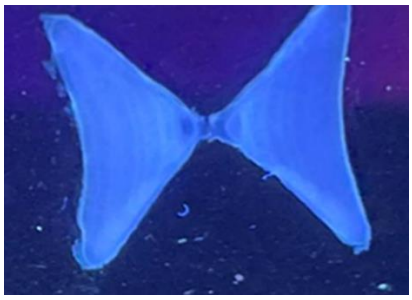

Figure E. 23 condition g with 70% ethanol immersion.

Figure E. 24 condition i with ethanol immersion.

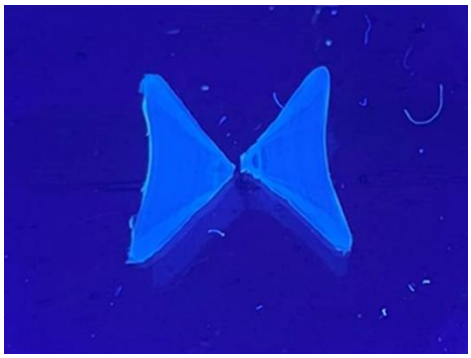

Figure E. 25 condition l with ethanol immersion.

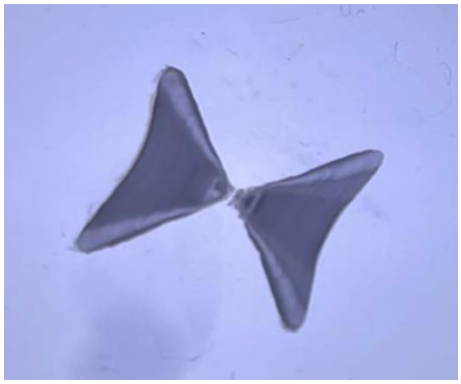

Sample ABKHGG004_T3

The cutting plane and position were the same as in Sample 1. The section's thinness was 0.6 mm.

Figure E. 26 condition a, and the sample was wet.

Figure E. 27 condition a, and the sample was dried.

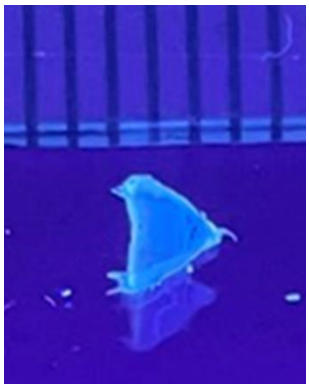

Figure E. 28 condition b, and the sample was wet.

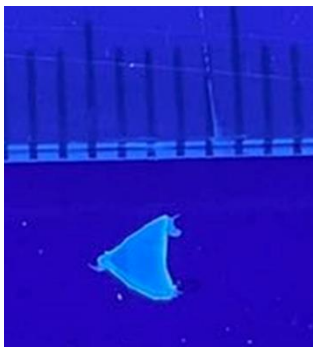

Figure E. 29 condition b, and the sample was dried.

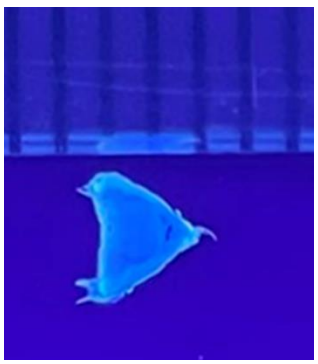

Figure E. 30 condition c, and the sample was wet.

Figure E. 31 condition e with ethanol immersion.

Figure E. 32 condition g with ethanol immersion.

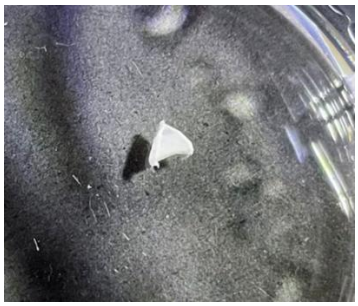

Figure E. 33 condition l with ethanol immersion.

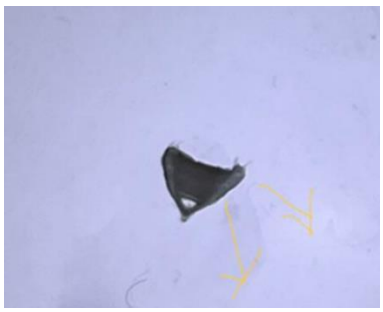

Sample JHARSOEGG18_B1

The cutting plane and position were the same as in Sample 4. The section's thinness was 1.5 mm.

Figure E. 34 condition k with ethanol immersion.

Figure E. 35 condition l with ethanol immersion.

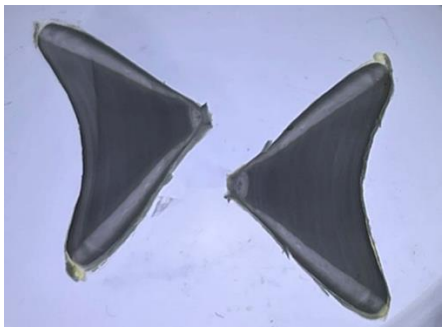

Sample ABKHGG004_B1

The cutting plane and position were the same as in Sample 1. The section's thinness was 0.6 mm.

Figure E. 36 condition m

Figure E. 37 condition n